

Coinage Metal Complexes for Near infrared Emission and Energy Transfer Photocatalysis

Dissertation

For the award of the academic degree of Doctor
of Natural Sciences (Dr.rer.nat)

from the Department of Chemistry and Chemical biology
of TU Dortmund University

submitted by

M.Sc. Sabyasachi Maity

Born on 10.06.1994 in Baharagora (Jharkhand), India

Dortmund, 2024

Submitted to the Department of Chemistry and Chemical Biology on: 25th October 2024

Reviewer of the written thesis:

1st reviewer: Prof. Dr. Andreas Steffen

2nd reviewer: Prof. Dr. Sebastian Henke

Examiners of the public doctoral colloquium:

1st examiner: Prof. Dr. Andreas Steffen

2nd examiner: Prof. Dr. Sebastian Henke

Chairman of the examination board: Prof. Dr. Max Martin Hansmann

Date of the public doctoral colloquium: 25th November 2024

For Maa and Pappa

„A ship is always safe at shore but that is not what it's built for.“

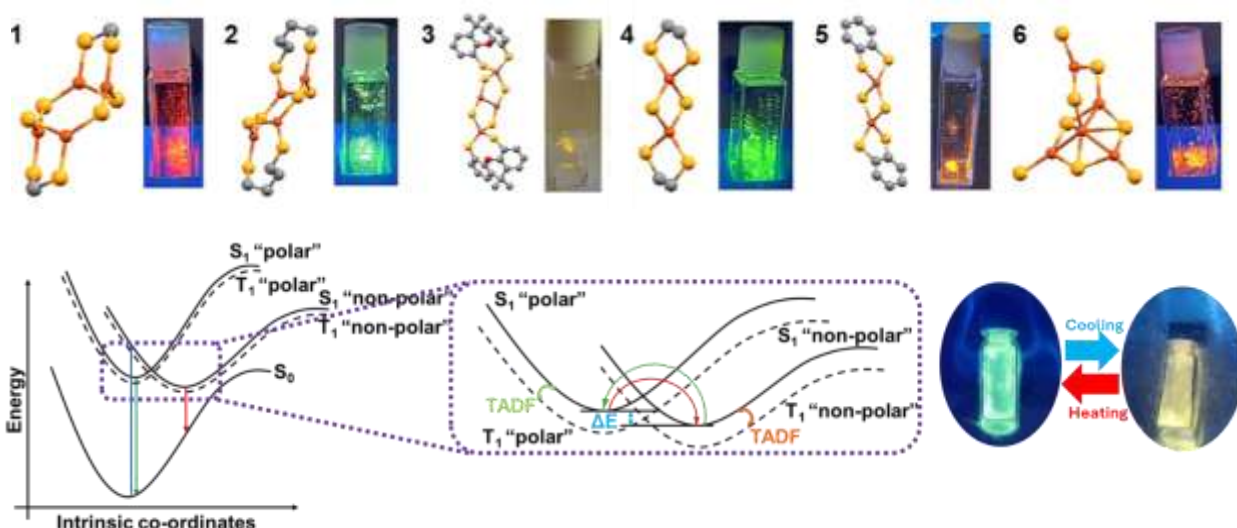
Albert Einstein

This thesis was written under the supervision of Prof. Dr. Andreas Steffen in the period from November 2020 to October 2024 at the TU Dortmund University in the Department of Inorganic Chemistry.

Abstract

Near-infrared- (NIR-) emitting compounds are an important subclass of luminescent materials because of their potential applications in sensors, night-vision displays, telecommunication, and solid-state lighting. However such type of compounds are mostly dominated by Ir or Pt based metal complexes which mostly emits via phosphorescence and thus have limited k_r . Thus, it's cheaper alternative based on Cu^I donor-acceptor complexes displaying low energy emissions via thermally activated delayed fluorescence (TADF) have gained interest over the years due to its potential to gain high k_r .

Herein we present comprehensive studies on synthesis, structure, and photophysical behavior of a series of luminescent Cu^I phosphide (-PPh₂) complexes supported by various mono- and bidentate phosphines displaying TADF behaviour. Depending upon the stoichiometry used **two** heteroleptic dimers and **four** heteroleptic polynuclear Cu^I clusters could be isolated from the self-assembly reaction of Cu^I-phosphide and phosphine ligand. X-ray structural analysis shows that the phosphide ligand is involved in the bridging - μ_2 or μ_3 coordination mode. In solid-state, these complexes are green-to-red (**1-2** & **4-6**) and NIR (**3**) photo-emitters with emission maxima varying over the range $\lambda_{\text{max}} = 515$ to 890 nm. Moderate to high photoluminescence quantum yield ($\Phi = 20-44\%$), with a relatively high radiative rate constant of up to $0.3 \times 10^6 \text{ s}^{-1}$, and short lifetimes $\tau = 0.1-34 \mu\text{s}$ were observed. Compounds **2** and **5** exhibit pronounced thermochromism and evidence of dual TADF behaviour originating from two different types of excited states.

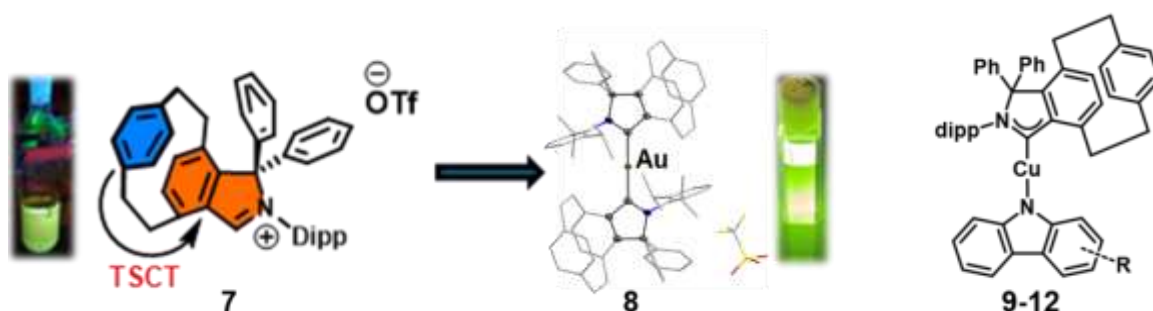


Another area of interest of photoluminescent transition metal complexes is the visible light catalysed organic reactions via energy transfer. The use of visible light instead of ultraviolet light generally required for traditional organic photochemistry has numerous benefits which includes lower cost and decreased energy demand of visible light sources; ability to conduct

photoreactions without specialized photoreactors or quartz glassware; and the ability to selectively photoexcite the transition metal photocatalyst without inducing undesired radical reactions of photochemically sensitive organic functional groups. The excited state energy as well as the lifetime of the photocatalyst are among the key factors for effective as well as efficient transformations.

We report a new sterically demanding, electrophilic [2.2]isoindolinophanyl-based carbene (iPC) that bears a [2.2]paracyclophane moiety. The iPC ligand is a very potent π -chromophore, which participates in low energy IL-“through-space”-CT transitions in $[\text{Au}(\text{iPC})_2]\text{OTf}$ (**8**) in the visible. The steric demand of the iPC leads to a high stability of **8** against air, moisture, or solvent attack, and ultralong-lived green phosphorescence with a lifetime of 185 μs is observed in solution. The beneficial photophysical and electronic properties of the iPC ligand, including a large accessible π surface area, were exploited by employing highly efficient energy transfer (EnT) photocatalysis in a [2+2] styrene cycloaddition reaction using **8**, which outperformed other established photocatalysts in comparison.

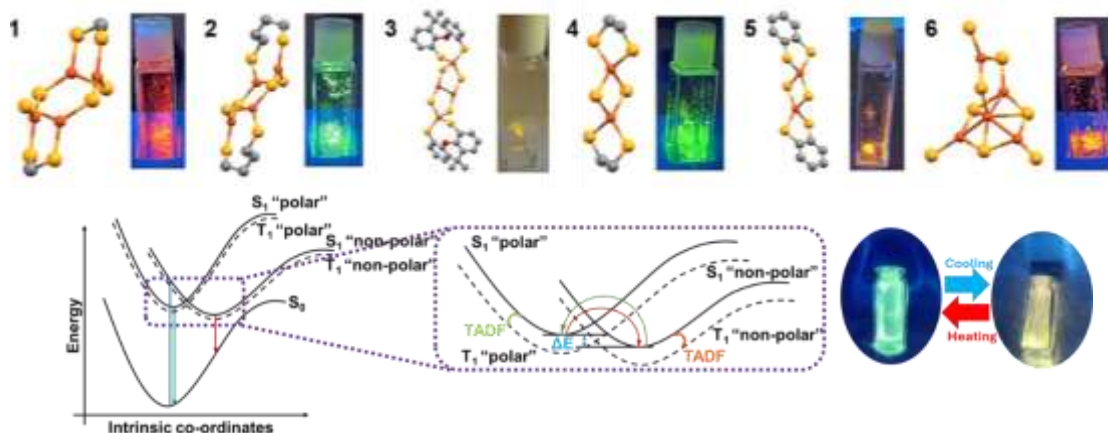
We also describe a series of linear copper(I) carbene carbazolate complexes (**9-12**) bearing the [2.2]isoindolino-phanyl-based carbene (iPC) ligand as a potent excited state π -acceptor. The compounds show efficient TADF from ligand-to-ligand charge transfer ($^1/3\text{LLCT}$) states with quantum yields of up to 0.8 and exceptional k_r of $0.8\text{-}1.9 \times 10^6 \text{ s}^{-1}$ that are among the fastest for Cu^{I} emitters, outcompeting traditional triplet emitters based on Ir^{III} and Pt^{II} . While yellow to orange emission is observed in single crystals, doping the complexes into polymer matrices or grinding shifts the luminescence into the deep red to near-IR. The mechanochromic TADF is due to the disruption of $\text{C-H} \cdots \pi$ interactions between the Cz and iPC ligands, which reduces the energy gap between the ground state and the $^1/3\text{LLCT}$ states.



Zusammenfassung

Im nahen Infrarot (NIR) emittierende Verbindungen sind eine wichtige Unterklasse lumineszierender Materialien aufgrund ihrer potenziellen Anwendungen in Sensoren, Nachtsichtgeräten, Telekommunikation und Festkörperbeleuchtung. Bei dieser Art von Verbindungen dominieren jedoch Metallkomplexe auf Ir- oder Pt-Basis, die hauptsächlich durch Phosphoreszenz emittieren und daher hinsichtlich ihrer strahlenden Ratenkonstante k_r limitiert sind. Die billigere Alternative auf der Basis von Cu^I-Donor-Akzeptor-Komplexen, die durch thermisch aktivierte verzögerte Fluoreszenz (TADF) eine niederenergetische Emission aufweisen, hat daher im Laufe der Jahre an Interesse gewonnen, da sie ein hohes k_r erreichen kann.

In dieser Arbeit stelle ich umfassende Studien zu Synthese, Struktur und zum photophysikalischen Verhalten einer Reihe von lumineszierenden Cu^I-Phosphid(-PPh₂)-komplexen vor, die zusätzlich von verschiedenen ein- und zweizähligen Phosphinen koordiniert werden und TADF-Verhalten zeigen. Je nach verwendeter Stöchiometrie konnten zwei heteroleptische Dimere und vier heteroleptische polynukleare Cu^I-Cluster aus der Selbstassemblierungsreaktion von Cu^I-Phosphid und Phosphinligand isoliert werden. Die Röntgenstrukturanalyse zeigt, dass der Phosphidligand μ_2 - oder μ_3 -verbrückend an die Kupferatome koordiniert. Im festen Zustand sind diese Komplexe grün-rote (**1-2 & 4-6**) und NIR(**3**)-Photoemitter mit Emissionsmaxima im Bereich von $\lambda_{\text{max}} = 515$ bis 890 nm. Es wurden mäßige bis hohe Photolumineszenzquantenausbeuten ($\Phi = 20$ -44 %) mit einer relativ hohen Strahlungsratekonstante von bis zu $0,3 \times 10^6 \text{ s}^{-1}$ und kurzen Lebensdauern $\tau = 0,1$ -34 μs beobachtet. Die Verbindungen **2** und **5** weisen einen ausgeprägten Thermochromismus und Anzeichen für ein duales TADF-Verhalten auf, das von zwei verschiedenen Arten angeregter Zustände herrührt.



Ein weiterer Bereich, in dem photolumineszente Übergangsmetallkomplexe von Interesse sind, sind durch sichtbares Licht katalysierte organische Reaktionen mittels Energietransfer. Die Verwendung von sichtbarem Licht anstelle von ultraviolettem Licht, das in der Regel für

die herkömmliche organische Photochemie benötigt wird, hat zahlreiche Vorteile. Dazu gehören niedrigere Kosten und ein geringerer Energiebedarf für sichtbare Lichtquellen, die Möglichkeit, Photoreaktionen ohne spezielle Photoreaktoren oder Quarzglasgeräte durchzuführen, und die Fähigkeit, den Übergangsmetall-Photokatalysator selektiv photozitieren zu können, ohne unerwünschte radikalische Reaktionen von photochemisch empfindlichen organischen Funktionsgruppen auszulösen. Die Energie des angeregten Zustands sowie die Lebensdauer des Photokatalysators gehören zu den Schlüsselfaktoren für effektive und effiziente Umwandlungen.

Wir berichten über ein neues sterisch anspruchsvolles, elektrophiles Carben auf [2.2]Isoindolinophanyl-Basis (iPC), das eine [2.2]Paracyclophan-Einheit trägt. Der iPC-Ligand ist ein sehr potenter π -Chromophor, der an niederenergetischen IL-„Durch-Raum“-CT-Übergängen in $[\text{Au}(\text{iPC})_2]\text{OTf}$ (**8**) im sichtbaren Bereich beteiligt ist. Der sterische Bedarf des iPC führt zu einer hohen Stabilität von **8** gegenüber Luft, Feuchtigkeit oder Lösungsmittelangriffen, und in Lösung wird eine ultralanglebige grüne Phosphoreszenz mit einer Lebensdauer von 185 μs beobachtet. Die vorteilhaften photophysikalischen und elektronischen Eigenschaften des iPC-Liganden, einschließlich einer großen zugänglichen π -Oberfläche, wurden durch den Einsatz hocheffizienter Energietransfer-Photokatalyse (EnT) in einer [2+2]-Styrol-Cycloaddition-Reaktion unter Verwendung von **8** ausgenutzt, die andere etablierte Photokatalysatoren im Vergleich übertraf.

Wir beschreiben außerdem eine Reihe linearer Kupfer(I)-Carben-Carbazolat-Komplexe (**9-12**), die den [2.2]Isoindolino-Phanyl-basierten Carben-Liganden (iPC) als potenten π -Akzeptor für angeregte Zustände tragen. Die Verbindungen zeigen effiziente TADF aus Ligand-zu-Ligand-Ladungstransfer-Zuständen ($^1/3\text{LLCT}$) mit Quantenausbeuten von bis zu 0,8 und außergewöhnlichen k_r von $0,8-1,9 \times 10^6 \text{ s}^{-1}$, die zu den schnellsten für Cu^{I} -Emitter gehören und herkömmliche Triplett-Emitter auf der Basis von Ir^{III} und Pt^{II} übertreffen. Während in Einkristallen eine gelbe bis orangefarbene Emission beobachtet wird, verschiebt sich die Lumineszenz durch Dotierung der Komplexe in Polymermatrizen oder durch Schleifen in den tiefroten bis nahen IR-Bereich. Die mechanochrome TADF ist auf die Unterbrechung der $\text{C-H} \cdots \pi$ -Wechselwirkungen zwischen den Cz- und iPC-Liganden zurückzuführen, wodurch die Energielücke zwischen dem Grundzustand und den $^1/3\text{LLCT}$ -Zuständen verringert wird.



List of Publications

„Highly Efficient Mechanochromic TADF in the Deep Red to Near-IR in Copper(I) [2.2]Isoindolinophanyl-Carbene Carbazolates“

A. M. T. Muthig, S. Maity, J. Krieger, A. Belyaev, B. Hupp, B. Ewald, J. Pflaum, A. Steffen, *Angew. Chem. Int. Ed.* **2024** (October) Submitted.

„A [2.2]Isoindolinophanyl-based Carbene (iPC) Ligand: Synthesis, Electronic and Photophysical Properties, and Application in Photocatalysis“

S. Maity, A. M. T. Muthig, I. Sen, O. Mrózek, A. Belyaev, B. Hupp, A. Steffen, *Angew. Chem. Int. Ed.* **2024**, 63, e202409115.

„Enhanced Intersystem Crossing, Yet Still Fluorescence Upon Introduction of Intermediate Charge-Transfer States in Hemicaged [Zn(bpy)₃]²⁺“

J. Kuhnt, M. Mitra, S. Maity, B. Hupp, C. M. Marian, A. Steffen, *J. Phys. Chem. Lett.* **2024**, 15, 6409.

Key Abbreviations and Symbols

A	Acceptor	ILCT	Interligand charge transfer
AC	Avoided crossing	iPC	[2.2]isoindolinophanyl-based carbene
acac	Acetate	(R)ISC	(Reverse) Intersystem Crossing
MeCN	Acetonitrile	k_r	Radiative rate constant
HMDS	Bis(trimethylsilyl)amine	LC	Ligand centered
br	broad signal	LLCT	Ligand-to-Ligand charge transfer
<i>t</i>Bu	<i>tert</i> -Butyl	LUMO	Lowest unoccupied molecular orbital
CPL	Circularly polarised luminescence	MAC	Monoamido-aminocarbene
CC	Cluster centered	MC	Metal centered
c	Concentration	mCP	9-(3-Carbazol-9-ylphenyl)carbazole
CAAC	Cyclic alkyl amino carbene	Me	Methyl
CAArC	Cyclic amino alkyl carbene	Mes	Mesityl
Cz	Carbazolate	MLCT	Metall-to-Ligand charge transfer
CMA	Carbene-metal-amide	MMLCT	Metal-Metal- to-Ligand charge transfer
CT	Charge transfer	NTO	Natural transition orbital
CI	Conical intersection	n.a.	not available
Et₂O	Diethyl ether	n.d.	not determined
d	Doublet	NIR	Near Infrared
D	Donor	NHC	<i>N</i> -Heterocyclic carbene
DAC	Diamidocarbene	NMR	Nuclear magnetic resonance
DCM	Dichloromethane	OLED	Organometallic light emitting diode
DET	Dexter-Energy transfer	PES	Potential energy surface
DFT	Density functional theory	Ph	Phenyl
Dipp	2,6-Diisopropyl	PL	Photoluminescence
EL	Electroluminescence	PMMA	Polymethylmethacrylate
ESI	Electronic supporting information	PS	Polystyrene
Et	Ethyl	<i>i</i>Pr	<i>iso</i> -Propyl
FCWD	Franck-Condon-weighted of states	RT	Room temperature
HOMO	Highest occupied molecular orbital	S	Singlet
HLCT	Hybrid local charge transfer	S₀	Singlet ground state
IC	Internal Conversion	S_n	nth Singlet excited state
		SSL	Solid-state lighting

sept	Septet
SOC	Spin orbit coupling
SVC	Spin vibronic coupling
T_m	mth Triplet excited state
TADF	Thermally activated delayed fluorescence
TD	Time dependent
THF	Tetrahydrofuran
Tf₂O	Trifluoromethanesulfonic anhydride
TSCT	Through-space charge transfer
UV	Ultraviolet
Vis	Visible light
VR	Vibrational relaxation
Zeff	Effective nuclear charge
ZFS	Zero-field splitting

Table of Contents

1. Introduction	1
1.1. Jablonski Diagram	3
1.1.1. Charge carrier recombination	5
1.1.2. Spin-orbit coupling and intersystem crossing	6
1.1.3. Phosphorescence	13
1.1.4. TADF	15
1.2. Photocatalysis	17
1.3. Phosphorescence starting from 4d and 5d transition metal complexes	24
1.3.1. [2+2] Cycloaddition of (E,E')-Dibenzyl Ether	26
1.4. NIR TADF Emission displayed by organic molecules	27
1.5. NIR Emission displayed by 4d and 5d transition metal complexes	30
1.6. NIR Emission displayed by Cu(I) complexes	33
2. Results and Discussions	36
2.1. Multimetallic Copper(I) Diphenylphosphides Displaying Thermally Activated Delayed Fluorescence (TADF) in the Visible to Near-IR	36
2.2. Hetero-di/multi-nuclear Copper(I) Diphenylphosphides Displaying Thermally Activated Delayed Fluorescence (TADF) in the Visible to Near NIR	44
2.3. A [2.2]Isoindolinophanyl-based Carbene (iPC) Ligand: Synthesis, Electronic and Photophysical Properties, and Application in Photocatalysis	67
2.4. Highly Efficient Mechanochromic TADF in the Deep Red to Near-IR in Copper(I) [2.2]Isoindolinophanyl-Carbene Carbazolates	74
3. Conclusion	82
4. References	86
5. Appendix	89

1. Introduction

Over the past years transition metal complexes have extensive application in the field of dye-sensitized solar cells, catalysis, photodynamic therapy (PDT), photothermal therapy (PTT), photoswitchers, bio-imaging etc.^[1] Another area which is emerging is their application in emitter materials specially as Thermally activated delayed fluorescence (TADF) emitters and near infrared (NIR) emitters.^[2] Applications of NIR light includes sensors, food and currency security etc. Further area which is of great interest is the application in information technology, in which the autofluorescence of and attenuation in, fiber optic cables impair the quality of data transport, light in the NIR range is thus a valuable tool. TADF emitters are used in OLEDs, where the emission occurs from the singlet state and thus this kind of emitter material can theoretically have 100 percent efficiency.^[3] Although, many TADF emitters based on transition metal complexes have been reported till date, but a few examples which emits red light or emits light in the NIR region have been reported till now.^[4,5] A general problem with the generation of NIR light with molecular emitters is that, compared to the generation of higher energy light, the radiative rate constant k_r is smaller, compared to the rate constant for non-radiative processes k_{nr} which increases according to the energy gap law (EGL). An additional area of interest of photoactive compounds is their usage in energy transfer (EnT) photocatalysis.^[6] Although the main principle behind EnT photocatalysis is the long-lived excited state species, excited state energy along with the efficiency of the photocatalyst is also of great importance.

For EnT Photocatalysis, NIR/deep-red emission, systems consisting of metal such as Ruthenium, Platinum and Iridium and ligands as bipyridine (bpy) derivatives, NHC, and CAACs, are mostly dominated which is being discussed in the next subchapters. The usage of coinage metals which are comparatively cheaper and also do not undergo non-radiative processes due to filled d-orbital are less explored. Also at the same time new types of ligands apart from bpy derivatives or NHCs are also of immense interest because of their interesting potential properties and behaviours.

The first chapter delve with tetrameric Cu(I) complexes based on strong donor phosphide ligand, their variable geometry, coordination, and first overview on the photophysics of such complexes. These complexes show moderately efficient TADF behaviour in the green-to-red/NIR region. Second chapter deals with synthesis and photophysical behaviour of dimeric and cluster based Cu(I) systems displaying efficient TADF behaviour. These complexes consists of strong cuprophilic interactions leading high SOC and thus high k_r at room temperature. Third chapter unveils synthesis of a new ligand i.e. iPC which is a derivative of

the known CAArCs. Its steric and electronic properties along with its photophysical insights are explored along with the synthesis of a Au(I) homoleptic complex which is stable in ambient conditions, and also outperforms well known photocatalyst in the [2+2] Cycloaddition of (E,E')-dicinnamyl ether. The fourth chapter revisits the new ligand along with its various Cu(I) metal-based complexes along with their photophysical insights, mechanochromic behavior, and their potential application in OLEDs have been displayed. The final chapter summarizes findings, presents a future outlook, and notes challenges.

It is important to say that the good things contained herein are undoubtedly a product of the inspiration imparted by my mentors, collaborators, colleagues and friends, while the errors and missteps are all my own.

1.1. Jablonski Diagram

In order to understand and optimize the photophysical properties of an emitter and to establish a structure-property relationship, a basic knowledge of photophysics is essential. The range of electromagnetic radiation detectable to the human eye extends from approx. 25000 cm^{-1} to 13333 cm^{-1} which, when transferred to molecules, is reflected in the energetic difference between different electronic states. Transitions between different electronic states are therefore particularly important for the generation of visible light at the molecular level, which can be visualized very well in a Jablonski diagram which is a drawing of molecular electronic state energy levels, with singlet and triplet states in separate columns. Often vibrational sublevels are shown schematically as well. Radiative transitions from one level to another are indicated by straight arrows and non-radiative ones by dot/dash arrows.

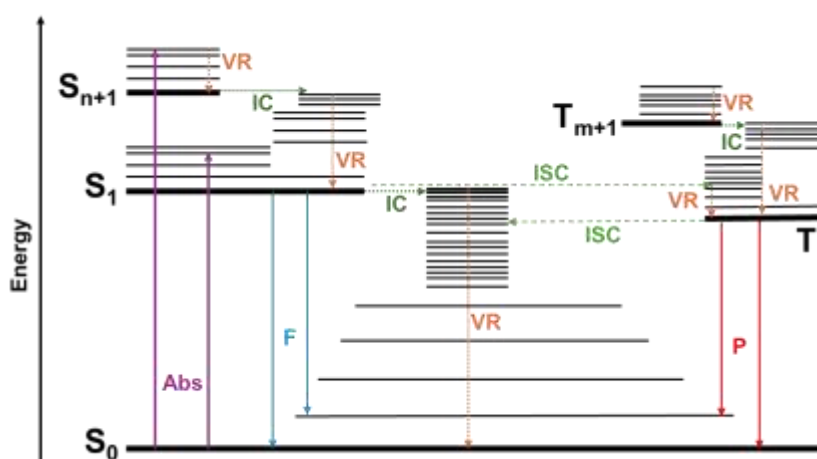


Figure 1. A simplified form of Jablonski diagram of a system with ground state S₀, showing the absorption (Abs), fluorescence (F), phosphorescence (P), internal conversion (IC), intersystem crossing (ISC) and vibrational relaxation (VR) between different electronic states and their vibration levels. Created based on Montalti et al.^[7]

As a rule, the colour of the emission of a luminophore results from the energy difference between its singlet ground state S₀ and the lowest excited singlet state S₁, or the lowest excited triplet state T₁. As it can be seen in the Jablonski diagram in Figure 1, a distinction is made depending on whether the emission of a photon results from the transition between S₁→S₀ (fluorescence (F)) or from T₁→S₀ (phosphorescence (P)). The excited states S_n and T_m, with n, m ≥ 1, are populated, for example, after absorption (Abs) of a photon of a suitable energy or after charge carrier recombination in electrically operated components. According to the Kasha rule, the higher excited states S_{n+1} subsequently decay rapidly to the lowest vibrational level of the lowest excited singlet state S₁.^[8] This rapid decay takes place through internal conversion (IC) and vibrational relaxation (VR), which occur within a very short time of 10⁻¹¹ - 10⁻⁹ s and 10⁻¹⁴ - 10⁻¹² s respectively and are therefore the fastest processes. The IC from S₁ to S₀ is forbidden at a large energy distance between the two states and

fluorescence becomes competitive (10^{-9} - 10^{-6} s). Alternatively, decay from S_n to T_m is also possible via intersystem crossing (ISC). Analogous to the decay of excited S_{n+1} , the higher excited states T_{m+1} also decay via fast IC and VR, therefore the lowest excited triplet state T_1 is quickly populated. Phosphorescence can also be competitive with non-radiative ISC if there is a large energy gap between T_1 and S_0 .^[7] ISC is particularly important when excited states are generated by charge carrier recombination in electrically driven components, because T_m and S_n cannot be converted into each other, and also result in a significant loss in efficiency.^[3] Two feasible and later discussed emission mechanisms in the upcoming subchapters, which utilize all excitons introduced into electrically operated excitons are phosphorescence and thermally activated delayed fluorescence (TADF). In both emission mechanisms, a red shift can be achieved by lowering the energy difference between the singlet ground state S_0 and the lowest excited states which can be achieved for molecular emitters using strategies such as the expansion of their π -systems, the introduction of push-pull effects and the substitution with higher homologues.^[9] However, at the same time as the red shift, there is a drop in k_r , which represents the main problem for NIR emitters. The other issue which arises is the non-radiative processes become more frequent, causing k_{nr} to increase disproportionately. As mentioned above, fluorescence is competitive at large $\Delta E(S_1-S_0)$, whereas non-radiative IC of $S_1 \rightarrow S_0$ dominates at smaller $\Delta E(S_1-S_0)$. A similar behaviour is observed for phosphorescence and ISC of $T_1 \rightarrow S_0$, where the latter dominates at small $\Delta E(T_1-S_0)$ predominates. The respective deactivation processes starting from S_1 and T_1 result in a complex interplay between radiative and non-radiative processes. With the exclusion of photoreactions, the quantum yield Φ , is calculated using Eq. (1),

$$\phi = \frac{k_r}{k_r + k_{nr}} \quad \text{Eq.(1)}$$

Emitters in an OLED must emit as quickly and efficiently as possible, whereby k_{nr} should be as low as possible. For the ideal limiting case of $k_r \gg k_{nr}$. This results in an approximate quantitative quantum yield of 1. k_r must not only be significantly greater than k_{nr} , but ideally should also have a high value of $> 10^5 \text{ s}^{-1}$ (corresponding to $\tau_r < 10 \mu\text{s}$).

1.1.1. Charge carrier recombination

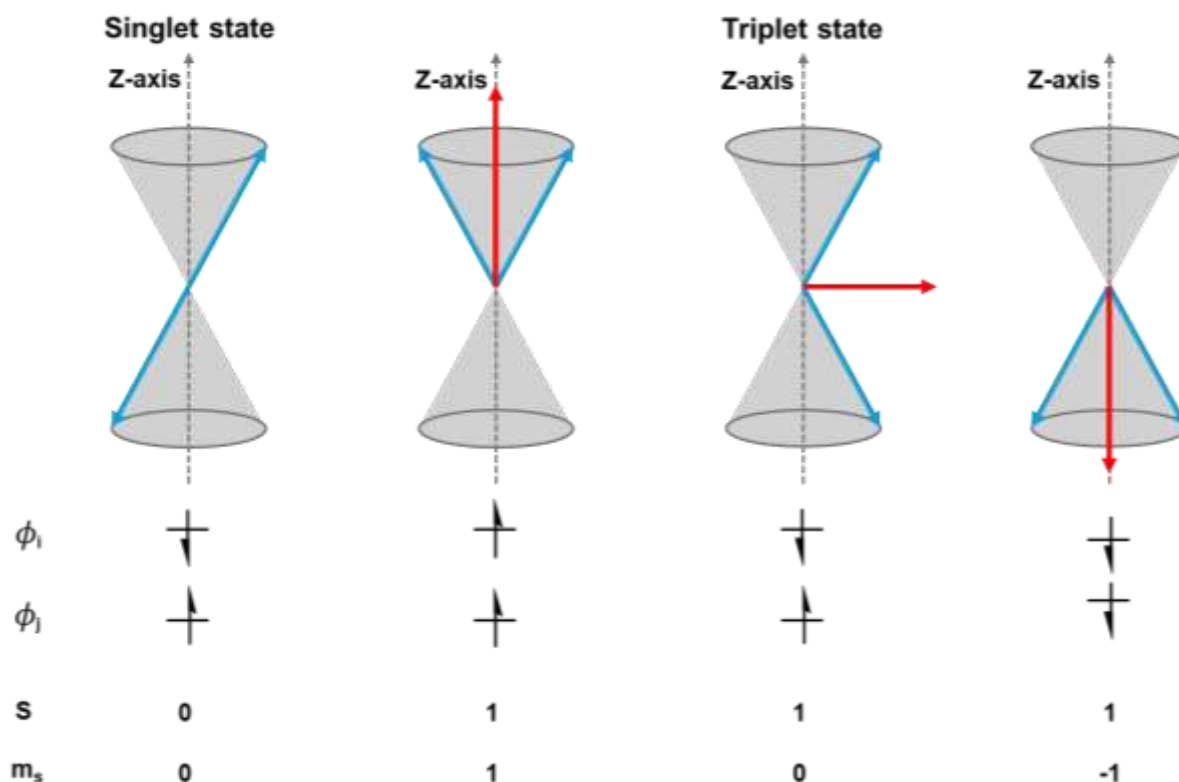


Figure 2. Vectorial representation of the individual spins of electrons in singlet and triplet states with associated spin quantum number S and magnetic quantum number m_s , created based on Turro et al.^[10] The precession of the two spin vectors of the individual electrons (blue arrow) around the magnetic z-axis and the total spin vector resulting from the combination of these individual spins (red arrow) are shown.

Charge carrier recombination in electrically operated components is a statistical process and generates excitons in a ratio of 25% S_n and 75% T_m .^[11] This can be understood from the possible arrangement of two electrons after recombination as shown in Figure 2. To simplify, a system with only two wave functions ϕ_i and ϕ_j is assumed. The distribution of two electrons, as particles with spin $\pm 1/2$, to the two wave functions results in the four possibilities as shown, with spin quantum number $S = 0; 1$ and magnetic quantum number $m_s = 0; \pm 1$.

If no paths are available for coupling of triplet and singlet states, the energy used to generate the 75% T_m would be lost as heat. The conversion of S_n and T_m into each other or T_1 into S_0 are therefore relevant processes that must be possible in modern emitter materials. These processes, i.e. ISC and phosphorescence, in which the spin multiplicity changes, are however prohibited according to the spin selection rule for electronic transitions. However, according to higher-order perturbation theory, there are several mechanisms by which these become possible such as the direct coupling of spin and orbital angular momentum

(spin-orbit coupling, SOC), spin-vibronic coupling (SVC) and conical intersection (CI), which occur during geometry changes, can contribute to the multiplicity change.

1.1.2. Spin-orbit coupling and intersystem crossing

From a classical point of view, the processes taking place under spin reversal violate orbital angular momentum conservation and are therefore prohibited according to the selection rules for electronic transitions. However, by coupling spin and orbital angular momentum - resulting in a total orbital angular momentum - such transitions are made possible. When considering the Schrödinger equation in higher-order perturbation theory ($> 0^{\text{th}}$ order), this spin orbit coupling (SOC) can be found in perturbation correction terms, where the associated SOC operator H_{SO}^{eff} can be described in a one-centre approximation according to Eq. (2).^[12]

$$H_{SO}^{eff} = \frac{1}{2m_e^2 c^2} \sum_A \sum_n \frac{Z_A^{eff}}{r_{An}^3} \hat{l}_n \hat{s}_n \quad \text{Eq.(2)}$$

Here \hat{l}_n corresponds to the orbital angular momentum operator and \hat{s}_n to the spin operator, Z_A^{eff} is the effective nuclear charge and r_{An} is the distance of the electron n to the nucleus A . The natural constants m_e and c can be summarized with Z_A^{eff} and, with the averaged cubic radial distribution of an electron (r^{-3}), result in the spin orbit coupling constant ζ , which is different for each nucleus (Eq. (3)).^[12]

$$\zeta = \frac{Z_A^{eff}}{2m_e^2 c^2 r^3} \quad \text{Eq.(3)}$$

Since the extent of the SOC (E_{SO}) between an initial and a final state, described by the wave functions ψ_i and ψ_f , according to Eq. (4)^[10] is dependent on the application of H_{SO}^{eff} to a wave function, the use of Slater atomic orbitals results in a dependency of E_{SO} proportional to Z^4 (Z = atomic number), as the expected value of r^{-3} with Slater atom orbitals contains Z^4 .^[13]

$$E_{SO} = \langle \Psi_i | H_{SO}^{eff} | \Psi_f \rangle \quad \text{Eq.(4)}$$

This in turn is responsible for the so-called heavy atom effect, which is why a drastic increase in SOC is assumed with increasing nuclear charge number. The extent of the SOC is in turn of great importance for the intersystem crossing (ISC), which becomes clear when considering the transition rate k_{ISC}^{nm} of a transition from a state S_n to a state T_m according to Eq. (5).^[14]

$$k_{ISC}^{nm} = \frac{2\pi}{\hbar} \langle S_n | \hat{H}_{SO} | T_m \rangle^2 \cdot FCWD \quad \text{Eq.(5)}$$

or SOC also defined as a mixture or perturbation of S_n and T_m with one another and is triggered by the interaction of spin and orbital angular momentum of an electron. The rate constant k_{ISC} for the transition from an initial state Ψ_i to a final Ψ_f by means of ISC is represented by Fermi's golden rule as Eq. (6)^[10]

$$k_{ISC}(i \rightarrow f) = \frac{2\pi}{\hbar} \langle \Psi_i | \hat{H}_{SO} | \Psi_f \rangle^2 \sum \langle \theta_{i,0} | \theta_{f,n} \rangle^2 \quad \text{Eq.(6)}$$

In addition to the size in SOC, this rate also depends on the Franck-Condon weighted density of states (FCWD), which describes the density of states available for coupling. On one hand, a high density of states enables a high k_{ISC}^{nm} due to the increased probability of a large coupling between two states and, on the other hand, a summation of many small couplings ultimately leads to a large effective coupling and thus to a large transition rate. Furthermore, the character of the singlet or triplet states involved is also decisive for k_{ISC}^{nm} , which was described qualitatively by El-Sayed using the example of nitrogen-containing heterocycles.^[15] El-Sayed's rule states that the nature of the excited state must change during the ISC process, whereby the spin reversal can be compensated by a changed orbital occupation and thus the total orbital angular momentum is conserved. This rule is not only applicable to nitrogen-containing heterocycles, but can also be applied to a wide variety of organic molecules. The El-Sayed rule will therefore be illustrated below using acetone as an example molecule. Figure 3 shows a section of the molecular orbital diagram of the CO fragment of acetone.

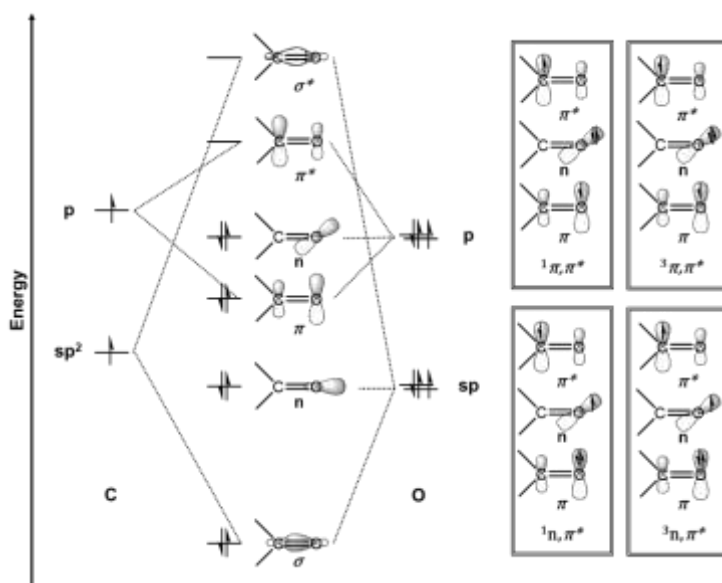


Figure 3. Section of the molecular orbital diagram of the CO fragment of acetone and the orbital occupation of the excited states $^1n, \pi^*$, $^3n, \pi^*$, $^1\pi, \pi^*$ and $^3\pi, \pi^*$.

By exciting an electron from the HOMO (n -orbital) into the LUMO (π^* -orbital), a singlet ($^1n,\pi^*$) or triplet ($^3n,\pi^*$) state can be formed. Similarly, a singlet ($^1\pi,\pi^*$) or triplet ($^3\pi,\pi^*$) state can be formed by exciting an electron from the HOMO-1 (π -orbital) into the LUMO (π^* -orbital). The resulting occupation of the orbitals is also shown in Figure 3.

This shows why the transition $^1(n\pi^*) \rightarrow ^3(\pi\pi^*)$ is more permissible and therefore faster than the transition $^1(n\pi^*) \rightarrow ^3(n\pi^*)$ in the case of acetone, as the spin reversal in the latter cannot be compensated by orbital changes, which is illustrated in Figure 4. The same reasoning applies to the $^1(\pi\pi^*) \rightarrow ^3(n\pi^*)$ transition allowed by El-Sayed and the $^1(\pi\pi^*) \rightarrow ^3(\pi\pi^*)$ transition forbidden by El-Sayed.

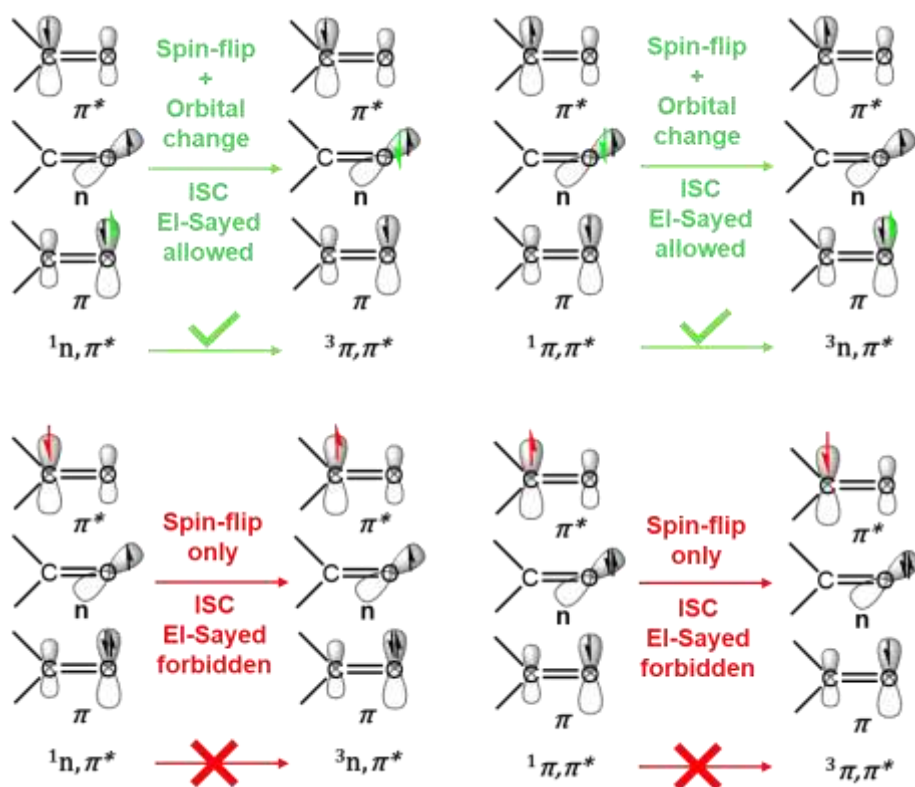


Figure 4. Illustration of El-Sayed's rule to explain possible ISC transitions in purely organic molecules using the example of acetone.

For NIR emitters, the last term of Eq. (6), the FCWD, is particularly important, as the so-called energy gap law (EGL) for nested potential curves, also known as the Siebrand rule, is derived from it.^[15,16,17]

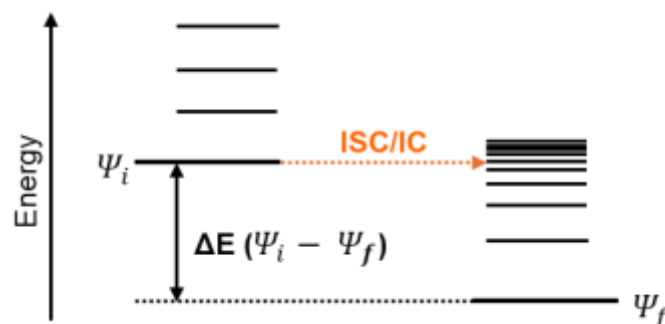


Figure 5. Simplified Jablonski diagram to illustrate the state densities of the states Ψ_i and Ψ_f involved in a non-radiation transition, such as intersystem crossing (ISC) or internal conversion (IC).

Even if, as can be seen in Figure 5, the density of states decreases for a non-radiative transition between the two states Ψ_i and Ψ_f as the energy gap $\Delta E(\Psi_i - \Psi_f)$ decreases, the overlap integral of the vibratory wave functions increases, and thus the FCWD, which also increases the k_{ISC} . On one hand, this means that the S_n and T_m can be converted into each other, but it also reveals a problem when moving to lower-energy emitters. The $k_{ISC} (T_1 \rightarrow S_0)$ can be regarded as the main component for the k_{nr} in triplet emitters if photoreactions and other quenching processes are excluded. The EGL also applies in parallel to fluorophores. Here, $k_{IC} (S_1 \rightarrow S_0)$ can be regarded as the main component for the k_{nr} and the Hamiltonian \hat{H}_{IC} , which couples the nuclear and electron motion as a perturbation operator, is used for calculation via Eq. (6).^[18]

In the literature, the increase in non-radiative decay when moving to lower-energy emitters is often reduced due to the EGL. In fact, however, it only applies strictly in the case of weak coupling. In the case of weak coupling, or nested potential wells are present in rigid molecules whose excited states undergo only little structural distortion compared to the electronic ground state, i.e. have a small reorganization energy λ_R . The effect of λ_R on the potential wells or the FCWD is shown in Fig. 6 or Eq. (7), with Boltzmann constants k_B and temperature T .^[12,16]

$$FCWD = \frac{1}{\sqrt{4\pi\lambda_R k_B T}} \exp \left[-\frac{(\Delta E + \lambda)^2}{4\lambda_R k_B T} \right] \quad \text{Eq.(7)}$$

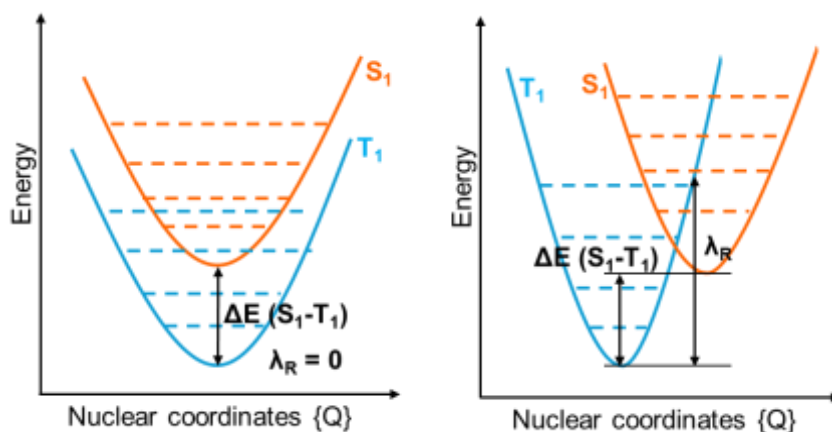


Figure 6. Schematic representation of weak (left) and strong (right) coupling limits, based on Penfold et al.^[12]

In the case of weak coupling, the FCWD follows an exponential dependence on the energetic distance between the potentials. In the case of strong coupling, i.e. with excited emitter molecules, which undergo large structural changes in their molecular structure compared to the ground state, the potential well of their excited states is strongly shifted along the nuclear coordinate Q . This occurs, for example, in charge transfer (CT) transitions. In such a case, a crossing of the potential energy surface (PES) can occur. The k_{ISC} then has a Gaussian dependence on $(\Delta E + \lambda)$, which leads to cases in which k_{ISC} decreases with smaller ΔE , i.e. during the transition to low-energy emission.^[19]

In addition to direct SOC, there are other mechanisms that should not be neglected, which couple S_n and T_m states with each other, but also decreases ΔE between low excited states and S_0 for increasing non-radiative decay. Both SVC and CI require molecular vibrations, i.e. the occupation of higher vibrational levels, which is possible at room temperature (RT). SVCs are simple and easy to describe for the molecular vibrations of ketones and simple aromatics.^[20] For larger systems, the investigation becomes complicated due to the large number of possible molecular vibrations, which is why we will again limit ourselves to acetone as an example. Figure. 7 can be used to explain how in acetone, despite the absence of a heavy atom, an El-Sayed forbidden transition between the S_1 with $^1\pi, \pi^*$ character and the T_1 with $^3\pi, \pi^*$ character is possible.

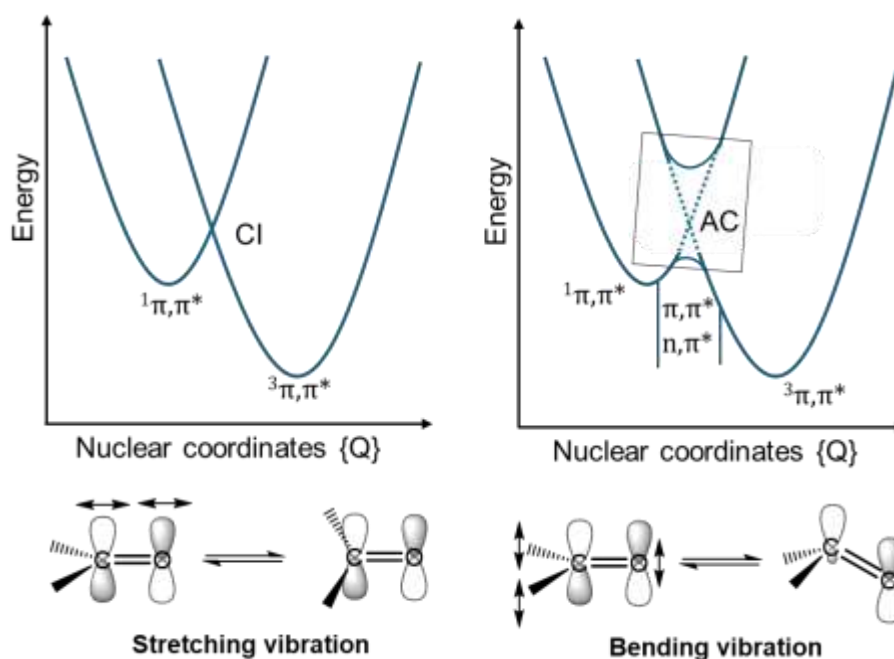


Figure 7. Illustration of the effect of different molecular vibrations on the ISC between electronic states using the example of the acetone molecule. Shown are the stretching vibration, which forms a conical intersection (CI) between $^1\pi,\pi^*$ - and $^3\pi,\pi^*$ - state is formed, as well as the bending vibration, through which the $^3n,\pi^*$ can mix in and an avoided crossing (AC) is formed. Created on the basis of Turro et al. and Klessinger et al.^[10,21]

The potentials associated with the states are shown along two specific molecular vibrations, i.e. structural distortion of the molecular geometry of the acetone molecule. The transition $^1\pi,\pi^* \rightarrow ^3\pi,\pi^*$ in acetone is possible via the bending vibration (Figure. 7, right), as this gives the π -orbital on the carbon atom of the π -bond a sp^n hybrid character. This character makes it possible to mix in an energetically higher n,π^* -state and the transition becomes more El-Sayed-allowed. This is referred to as the formation of an avoided crossing (AC). The mixing coefficient π_m between two states is given by Eq. (8):

$$\lambda_m = \left| \frac{\langle n, \pi^* | H | \pi, \pi^* \rangle^2}{E(\pi, \pi^*) - E(n, \pi^*)} \right| \quad \text{Eq.(8)}$$

It is noticeable that the first-order mixing of two states Ψ_i and Ψ_f increases with smaller $\Delta E[(\Psi_i)-(\Psi_f)]$ between the states.^[22] Energetically close, higher-order states of suitable symmetry therefore help with ISC by mixing. This fact helps in the design of emitter materials. Compounds or substituents can be deliberately selected in order to introduce states or change their energetic position. These then help with triplet harvesting in order to convert the 25% singlet excitons generated into triplets, which can then be used via phosphorescence. Conversely, the matching states also help to enable reverse-ISC (RISC), where the emitter molecules are transferred from their excited T_1 to the energetically close S_1 , which enables singlet harvesting or TADF.

However, it is also conceivable here that higher-energy states mediate non-radiative processes to the ground state, which can mean a further increase in k_{nr} for NIR emitters. By lowering the energy of S_1 or T_1 using established strategies, the higher S_{n+1} or T_{m+1} states are also lowered. As a result, λ_m is increased and the radiating states are transferred to the S_0 in a non-radiating manner via an AC.

In contrast to the bending oscillation, no rehybridization takes place in the stretching oscillation (Figure. 7, left); the two potentials cross and form a CI. When passing through a CI, there is a probability that energetically higher states "funnel" non-radiatively into lower ones. A semi-classical description of such intersections is possible using the Landau-Zener model. The probability p_{12} of remaining in the original state during a passage through a crossing point, i.e. a molecular geometry and energy in which two states are indistinguishable, is given by equation (9).^[23]

$$p_{12} = \left(\frac{-4\pi^2 V_{12}^2}{\hbar v |s_1 - s_2|} \right) \quad \text{Eq.(9)}$$

Included are the electronic coupling term V_{12} at the crossing point, the Planck constant \hbar , the core velocity v (not frequency ν) with which the crossing point is approximated, and $|s_1 - s_2|$ is the difference between the slopes of the two PES. The more different the gradient, the more likely the system remains in its original state. The electronic coupling term V_{12} is very small for transitions between states of different multiplicities. CI are therefore more relevant for IC, but are also relevant for ISC. At crossings, the Franck-Condon factors become large, since amplitudes of the vibrational wave functions of energetically higher excited vibrational levels are large at the edges. Vibrational levels of states that are energetically close to the intersection will therefore have a non-negligible contribution. This aspect also means that for organic molecules, which exhibit little operational SOC, ISC via CI is an effective way to non-radiatively transfer triplets generated in electrically driven devices, for example, to the S_0 state.^[24]

Although the probability of undergoing a state change via CI is not directly dependent on the energy gap $\Delta E[(\Psi_i)-(\Psi_f)]$, the occurrence of these crossings still potentially leads to an increase in the non-radiative rate constant k_{nr} . For energetically close PESs, such as those present in NIR emitters, CIs are undergone more frequently and non-radiative decay becomes more likely, even in flexible systems that circumvent the Siebrand rule.^[25]

In summary, non-radiative decay is favoured when radiative states are lowered, which is a fundamental contradiction to the existence of efficient NIR emitters. It may be worthwhile to identify the mechanisms that transfer the excited states non-radiatively to the S_0 state in individual cases and to reduce them specifically by varying the molecular design. However,

this is sometimes very complicated and presents synthetic challenges. A high radiative rate constant k_r is generally useful for emitter molecules, but given the increase in non-radiative processes when going to NIR emitters, maximizing k_r becomes even more important to compensate for the increasing non-radiative rate constant k_{nr} .

After considering which processes contribute to the efficient population of radiative states and which challenges arise for the design of efficient NIR emitters, radiative processes and their dependence on the emission energy are now considered.

1.1.3. Phosphorescence

Like ISC, phosphorescence is a spin-forbidden process between states of different spin multiplicity. However, SOC ensures that the pure multiplicities are cancelled by mixing in further energetically higher states of different multiplicities. As shown in Figure. 8, singlet states are added to T_1 and excited triplet states are added to S_0 .

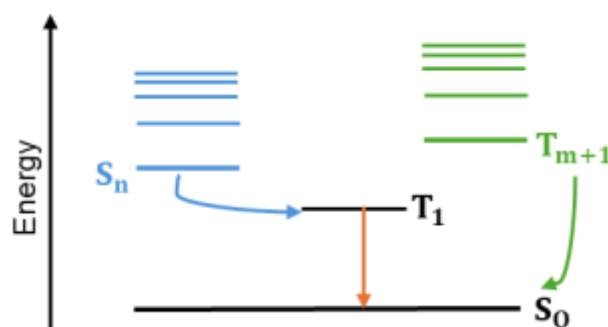


Figure 8. Simplified Jablonski diagram to illustrate the addition of excited S_n or T_{m+1} states to the T_1 or S_0 states.

The radiative rate constant of phosphorescence k_p is given by Eq. (10), which is divided into three terms.^[26]

$$k_p = \frac{4e^2}{3c^2\hbar^4} (\Delta E(T_m - S_0))^3 \cdot \left[\sum_{n=0}^{\infty} \frac{\langle S_n | \hat{H}_{SO} | T_1 \rangle \langle S_0 | \sum_n \vec{M} | S_n \rangle}{\Delta E(S_n - T_1)} + \sum_{m=1}^{\infty} \frac{\langle S_0 | \hat{H}_{SO} | T_m \rangle \langle T_m | \sum_m \vec{M} | T_1 \rangle}{\Delta E(T_m - S_0)} \right]^2 \quad \text{Eq.(10)}$$

Term 1 (red) indicates the relationship between k_p and the smaller energy gap $\Delta E(T_1-S_0)$. This term decreases exponentially with decreasing energy. This reveals a further challenge in addition to the suppression of non-radiative processes: in order for k_p to remain competitive with the non-radiative rate constant k_{nr} , the contributions of the other terms 2 (blue) and 3 (green) must be large. The second term (blue) indicates the mentioned admixture of excited singlet states S_n to T_1 and the third (green) the proportion of admixture of excited triplet states T_m to S_0 . Both terms contain the mixing coefficient λ_m of the interfering states, which corresponds to the break, as well as the transition dipole moment \vec{M}

of the transitions of the respective interfering states S_n or T_m to the interfered S_0 or T_1 . The mixing coefficient λ_m is dependent on the integral of the direct SOC $\langle \Psi_i | \hat{H}_{SO} | \Psi_f \rangle$ and the energy difference $\Delta E(S_n-T_1)$ or $\Delta E(T_m-S_0)$. The greater the direct SOC and the smaller the energy difference, the greater the admixture of the respective states.

By mixing, the "pure" multiplicities of the S_0 and T_1 states are cancelled and large transition dipole moments \vec{M} of selected transitions between excited states $S_n \rightarrow S_0$ or $T_m \rightarrow T_1$ can be used. Intensity is "borrowed" from the allowed $S_n \rightarrow S_0$ or $T_m \rightarrow T_1$ transitions to the $T_1 \rightarrow S_0$ transition. The S_n or T_m states that are particularly relevant here are those that have a matching orbital constitution to the S_0 or T_1 . In contrast to the transition between states of different multiplicity, however, orbital overlap is important here, as no change in spin is necessary and the orbital angular momentum must therefore also be maintained. The admixture of higher states allows in part a high oscillator strength f for the $T_1 \rightarrow S_0$ transition and can compensate the exponential drop in k_P during the transition to low-energy emission in term 1 (red).

As mentioned, the mixing coefficient λ_m increases with a larger operational SOC, which in turn occurs for the radiative transition $T_1 \rightarrow S_0$ analogous to the factors discussed for ISC. Of particular interest is the dependence of the Hamiltonian \hat{H}_{SO} on the spin-orbit coupling constants ξ_c of the atoms involved. The large SOC constants of heavy atoms are particularly effective when their orbitals are involved in the transition. This is the case, for example, when excited states have MLCT character and heavy metals such as Ir^{III} , Pt^{II} , Au^{I} or Os^{II} are involved.

The use of complexes of these heavy transition metals for triplet emission offers a further advantage resulting from the availability of their d orbitals. The large number of energetically close d-orbitals results in a large number of possible states, all of which are potentially suitable for perturbing the low-energy states. The enormous density of states can be illustrated using the example of an octahedral Ir^{III} complex. Involving only the 5d-metal orbitals and the boundary orbitals of the ligands already results in 18 S_n - and 54 T_m - states, which are energetically close to each other. These metal-to-ligand charge transfer (MLCT), ligand-to-ligand charge transfer (LLCT) or interligand charge transfer (ILCT) states can, with the right design, even achieve large mixing coefficients λ_m of up to 0.1 and thus benefit from the high rate constant of spin-allowed fluorescence k_F . Even without a single contribution of this size, the summation over smaller contributions leads to the effective elimination of the "pure" multiplicity of T_1 or S_0 simply due to the large number of states.^[13] Here, too, the states with $^3\text{MLCT}$ (d, π^*) character are more relevant, as these can mix particularly

efficiently with other ^{1,3}MLCT states.^[27] The result is that transition metal-based triplet emitters certainly realise phosphorescence rate constants $k_p > 10^5 \text{ s}^{-1}$. Systems are also known in the red and NIR range in which k_p is competitive with the non-radiative rate constant k_{nr} , i.e. both rates are of the same order of magnitude.^[28] Many NIR emitters used today are therefore based on complexes of these metals. In comparison, typical organic triplet emitters offer $k_p \approx 10^{-1}-10^2 \text{ s}^{-1}$.^[13]

However, the fact that the use of iridium, platinum and other rare transition metals as luminescence sources is not sustainable speaks against the use of these elements.^[29] Furthermore, the k_p of heavy metal emitters cannot be increased indefinitely with increasing SOC. The limitation to $k_p \approx 10^6 \text{ s}^{-1}$ is empirically attributed to the zero-field splitting (ZFS) of the triplet levels of the T_1 state. The three triplet sublevels in Figure. 2 are actually degenerate, but split due to the ZFS, which also increases with SOC. A Boltzmann distribution is formed over the triplet sublevels, where the energetically highest state, which is the least frequently occupied at high ZFS, is the state with the largest k_p . The reduced "fast" contribution leads to a stagnation of the total k_p of the system. This behavior of the triplet sublevels was found for octahedral Ir^{III} complexes and is observed for all octahedral transition metals and also for square planar complexes, e.g. of Pt^{II} .^[27] An alternative emission mechanism, where the use of rare elements is not necessary and with which the radiative rate constant k_r can be increased compared to phosphorescence, is TADF.

1.1.4. TADF

TADF is increasingly establishing itself as a relevant emission mechanism since Adachi,^[30] Yersin^[27] and others have proposed it as a possible radiative mechanism in optoelectronic devices. Since the radiative process is fluorescence and therefore not formally a forbidden transition, no rare or expensive heavy elements, such as iridium or platinum, are required.

At room temperature (RT), energetically higher vibration levels (of T_1) are thermally occupied according to a Boltzmann distribution. As can be seen in the Jablonski diagram in Figure. 9, a reverse-ISC (RISC) can occur from these levels. The population of S_1 can then be followed by fast, as spin-permitted, delayed fluorescence.

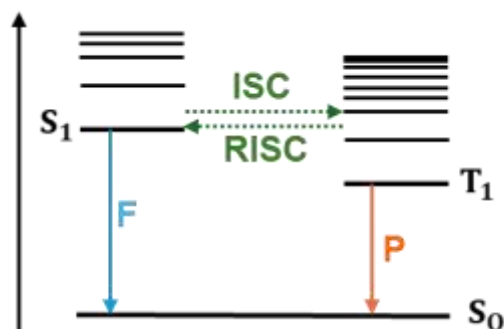


Figure 9. Section of a Jablonski diagram illustrating the TADF process in which delayed fluorescence (F) instead of phosphorescence (P) occurs after reverse intersystem crossing (RISC) $T_1 \rightarrow S_1$. Created on the basis of Yersin et al.^[31]

In addition to the factors described for the ISC process, a small $\Delta E(S_1-T_1)$ is particularly relevant for occupying the S_1 state. Values $\Delta E(S_1-T_1) < 3000 \text{ cm}^{-1}$ ($= 0.37 \text{ eV}$) are usually specified for an efficient RISC process. The relevance of the small energy gap can be recognized by considering the radiative rate constant for TADF i.e., k_{TADF} in Eq. (11).^[32]

$$k_{\text{TADF}} = \frac{k_{\text{P}} + k_{\text{F}} \cdot \exp\left[-\frac{\Delta E(S_1 - T_1)}{k_{\text{B}}T}\right]}{3 + \exp\left[-\frac{\Delta E(S_1 - T_1)}{k_{\text{B}}T}\right]} \quad \text{Eq.(11)}$$

$$k_{\text{r}}(S_1) = \frac{64\pi^4 \nu^3}{3\hbar c^3} \langle S_1 | \hat{M} | S_0 \rangle^2 \quad \text{Eq.(12)}$$

For example, at RT and small $\Delta E(S_1-T_1) < 750 \text{ cm}^{-1}$ the exponential term of Eq. (11), which evaluates the fluorescence rate constant k_{F} , would certainly assume values >0.1 . If one assumes that $k_{\text{F}} \gg k_{\text{P}}$, whereby the former can certainly be greater by a factor of 10^6 in organic molecules, one recognizes how the k_{TADF} can also be increased by a factor of $>10^4$ by small exponential terms <0.1 .

Eq. (11) also shows the exponential dependence of k_{F} on the emission energy. Analogous to phosphorescent emitters, *vide supra*, it follows that emitters in the low-energy, such as the NIR range, can only have a high radiative rate constant if the other factors in Eq. 11 and 12, such as the transition dipole moment \vec{M} of the $S_1 \rightarrow S_0$ transition is large or the energy gap $\Delta E(S_1-T_1)$ is small.^[33] The latter can be realized, for example, by increasing spatial separation of the donor and acceptor orbitals in D-A systems, or by increasing torsion angles γ between the ligand planes or boundary orbitals. Theoretically, $\Delta E(S_1-T_1)$ can thus be reduced as desired and the RISC process is improved. However, the transition dipole moment $\langle S_1 | \hat{M} | S_0 \rangle$ also depends on the spatial overlap. Increasing spatial separation leads

to a decrease in the oscillator strength of the $S_1 \rightarrow S_0$ transition. The result would be that the fluorescence becomes less likely or k_F becomes smaller. The design of efficient TADF emitters thus requires a careful approach in order to find a balance between increasing k_{RISC} and decreasing k_F with decreasing $\Delta E(S_1-T_1)$.^[31]

A further challenge in the design of efficient TADF emitters arises from the fact that these are mostly D-A systems whose lowest excited states have 1CT or 3CT character and the transition between these states is El-Sayed forbidden. From this fact arises the importance of further excited CT, π, π^* and n, π^* states that mix into the low CT states and thus facilitate RISC.^[34] Here, too, the incorporation of transition metals to increase the available amount of low-energy states appears to make sense. In fact, $k_{TADF} > 10^6 \text{ s}^{-1}$ has already been achieved with transition metal-based TADF emitters. In comparison, purely organic TADF emitters are almost always limited to $k_r < 2 \cdot 10^5 \text{ s}^{-1}$.^[3] In addition to the increase in density of states, other factors are plausible for the increase in k_{TADF} compared to organic molecules. On the one hand, k_p in Eq. (11) is increased by the effective elimination of pure spin multiplicity, whereby the participation of the metal orbitals also contributes. On the other hand, k_{RISC} and thus the population of S_1 is improved.

Due to the fact that both k_F and k_p become smaller during the transition to bathochromic emission, but at the same time k_{nr} increases disproportionately, thus a system must be found whose intrinsic k_r is competitive with k_{nr} . As has been shown, a high k_r also results from the increasing transition dipole moment \vec{M} .

1.2. Photocatalysis

Starting from an excited state, a large number of radiative and non-radiative transitions are possible, as described in the previous subchapters. Transitions to other molecules, such as a substrate, have not yet been considered. In the following, we will discuss how transfer reactions work and how they can be used in the context of photocatalysis.

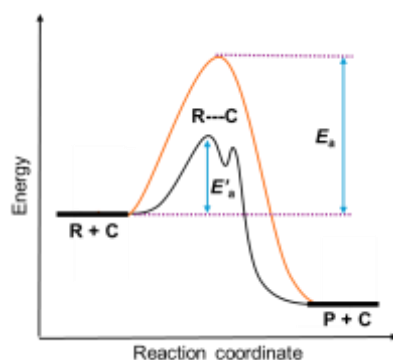


Figure 10. Schematic representation of a thermally catalysed reaction (black line) and a non-catalyzed reaction (orange line). Starting from the reactant R and the catalyst C, the activation energy barrier E'_a is lowered via an R...C transition state and the product P is obtained. The catalyst C emerges unchanged during the reaction.^[35]

In principle, there are various ways to influence chemical reactions, for example using a catalyst, which was defined by OSTWALD: "A catalyst is a substance that increases the rate of a chemical reaction without itself being consumed and without changing the final position of the thermodynamic equilibrium of this reaction."^[36] In catalysis, a catalyst therefore only changes the reaction kinetics, but not the thermodynamic position of the reactants R and products P.^[35,37] The reduction of the activation energy E_a by a catalyst C can be achieved, for example, by introducing an alternative reaction pathway or by distributing the reaction over several sub-steps (Figure 10). This increases the reaction rate, whereby in equilibrium reactions the forward and reverse reactions are changed in the same way. However, equilibrium is reached more quickly in this case. It is also crucial for a catalyst that it remains unchanged after the reaction and is not consumed. During the catalysis of transition metal complexes, whether homogeneous or heterogeneous, the reactants are coordinated to the metal centre, bringing them into close proximity to each other. By forming a metal-substrate bond, the reaction can be promoted by activating the substrate, facilitating a nucleophilic attack on the substrate or, if the catalyst is chiral, exerting an asymmetric induction on the substrate and thus enabling enantioselective syntheses.^[38,39]

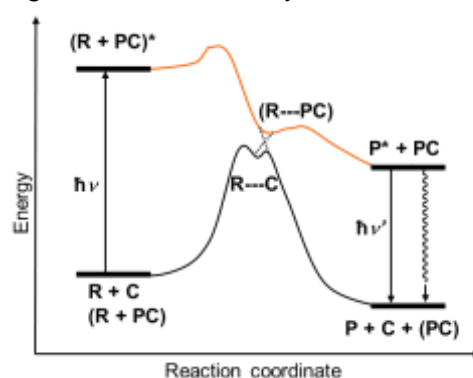


Figure 11. Schematic representation of a thermally catalysed reaction (black line) and a photo-chemical reaction (orange line). By absorbing a photon, the photocatalyst (PC) is transferred to a higher-energy state. This transfers the energy to the reactant (R). Excess energy can be released from the excited state of the product (P^*) in a non-radiative or radiative manner. The photocatalyst (PC) emerges from the reaction unchanged.^[35]

As an alternative to thermal catalysis is a reaction which can be catalysed by light. The advantage of photocatalysis is that light is available in unlimited quantities and is therefore a cheap resource, also with regard to green chemistry.^[40] Photoexcited metal catalysis is particularly promising, as it opens up an alternative reaction pathway compared to thermal catalysis (Figure 11). However, predicting the reactivity of the excited molecules is problematic, which hinders the development of these systems. As a result, the majority of systems known in the literature involve ligand dissociation by light, which generates the catalytically active species. Reactions in which the activation of a catalyst is light-induced and occurs without intermolecular electron transfer are hardly known. In recent literature, the distinction between photocatalytic reactions and catalytic photoreactions (via photocatalyst) and photosensitized catalysis (via photosensitizer) has been established.^[35] The latter can be further subdivided into photo-induced and photo-assisted catalytic reactions. In a photocatalyst (PC), absorption and chemical transformation take place in one unit, whereas in a photosensitizer (PS), also known as a light harvester, they are spatially separated. By absorbing light, the energy obtained from the photosensitizer can also be transferred to a metal catalyst or directly to a substrate. In the latter case, the conversion to the product is carried out by the substrate in the excited state without further interaction with a catalyst.^[38,41]

In principle, various processes can take place during a photocatalytic reaction. On the one hand, an energy transfer (EnT) or a single electron transfer (SET) can take place, which are explained in more detail below (Figure 12). In the latter case, re-oxidation and reduction is possible by means of a non-excited reaction partner or the addition of another reaction component. The energy transfer is a photophysical process from an excited donor D^* to an acceptor molecule A , which is thermodynamically only possible if the energy D^* is equal to or higher than that of the acceptor A^* . Since the donor molecule undergoes no chemical change, it is referred to as a photosensitizer.^[10]

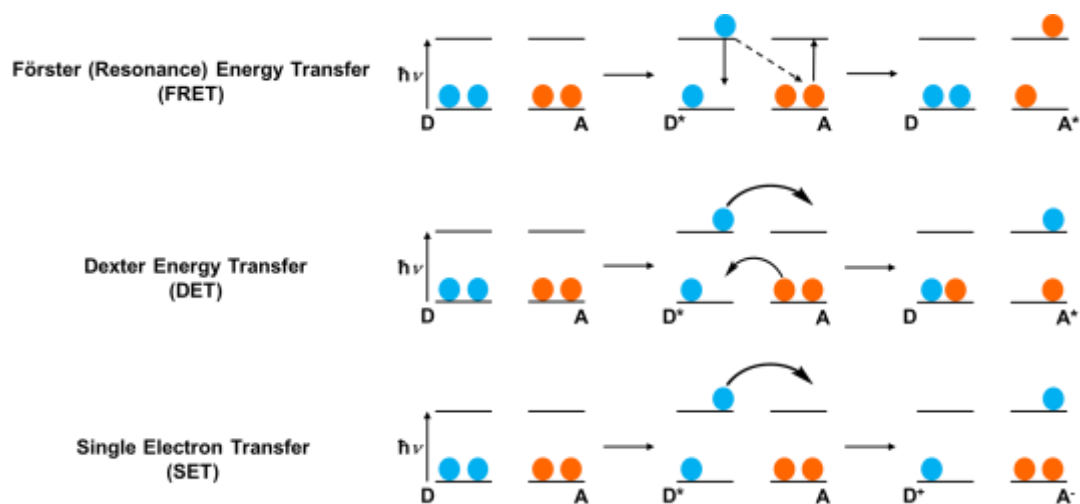


Figure 12. Graphical representation of relevant energy and charge transfer mechanisms.

In general, there are four possible energy transfer options:

1. Radiative energy transfer (trivial energy transfer): In the case of radiative energy transfer, D^* emits a photon which is directly absorbed by the acceptor A. As a prerequisite for this transfer, the absorption spectrum of A must overlap with the emission spectrum of D, whereby the distance does not matter. An example of this is the absorption of sunlight by chlorophyll during photosynthesis.

2. Förster (resonance) energy transfer (FRET): This energy transfer is also commonly referred to as the coulomb, dipole-dipole or resonance mechanism. This is a non-radiative process, in which the lifetime of D^* , in contrast to trivial energy transfer, depends on the concentration of the acceptor. The lifetime of D^* decreases with increasing concentration. In FRET, the dipole moment of D^* induces a dipole in A, creating a coulomb interaction. If there is a spectral overlap, i.e. an overlap of the wave functions of Ψ_A^* and Ψ_B^* , an energy transfer occurs. Here, the FRET rate is proportional to the integral of the spectral overlap, but inversely proportional to the sixth power of the donor-acceptor distance. This is a pure singlet-singlet transfer.

$$k_{FRET} = k_{r,D} \frac{R_0^6}{r^6} = \frac{R_0^6}{\tau_D \cdot r^6} \quad \text{Eq.(13)}$$

k_{FRET} indicates the transfer rate, $k_{r,D}$ the radiation emission rate of the donor, τ_D the fluorescence lifetime, r the distance between donor and acceptor and R_0 the Förster radius, i.e. the distance between the two centers where the efficiency of energy transfer via FRET is 50%. FRET is usually performed at distances of 100 Å to 5 Å.

3. Dexter energy transfer or electron exchange: For Dexter energy transfer, a sufficient overlap of the orbitals of D and A is required. Typical distances are less than or equal to 10 Å. This is a synchronous double exchange of electrons, where the total spin of the donor-acceptor pair is maintained. Both triplet-triplet transfer and singlet-singlet transfer are possible, although the latter are rather rare.

$$k_{dexterET} \propto J \cdot e^{-\frac{2r}{L}} \quad \text{Eq.(14)}$$

Here $k_{dexterET}$ indicates the transfer rate, r the distance between donor and acceptor, J the integral of the overlapping spectra of donor and acceptor and L the penetration depth. The transfer rate decreases exponentially with increasing distance between donor and acceptor.

4. Energy hopping or energy migration: Energy is transferred in crystalline solids via excitons. An exciton is a bound electron-hole pair. A distinction is made between FRENKEL excitons, where the binding energy is high, and WANNIER excitons, where the binding energy is low. This process plays no role in catalysis.^[35,42]

In addition to energy transfer reactions, there is also the possibility of electron transfer to a substrate. In the case of electron transfer, the sensitizer is oxidised or reduced, making further additions to the reaction necessary in order to enable its degradation. If the excited molecule RH^* has a more negative reduction potential than the substrate, it donates an electron to the acceptor. If it is more positive, it accepts an electron as a donor. The redox potentials can be estimated as follows:

$$E_{red}^0 = E_{red}^0 - E_{0-0}, \quad \text{Eq.(15)}$$

$$E_{ox}^0 = E_{ox}^0 - E_{0-0}, \quad \text{Eq.(16)}$$

E_{0-0} , describes the energy of the transition between the lowest vibrational levels of the electronic ground state (S_0) and the lowest excited state (S_1). From this equation it follows that the excited state is both a better oxidizing agent and reducing agent than the ground state. Due to the short average lifetime of excited singlet states, SET is mostly performed by molecules in a triplet state, which can be easily generated by effective ISC through transition metals,^[10,35] for example.

The process of photosensitization occurs in the excited state and can usually take place by energy transfer. Rarely, proton transfer can occur, which is not described in detail here. Usually, the photosensitizer (PS) absorbs light with a higher wavelength than the substrate A. In order to prevent absorption of the substrate, the absorption spectra must differ significantly. Rapid conversion to product B takes place with efficient triplet energy transfer if efficient ISC is present and the energy of the excited sensitizer is equal to or higher than that of the substrate or acceptor. The use of a photosensitizer is necessary because, as already mentioned, the population of the triplet state by ISC is usually inefficient. In summary, the reaction mechanism is carried out according to the following scheme, whereby the PS is first converted into an excited state by light. Subsequently, energy is transferred to the acceptor A in a triplet-triplet transfer, whereby the sensitizer is transferred back to the ground state. Finally, the excited acceptor reacts to form product B.



The energy requirements for DEXTER energy transfer are shown in Figure 13. Favourable conditions are therefore present if the sensitizer has a small and the acceptor a large singlet-triplet splitting. Since the substrates are usually purely organic molecules, they have intrinsically large energy gaps.^[35]

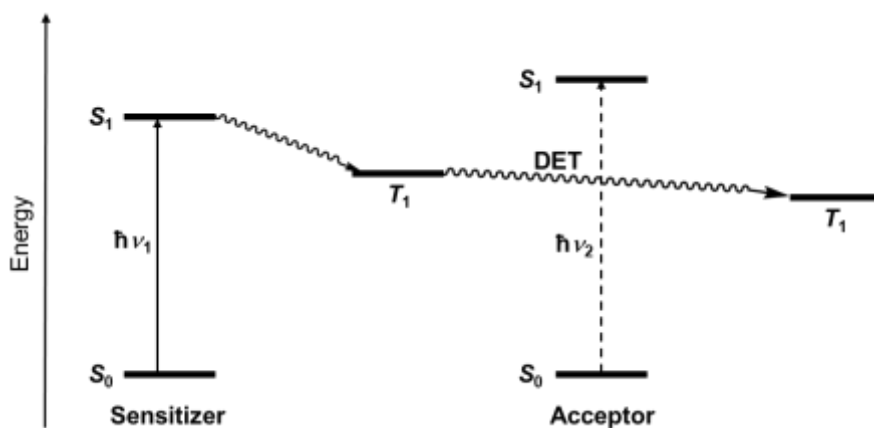


Figure 13: Electronic state diagram for the sensitization of a DEXTER energy transfer.^[35]

If sensitization takes place via a reductive energy transfer, a reduction potential is required for the photosensitizer PS in the excited state, which is more negative or at least equal to the acceptor potential (Figure 14). Consequently, a positive potential is required for oxidative sensitization. The mechanism of a reductive one-electron transfer is described below. First, PS is converted into an excited state by light absorption. By transferring electrons to acceptor A, A is reduced and PS is oxidized. For the recovery of PS, a donor (D) is added, which reduces PS and oxidizes itself in the process, as shown below.^[35]

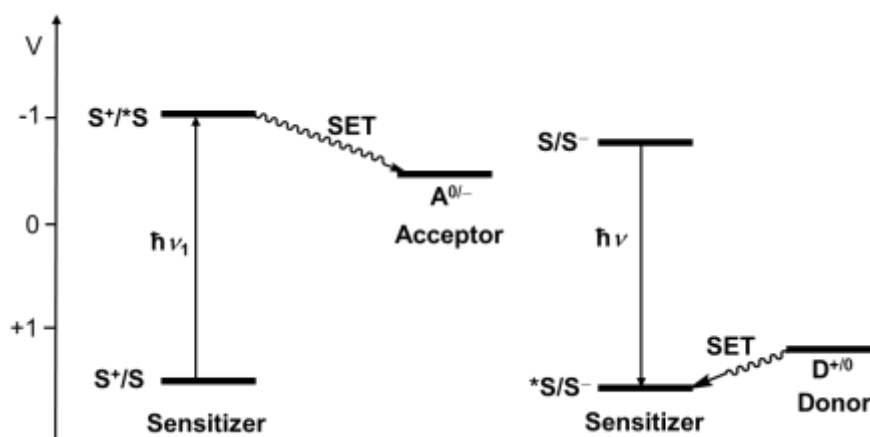
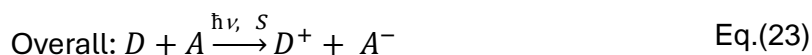


Figure 14: Illustration of the electrochemical potentials for reductive (left) and oxidative (right) electron transfer sensitization.^[35]

In addition to organic molecules with a conjugated π -system, metal transition complexes can also be used as photosensitizers, which cover a wide range of triplet energies. Some examples can be found in Figure 15.^[43,44]

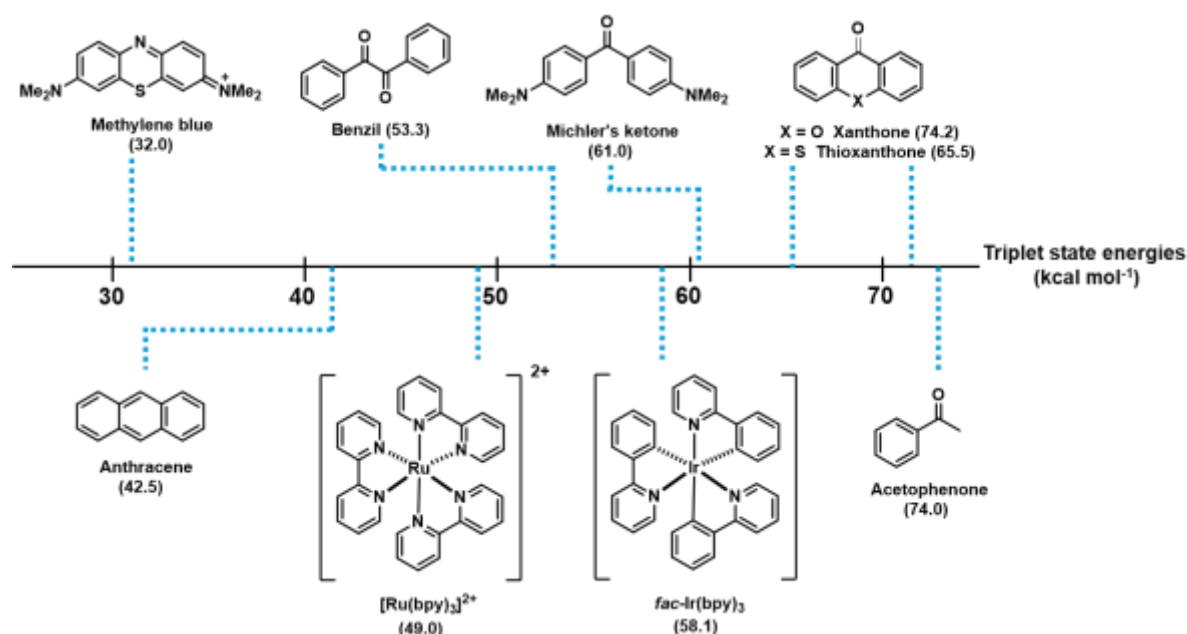


Figure 15. Overview of some photosensitizers known in the literature, sorted by triplet energies. Graphic created based on STRIETH-KALTHOFF et al.^[43]

[Ru(bpy)₃]²⁺ is considered one of the best-researched photosensitizers in the literature.^[41,45] Due to its chemical and photophysical properties, the cationic transition metal complex has been intensively studied as a photocatalyst and shows an absorption band in the visible range (450 nm in ethanol, $\epsilon \approx 18,000 \text{ M}^{-1}\text{cm}^{-1}$).^[46] After an MLCT ($t_{2g} \rightarrow \pi^*$), this photocatalyst undergoes rapid ISC with high quantum yield due to SOC, resulting in the formation of long-lived ($\tau = 1100 \text{ ns}$) excited states in acetonitrile with high efficiency.^[47] The reduction potential of the half reaction $[\text{Ru}(\text{bpy})_3]^{3+} + e^- \rightarrow [\text{Ru}(\text{bpy})_3]^{2+*}$ with $E_{1/2}^{\text{M}^+/\text{M}^*} = -0.81 \text{ V}$ is significantly lower than that of the ground state $[\text{Ru}(\text{bpy})_3]^{2+}$ with $E_{1/2}^{\text{M}^+/\text{M}} = 1.29 \text{ V}$ and shows that the excited electron in the system leads to a significantly higher electron donor capability. At the same time, the reduction potential of the excited state with $E_{1/2}^{\text{M}^*/\text{M}^-} = 0.77 \text{ V}$ shows that it is a stronger oxidizing agent than in the ground state ($E_{1/2}^{\text{M}^*/\text{M}} = -1.33 \text{ V}$).^[35,48]

As photosensitizers or photocatalysts, monometallic complexes are limited to reactions based on charge or electron transfer. In addition, modifications of the ligands lead to changes in both catalytic and photophysical properties. Since none of the properties can be kept constant, optimizing the catalyst is difficult.^[47] If a photocatalyst has to catalyze via organometallic means, ligands must inevitably dissociate or associate, which changes the geometry. All these factors lead to an altered ligand field, which is of immense importance in photophysics and further restricts perfect "tuning".

1.3. Phosphorescence starting from 4d and 5d transition metal complexes

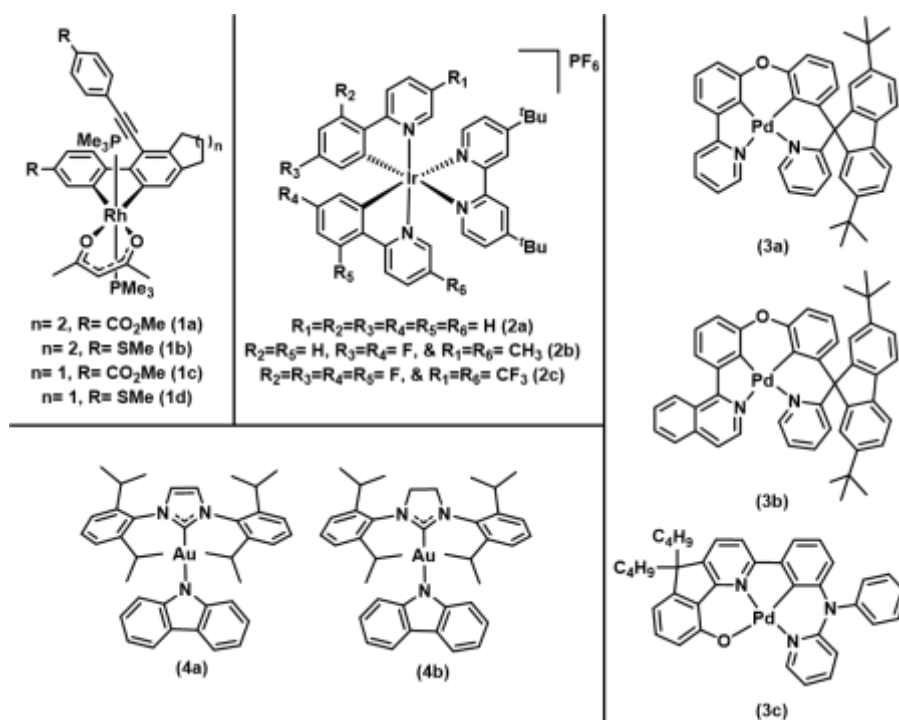


Figure 16. Overview of some 4d and 5d transition metal complexes with long-lived triplet state and high triplet energy known in the literature.^[49–54]

Table 1. Selected photophysical data of complexes **1a-4b** at RT.

	Solvent	λ_{em} (nm)	τ (μ s)	Φ	k_r (10^2 s ⁻¹)
1a	Toluene	545	162	0.12	7.40
1a	2-MeTHF	544	372	0.33	8.87
1b	Toluene	542	89	0.01	1.12
1b	2-MeTHF	577	81	0.02	2.46
1c	Toluene	540	181	0.14	7.73
1c	2-MeTHF	541	338	0.16	4.73
1d	Toluene	535	63	0.02	3.17
1d	2-MeTHF	534	646	0.10	1.54
2a	CH ₃ CN	581	0.6	0.23	3833.33
2b	CH ₃ CN	543	1.1	0.26	2363.63
2c	CH ₃ CN	470	2.3	0.68	2956.52
3a	CH ₂ Cl ₂	466	106	0.47	44.33
3b	CH ₂ Cl ₂	599	44	0.07	15.90
3c	CH ₂ Cl ₂	515	272	0.18	6.61
4a	THF	431	335	0.33	9.85
4b	THF	429	266	0.32	12.03

In general the 3d transition metal complexes of Cr, Mn, Fe and Co consists of d-electrons and thus undergo d-d transition and decay non-radiatively with low photoluminescence quantum yield in solution, together with have low emission intensity, or short or unmeasurable decay times which make them less attractive species for solution state studies and application. However few of 4d and 5d transition metal complexes displays remarkable phosphorescence at room temperature with long lifetimes and moderate to high photoluminescence quantum yield and thus makes ideal for application such as energy transfer (EnT) photocatalysis.

Some of the prominent examples include Rh(I) compounds **1a-1d** reported by Marder and coworkers, which consisted of small values of the radiative rate constants k_r in toluene, indicating that the nature of the T_1 state was purely 3IL with weak SOC mediated by the Rh atom which was further confirmed by luminescence measurements on the compounds in 2-MeTHF.^[54] The exceptionally long lifetimes and small radiative rate constants of the rhodium biphenyl complexes in comparison to other 3IL emitters presumably were a result of the long conjugation of the organic ligand π -system. According to the TD-DFT studies, the T_1 state involved charge-transfer from the biphenyl ligand into the arylethynyl moiety away from the rhodium atom, which reduces SOC of the metal center, which would be necessary for fast phosphorescence.

Other examples of such behavior from group 9 elements consists of Ir(III) complexes **2a-c** with the ppy-bpy scaffold reported by Malliaras, Bernhard, and coworkers, where the emission was derived from a mixed excited-state involving 3MLCT ($t_{2g} \rightarrow \pi^*_{N\wedge N}$) and 3LC ($\pi_{C\wedge N} \rightarrow \pi^*_{C\wedge N}$) transitions.^[51-53] The emitted light could be described by the wave equation Φ

$$\Phi = a\Phi(^3MLCT) + b\Phi(^3LC) \quad \text{Eq.(24)}$$

where a and b are normalized coefficients that describe the contribution of 3MLCT and 3LC transitions to the observed emission. As $a < b$, the emitted light has greater ligand-centered character, which was reflected in the shape (vibrationally structured) and position (hypsochromic shift) of the emission band.

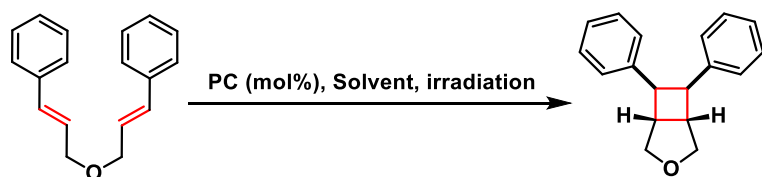
More such well known examples of compounds displaying appreciable phosphorescence in solution state includes the Pd(II) complexes **3a-c** reported by Che and workers, where the emission was mainly derived from 3IL $\pi \rightarrow \pi^*$ excited states.^[50] The emission energy of compound **3a** could be tuned by ligand modification such as in compound **3b**, with a 1-isoquinoline ring instead of the pyridine ring, shows red-shifted emission band. The long decay time in **3c** in comparison to **3a** was because of slower k_r which was due to orbitals being delocalized over the tetradentate ligand in the T_1 excited state, thus the $T_1 \rightarrow S_0$

transition was conceived to be accompanied with a small structural distortion in **3a** as compared to **3c**, also metal contribution in T_1 was found to be smaller in the case of **3c** than in **3a** and thus the smaller SOC, hence the slower k_r .

The Au(I) complexes **4a-b** described by Steffen, Nolan, and coworkers, also exhibited emission via phosphorescence in THF solution from a high-energy $^3\text{C}_{bz}$ state with exceptionally long lifetimes of $\tau = 335$ and $266 \mu\text{s}$.^[49] The stronger SOC of Au apparently facilitated ISC $S_1 \rightarrow T_n$ with much higher efficiency, thus quenching any prompt fluorescence. The nature of the carbene ligand didn't seem to influence the luminescence properties, although the TD-DFT calculations predicted the $^3\text{LLCT}$ state to be lowest in energy for the complex **4b**, while the weaker π - acceptor in **4a** leads to a T_1 state of ^3LC character localized at the Cz ligand. Complex **4b** displayed better photo-stability in comparison to **4a** in solution.

Ag(I) compounds often tend to undergo photodecomposition and/or have photostability issues and thus are not discussed here,^[49] whereas in general the Pt(II) compounds displays unstructured phosphorescence at room temperature in solution, yet mostly have short or unmeasurable lifetimes in comparison to other 4d and 5d transition metal complexes.^[55] Although subsequent process have been made over the past years in the development of Pt complexes and the proposed Pt analogue of Ir(III) complexes **2a-b** displays promising triplet emission in the high energy region which as can utilized for EnT photocatalysis reactions.^[56]

1.3.1. [2+2] Cycloaddition of (E,E')-Dicinnyl Ether



Photocatalysts (loading)	λ_{ex}	Solvent	Time	Yield
2c : [Ir(dF(CF ₃)ppy) ₂ (dtbbpy)]PF ₆ (1 mol%)	CFL	DMSO	4 h	89 %
4b : [Au(Cz)(SIPr)] 5 mol%	365 nm	THF	4 h	>99 %
3a : [Pd-B-1] (1 mol%)	>350 nm	ACN	3 h	88 %
3c : [Pd-N-1] (1 mol%)	462 nm	ACN	4 h	97%

Scheme 1. [2+2] cycloaddition of (E,E')-dicinnyl ether by photo-induced EnT comparison with various established photocatalysts.^[49,50,57]

In terms of reaction duration the Pd(II) compound **3a** was found to be most efficient photocatalyst with 3 hours reaction time,^[50] where as in terms of conversion or yield of the

reaction the Au(I) compound **4b** was found to be most effective to carry out the EnT photocatalysis.^[49]

1.4. NIR TADF Emission displayed by organic molecules

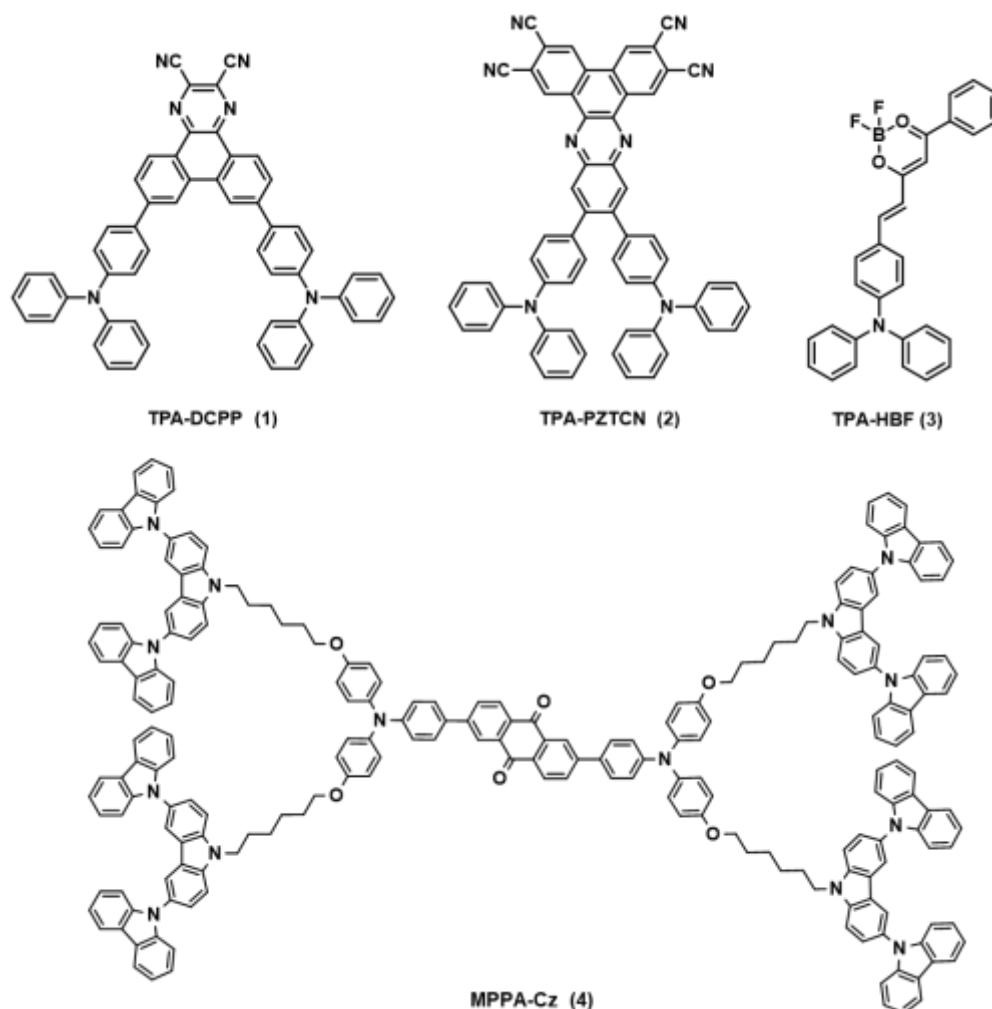


Figure 17. Selected examples of organic NIR TADF emitters known from literature.^[58]

Table 2. Selected photophysical data of complexes 1-4 at RT.

	λ_{em} (nm)	τ (μ s)	Φ	k_r ($10^5 s^{-1}$)
1 (100 wt% in TPBi films)	708	0.76	0.14	1.84
2 (10 wt% in mCBP films)	729	18.6	0.22	0.11
3 (40 wt% in CBP films)	712	0.0005, 0.0032	0.14	2800, 438
4 (in thin films) ^a	715	0.56	0.06	1.07

^aFilms preparation: The quartz plate substrates were precleaned carefully and treated by UV ozone for 4 min. The solutions with the concentration of 10 mg mL⁻¹ were spin coated onto the quartz plate substrate and dried in vacuum.

The first organic NIR-TADF was reported by Wang and co-workers,^[59] compound **1** had a V-shaped D- π -A- π -D type of structure, where 2,3-dicyanopyrazino phenanthrene (DCPP) was used as the acceptor (A) due to the presence of large and rigid π -conjugation and strong electron-withdrawing capability, whereas diphenylamine (DPA) was used as an electron donor (D) due to its excellent hole-transporting ability and to mitigate the effect of aggregation-induced quenching. According to the DFT calculations a small the dihedral angle of 35 ° was found between DCPP and the phenyl-conjugated bridge which suggested a near-planar arrangement and a reasonable orbital overlap, enhancing the fluorescence rate ($k_F = 9.0 \times 10^{-7} \text{ s}^{-1}$) and from the TD-DFT calculation, a small ΔE_{ST} value of 0.20 eV was estimated. In CHCl_3 , compound **1** displayed NIR emission (λ_{em} , 720 nm) with associated τ_F , τ_{TADF} , and the photoluminescence quantum yield Φ values of 1.7 ns, 9.1 ns, and 3%, respectively. In THF, compound **1** exhibited more red-shifted NIR emission (λ_{em} , 780 nm) with τ_F , τ_{TADF} , and Φ values of 0.4 ns, 4.0 ns, and 1%, respectively. With increasing polarity to DCM, the emission was further red-shifted (λ_{em} , 810 nm). The TADF emission was attributed to a reverse internal conversion (RIC) from the π - π^* state to the ^3CT state, followed by RISC to the emissive ^1CT state. The pure thin film **1** exhibited a broad NIR emission at 708 nm with associated τ_F , τ_{TADF} , and Φ values of 20.8 ns, 0.76 μs , and 14% due to the AIE (aggregation-induced emission).

Adachi and coworkers in 2021 reported a D-A type emitter, 11,12-bis(4-(diphenylamino)dibenzo[a,c]phenazine-2,3,6,7-tetracarbonitrile (TPA-PZTCN), **2**, in which a rigid moiety dibenzo[a,c]phenazine-2,3,6,7-tetracarbonitrile (PZTCN) acted as an electron acceptor with two TPA as electron donors (Figure 17).^[60] The 10 wt% of **2** doped mCBP film exhibited emission at $\lambda_{em} = 729 \text{ nm}$ with associated τ_{TADF} (300 K), Φ_{PL} , Φ_{TADF} values of 18.6 μs , 19.1%, and 21.7%, respectively. From the temperature-dependent transient PL measurement on the 10 wt% of **2** in mCBP film, the TADF nature ($\Delta E_{ST} = 0.10 \text{ eV}$) was estimated with a long-delayed fluorescence lifetime of 18.6 μs and also with microsecond regime τ_{TADF} values at the high-temperature region (200–300 K). The calculated k_{RISC} value of $7.6 \times 10^4 \text{ s}^{-1}$ for the 10 wt% doped films at 300 K. An increase in overlap integral ($I_{H/L}$) between the highest occupied NTO (HONTO) and the lowest unoccupied NTO (LUNTO) was observed in the T_2 state, indicating the latter achieved a hybrid local-CT character ($^3\text{HLCT}_2$). The calculation predicted that the spin-flip event was effectual not only by small ΔE_{ST} but also by the energetically close T_2 state through the equilibrium $^3\text{HLCT}_2 \leftrightarrow ^3\text{CT}_2 \leftrightarrow ^1\text{CT}_1$.

Aléo and coworkers synthesized a novel hemicurcuminoid molecule (TPA-HBF), **3** in which TPA and acetylacetonate boron difluoride acted as a donor and an acceptor, respectively.^[61] The photophysical properties of the molecule were examined in various solvents. In DCM,

molecule **3** exhibited an emission peak at 736 nm, whereas in MeCN, it displayed emission at 787 nm ($\Phi = 0.03\%$) due to the formation of a more polar excited state. On changing the solvent from DCM to acetone to acetonitrile, the intensity of the locally excited band was found to be increasing in comparison to that of the CT emission. Molecule **3** in a neat film showed Φ of 5.5%. For the blend film, CBP was chosen as the host because of its HOMO and LUMO energy levels that fit well with those of emitter **3**, thus disabling the exciplex formation and enabling the Förster (resonance) energy transfer (FRET). At an excitation value of 340 nm, the thin film of molecule **3** with 40 and 60 wt% in CBP exhibited emissions at 712 and 716 nm, respectively, with $\tau_F = 0.52$, $\tau_{TADF} = 3.21$ ns and $\Phi = 19\%$ (for 40 wt%) and $\tau_F = 0.47$, $\tau_{TADF} = 3.04$ ns and $\Phi = 12\%$ (for 60 wt%). It was observed that for both the doping concentrations, at high energy, the NIR emission originated from the monomeric structure with a short-lived emission, and at the lower energy, the same was instigated from the dimeric structure with longer-lived emission.

Sun, Jiang, and coworkers reported for the first time NIR D- π -A- π -D type TADF dendrimers, MPPA-3Cz, **4** with non-conjugated tricarbazole as peripheral dendrons.^[62] To compare the photophysical properties of molecules **4**, a simple donor-acceptor moiety 2,6-bis(4-(bis(4-methoxyphenyl)amino)phenyl)anthracene 9,10-dione (MPPA) was also synthesized. The DFT calculation suggested a ΔE_{ST} value of 0.18 eV for MPPA where the HOMO orbital was mostly confined over the methoxy triphenylamine units, and the LUMO was distributed on the anthraquinone-acceptor and partially on the phenyl substituent. The ΔE_{ST} and the HOMO-LUMO distribution of **4** were nearly similar to the emissive core MPPA and matched well with the experimentally observed ΔE_{ST} ranging from 0.17 eV. Neat films of **4** exhibited λ_{em} at 715 nm, whereas the same for MPPA was not detected. This observation suggested that the introduction of nonconjugated aliphatic chain carbazole dendrons would enhance the emission by decreasing the aggregation caused quenching, thus inducing the Φ value of 6% compared to the non-emitting MPPA.

Overall in general organic based NIR emitters often have low Φ in solution state, shows low energy emission up to >800 nm with broad emission band due to structural reorganisation in excited state. They are often doped in high concentration in films/polymer matrices leading to aggregation induced emissions or sometimes aggregation induced quenching and are prone to photodegradation.

1.5. NIR Emission displayed by 4d and 5d transition metal complexes

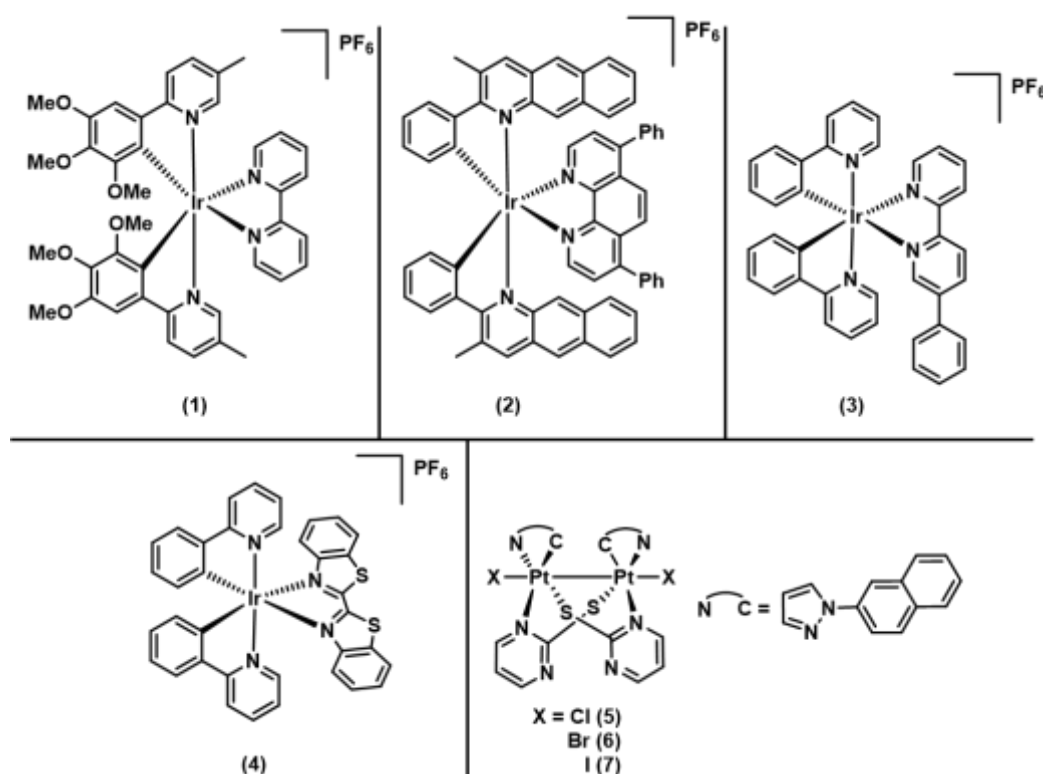


Figure 18. Selected examples of 4d and 5d transition metal based NIR emitters known from literature.^[63–67]

Table 3. Selected photophysical data of complexes 1-7 at RT.

	λ_{em} (nm)	τ (μ s)	Φ	k_r ($10^5 s^{-1}$)
1 (in MeCN)	720	0.0016	0.002	12.5
2 (in MeCN)	755	0.35	0.002	0.05
3 (in MeCN)	710	0.040	0.009	2.25
4 (in MeCN)	744	0.044	0.004	0.90
5 (solid state; ground)	985	0.023	n.a. ^a	-
6 (solid state; ground)	985	0.033	n.a. ^a	-
7 (solid state; ground)	1070	0.014	n.a. ^a	-

^aValues not available in the publication, might be due to weak emission behaviour ($\Phi < 1\%$).

Zysman-Colman and coworkers explained the photophysical behaviour of compound **1**.^[63] The emission profiles were broad and featureless with emission maxima ranging at 730 nm. The near infrared emission was assigned to a mixed metal-to-ligand and ligand-to-ligand charge transfer transitions (³MLCT and ³LLCT), commonly observed for heteroleptic cationic iridium complexes. The presence of iridium and the large observed Stokes shifts, clearly indicated phosphorescence despite the short emission state lifetimes. The markedly low quantum yields accompanied by very short, nanosecond emission lifetimes. The structural commonality in these poorly emissive complexes was due the presence of the 3-MeO

groups on the C^N ligands. According to TD-DFT studies T₁ state was described predominantly by a LUMO→HOMO transition implying an emission resulting from an admixture of ³MLCT/³LLCT. This assignment was consistent with the TD-DFT results and the observed broad and unstructured emission at 298 K in MeCN.

Qiu and co-workers measured the absorption spectra of **2**,^[64] the intense absorption bands below 350 nm were assigned to spin-allowed intraligand (IL) ($\pi \rightarrow \pi^*$) transitions, whereas the less intense long tails extending to 600 nm correspond to mixed transitions of MLCT (metal-to-ligand charge transfer) with LLCT (ligand-to-ligand charge transfer). Owing to the additional sp²-hybridized N, complex **2** gives clearly red-shifted MLCT bands and ³ π - π^* transitions around 398, 466, and 530 nm. For the PL spectra, **2** was first checked for any possible visible emission with a photomultiplier tube (PMT) detector (calibrated up to 870 nm) and showed maxima at 755 nm. The NIR characteristics were further measured with a Ge detector (calibrated from 800 to 1700 nm), suitable for recording NIR PL spectra. According to the TD-DFT studies the T₁ and T₂ states of **2** are degenerate, and their compositions are quite complicated as well. For complex **2**, T₁ state originates from 24% HOMO - 2 → LUMO + 2, 20% HOMO - 1 → LUMO + 3, 16% HOMO - 1 → LUMO + 1, and other smaller contributors. The mixed characters of the lowest triplet states result in broad but well-resolved phosphorescence spectra. Moreover, the LUMO consists of the π^* orbital of the mpbx-g ligands (77%) in complex **2** which makes sense in that the use of a second electron-withdrawing N atom in the heterocyclic part of cyclometalated ligands lowers the LUMO significantly and the unfavourable interligand charge transfer is suppressed as well.

Zysman-Colman and coworkers reported the photophysical behaviour of **3**,^[65] where the emission spectrum was found to be broad and featureless with an emission maximum at 710 nm. At low temperature, the emission shifted to higher energy ($\Delta E \sim 2900 \text{ cm}^{-1}$) and became slightly more structured. This rigidochromic shift at low temperature was an indication of a significant excited state dipole moment, and suggested that the emissive state was charge transfer (CT) rather than ligand centered (LC) in nature. This deep-red emission was distinctive by comparison to most other red-emitting ($\lambda_{em} > 620 \text{ nm}$ in ACN) complexes of the form [Ir(ppy)₂(N^N)]⁺ due to (i) the very low emission energy and (ii) the relatively nonconjugated nature or absence of electron-withdrawing groups decorating the ancillary ligand. From the TD-DFT studies it was found that the HOMO is distributed approximately equally on the iridium and ppy ligands with only a 5% contribution arising from the 2,5-dpp. In **3**, the HOMO - 2 through HOMO - 4 electron distributions parallel that found for the HOMO while HOMO - 1 is predominantly ppy-based (90%). The LUMO and LUMO + 1 for was localized on the π^* orbitals of the 2,5-dpp (>90%). The LUMO + 2 and LUMO + 3 were

concentrated mainly on the π^* orbitals of the ppy ligands while LUMO + 4, like LUMO, is mostly $\pi^*_{2,5\text{-dpp}}$.

Zysman-Colman and coworkers also described the absorption behaviour of complex **4**.^[66] The singlet ligand-centered $\pi \rightarrow \pi^*$ transitions (^1LC) extend up to 407 nm, as was predicted by TD-DFT, due to increased conjugation. The set of absorption bands clustered around 363 nm in **4**. The nature of these transitions is more CT in character and comprises $^1\text{MLCT}$ from $\text{Ir}(d\pi) \rightarrow \text{L}2(\pi^*)$ ($\text{N}^{\wedge}\text{N}$ ligand) and singlet ligand-to-ligand charge transfer ($^1\text{LLCT}$) from $\text{ppy}(\pi) \rightarrow \text{L}2(\pi^*)$, as suggested by TD-DFT studies. The lowest energy absorption maxima for **4** appear at 599 nm. These bands are assigned as a mixture of spin-allowed and spin-forbidden $^1\text{MLCT}/^3\text{MLCT}$ and ligand-to-ligand charge transfer ($^1\text{LLCT}/^3\text{LLCT}$) transitions. The emission profile of **4** in acetonitrile which was found to be broad and featureless, and indicative of mixed ^3CT emission. The spin density distribution of the excited-state corroborates this assignment as well.

Sicilia and coworkers reported the emission behaviour of powdery samples of the dimeric $\text{Pt}_2(\text{III},\text{III})$ compounds (**5-7**),^[67] which shows at room temperature NIR emissions with maxima ranging from 985 to 1070 nm that are strongly dependent on the axial ligand X. Upon cooling down to 77 K, these emissions experience a hypsochromic shift and undergo a 100-fold increase in their lifetime decays. From the TD-DFT studies, the calculated the spin-density distributions in the optimized first excited states (T_1) was located along the X-Pt-Pt-X axis, essentially on the X ligand (0.778 in **5**, 1.031 in **7**) and the Pt center (0.857 in **5**, 0.669 in **7**). There are also minor contributions from the $\text{N}^{\wedge}\text{S}$ (0.237 in **5**, 0.184 in **7**) and $\text{C}^{\wedge}\text{N}$ (0.128 in **5**, 0.116 in **7**) groups. Thus, the emissions would be mainly attributed to $^3\text{XMMCT}$ [$\sigma(\text{X}) \rightarrow d\sigma^*(\text{Pt-Pt})$] excited states with a minor contribution of the $\text{S}^{\wedge}\text{N}$ group that become slightly more important in **5**. The optimized geometries of the T_1 states for **5** and **7** show a similar structure to that of the S_0 state but with a substantial elongation of the Pt-Pt distance from 2.675 Å (S_0) to 2.988 Å (T_1) in **5** and would be consistent with a decrease in the Pt-Pt BO as a consequence of the electron promoted to the $d\sigma^*(\text{Pt})_2$ orbital in the excitation process. To evaluate Pt-Pt bonding, Mayer BO analyses were carried out in the S_0 and T_1 states. The Pt-Pt interaction is significantly weakened in the first excited state of both complexes, **5** and **7**, which would be supporting the $^3\text{XMMCT}$ character of these emissions.

From these reported photophysical behaviours and others, we can determine that the NIR emitters based on heavy metals such as Ir and Pt mostly outperforms the NIR emitters based on organic molecules as they can show low energy emission up to 1070 nm, mostly have higher k_r in solution/solid-state, often have structured emissions and also their low

emission behaviour is mostly an intrinsic property rather than due to energy transfer like FRET between the host and acceptor.

Along with the advantages of the heavy metals-based NIR emitters, there are also multiple disadvantages, such as the low natural abundance and the environmental contamination associated with the often-used heavy metals in OLEDs, which enhance the overall cost of commercialized materials. Other drawbacks include the degradation of the device due to the annihilation of the high energy polarons (singlet or triplet) and also the dissociation of the ligand by forming unstable radical cation in the complex.

One of the ways to minimize the above factors is to find a cheaper and possibly an efficient alternative such as Cu(I)-based NIR emitters.

1.6. NIR Emission displayed by Cu(I) complexes

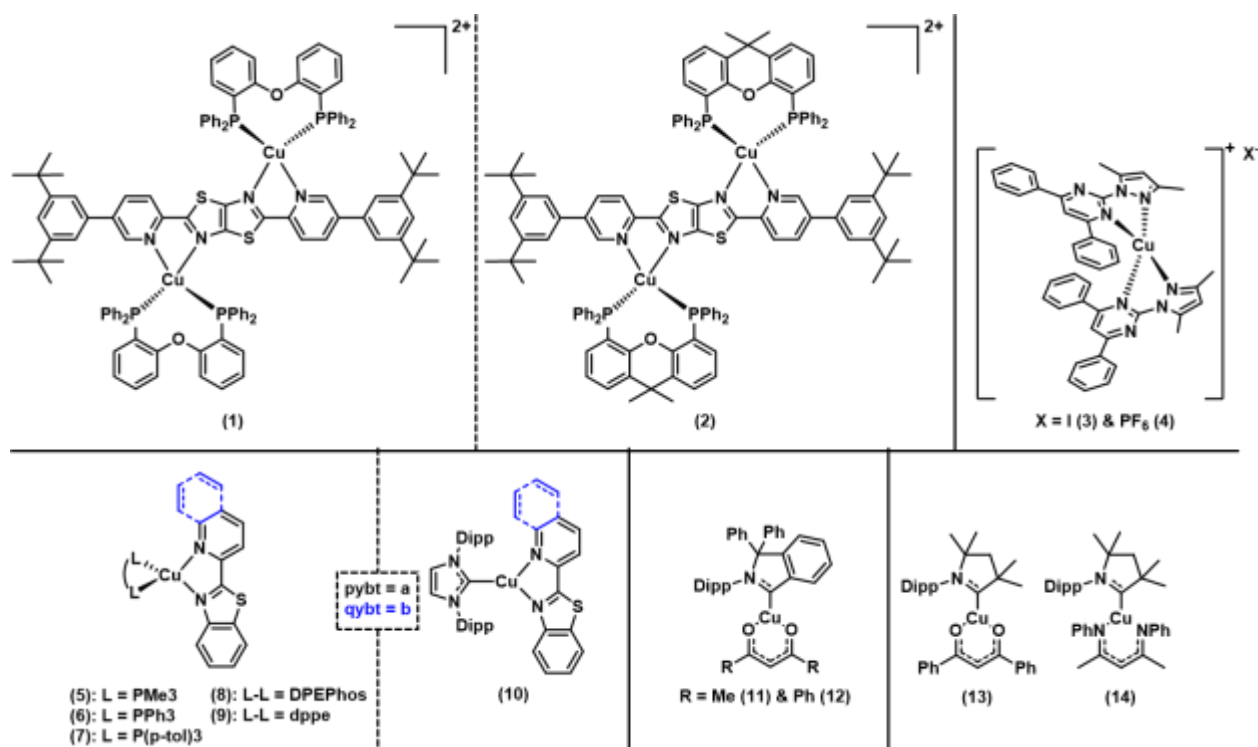


Figure 19. Selected examples of Cu(I)-based NIR emitters known from literature.

Table 3. Selected photophysical data of complexes **1-14** at RT.

	λ_{em} (nm)	τ (μ s)	Φ	k_r ($10^5 s^{-1}$)
1 (in DCM)	746	0.066	0.13	19.69
2 (in DCM)	732	0.014	0.06	42.85
3 (solid-state; ground)	712	0.100 ^a	0.024	2.4
4 (solid-state; ground)	715	0.080 ^a	0.029	3.62
5a (solid-state; ground)	752	0.506	0.01	0.19
5b (solid-state; ground)	724	0.408	0.01	0.24
9b (solid-state; ground)	727	n.d.	0.01	-
11 (solid-state; ground)	760	0.068	0.01	1.47
12 (solid-state; ground)	772	0.050	0.01	2
13 (solid state; ground)	762	n.d.	n.d.	-
14 (solid state; ground)	739	n.d.	n.d.	-

^aValues estimated from the graph in the main paper.

Su, Mauro, and coworkers reported two binuclear cationic Cu(I) complexes, **1-2** which displayed photoluminescence into the NIR region in solution with maximum centered at 746 and 732 nm, respectively.^[68] A hypsochromic shift was being observed going from solution to solid state samples, but the emission still remained in the NIR region. The emission was achieved due to the dinuclearisation strategy and establishment of two π - π stacking interligand interactions which provided a doubly locked architecture, disfavoring large, excited state geometrical distortion. The radiative process was assigned to a long-lived excited state with ³MLCT character and was supported by photophysical and computational analysis. Despite the Φ values being moderate, the k_r were amongst the highest for Cu(I) derivatives.

Mononuclear copper(I) complexes **3** and **4** were described by Bushueva and coworkers.^[69] In the structures of complex cations $[CuL_2]^+$ ions was coordinated with two L molecules (N,N-chelating coordination). Extended π -systems of the L molecules in $[CuL_2]^+$ favoured the formation of paired π - π stacking intramolecular interactions between the pyrimidine and phenyl rings leading to significant distortions of tetrahedral coordination cores, CuN_4 . The free ligand L demonstrated dual excitation wavelength dependent luminescence in the UV and violet regions, which was attributed to $S_1 \rightarrow S_0$ fluorescence and $T_1 \rightarrow S_0$ phosphorescence with intraligand charge transfer character. Complexes **3** and **4** demonstrated $T_1 \rightarrow S_0$ phosphorescence in the near-infrared region. Theoretical investigations pointed towards its ligand-to-metal charge transfer (LMCT) nature. Spin-orbit coupling computations revealed that the most effective intersystem crossing channels for

[CuL₂]⁺ appeared in high-lying excited states, while the S₁→T₁ transition is unfavourable according to El-Sayed's rule and the energy gap law.

Steffen and co-workers had reported various Cu(I)-based NIR emitters over the years. In 2017 they had reported trigonal and tetrahedral cationic Cu(I) complexes **5a-10a** bearing phosphine or N-heterocyclic carbene ligands as donors, with benzthiazol-2-pyridine (pybt) and benzthiazol-2-quinoline (qybt) acting as π-chromophores.^[70] The emission behaviour of this series of complexes were checked in DCM where compounds **6b**, **7b**, **8a**, **8b**, and **9b** displayed emission in the NIR region with poor Φ, whereas in 1 wt% PMMA films **5a-10a** displayed emission maxima ranging from yellow-to-NIR. The emission originated from a ³(Cu→pybt/qybt)MLCT state and supported by DFT/TD-DFT calculations, also no clear indication for thermally activated delayed fluorescence was found. The red to near-IR emission was a result of incorporation of the sulphur into the chromophore ligand. In 2020, the monometallic Cu(I) compounds **11** and **12** based on cyclic (amino) (aryl) carbene (CAArC) ligand were reported.^[4] Complexes **11** and **12** showed two featureless low-energy absorption bands around 410 nm and 500 nm, which according to the TD-DFT studies were attributed to mixed (Cu → CAArC)/LL(acac → CAArC)CT and weakly allowed dσ→π*(CAArC) MLCT transitions. **12** also exhibited allowed dπ→π*(acac)/π→π*(acac) transitions involving the phenyl substituents of the acac ligand at 365 nm. The origin on emission was due to phosphorescence from ³MLCT/LLCT states which was supported by theoretical calculations as well. In 2022, the trigonal neutral Cu(I)-CAAC (cyclic (amino) (alkyl) carbene) complexes **13** and **14** bearing chelating ligands with O and N donor atoms were studied.^[71] These compounds displayed weak low-energy absorption in solution between 400 and 500 nm due to mixed Cu→CAAC ¹MLCT/LLCT states. In the solid-state, the origin of emission was from phosphorescence from dominant ³(Cu→CAAC) CT states and was supported by DFT/TD-DFT calculations as well.

As there are dearth of examples of red-to-NIR emissive copper(I) complexes, so new systems consisting of various donors, and acceptors have always remained an area of great interest.

2. Results and Discussions

2.1. Multimetallic Copper(I) Diphenylphosphides Displaying Thermally Activated Delayed Fluorescence (TADF) in the Visible to Near-IR

This subchapter as part of this partially cumulative dissertation work is currently under “manuscript under preparation” status and is planned to be submitted as an edge article in “*Chemical Science*” journal of Royal Society of Chemistry.

Summary : This case study on a series of luminescent heteroleptic Cu(I) phosphide (-PPh₂) complexes [Cu₄(μ₂-PPh₂)₄(dppm)₂] (**1**), [Cu₄(μ₂-PPh₂)₄(dppb)₂] (**2**), and [Cu₄(μ₂-PPh₂)₄(xantphos)₂] (**3**). **1-3** shows deep red-to-green (**1** and **2**) and NIR (**3**) emission at room temperature with a high photoluminescence quantum yield of up to 44% and short lifetimes (0.3-34 μs) in the solid state with moderately efficient TADF behaviour. The beneficial coordination geometry around the Cu center along with the bite angles of the phosphines involved can largely impact the steric, photophysical, and electronic properties of the complexes. The formation of conformers in (**2**), due to the steric constraint of the C4 bridge of dppb, was exploited by pronounced reversible thermochromic behaviour arising from two different excited states displaying dual TADF behaviour.

Own contribution in the experimental part: approx. 85 %

Own contribution in the writing part: approx. 70%

2.2. Hetero-di/multi-nuclear Copper(I) Diphenylphosphides Displaying Thermally Activated Delayed Fluorescence (TADF) in the Visible to Near NIR

This subchapter as part of this partially cumulative dissertation work is currently under “manuscript under preparation” status and is planned to be submitted as a short article in “*Inorganic Chemistry*” journal by the American Chemical Society.

Summary : Phosphides have been known as very useful ligands for catalytic applications such as hydrophosphination; their transition metal complexes display fascinating luminescence behaviour, which can be used for diverse photonic applications. In this contribution, we describe the usage of strong donor phosphide (-PPh₂) ligand in facile synthesis, structural, and photophysical behavior of a series of luminescent di/multinuclear Cu(I)-phosphide complexes [Cu₂(μ₂-PPh₂)₂(dppe)₂] (**1**), [Cu₂(μ₂-PPh₂)₂(dppben)₂] (**2**), and [Cu₅(μ₂-PPh₂)₂(μ₃-PPh₂)₃(PPh₃)₃] (**3**). **1-3** exhibits green to red emission at room temperature with a high photoluminescence quantum yield up to 32% and short lifetimes (0.1 - 8 μs) in solid state with efficient TADF (thermally activated delayed fluorescence) behavior. The beneficial coordination geometry around the Cu center along with the π-acceptor character of the phosphines involved can largely impact steric, photophysical, and electronic properties. Short TADF decay times were achieved by the molecular crystal theory of coupling symmetry-related transition dipole moments in compound **2**, which also at low temperatures shows evidence of dual TADF emissions.

Own contribution in the experimental part: approx. 80 %

Own contribution in the writing part: approx. 70%

2.3. A [2.2]Isoindolinophanyl-based Carbene (iPC) Ligand: Synthesis, Electronic and Photophysical Properties, and Application in Photocatalysis

This subchapter as part of this partially cumulative dissertation work was published in collaboration with Wiley-VCH GDCh. Reprinted with permission from *Angew. Chem. Int. Ed.* **2024**, 63, e202409115 (doi.org/10.1002/anie.202409115). Copyright © 2024 John Wiley & Sons, Inc.

Summary : Cyclic amino(alkyl) and cyclic amino(aryl) carbenes (cAACs and cAARCs) have been established as very useful ligands for catalytic and photonic applications of transition metal complexes. Herein, we describe the synthesis of a structurally related sterically demanding, electrophilic [2.2]isoindolinophanyl-based carbene (iPC) that bears a [2.2]paracyclophane moiety. The latter leads to more delocalized frontier orbitals and intense green fluorescence of (HiPC)OTf (**2**) from an intra-ligand charge transfer (¹ILCT) state in the solid state. Base-promoted synthesis of the free carbene led to an unusual ring expansion and subsequent dimerization reaction, but the beneficial ligand properties can be exploited by trapping in situ at a metal center. The iPC ligand is a very potent π -chromophore, which participates in low energy metal-to-ligand (ML)CT transitions in [RhCl(CO)₂(iPC)] (**4**) and IL-“through-space”-CT transitions in [Au(iPC)₂]OTf (**5**) in the visible. The steric demand of the iPC leads to high stability of **5** against air, moisture, or solvent attack, and ultralong-lived green phosphorescence with a lifetime of 185 μ s is observed in solution. The beneficial photophysical and electronic properties of the iPC ligand, including a large accessible π surface area, were exploited by employing highly efficient energy transfer (EnT) photocatalysis in a [2+2] styrene cycloaddition reaction using **5**, which outperformed other established photocatalysts in comparison.

Own contribution in the experimental part: approx. 80 %

Own contribution in the writing part: approx. 20%

Carbene Chemistry

A [2.2]Isoindolinophanyl-Based Carbene (iPC) Ligand: Synthesis, Electronic and Photophysical Properties, and Application in Photocatalysis**

Sabyasachi Maity, André M. T. Muthig, Indranil Sen, Ondřej Mrózek, Andrey Belyaev, Benjamin Hupp, and Andreas Steffen*

Abstract: Cyclic amino(alkyl) and cyclic amino(aryl) carbenes (cAACs/cAArCs) have been established as very useful ligands for catalytic and photonic applications of transition metal complexes. Herein, we describe the synthesis of a structurally related sterically demanding, electrophilic [2.2]isoindolinophanyl-based carbene (iPC) that bears a [2.2]paracyclophane moiety. The latter leads to more delocalized frontier orbitals and intense green fluorescence of (HiPC)OTf (2) from an intra-ligand charge transfer (¹ILCT) state in the solid state. Base-promoted synthesis of the free carbene led to an unusual ring expansion and subsequent dimerization reaction, but the beneficial ligand properties can be exploited by trapping in situ at a metal center. The iPC ligand is a very potent π -chromophore, which participates in low energy metal-to-ligand (ML)CT transitions in [RhCl(CO)₂(iPC)] (4) and IL-“through-space”-CT transitions in [Au(iPC)₂]OTf (5). The steric demand of the iPC leads to high stability of 5 against air, moisture, or solvent attack, and ultralong-lived green phosphorescence with a lifetime of 185 μ s is observed in solution. The beneficial photophysical and electronic properties of the iPC ligand, including a large accessible π surface area, were exploited by employing highly efficient energy transfer (EnT) photocatalysis in a [2+2] styrene cycloaddition reaction using 5, which outperformed other established photocatalysts in comparison.

N-heterocyclic carbenes (NHCs) have become very important spectator ligands in transition metal chemistry to specifically modify the electronic and steric properties of the

[*] S. Maity, Dr. A. M. T. Muthig, I. Sen, Dr. O. Mrózek, Dr. A. Belyaev, Dr. B. Hupp, Prof. Dr. A. Steffen
 Department of Chemistry and Chemical Biology
 TU Dortmund University
 Otto-Hahn-Str. 6, 44227 Dortmund, Germany
 E-mail: andreas.steffen@tu-dortmund.de

[**] A previous version of this manuscript has been deposited as a preprint on ChemRxiv.

© 2024 The Authors. Angewandte Chemie International Edition published by Wiley-VCH GmbH. This is an open access article under the terms of the Creative Commons Attribution License, which permits use, distribution and reproduction in any medium, provided the original work is properly cited.

complexes, which has resulted in a wide range of applications in catalysis and materials science.^[1–3] Among the many carbene scaffolds available today, very electrophilic carbenes, such as cyclic amino(alkyl) and cyclic amino(aryl) carbenes (cAAC/cAArC), have been established as potent chromophore ligands in photoactive metal complexes.^[4–6] The lowest unoccupied molecular orbital (LUMO) with π -symmetry is suitable to act as an acceptor unit to be involved in low energy metal-to-ligand charge transfer (MLCT) and ligand-to-ligand (LL)CT transitions, providing intense absorption in the visible region of the electromagnetic spectrum. In addition, the metal contribution to the CT mediates strong spin-orbit coupling (SOC), while the significant CT distance can lead to small energy gaps ΔE_{ST} between the singlet and triplet excited states S_1 and T_1 , allowing spin-forbidden intersystem-crossing (ISC) $S_1 \rightarrow T_1$ to occur competitively to fluorescence. The triplet excited states in transition metal carbene complexes are often phosphorescent, rendering them interesting candidates for application in OLEDs and other photonic technologies.^[2,4,7] Long-lived triplet states are also relevant for photocatalysis via single electron transfer (SET) or energy transfer (EnT), which offers different reaction patterns and product distributions than thermal conversions.^[8]

The use of strongly σ -donating, π -electrophilic carbenes as chromophore units has revolutionized the field of photoactive d^{10} metal complexes in particular.^[4,5,9,10] Linearly coordinated coinage metal compounds, for example, are now among the most efficient molecular luminophores involving triplet states with exceptional radiative rate constants k_r of up to $4 \times 10^6 \text{ s}^{-1}$ and excellent luminescence quantum yields ϕ of up to unity.^[11–14] However, a potential limitation in the development of useful carbenes for photonic applications is the high reactivity of the ligands themselves as well as of the M–C bond. For instance, while [CuCl(IMes/IDipp)] are stable towards air and moisture,^[15] its cAAC and cAArC analogues are highly sensitive,^[13,16] requiring careful adjustment of the steric protection. Another challenge for molecular luminophores is the realization of low energy triplet emission in the deep red to near-IR for photonic information technologies,^[17] which can be achieved by design of acceptor units with LUMOs of enhanced delocalization resulting in long-distance CT. We found such effects in [Cu(Cz)(carbene)] (Cz = carbazolate) by using the more conjugated cAArC instead of cAAC, leading to an enormous bathochromic emission shift from $\lambda_{max} = 474 \text{ nm}$ to

638 nm and 2-fold enhanced k_f of $6.8 \times 10^5 \text{ s}^{-1}$ in polymer matrices.^[13] However, the cAArC-based complexes are indeed highly reactive and sensitive towards air and moisture. We are therefore interested in modifying the steric, electronic and photophysical properties of cAArC-like ligands in particular. Inspired by the work of Fürstner and co-workers,^[18] who showed for an NHC that can act as a paracyclophane (PCP) moiety that some electronic “through-space” communication exists between the two aromatic π -planes, we were curious whether the steric and photophysical properties of cAArC could be beneficially influenced by extension with a PCP unit. Thus, we herein report on the development of an electrophilic [2.2]isoindolinophanyl-based carbene (iPC) that can act as a very potent π -chromophore for photoactive transition metal complexes with potential application in luminescent devices and photocatalysis.

The protonated racemic ligand salt (HiPC)OTf (**2**) could be prepared from 4-bromo-5-formyl[2.2]paracyclophane, which was previously described by Bräse et al.,^[19] following the strategy reported for (HcAArC)OTf,^[20] except that for the step of imine condensation to obtain **1** we had to add 0.5 eq. TiCl_4 as a strong Lewis acid (Figure 1). The product formation of **2** can be observed as a yellow precipitate that fluoresces green under UV irradiation.

The steric and electronic influence of the PCP moiety on the carbene ring system is manifested in the ^1H NMR spectrum of the iminium salt **2**, with the resonances of the *ortho* and *meta* hydrogen substituents of the phenyl groups being broad, which suggests limited rotation in solution (Figure S3). Furthermore, the resonances of the methine hydrogens of the Dipp at $\delta = 3.32$ and 0.87 ppm are shifted in comparison to those of cAAC compounds to lower and higher field, respectively, while the methyl groups at $\delta = 1.32, 0.72, 0.50$ and -0.11 ppm are all found at higher field.

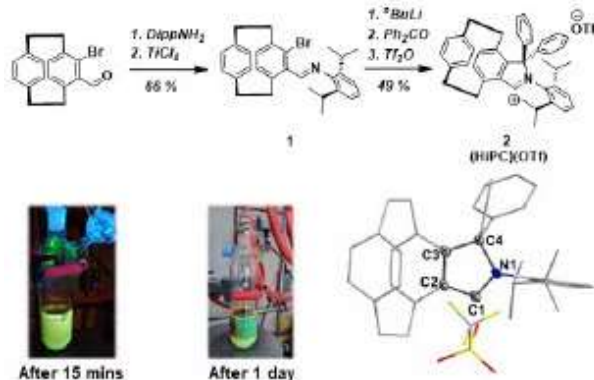


Figure 1. Synthesis and molecular structure of (S)-(HiPC)OTf (**2**) determined by SC-XRD studies (hydrogen atoms and (R)-isomer omitted for clarity). Photographs show green fluorescence upon UV lamp excitation (360 nm) of **2** precipitating from the reaction mixture. Selected bond lengths (Å) and angles [deg]: C1–C2 1.423(2), C2–C3 1.414(2), C3–C4 1.528(3), C4–N1 1.541(2), N1–C1 1.305(2), C2–C1–N1 112.6(1).

Yellow single crystals of **2** suitable for X-ray diffraction (SC-XRD) studies were obtained from diffusion of diethyl ether into a saturated THF solution. The steric congestion of the PCP fragment leads to an orthogonal arrangement of the phenyl moiety of the “upper hemisphere” with regard to the isoindoline plane, and the Dipp *N*-substituent is bent away from the PCP.

The iminium salt **2** appears yellow in color due to a broad absorption band between 300–475 nm with an extinction coefficient at the maximum of $\epsilon_{355\text{nm}} = 6,000 \text{ M}^{-1} \text{ cm}^{-1}$ (Figure 2). According to our TD-DFT calculations, the lowest energy excited states S_1 to S_7 are dominated by CT transitions from the upper aromatic ring of the PCP fragment and the phenyl ring of the same hemisphere to the LUMO, which is delocalized in the bicyclic carbene plane (Figure S51). As noted during the synthesis, **2** shows intense green emission in the solid state with $\lambda_{\text{max}} = 520 \text{ nm}$ and a high photoluminescence quantum yield of 0.32, which we assign to fluorescence from the first singlet excited state S_1 according to the short luminescence lifetime of $\tau = 6 \text{ ns}$. In solution, the emission is broader, and λ_{max} is bathochromically shifted to 585 nm, presumably due to the higher degree of structural reorganization in fluid media and specific solvent interactions of the ^1CT state.

Attempts to isolate the free carbene by base-promoted deprotonation, even at low temperatures, were not successful. Instead, the iPC appears to undergo fast C–H insertion of the pendant phenyl ring with subsequent ring expansion, as reported for free cAArCs,^[21] and finally C–C coupling of two in-plane PCP moieties would provide dimer **3** (Figure 3, and Figures S8–S11). The mechanism of the last reaction step is not clear, but formal loss of H_2 has occurred as single crystal X-ray diffraction studies suggest C=C double bond formation between the aromatic bridgehead carbon C3 and the ethyl bridge C17. As ^{77}Se NMR of carbene selenium adducts provides useful information on the π -acceptor properties of the free carbene,^[22] we thus reacted the iminium salt **2** with a base in the presence of elemental Se, but only dimer **3** could be isolated.

However, the free carbene formed in situ at low temperatures can be trapped by coordination to a metal center as demonstrated by the reaction with $[\text{RhCl}(\text{CO})_2]_2$, which led

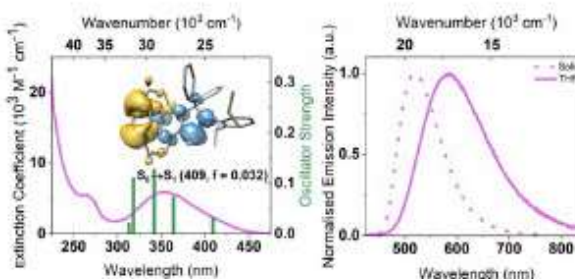


Figure 2. Left: Absorption spectrum of **2** in THF solution, TD-DFT calculated oscillator strengths, and electron density difference of the $S_0 \rightarrow S_1$ transition (loss: yellow, gain: blue). Right: emission spectra of **2** in THF solution (solid) and in the solid state (dotted).

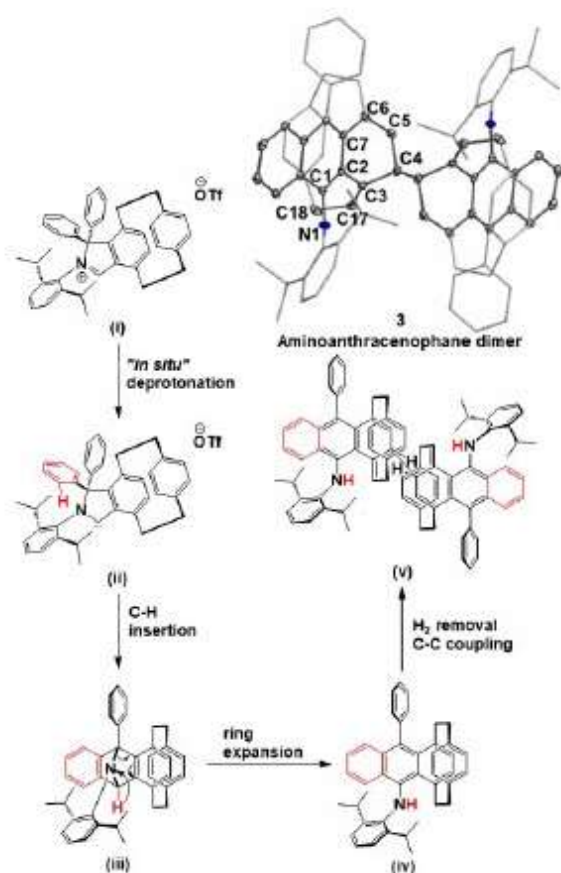


Figure 3. Tentative mechanism for the formation of **3** and its molecular structure determined by SC-XRD. Selected bond lengths (Å) and angles [deg]: C4-C4 1.548(2), C4-C3 1.509(2), C3-C2 1.486(2), C3-C17 1.343(2), C17-C18 1.529(2), C1-N1 1.393(2), C2-C3-C4 112.0(1), C3-C17-C18 126.4(1).

to the isolation of racemic square-planar $[\text{RhCl}(\text{CO})_2(\text{iPC})]$ (**4**) as confirmed by single crystal X-ray diffraction studies (Figure 4). The ¹³C NMR resonance of the carbene carbon in **4** is observed at $\delta = 244.6$ ppm as a doublet with $^1J_{\text{C-Rh}} = 39$ Hz, while the IR stretching frequencies of the CO ligands are found at 2077 and 1996 cm^{-1} , respectively, giving a Tolman electronic parameter (TEP) of 2050 cm^{-1} (Figures S13 and S35). Thus, the new iPC ligand is a much stronger σ -donor than most NHC ligands and very similar to cAArCs.^[23] However, we determined a buried volume V_{bur} of 52 % inflicted by our iPC ligand, while the cAArC covers only 44 % as in $[\text{CuCl}(\text{cAArC})]$ (Figures S44 and S45).

The same preparation method as for the Rh^I compound **4** can be employed to access the linearly coordinated bis(carbene) gold(I) complex $[\text{Au}(\text{iPC})_2]\text{OTf}$ (**5**) in good yields (Figure 4), which we isolated as a mixture of the ligand combinations *R,S*, *R,R* and *S,S*. **5** is highly stable even in solution towards air and moisture, although related d¹⁰ coinage metal cAArC complexes are highly sensitive. The space-filling model obtained from single-crystal X-ray

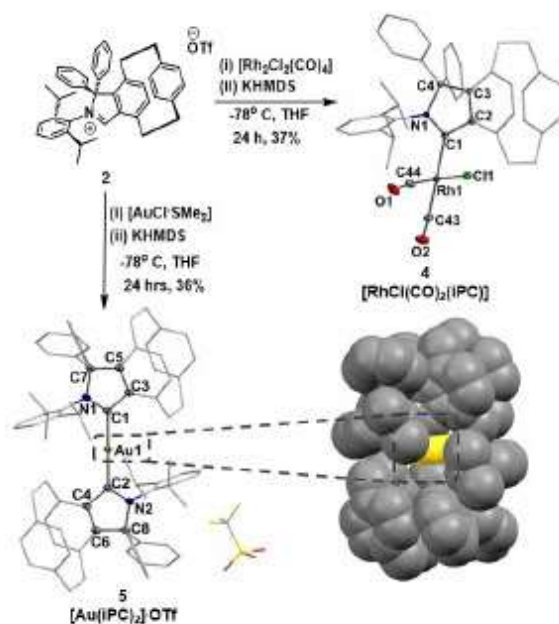


Figure 4. Top: synthesis of Rh^I iPC complex **4** and its molecular structure (racemate) determined by SC-XRD. Bottom: synthesis of $[\text{Au}(\text{iPC})_2]\text{OTf}$ (**5**), its molecular structure (*R,S*-conformer) determined by SC-XRD studies and space filling model.

diffraction studies shows that the M-C bonds are sterically protected against nucleophilic attack as the two iPC ligands together occupy 88 % of the volume around the metal center.

Bearing in mind the visible light absorption and fluorescence of the carbene precursor (HIPC)OTf (**2**), and the steric protection that the iPC ligand offers for the metal center, we were curious whether these photophysical properties are maintained upon metal coordination, which is of relevance for future luminescence or photocatalytic applications. Indeed, the rhodium(I) complex **4** exhibits broad absorption bands in the visible between 350–520 nm with extinction coefficients of ca. $\epsilon = 2,500\text{--}4,500$ $\text{M}^{-1}\text{cm}^{-1}$ at the respective maxima due to CT transitions that often involve the iPC ligand (Figure 5). The lowest energy vertical singlet transition $S_0 \rightarrow S_1$ is dominated by a $\text{Rh}(d_{z^2}) \rightarrow \text{iPC}(\pi^*)$ CT, which is responsible for the orange color of **4**. This band is bathochromically shifted due to the more delocalized LUMO of the iPC ligand and the resulting longer CT distance in comparison to other $[\text{RhCl}(\text{NHC})(\text{CO})_2]$ complexes or the cAArC analogue, which have been described as yellow powders. The S_2 state originates from an iPC ¹ILCT and the S_3 state is $\text{Rh}(d_{z^2}) \rightarrow \text{CO}(\pi^*)$ CT in nature (Figure S52). The energetically higher lying singlet transitions are complex mixtures of those already described and exhibit significantly higher oscillator strengths, thus explaining the higher ϵ values in the UV region.

Upon UV irradiation of **4** in solution at 365 nm, blue fluorescence with $\lambda_{\text{max}} = 450$ nm from a high energy ¹ILCT state of the iPC ligand is observed, indicating that internal

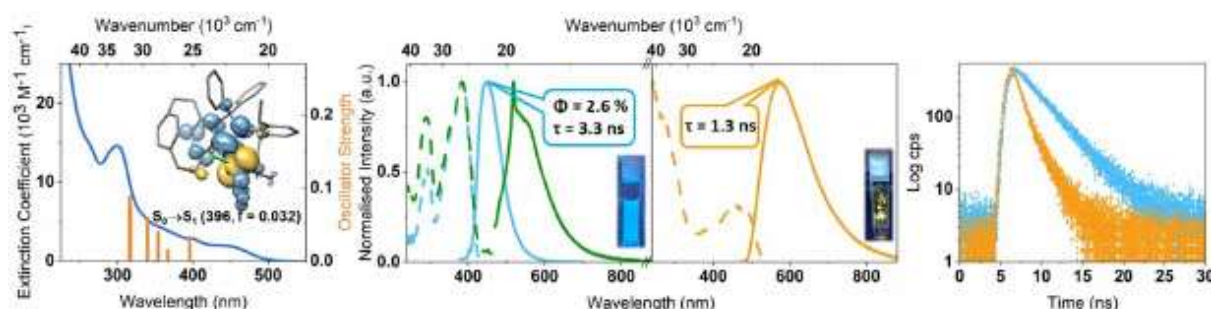


Figure 5. Left to right: Absorption spectrum of **4** in THF, TD-DFT calculated oscillator strengths, and electron density difference of the $S_0 \rightarrow S_1$ transition (loss: yellow, gain: blue), fluorescence (solid) spectra in THF solution (sky blue: $\lambda_{\text{em}} = 360$ nm, green: $\lambda_{\text{em}} = 450$ nm, the sharp spike at 520 nm is due to scattering), fluorescence (solid) in the solid state (orange; $\lambda_{\text{em}} = 450$ nm), and respective excitation spectra (dashed), fluorescence lifetime decays in THF solution (sky blue, $\lambda_{\text{em}} = 450$ nm) and in the solid state (orange, $\lambda_{\text{em}} = 575$ nm).

conversion (IC) to the S_1 state and ISC are both slow (Figure 5). However, excitation in the lowest energy absorption band at 450 nm gives weak yellow fluorescence from the $^1\text{MLCT}$ state with a short lifetime of 1.3 ns in the solid state due to inefficient SOC from Rh and slow ISC $S_1 \rightarrow T_1$, with no phosphorescence observable even at 77 K in 2-MeTHF or in the solid state (Figures S39–43), similar to 2,5-aryl-ethynylrhodacyclopenta-2,5-dienes reported by Marder et al.^[23]

The absorption spectrum of the gold(I) bis(iPC) complex **5** is similar to that of (HiPC)OTf (**2**), with broad low energy absorption bands that reach out into the visible region of the electromagnetic spectrum to 425 nm, albeit with smaller extinction coefficients ($\epsilon_{350\text{nm}} = 1,850 \text{ M}^{-1} \text{ cm}^{-1}$) (Figure 6). According to our TD-DFT calculations, the latter finding is due to the photophysical ground state properties of **5** being dominated by ^1IL “through-space” CT transitions with

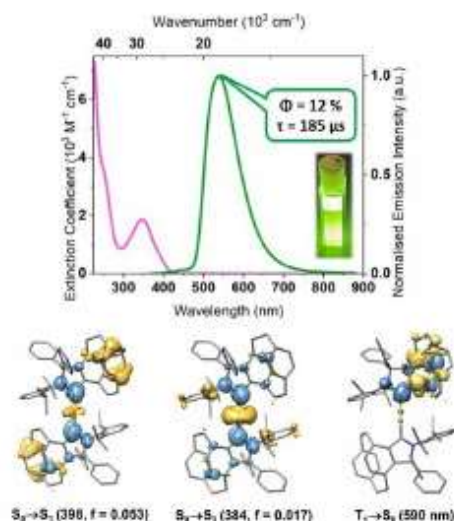


Figure 6. Top: absorption (purple) and emission (green) spectra of $[\text{Au}(\text{iPC})_2]\text{OTf}$ (**5**) in CH_2Cl_2 solution. Bottom: TD-DFT electron density differences of selected transitions of $S_0 \rightarrow S_1$ (loss: yellow, gain: blue).

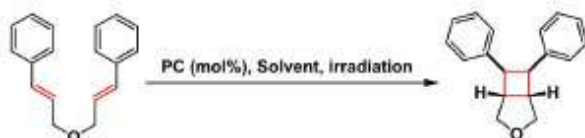
MLCT admixtures, except for the $S_0 \rightarrow S_3$ transition, which is $\text{Au}(d_z^2) \rightarrow \text{iPC}(\pi^*)$ in nature. We note that the calculated absorption properties of the different diastereomers of **5** are very similar and cannot be experimentally distinguished from each other due to the broad spectral character (see also Figures S53–54, and Tables S13–14).

While **2** undergoes efficient spin-allowed fluorescence on the nanosecond timescale only in the solid state due to facile non-radiative decay in solution, the enhanced rigidity imposed by the iPC ligands and SOC mediated by the Au^{I} ion in **5** leads to ultralong-lived green phosphorescence ($\lambda_{\text{max}} = 540$ nm) with $\tau = 185 \mu\text{s}$ and $\phi = 0.12$ in CH_2Cl_2 solution from a $^3\text{ILCT}$ state, of which the assignment is supported by DFT calculations (Figure 6, and Figure S54). The broad spectral appearance and its excited state lifetime combined with the large accessible surface area of the iPC ligands render $[\text{Au}(\text{iPC})_2]\text{OTf}$ (**5**) a potentially useful photocatalyst by energy transfer (EnT). Indeed, its application in 1 mol-% catalyst loading for the [2+2] cycloaddition of (E,E)-dicinnamyl ether led to full conversion to the desired product upon irradiation at 405 nm for 2 hours (Scheme 1). ^1H NMR spectroscopic studies and UV/Vis absorption measurements upon exposure of complex **5** in the presence of 1 eq. of the organic substrate to 405 nm light irradiation shows that the photocatalyst is stable under the reaction conditions (Figures S46–47). Also, the photoinduced reaction occurs without induction period, which excludes formation of a photocatalytically active impurity being responsible for the product formation.

The EnT of **5** to the substrate appears to be much more efficient in comparison to many other well-established photocatalysts^[24] that have been tested in this application scenario because the required reaction time is significantly shorter, although we have excited at the low energy absorption edge with small $\epsilon_{405} = 300 \text{ M}^{-1} \text{ cm}^{-1}$.

We have developed a new electrophilic [2.2]isoidolinophenyl-based carbene, which is structurally related to previously reported cAAC and cAArC ligands, with very similar σ -donor strength. However, the paracyclophane moiety is electronically coupled to the carbene framework and facilitates visible light absorption and $^1\text{ILCT}$

[2+2] Cycloaddition of (E,E')-Dicinnamyl Ether



Photocatalysts (loading)	λ_{exc}	Solvent	Time	Yield
[Ir(dF(CF ₃)ppy) ₂ (dtbbpy)]PF ₆ (1 mol%)	CFL	DMSO	4 h	89 %
[Au(Cz)(SIPr)] (5 mol%)	365 nm	THF	4 h	>99 %
[Pd-B-1] (1 mol%)	>350 nm	ACN	3 h	88 %
[Pd-N-1] (1 mol%)	462 nm	ACN	4 h	97 %
[Au(iPC) ₂](OTf) (5) (1 mol%)	405 nm	DCM	2 h	>99 %

Scheme 1. [2+2] cycloaddition of (E,E')-dicinnamyl ether by photo-induced EnT using **5** as a catalyst, and comparison with other established photocatalysts (dF(CF₃)ppy = 2-(2,4-difluorophenyl)-5-trifluoromethylpyridine, dtbbpy = 4,4'-di-tert-butyl-2,2'-dipyridyl, SIPr = 1,3-bis(2,6-diisopropylphenyl)-2-imidazolidinylidene, Pd-B-1 and Pd-N-1 = see Figure S55). CFL = candescent fluorescence lamp.

fluorescence of the salt (HiPC)OTf (**2**). The beneficial photophysical properties of the iPC can be transferred to its metal complexes [RhCl(CO)₂(iPC)] (**4**) and [Au(iPC)₂](OTf) (**5**), where it acts as a very potent excited state π -acceptor ligand and yellow ¹MLCT fluorescence and ³ILCT/MLCT “through space” phosphorescence are observed, respectively. The large steric demand of the iPC ligand in homoleptic **5** leads to a very long lifetime of 185 μ s of the excited state with a quantum yield of 12 % in solution, and in combination with the extended π -surface highly efficient triplet EnT for photocatalytic applications can be realized.

Supporting Information

The authors have cited additional references within the Supporting Information.^[26–38]

Acknowledgements

We thank MSc. Paul Ruer for assistance with the collection of some of the SC-XRD data. This work was supported by Deutsche Forschungsgemeinschaft [DFG, Priority Program SPP 1928 “COORNETs—Koordinationsnetzwerke als Bausteine für Funktionssysteme” (STE1834/9-1)]. Open Access funding enabled and organized by Projekt DEAL.

Conflict of Interest

The authors declare no conflict of interest.

Data Availability Statement

The data that support the findings of this study are available in the supplementary material of this article.

Keywords: Carbene · Paracyclophane · Luminescence · Coordination Chemistry · Photocatalysis

- [1] a) F. E. Hahn, *Chem. Rev.* **2018**, *118*, 9455; b) M. N. Hopkinson, C. Richter, M. Schedler, F. Glorius, *Nature* **2014**, *510*, 485.
- [2] H. Amouri, *Chem. Rev.* **2023**, *123*, 230.
- [3] a) R. Jazzar, M. Soleilhavoup, G. Bertrand, *Chem. Rev.* **2020**, *120*, 4141; b) B. Hupp, J. Nitsch, T. Schmitt, R. Bertermann, K. Edkins, F. Hirsch, I. Fischer, M. Auth, A. Sperlich, A. Steffen, *Angew. Chem. Int. Ed.* **2018**, *57*, 13671; c) L. Zapf, S. Peters, U. Radius, M. Finze, *Angew. Chem. Int. Ed.* **2023**, *62*, e202300056.
- [4] A. Steffen, B. Hupp, in *Comprehensive Coordination Chemistry III* (Eds.: E. C. Constable, G. Parkin, L. Que Jr), Elsevier, Oxford **2021**, pp. 466.
- [5] T.-Y. Li, S.-J. Zheng, P. I. Djurovich, M. E. Thompson, *Chem. Rev.* **2024**, *124*, 4332.
- [6] a) S. Bai, Y.-F. Han, *Acc. Chem. Res.* **2023**, *56*, 1213; b) C. M. Hendrich, K. Sekine, T. Koshikawa, K. Tanaka, A. S. K. Hashmi, *Chem. Rev.* **2021**, *121*, 9113; c) J. Beaudelot, S. Oger, S. Peruško, T.-A. Phan, T. Teunens, C. Moucheron, G. Evano, *Chem. Rev.* **2022**, *122*, 16365.
- [7] a) F. Wurl, S. Stipurin, J. I. Kollar, T. Strassner, *Angew. Chem. Int. Ed.* **2023**, *62*, e202301225; b) A. K. Pal, S. Krotkus, M. Fontani, C. F. R. Mackenzie, D. B. Cordes, A. M. Z. Slawin, I. D. W. Samuel, E. Zysman-Colman, *Adv. Mater.* **2018**, *30*, 1804231.
- [8] a) M. A. Bryden, F. Millward, O. S. Lee, L. Cork, M. C. Gather, A. Steffen, E. Zysman-Colman, *Chem. Sci.* **2024**, *15*, 3741; b) J. Twilton, C. Le, P. Zhang, M. H. Shaw, R. W. Evans, D. W. C. MacMillan, *Nat. Chem. Rev.* **2017**, *1*, 0052; c) S. Dutta, J. E. Erchinger, F. Strieth-Kalthoff, R. Kleinmans, F. Glorius, *Chem. Soc. Rev.* **2024**, *53*, 1068.
- [9] a) D. Di, A. S. Romanov, L. Yang, J. M. Richter, J. P. H. Rivett, S. Jones, T. H. Thomas, M. Abdi Jalebi, R. H. Friend, M. Linnolahti, M. Bochmann, *Science* **2017**, *356*, 159; b) R. Hamze, J. L. Peltier, D. Sylvinson, M. Jung, J. Cardenas, R. Haiges, M. Soleilhavoup, R. Jazzar, P. I. Djurovich, G. Bertrand M E Thompson, *Science* **2019**, *363*, 601.
- [10] a) M. Mitra, O. Mrózek, M. Putscher, J. Guhl, B. Hupp, A. Belyaev, C. M. Marian, A. Steffen, *Angew. Chem. Int. Ed.* **2024**, *63*, e202316300; b) O. Mrózek, M. Mitra, B. Hupp, A. Belyaev, N. Lütke, D. Wagner, C. Wang, O. S. Wenger, C. M. Marian, A. Steffen, *Chem. Eur. J.* **2023**, *29*, e202203980.
- [11] C. N. Muniz, J. Schaab, A. Razgoniaev, P. I. Djurovich, M. E. Thompson, *J. Am. Chem. Soc.* **2022**, *144*, 17916.
- [12] T.-Y. Li, S.-J. Zheng, P. I. Djurovich, M. E. Thompson, *Chem. Rev.* **2024**, *124*, 4332.
- [13] M. Gemert, L. Balles-Wolf, F. Kerner, U. Müller, A. Schmiedel, M. Holzapfel, C. M. Marian, J. Pflaum, C. Lambert, A. Steffen, *J. Am. Chem. Soc.* **2020**, *142*, 8897.
- [14] A. Ruduss, A. Jeco, K. A. Stucere, K.-W. Chen, B. Turovska, S. Belyakov, A. Vembris, C.-H. Chang, K. Traskovskis, *J. Mater. Chem. C* **2024**, *12*, 2968.
- [15] H. G. Raubenheimer, S. Cronje, P. J. Olivier, *J. Chem. Soc. Dalton Trans.* **1995**, 313.
- [16] M. Gernert, U. Müller, M. Haehnel, J. Pflaum, A. Steffen, *Chem. Eur. J.* **2017**, *23*, 2206.
- [17] a) H. Xiang, J. Cheng, X. Ma, X. Zhou, J. J. Chruma, *Chem. Soc. Rev.* **2013**, *42*, 6128; b) Y. Zheng, X. Zhu, *Org. Mat.* **2020**, *02*, 253; c) M. Vasilopoulou, A. Fakharuddin, F. P. Gar-

- cia de Arquer, D. G. Georgiadou, H. Kim, A. R. b Mohd Yusoff, F. Gao, M. K. Nazeeruddin, H. J. Bolink, E. H. Sargent, *Nat. Photonics* **2021**, *15*, 656; d) M. Nothaft, S. Höhla, F. Jelezko, N. Frühauf, J. Pflaum, J. Wrachtrup, *Nat. Commun.* **2012**, *3*, 628.
- [18] a) A. Fürstner, M. Alcarazo, H. Krause, C. W. Lehmann, *J. Am. Chem. Soc.* **2007**, *129*, 12676; b) M. Alcarazo, T. Stork, A. Anoop, W. Thiel, A. Fürstner, *Angew. Chem. Int. Ed.* **2010**, *49*, 2542.
- [19] J. J. P. Kramer, C. Yildiz, M. Nieger, S. Bräse, *Eur. J. Org. Chem.* **2014**, *2014*, 1287.
- [20] B. Rao, H. Tang, X. Zeng, L. L. Liu, M. Melaimi, G. Bertrand, *Angew. Chem. Int. Ed.* **2015**, *54*, 14915.
- [21] J. Lorkowski, M. Krauß, M. Kubicki, U. Radius, C. Pietraszuk, *Chem. Eur. J.* **2019**, *25*, 11365.
- [22] T. Hölzel, C. Ganter, *J. Organomet. Chem.* **2020**, *915*, 121234.
- [23] a) C. Sieck, M. G. Tay, M.-H. Thibault, R. M. Edkins, K. Costuas, J.-F. Halet, A. S. Batsanov, M. Haehnel, K. Edkins, A. Lorbach, A. Steffen, T. B. Marder, *Chem. Eur. J.* **2016**, *22*, 10523; b) A. Steffen, M. G. Tay, A. S. Batsanov, J. A. K. Howard, A. Beeby, K. Q. Vuong, X.-Z. Sun, M. W. George, T. B. Marder, *Angew. Chem. Int. Ed.* **2010**, *122*, 2399.
- [24] a) P.-K. Chow, G. Cheng, G. S. M. Tong, C. Ma, W.-M. Kwok, W.-H. Ang, C. Y.-S. Chung, C. Yang, F. Wang, C.-M. Che, *Chem. Sci.* **2016**, *7*, 6083; b) Z. Lu, T. P. Yoon, *Angew. Chem. Int. Ed.* **2012**, *51*, 10329; c) N. V. Tzouras, E. A. Martynova, X. Ma, T. Scattolin, B. Hupp, H. Busen, M. Saab, Z. Zhang, L. Falivene, G. Pisanò, et al., *Chem. Eur. J.* **2021**, *27*, 11904.
- [25] Deposition numbers 2271625 (for 2), 2271626 (for 3), 2271627 (for 4), and 2349442 (for 5) contain the supplementary crystallographic data for this paper. These data are provided free of charge by the joint Cambridge Crystallographic Data Centre and Fachinformationszentrum Karlsruhe Access Structures service.
- [26] W. L. F. Armarego, *Purification of laboratory Chemicals*, Butterworth Heinemann, Oxford; Boston **1996**.
- [27] G. M. Sheldrick, *Acta Crystallogr. Sect. C* **2015**, *71*, 3.
- [28] O. V. Dolomanov, L. J. Bourhis, R. J. Gildea, J. A. K. Howard, H. Puschmann, *J. Appl. Crystallogr.* **2009**, *42*, 339.
- [29] A. L. Spek, *Acta Crystallogr.* **2015**, *71*, 9.
- [30] a) L. Falivene, Z. Cao, A. Petta, L. Serra, A. Poater, R. Oliva, V. Scarano, L. Cavallo, *Nat. Chem.* **2019**, *11*, 872; b) A. Poater, F. Ragone, S. Giudice, C. Costabile, R. Dorta, S. P. Nolan, L. Cavallo, *Organometallics* **2008**, *27*, 2679; c) A. Poater, F. Ragone, R. Mariz, R. Dorta, L. Cavallo, *Chem. Eur. J.* **2010**, *16*, 14348.
- [31] F. Neese, *WIREs Comput. Mol. Sci.* **2012**, *2*, 73.
- [32] a) C. Adamo, V. Barone, *J. Chem. Phys.* **1999**, *110*, 6158; b) J. P. Perdew, K. Burke, M. Ernzerhof, *Phys. Rev. Lett.* **1996**, *77*, 3865; c) J. P. Perdew, K. Burke, M. Ernzerhof, *Phys. Rev. Lett.* **1997**, *78*, 1396; d) C. Cardoso, A. T. Costa, A. H. MacDonald, J. Fernández-Rossier, *Phys. Rev. B Condens. Mater.* **1996**, *105*, 9982; e) M. Ernzerhof, G. E. Scuseria, *J. Chem. Phys.* **1999**, *110*, 5029; f) J. Tao, J. P. Perdew, V. N. Staroverov, G. E. Scuseria, *Phys. Rev. Lett.* **2003**, *91*, 146401; g) J. P. Perdew, J. Tao, V. N. Staroverov, G. E. Scuseria, *J. Chem. Phys.* **2004**, *120*, 6898.
- [33] a) A. Schäfer, H. Horn, R. Ahlrichs, *J. Chem. Phys.* **1992**, *97*, 2571; b) F. Weigend, R. Ahlrichs, *Phys. Chem. Chem. Phys.* **2005**, *7*, 3297.
- [34] a) S. Grimme, J. Antony, S. Ehrlich, H. Krieg, *J. Chem. Phys.* **2010**, *132*, 154104; b) S. Grimme, S. Ehrlich, L. Goerigk, *J. Comput. Chem.* **2011**, *32*, 1456.
- [35] a) F. Weigend, *Phys. Chem. Chem. Phys.* **2006**, *8*, 1057; b) D. A. Pantazis, F. Neese, *J. Chem. Theory Comput.* **2009**, *5*, 2229; c) D. A. Pantazis, F. Neese, *Theor. Chem. Acc.* **2012**, *131*, 1292; d) D. A. Pantazis, F. Neese, *J. Chem. Theory Comput.* **2011**, *7*, 677.
- [36] V. Barone, M. Cossi, *J. Phys. Chem. A* **1998**, *102*, 1995.
- [37] D. A. Pantazis, X. Y. Chen, C. R. Landis, F. Neese, *J. Chem. Theory Comput.* **2008**, *4*, 908.
- [38] E. F. Pettersen, T. D. Goddard, C. C. Huang, G. S. Couch, D. M. Greenblatt, E. C. Meng, T. E. Ferrin, *J. Comput. Chem.* **2004**, *13*, 1605.

Manuscript received: May 14, 2024

Accepted manuscript online: July 4, 2024

Version of record online: September 5, 2024

2.4. Highly Efficient Mechanochromic TADF in the Deep Red to Near-IR in Copper(I) [2.2]Isoindolinophanyl-Carbene Carbazolates

This subchapter as part of this partially cumulative dissertation work was recently submitted in *Angew. Chem. Int. Ed.* **2024** (October) published by Wiley-VCH on behalf of GDCh.

Some aspects of this publication were developed as part of this thesis, which includes synthesis of complexes [iPC-Cu-Br] **2**, [iPC-Cu-Cz] **3**, and [iPC-Cu-Cz^{bu}] **4** along with their photophysical studies in PMMA and PS. Rest of it was done mostly by Dr. André M.T. Muthig. The OLED architecture and analysis were conducted in collaboration with Prof. Dr. Jens Pflaum from Julius-Maximilians University of Würzburg.

Summary : Low energy triplet emitters are highly relevant for the development of red to near-IR OLEDs and future photonic IT applications, but typically suffer from non-radiative decay due to the energy gap law (EGL). Premature excited state deactivation can be limited by enhancing the radiative decay rate k_r via thermally activated delayed fluorescence (TADF), by passing spin-forbidden slow phosphorescence. We report on a series of linear copper(I) carbene carbazolate complexes bearing a recently reported [2.2]isoindolino-phenyl-based carbene (iPC) ligand as a potent excited state π -acceptor. The compounds show efficient TADF from ligand-to-ligand charge transfer (^{1/3}LLCT) states with quantum yields of up to 0.8 and exceptional k_r of 0.8-1.9·10⁶ s⁻¹ that are among the fastest for Cu^I emitters, outcompeting traditional triplet emitters based on Ir^{III} and Pt^{II}. While yellow to orange emission is observed in single crystals, doping the complexes into polymer matrices or grinding shifts the luminescence into the deep red to near-IR. The mechanochromic TADF is due to disruption of C–H··· π interactions between the Cz and iPC ligands, which reduces the energy gap between the ground state and the ^{1/3}LLCT states. The Cu^I iPC complexes also bear potential for devices operating under electroluminescent conditions as demonstrated by a proof-of-concept deep-red OLED application.

Own contribution in the experimental part: approx. 25 %

Own contribution in the writing part: approx. 20%

3. Conclusion

Cu^I-phosphides have been known for years because of their diverse structure and application in catalysis, such as hydrophosphination reactions. I presented the first insight into the photophysical behaviour of such types of complexes where they undergo excited state charge transfer. The various structures of the complexes, the coordination of copper (I), and the types of phosphines used as acceptor molecules are among the key factors in determining their emission energy. However, increased rigidity due to cuprophilic interactions, co-crystallised solvent molecules, and increased conjugation of the phosphine also influence photophysical behaviour to a great extent. We had achieved six different types of complexes, which can be classified broadly into four types: dimers, cluster-A, cluster-B, and cluster-C.

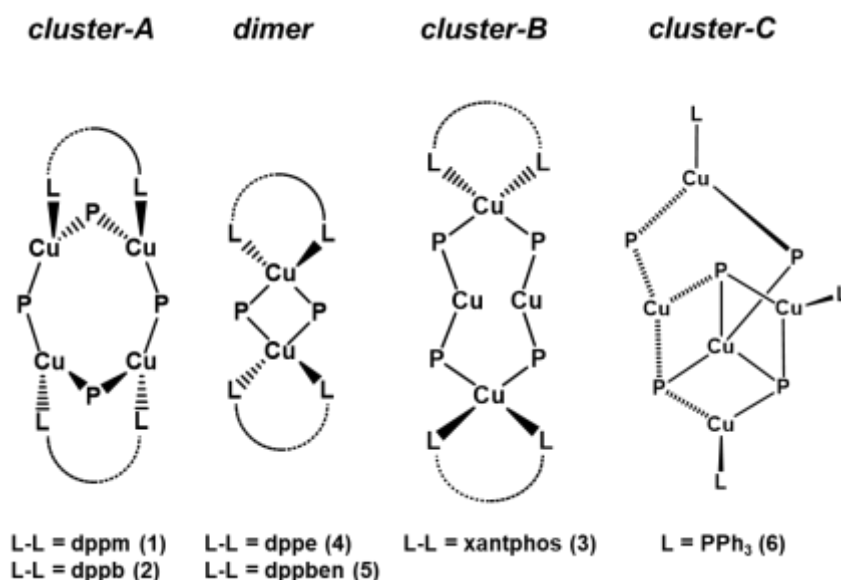


Figure 20. Various structural motifs of Cu^I-phosphides.

Compound **3** shows NIR emission with maxima around 900 nm at room temperature, which surpasses the previously reported NIR emitters based on Cu^I and Ir^{III} complexes. **1**, **4** and **6** display efficient to moderately efficient TADF behaviour with compound **4** being the one of the best TADF emitter with k_r of ca. $2 \times 10^5 \text{ s}^{-1}$. Interestingly, compound **2** and **5** exhibited pronounced reversible thermochromic behaviour along with dual TADF behaviour arising from two different excited states. The dual TADF behaviour in such types of compounds is the first of its kind and hasn't been explored till now, also such behaviour holds up great potential in different possible photonic applications as well.

Apart from the advantages, there are also a few challenges associated with these complexes; one among them is the dynamic behaviour in solution, i.e., the existence of

multiple species in solution that are in equilibrium with one another and cannot be isolated even at low temperatures. One of the solutions to resolve this issue could be the linking of the aryl parts of the phosphine and the phosphide, thus increasing the overall rigidity of the system and reducing the possibility of any dissociation in solution.

Another solution could be increasing the steric constraint of the phosphide ligand, i.e., the use of dimesityl phosphides instead of diphenyl phosphides, the resulting compound due to the higher steric demand can possibly form a monomeric structure and thus can be stable in solution state as well. Various carbenes can be used instead of the phosphines as the acceptor moiety and thus emission behaviour can be possibly tuned in the deep-red to NIR region along with the introduction of chirality in the carbene part can also lead to other interesting phenomena such as CPL (circularly polarised luminescence). This project is currently carried out by M.Sc. Paul Ruer from our group.

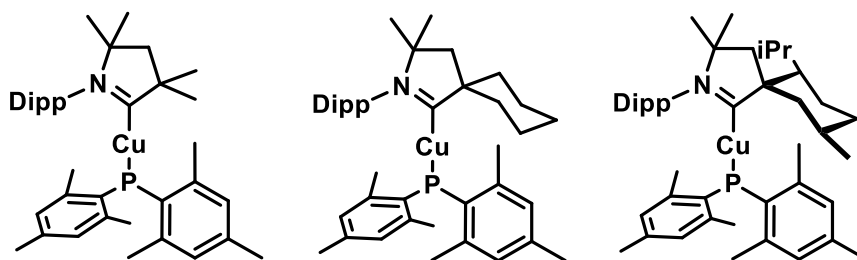


Figure 21. Proposed monometallic Cu^I-phosphide complexes.

Further such type of complexes (monometallic or Multimetallic) should be tested under electroluminescence conditions, by vapour deposition or solution-processed OLED architecture.

I had reported a new sterically demanding, electrophilic [2.2]isoindolinophanyl-based carbene (iPC) that bears a [2.2]paracyclophane moiety. The iPC ligand is a very potent π -chromophore, which participates in low energy IL-“through-space”-CT transitions in [Au(iPC)₂]OTf (**8**) in the visible. The beneficial photophysical and electronic properties of the iPC ligand, including a large accessible π surface area, were exploited by employing highly efficient energy transfer (EnT) photocatalysis in a [2+2] styrene cycloaddition reaction using **8**, which outperformed other established photocatalysts in comparison. We had also described a series of linear copper(I) carbene carbazolate complexes (**9-12**) bearing the [2.2]isoindolino-phanyl-based carbene (iPC) ligand. The compounds show efficient TADF from ligand-to-ligand charge transfer (^{1/3}LLCT) states with quantum yields of up to 0.8 and

exceptional k_r of $0.8\text{-}1.9 \times 10^6 \text{ s}^{-1}$ that are among the fastest for Cu^{I} emitters, outcompeting traditional triplet emitters based on Ir^{III} and Pt^{II} .

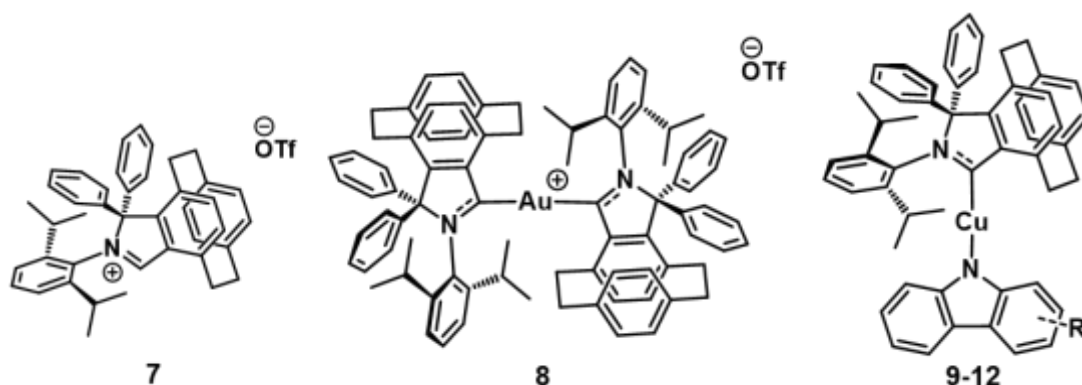


Figure 22. Current overview of iPC-based compounds.

All the compounds obtained were in their racemic form, but introduction of chirality into the system can increase its applications to a great extent such as in enantio-selective catalysis, CPL etc.

Thus various attempts have been made to for the chiral resolution of **7** such as synthesis of the respective conformers, crystallisation in various solvents, exchanging the triflate anion by a chiral anion by ion exchange resin, and the use of chiral TLC plates, yet none of the attempts were successful so far. Further attempts such as the use of chiral HPLC or a possibly different synthetic route should be used to isolate the conformers of **7**. However crystals of different isomers of **8** were isolated from the mixture by crystallisation in different solvent systems. Same conditions should be employed to a much higher quantity (800-900 mg) of racemate **8**, and a closer look on crystallisation can possibly result in isolation the different isomers completely.

Compound **8** should be subjected to various other photocatalysis reactions such as the DeMayo reaction as well as in various photoredox catalysis reactions. Compounds (**9-12**) could also be modified by introduction of the adamantyl group instead of the Dipp group, thus increasing the steric constraint and also restricting the movement of the Cz group which will possibly lead to small torsional angle between the carbene and the Cz backbone resulting in higher k_r . The Au^{I} and Ag^{I} analogue of compounds **9-12** should be studied as well as they too can also lead to high k_r values. The use stronger donor carbazoles such as phenoxazine and phenothiazine can further push the emissions into the NIR range. Currently this work is continued by M.Sc Andreas Prüfer from our group.

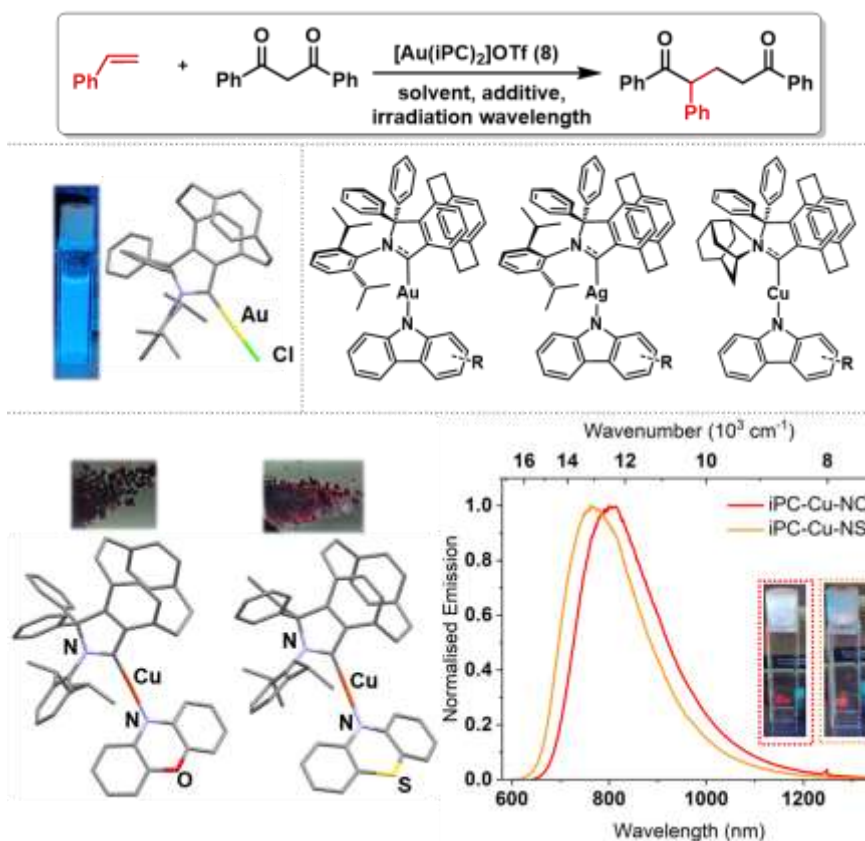
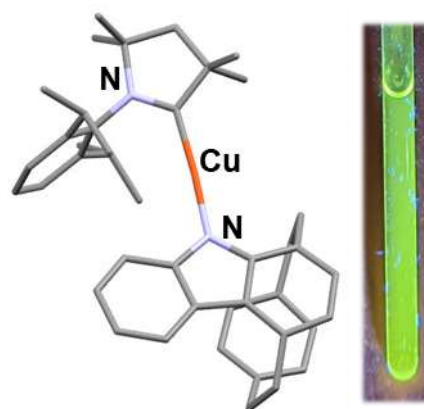


Figure 23. Top: Proposed DeMayo reaction with **8** as photocatalyst; Middle left: iPC-Au-Cl (photographs under 365 nm irradiation; intense blue emission in THF); Middle left: Proposed coinage metal complexes for potentially high k_r ; Down: iPC-Cu-NO/NS complexes for NIR emission in microcrystalline state ($\lambda_{max} = 805$ nm & 770 nm).

During end of 2021, I was also interested in the emission properties of the complexes consisting of the paracyclophane moiety at the donor side i.e., on the carbazole fragment. This project was started in collaboration with Prof. Dr. Eli Zysman-Colman from University of St. Andrews and Prof. Dr. Stefan Bräse from Karlsruher Institut für Technologie (KIT). The first compound which I synthesized using the carbazolophane (CzP) was CAAC^{Me}-Cu-CzP which displayed intense green emission in solution as well as in solid-state. It was interesting to note that the paracyclophane moiety of CzP and the Dipp fragment of the CAAC were on opposite sides. A small torsional angle of 16.4(1) ° as found, which makes them interesting candidates for high k_r values. To increase the rigidity and hence the Φ , the methyl fragment was replaced by the ethyl fragment. During end of 2022, this project was transferred to M.Sc. Indranil Sen for further studies.



4. References

- [1] a) G. Markiewicz, A. Walczak, F. Perlitius, M. Piasecka, J. M. Harrowfield, A. R. Stefankiewicz, *Dalton Trans.* **2018**, 47, 14254; b) S. Monro, K. L. Colón, H. Yin, J. Roque, P. Konda, S. Gujar, R. P. Thummel, L. Lilge, C. G. Cameron, S. A. McFarland, *Chem. Rev.* **2019**, 119, 797; c) B. Pashaei, H. Shahroosvand, P. Abbasi, *RSC Adv.* **2015**, 5, 94814; d) J. Takaya, *Chem.Sci.* **2020**, 12, 1964; e) S.-S. Xue, Y. Pan, W. Pan, S. Liu, N. Li, B. Tang, *Chem. Sci.* **2022**, 13, 9468; f) J. Zhao, K. Yan, G. Xu, X. Liu, Q. Zhao, C. Xu, S. Gou, *Adv. Funct. Mater.* **2021**, 31.
- [2] a) T. Li, J. Schaab, P. I. Djurovich, M. E. Thompson, *J. Mater. Chem. C* **2022**, 10, 4674; b) C. Borek, K. Hanson, P. I. Djurovich, M. E. Thompson, K. Aznavour, R. Bau, Y. Sun, S. R. Forrest, J. Brooks, L. Michalski et al., *Angew. Chem. Int. Ed.* **2007**, 46, 1109; c) A. Minotto, P. A. Haigh, Ł. G. Łukasiewicz, E. Lunedei, D. T. Gryko, I. Darwazeh, F. Cacialli, *Light Sci. Appl.* **2020**, 9, 70.
- [3] D. S. M. Ravinson, M. E. Thompson, *Mater. Horiz.* **2020**, 7, 1210.
- [4] M. Gernert, L. Balles-Wolf, F. Kerner, U. Müller, A. Schmiedel, M. Holzapfel, C. M. Marian, J. Pflaum, C. Lambert, A. Steffen, *J. Am. Chem. Soc.* **2020**, 142, 8897.
- [5] a) G. K.-M. So, G. Cheng, J. Wang, X. Chang, C.-C. Kwok, H. Zhang, C.-M. Che, *Chem. Asian J.* **2017**, 12, 1490; b) P. L. dos Santos, P. Stachelek, Y. Takeda, P. Pander, *Mater. Chem. Front.* **2024**, 8, 1731.
- [6] C. K. Prier, D. A. Rankic, D. W. C. MacMillan, *Chem. Rev.* **2013**, 113, 5322.
- [7] M. Montalti, S. L. Murov, *Handbook of photochemistry*, CRC/Taylor & Francis, Boca Raton, **2006**.
- [8] M. Kasha, *Discuss. Faraday Soc.* **1950**, 9, 14.
- [9] a) M. Hissler, P. W. Dyer, R. Réau, *Coord. Chem. Rev.* **2003**, 244, 1; b) M. Stępień, E. Gońka, M. Żyła, N. Sprutta, *Chem. Rev.* **2017**, 117, 3479.
- [10] W. Nau, *ChemPhysChem* **2011**, 12, 2496.
- [11] a) A. R. Brown, K. Pichler, N. C. Greenham, D. Bradley, R. H. Friend, A. B. Holmes, *Chem. Phys. Lett.* **1993**, 210, 61; b) H. Yersin, R. Beaulac (Eds.) *Topics in Current Chemistry*, Vol. 241, Springer, Berlin [etc.], **op. 2004**; c) H. Yersin in *Topics in Current Chemistry*, Vol. 241 (Eds.: H. Yersin, R. Beaulac), Springer, Berlin [etc.], **op. 2004**, pp. 1–26.
- [12] T. J. Penfold, E. Gindensperger, C. Daniel, C. M. Marian, *Chem. Rev.* **2018**, 118, 6975.
- [13] G. Baryshnikov, B. Minaev, H. Ågren, *Chem. Rev.* **2017**, 117, 6500.
- [14] A. Steffen, B. Hupp in *Comprehensive Coordination Chemistry III* (Eds.: E. Constable, G. Parkin, L. Que), Elsevier, San Diego, **2021**, pp. 466–502.
- [15] M. A. El-Sayed, *J. Chem. Phys.* **1963**, 38, 2834.
- [16] R. Englman, J. Jortner, *Mol. Phys.* **1970**, 18, 145.
- [17] a) W. Siebrand, *J. Chem. Phys.* **1967**, 46, 440; b) W. Siebrand, *J. Chem. Phys.* **1967**, 47, 2411.
- [18] P. Klán, J. Wirz, *Photochemistry of organic compounds. From concepts to practice*, Wiley, Chichester, **2009**.
- [19] M. Etinski, C. M. Marian, *Phys. Chem. Chem. Phys.* **2010**, 12, 15665.
- [20] D. H. A. ter Steege, A. C. Wirtz, W. J. Buma, *J. Chem. Phys.* **2002**, 116, 547.
- [21] T. A. Nguyen, *Frontier orbitals. A practical manual*, John Wiley & Sons, Chichester, England, Hoboken, NJ, **2007**.
- [22] M. Klessinger, J. Michl, *Excited states and photochemistry of organic molecules*, VCH, New York, **1995**.
- [23] P. Klán, J. Wirz, *Photochemistry of organic compounds. From concepts to practice*, Wiley, Chichester, **2009**.
- [24] C. M. Marian in *Reviews in Computational Chemistry* (Eds.: K. B. Lipkowitz, D. B. Boyd), Wiley-VCH, New York [u.a.], **2001**, pp. 99–204.
- [25] F. Bernardi, M. Olivucci, M. A. Robb, *Chem. Soc. Rev.* **1996**, 25, 321.
- [26] A. Steffen, B. Hupp in *Comprehensive Coordination Chemistry III* (Eds.: E. C. Constable, G. Parkin, L. Que Jr), Elsevier, Oxford, **2021**, pp. 466–502.

- [27] H. Yersin, A. F. Rausch, R. Czerwieńiec, T. Hofbeck, T. Fischer, *Coord. Chem. Rev.* **2011**, 255, 2622.
- [28] a) J. C. Deaton, R. H. Young, J. R. Lenhard, M. Rajeswaran, S. Huo, *Inorg. Chem.* **2010**, 49, 9151; b) K. Chen, Y.-M. Cheng, Y. Chi, M.-L. Ho, C.-H. Lai, P.-T. Chou, S.-M. Peng, G.-H. Lee, *Chem. Asian J.* **2007**, 2, 155.
- [29] D. Volz, M. Wallesch, C. Fléchon, M. Danz, A. Verma, J. M. Navarro, D. M. Zink, S. Bräse, T. Baumann, *Green Chem.* **2015**, 17, 1988.
- [30] a) A. Endo, M. Ogasawara, A. Takahashi, D. Yokoyama, Y. Kato, C. Adachi, *Adv. Mater.* **2009**, 21, 4802; b) H. Uoyama, K. Goushi, K. Shizu, H. Nomura, C. Adachi, *Nature* **2012**, 492, 234; c) A. Endo, K. Sato, K. Yoshimura, T. Kai, A. Kawada, H. Miyazaki, C. Adachi, *Appl. Phys. Lett* **2011**, 98.
- [31] H. Yersin, R. Czerwieńiec, M. Z. Shafikov, A. F. Suleymanova, *ChemPhysChem* **2017**, 18, 3508.
- [32] J. Föllner, M. Kleinschmidt, C. M. Marian, *Inorg. Chem.* **2016**, 55, 7508.
- [33] V. Balzani, G. Bergamini, S. Campagna, F. Puntoriero in *Topics in Current Chemistry* (Ed.: V. Balzani), Springer, Berlin, Heidelberg, **2007**, pp. 1–36.
- [34] a) I. Lyskov, C. M. Marian, *J. Phys. Chem. C* **2017**, 121, 21145; b) J. Gibson, A. P. Monkman, T. J. Penfold, *ChemPhysChem* **2016**, 17, 2956.
- [35] H. Kisch, *Semiconductor Photocatalysis. Principles and applications*, Wiley, Weinheim, Germany, **2015**.
- [36] Ostwald, *Ann. Naturphilos.* **1910**, 1.
- [37] W. Reschetilowski, *Einführung in die Heterogene Katalyse*, Springer Berlin Heidelberg, Berlin, Heidelberg, **2015**.
- [38] B. König, *Chemical Photocatalysis*, De Gruyter, Berlin/Boston, **2013**.
- [39] K. J. Zink, M. J. Thul, J. Hoffmann, A. Fleck in *Fehlzeiten-Report, Vol. 2008* (Eds.: B. Badura, M. L. Bienert), Springer, Heidelberg, **2009**, pp. 171–186.
- [40] P. Anastas, N. Eghbali, *Chem. Soc. Rev.* **2010**, 39, 301.
- [41] C. R. J. Stephenson, T. P. Yoon, D. W. C. MacMillan (Eds.) *Visible light photocatalysis in organic chemistry*, Wiley-VCH Verlag GmbH & Co, Weinheim, Germany, **2018**.
- [42] a) J. Frenkel, *Phys. Rev.* **1931**, 37, 17; b) G. H. Wannier, *Phys. Rev.* **1937**, 52, 191.
- [43] F. Strieth-Kalthoff, M. J. James, M. Teders, L. Pitzer, F. Glorius, *Chem. Soc. Rev.* **2018**, 47, 7190.
- [44] a) S. E. Braslavsky, A. M. Braun, A. E. Cassano, A. V. Emeline, M. I. Litter, L. Palmisano, V. N. Parmon, N. Serpone, *Pure Appl. Chem.* **2011**, 83, 931; b) B. M. Hockin, C. Li, N. Robertson, E. Zysman-Colman, *Catal. Sci. Technol.* **2019**, 9, 889.
- [45] a) V. Balzani, P. Ceroni, A. Credi, M. Venturi, *Coord. Chem. Rev.* **2021**, 433, 213758; b) P. Dongare, B. D. Myron, L. Wang, D. W. Thompson, T. J. Meyer, *Coord. Chem. Rev.* **2017**, 345, 86; c) N. H. Damrauer, G. Cerullo, A. Yeh, T. R. Bousie, C. V. Shank, J. K. McCusker, *Science* **1997**, 275, 54; d) D. M. Roundhill, *Photochemistry and Photophysics of Metal Complexes*, Springer International Publishing; Springer Nature, Cham, **20**; e) J. I. Day, K. Teegardin, J. Weaver, J. Chan, *Org. Process Res. Dev.* **2016**, 20, 1156; f) D. M. Arias-Rotondo, J. K. McCusker, *Chem. Soc. Rev.* **2016**, 45, 5803.
- [46] V. Balzani, *Photochemistry and photophysics : concepts, research, applications. Concepts, research, applications*, Wiley-VCH, Weinheim, Germany, **uuuu-uuuu**.
- [47] A. Inagaki, M. Akita, *Coord. Chem. Rev.* **2010**, 254, 1220.
- [48] a) K. Kalyanasundaram, *Coord. Chem. Rev.* **1982**, 46, 159; b) A. Juris, V. Balzani, P. Belser, A. von Zelewsky, *Helv. Chim. Acta* **1981**, 64, 2175.
- [49] N. V. Tzouras, E. A. Martynova, X. Ma, T. Scattolin, B. Hupp, H. Busen, M. Saab, Z. Zhang, L. Falivene, G. Pisanò et al., *Chem. Eur. J.* **2021**, 27, 11904.
- [50] P.-K. Chow, G. Cheng, G. S. M. Tong, C. Ma, W.-M. Kwok, W.-H. Ang, C. Y.-S. Chung, C. Yang, F. Wang, C.-M. Che, *Chem. Sci.* **2016**, 7, 6083.
- [51] J. D. Slinker, C. Y. Koh, G. G. Malliaras, M. S. Lowry, S. Bernhard, *Appl. Phys. Lett.* **2005**, 86.

- [52] J. D. Slinker, A. A. Gorodetsky, M. S. Lowry, J. Wang, S. Parker, R. Rohl, S. Bernhard, G. G. Malliaras, *J. Am. Chem. Soc.* **2004**, *126*, 2763.
- [53] M. S. Lowry, J. I. Goldsmith, J. D. Slinker, R. Rohl, R. A. Pascal, G. G. Malliaras, S. Bernhard, *Chem. Mater.* **2005**, *17*, 5712.
- [54] C. Sieck, M. G. Tay, M.-H. Thibault, R. M. Edkins, K. Costuas, J.-F. Halet, A. S. Batsanov, M. Haehnel, K. Edkins, A. Lorbach et al., *Chem. Eur. J.* **2016**, *22*, 10523.
- [55] E. S.-H. Lam, D. P.-K. Tsang, W. H. Lam, A. Y.-Y. Tam, M.-Y. Chan, W.-T. Wong, V. W.-W. Yam, *Chem. Eur. J.* **2013**, *19*, 6385.
- [56] M. Jiao, B. Zhang, Z. Wang, B.-Z. Chen, *Appl. Organomet. Chem.* **2022**, *36*.
- [57] Z. Lu, T. P. Yoon, *Angew. Chem. Int. Ed.* **2012**, *51*, 10329.
- [58] M. Y. Wong, E. Zysman-Colman, *Adv. Mater.* **2017**, *29*.
- [59] S. Wang, X. Yan, Z. Cheng, H. Zhang, Y. Liu, Y. Wang, *Angew. Chem. Int. Ed.* **2015**, *54*, 13068.
- [60] U. Balijapalli, R. Nagata, N. Yamada, H. Nakanotani, M. Tanaka, A. D'Aléo, V. Placide, M. Mamada, Y. Tsuchiya, C. Adachi, *Angew. Chem. Int. Ed.* **2021**, *60*, 8477.
- [61] A. D'Aléo, M. H. Sazzad, D. H. Kim, E. Y. Choi, J. W. Wu, G. Canard, F. Fages, J.-C. Ribierre, C. Adachi, *Chem. Comm.* **2017**, *53*, 7003.
- [62] K. Sun, Da Chu, Y. Cui, W. Tian, Y. Sun, W. Jiang, *Org. Electron.* **2017**, *48*, 389.
- [63] K. Hasan, A. K. Bansal, I. D. W. Samuel, C. Roldán-Carmona, H. J. Bolink, E. Zysman-Colman, *Sci. Rep.* **2015**, *5*, 12325.
- [64] R. Tao, J. Qiao, G. Zhang, L. Duan, L. Wang, Y. Qiu, *J. Phys. Chem. C* **2012**, *116*, 11658.
- [65] L. Donato, C. E. McCusker, F. N. Castellano, E. Zysman-Colman, *Inorg. Chem.* **2013**, *52*, 8495.
- [66] A. K. Pal, D. B. Cordes, A. M. Z. Slawin, C. Momblona, A. Pertegás, E. Ortí, H. J. Bolink, E. Zysman-Colman, *RSC Adv.* **2017**, *7*, 31833.
- [67] I. Melendo, S. Fuertes, A. Martín, V. Sicilia, *Inorg. Chem.* **2024**, *63*, 5470.
- [68] A. Jouaiti, L. Ballerini, H.-L. Shen, R. Viel, F. Polo, N. Kyritsakas, S. Haacke, Y.-T. Huang, C.-W. Lu, C. Gourlaouen et al., *Angew. Chem. Int. Ed.* **2023**, *62*, e202305569.
- [69] N. A. Shekhovtsov, T. E. Kokina, K. A. Vinogradova, A. Y. Panarin, M. I. Rakhmanova, D. Y. Naumov, N. V. Pervukhina, E. B. Nikolaenkova, V. P. Krivopalov, R. Czerwieniec et al., *Dalton Trans.* **2022**, *51*, 2898.
- [70] B. Hupp, C. Schiller, C. Lenczyk, M. Stanoppi, K. Edkins, A. Lorbach, A. Steffen, *Inorg. Chem.* **2017**, *56*, 8996.
- [71] A. M. T. Muthig, M. Krumrein, J. Wieland, M. Gernert, F. Kerner, J. Pflaum, A. Steffen, *Inorg. Chem.* **2022**, *61*, 14833.

5. Appendix

SI of the publications of the cumulative part of this work

Supporting Information

Multimetallic Copper(I) Diphenylphosphides Displaying Thermally Activated Delayed Fluorescence (TADF) in the Visible to Near-IR

Sabyasachi Maity, Andrey Belyaev, Benjamin Hupp, Ondřej Mrózek, and Andreas Steffen

Table of Contents

1. General Procedures	S1
2. Characterization Data	S2
3. NMR spectra	S4
4. ATR-IR	S10
5. X-ray characterization data	S12
6. Structural details of 1-3	S16
7. Photophysical Measurements	S20
8. Emission Studies	S21
9. Thermal stability of compound 1-3	S28
10. TD-DFT calculations	S29
11. References	S37

1. General Procedures

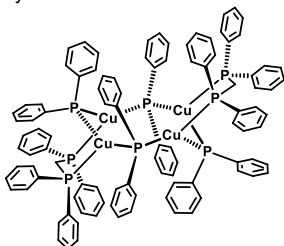
All manipulations were carried out under an inert atmosphere of argon using standard Schlenk link^[1] or glovebox techniques (GS MEGA E-Line, <0.5 ppm of H₂O and O₂). All reagents were used as supplied. Solvents such as tetrahydrofuran (THF), toluene, and pentane were used at HPLC grade purity from commercial sources (VWR and Fisher Chemicals) and dried using PureSolv MD 7 drying system. After being dried, diethyl ether was kept in 4 Å molecular sieves.

NMR spectra were recorded on a Bruker Avance III HD NanoBay 400 MHz; ¹H and chemical shifts (δ) are given in ppm relative to TMS, coupling constants (J) in Hz. The solvent signals were used as references, and the chemical shifts were converted to the TMS scale. ATR-IR spectra were measured on a Bruker Alpha-II IR Spectrometer, and CHN elemental analyses were performed on a Micro cube (Elementar).

Copper(I) *tert*-butanolate and [Cu(PPh)₂]₈ were synthesised according to literature procedures.^[2]

2. Characterization Data

Synthesis of 1

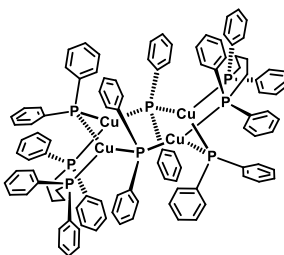


$\text{Cu}(\text{PPh})_2$ (50 mg, 0.2 mmol) and 1,2-bis(diphenylphosphino) methane (dppm) (39 mg, 0.1 mmol) were added to 6 mL anhydrous THF. After 24 hours the reaction mixture was filtered over a pipette containing celite and basic aluminium oxide. A deep orange transparent filtrate was obtained which was co-crystallized with toluene (2:1). Deep red crystals were obtained which were washed with 2 mL toluene. Yield: 23% (40 mg). **EA** calc. for $[\text{C}_{98}\text{H}_{84}\text{Cu}_4\text{P}_8]$ C, 66.74; H, 4.80. Found: C, 67.0; H, 5.1. **IR (ATR)** $[\text{cm}^{-1}]$: $\bar{\nu} = 3047.54, 1580.44, 1475.35, 1432.08, 1182.75, 1090.02, 1024.09, 997.30, 772.70, 733.55, 690.28, 506.89, 473.92, 412.10$.

On measuring the $^1\text{H-NMR}$ spectra at room temperature, the number of protons were more than the expected structure and also the aromatic peaks were merged. In the $^{31}\text{P}\{^1\text{H}\}$ NMR at room temperature shows multiple peaks indicating presence of multiple species in solution. On cooling down to -80°C , $^1\text{H-NMR}$ spectra shows better resolution in the aromatic part, yet number of protons were more than the expected structure. $^{31}\text{P}\{^1\text{H}\}$ NMR shows less peaks at -80°C , but when warmed up to room temperature shows the extra peaks which were missing. This indicates the presence of multiple species in solution which are at equilibrium to one another and can't be separated even at low temperatures.

$^1\text{H-NMR}$ (d_8 -THF, 400 MHz, 298 K): 8.00 - 6.41 (m, Ar-H), 2.76 (bs), 2.30 (s); $^{31}\text{P}\{^1\text{H}\}$ NMR (d_8 -THF, 400 MHz, 298 K): 24.11, - 5.37, - 8.62, - 15.59, - 21.47.

Synthesis of 2



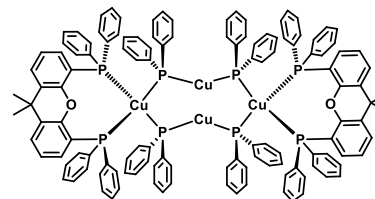
$[\text{Cu}(\text{PPh})_2]_8$ (50 mg, 0.2 mmol) and 1,2-bis(diphenylphosphino) butane (43 mg, 0.1 mmol) were taken. Compound **2** was obtained using a similar procedure to that reported for compound **1** as yellowish green crystals were obtained on recrystallisation with pentane (2:1).

Yield: 24% (45 mg). **EA** calc. for $[\text{C}_{104}\text{H}_{96}\text{Cu}_4\text{P}_8]$ C, 67.60; H, 5.24. Found: C, 67.6; H, 5.4. **IR (ATR)** $[\text{cm}^{-1}]$: $\bar{\nu} = 3043.42, 1576.31, 1473.29, 1430.02, 1143.60, 1094.15, 1073.54, 1024.09, 997.30, 886.03, 789.18, 731.49, 688.22, 506.89, 475.98, 440.95, 414.17$.

On measuring the $^1\text{H-NMR}$ spectra at room temperature, the number of protons were more than the expected structure and also the aromatic peaks were merged. In the $^{31}\text{P}\{^1\text{H}\}$ NMR at room temperature shows multiple peaks indicating presence of multiple species in solution. On cooling down to -80°C , $^1\text{H-NMR}$ spectra shows better resolution in the aromatic part, yet number of protons were more than the expected structure. $^{31}\text{P}\{^1\text{H}\}$ NMR shows less peaks at -80°C , but when warmed up to room temperature shows the extra peaks which were missing. This indicates the presence of multiple species in solution which are at equilibrium to one another and can't be separated even at low temperatures.

$^1\text{H-NMR}$ (d_8 -THF, 400 MHz, 298 K): 7.89 - 6.63 (m, Ar-H), 2.41 (s), 1.31 - 1.25 (bs), 0.84 (t); $^{31}\text{P}\{^1\text{H}\}$ NMR (d_8 -THF, 400 MHz, 298 K): 26.80, 26.47, 19.94, - 15.56, - 17.26,.

Synthesis of 3



$[\text{Cu}(\text{PPh})_2]_8$ (50 mg, 0.2 mmol) and 4,5-Bis(diphenylphosphino)-9,9-dimethylxanthene (58 mg, 0.1 mmol) were taken. Compound **3** was obtained using a similar procedure to that reported for compound **1** as yellowish crystals were obtained on recrystallisation with pentane (1:2). Yield: 20% (44 mg). **EA** calc. for $[\text{C}_{126}\text{H}_{104}\text{Cu}_4\text{O}_2\text{P}_8]$ C, 70.32; H, 4.87. Found: C, 70.3; H, 5.0. **IR (ATR)** $[\text{cm}^{-1}]$: $\bar{\nu} = 3047.54, 1578.37, 1473.29, 1432.08, 1407.35, 1236.32, 1087.96, 1065.30, 1022.03, 997.30, 879.85, 844.82, 789.18, 754.16, 735.61, 692.34, 533.68, 502.77, 480.10, 455.38, 432.71, 410.04$.

On measuring the $^1\text{H-NMR}$ spectra at room temperature, the number of protons were more than the expected structure and also the aromatic peaks were merged. In the $^{31}\text{P}\{^1\text{H}\}$ NMR at room temperature shows multiple peaks indicating presence of multiple species in solution. On cooling down to -80°C , $^1\text{H-NMR}$ spectra shows better resolution in the aromatic part, yet number of protons were more than the expected structure. $^{31}\text{P}\{^1\text{H}\}$ NMR shows less peaks at -80°C , but when warmed up to room temperature shows the extra peaks which were missing. This indicates the presence of multiple species in solution which are at equilibrium to one another and can't be separated even at low temperatures.

$^1\text{H-NMR}$ (d_8 -THF, 400 MHz, 298 K): 7.54 - 6.46 (m, Ar-H), 5.90 - 5.85 (bs, Ar-H), 5.15 - 5.11 (bs, Ar-H), 1.62 (s), 1.29 - 1.25 (m), 0.89 - 0.85 (m); $^{31}\text{P}\{^1\text{H}\}$ NMR (d_8 -THF, 400 MHz, 298 K): 23.78, - 13.63, - 15.60, - 18.25, - 22.53, - 36.74.

3. NMR spectra

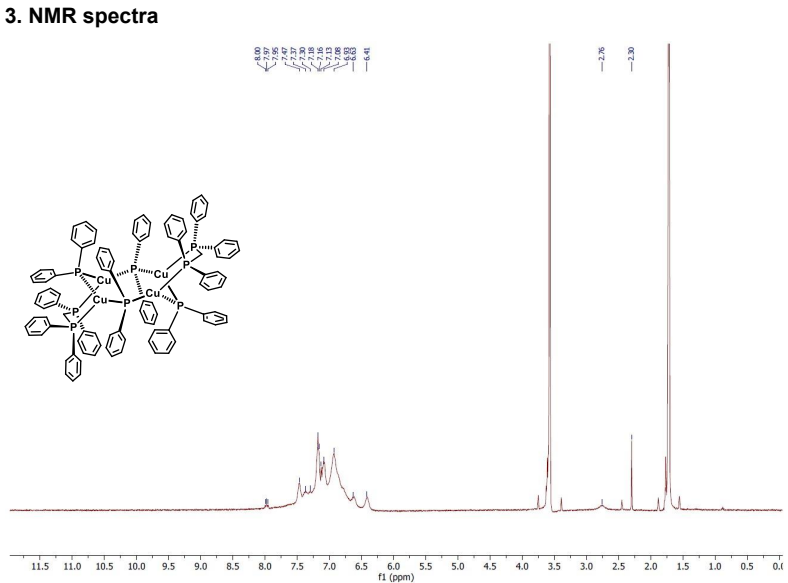


Figure S1. $^1\text{H-NMR}$ (400 MHz, THF-d_8 , 298 K) of **1**.

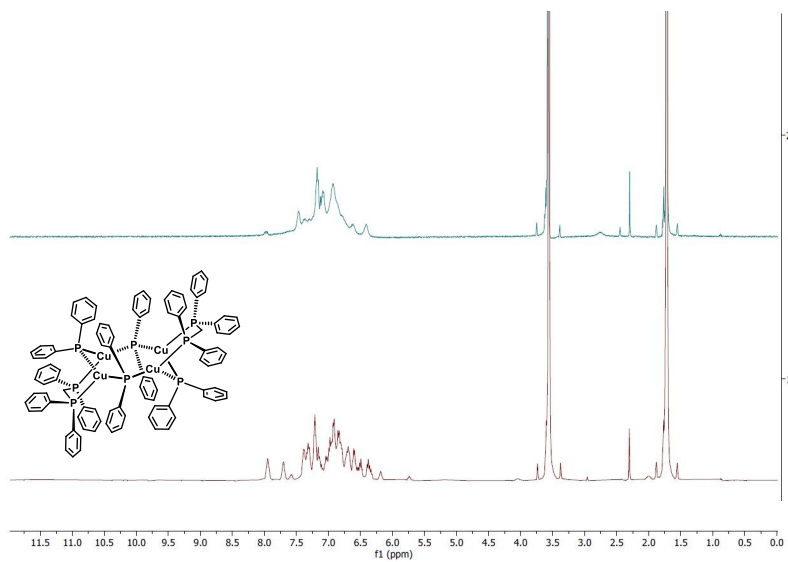


Figure S2. $^1\text{H-NMR}$ (400 MHz, THF-d_8 , top: 298 K, bottom: 193 K) of **1**.

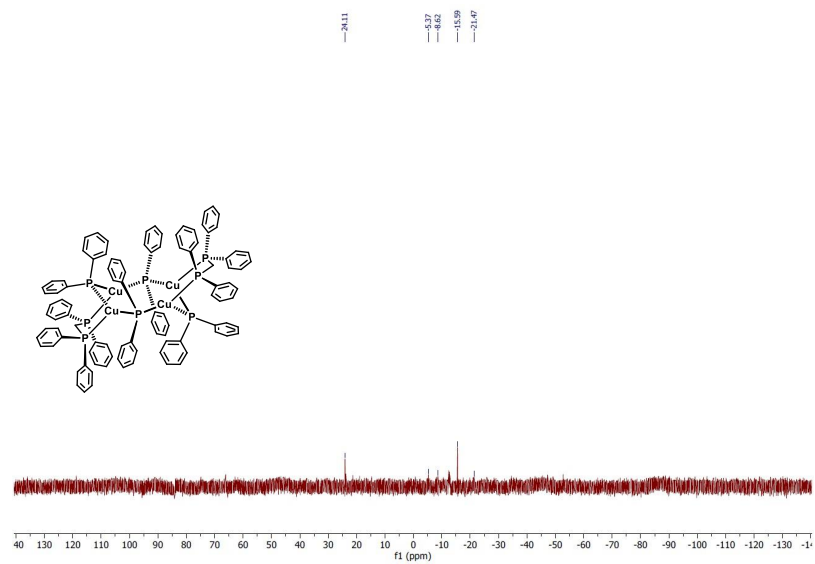


Figure S3. $^{31}\text{P-NMR}$ (400 MHz, THF-d_8 , 298 K) of **1**.

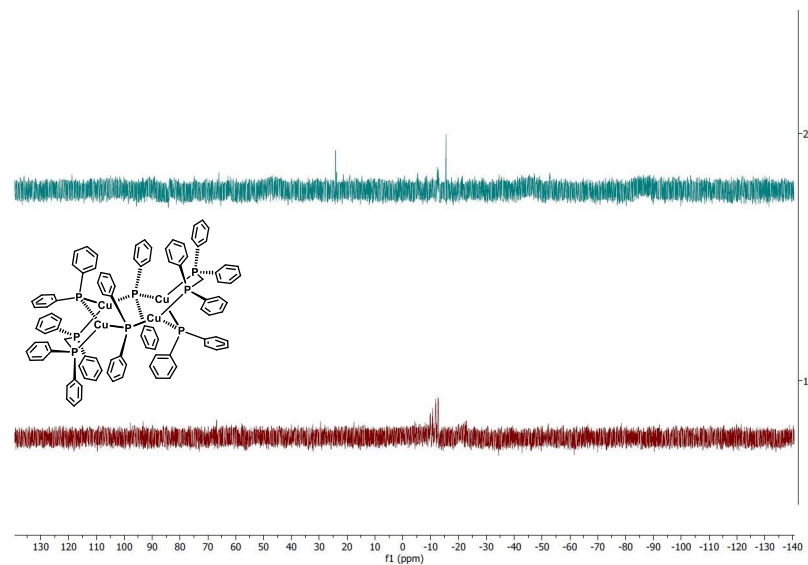


Figure S4. $^{31}\text{P-NMR}$ (400 MHz, THF-d_8 , top: 298 K, bottom: 193 K) of **1**.

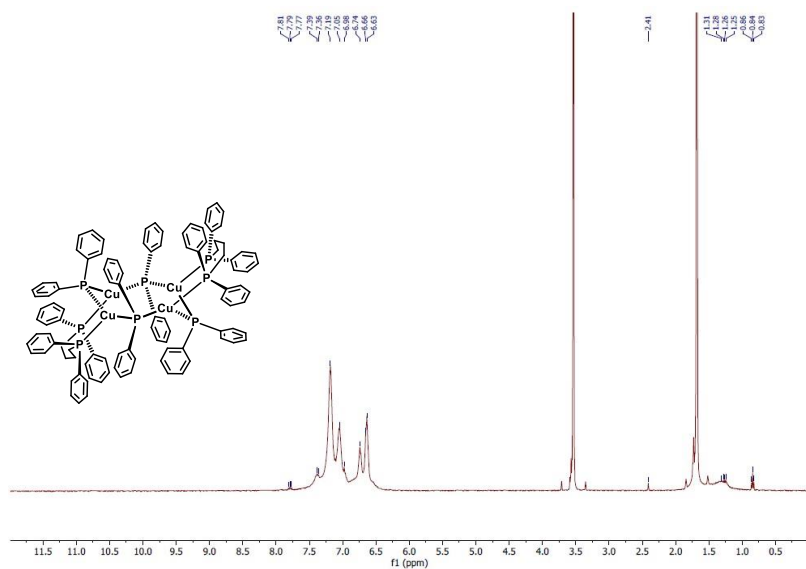


Figure S5. $^1\text{H-NMR}$ (400 MHz, THF-d_8 , 298 K) of **2**.

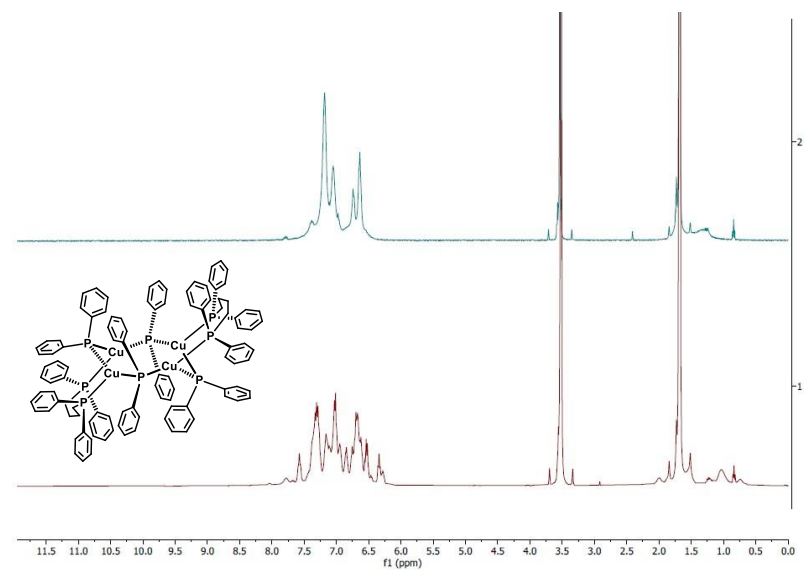


Figure S6. $^1\text{H-NMR}$ (400 MHz, THF-d_8 , top: 298 K, bottom: 193 K) of **2**.

S-6

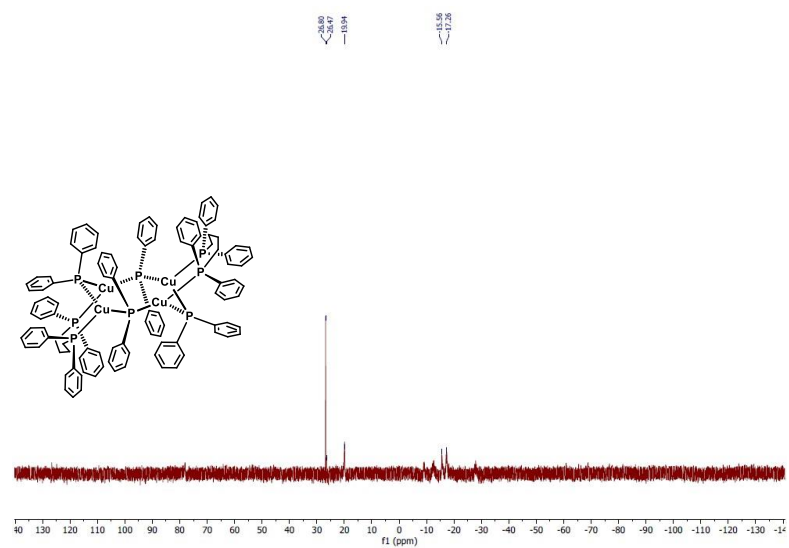


Figure S7. $^{31}\text{P-NMR}$ (400 MHz, THF-d_8 , 298 K) of **2**.

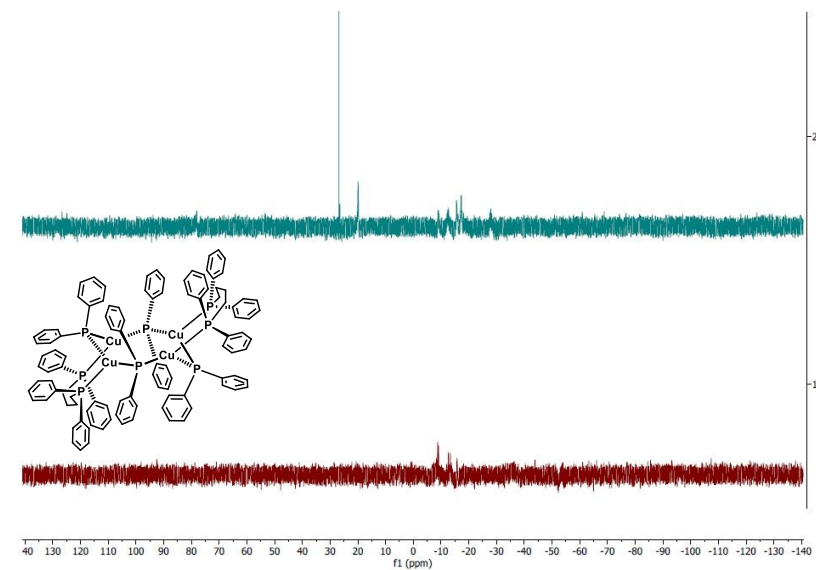


Figure S8. $^{31}\text{P-NMR}$ (400 MHz, THF-d_8 , top: 298 K, bottom: 193 K) of **2**.

S-7

4. ATR-IR

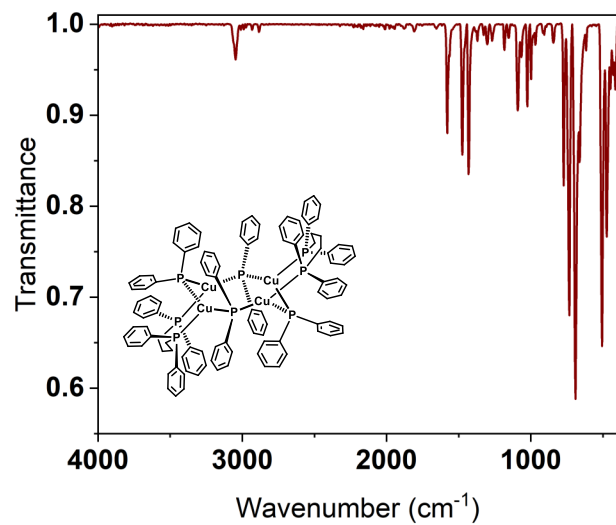


Figure S13. ATR-IR spectrum of 1.

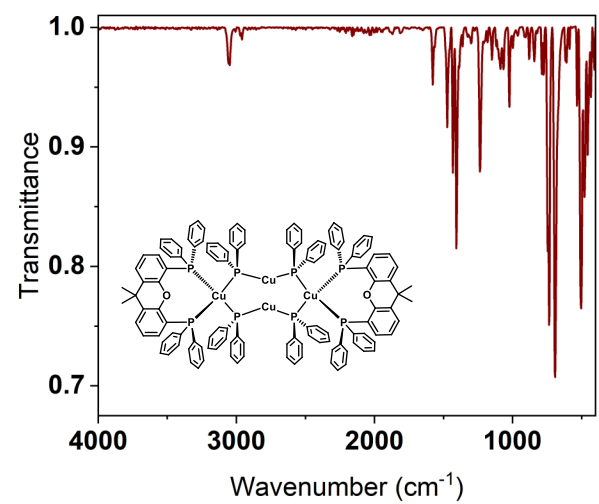


Figure S15. ATR-IR spectrum of 3.

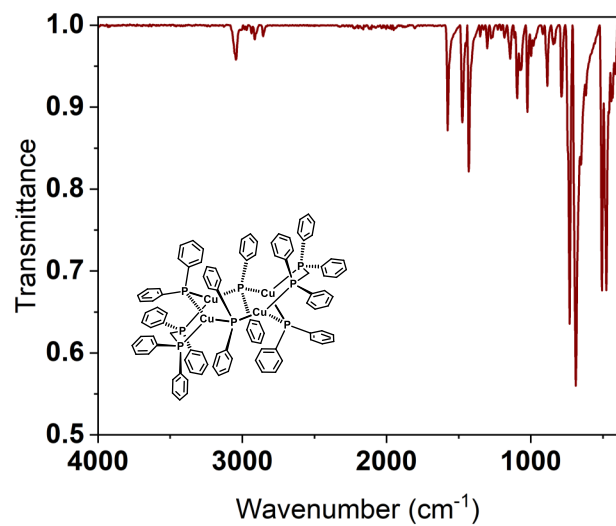


Figure S14. ATR-IR spectrum of 2.

5. X-ray characterization data

General part

X-ray diffraction determination

The crystals of **1–3** were immersed in a film of NVH or perfluoropolyether oil, mounted on a polyimide microloop (MiTeGen) and transferred to a stream of cold nitrogen (Bruker Kryoflex2), and measured at a temperature of 100 K. The X-ray diffraction data were collected on a Bruker D8 diffractometer with a CMOS Photon 100 and multilayer optics monochromated MoK α (0.71073Å) radiation (INCOATEC microfocus sealed tube). The frames were integrated with the Bruker SAINT software package using a narrow-frame algorithm. The APEX3 v2018.7-0 program package was used for cell refinements and data reductions. The structure was solved using the intrinsic phasing method,^[3] refined and visualized with the OLEX2-1.5 program.^[4] A semiempirical absorption correction (SADABS) was applied to all data. All non-hydrogen atoms were refined anisotropically. Hydrogen atoms were included in structure factors calculations. All Hydrogen atoms were assigned to idealized geometric positions. The unit cells of the **1–3** contain disordered solvent molecules which have been treated as a diffuse contribution to the overall scattering without specific atom positions by SQUEEZE/PLATON.^[5] The crystallographic details are summarized in **Table S1**. CCDC **2379890–2379892** contains the supplementary crystallographic data for this paper.

X-ray Structures

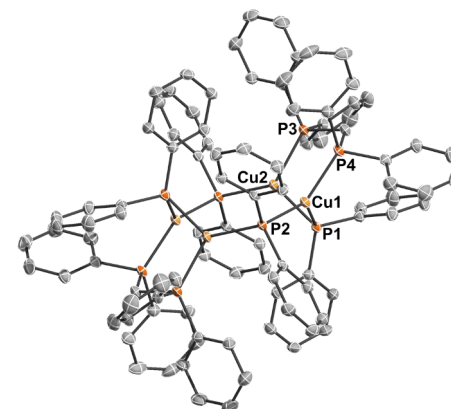


Figure S16. X-ray solid-state structure of **1**. Thermal ellipsoids were drawn at the 50% probability level; H atoms and solvent molecules have been omitted for clarity. Selected bond lengths (Å) and angles [deg]: Cu1-P1 2.2423(6), Cu1-P4 2.2551(6), Cu1-P2 2.2605(6), Cu2-P1 2.2882(5), Cu2-P3 2.2846(6), Cu2-P2 2.2712(6), P4-Cu1-P2 131.49(2), P3-Cu2-P2 127.53(2).

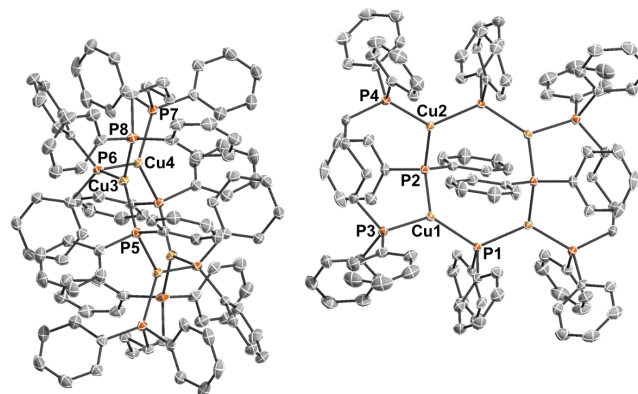


Figure S17. X-ray solid-state structure of **2**. Thermal ellipsoids were drawn at the 50% probability level; H atoms and solvent molecule have been omitted for clarity. Selected bond lengths (Å) and angles [deg]: Cu1-P1 2.2875(5), Cu1-P3 2.2615(6), Cu1-P2 2.2761(6), Cu2-P1 2.2882(5), Cu2-P4 2.2521(6), Cu2-P2 2.2636(5), Cu3-P5 2.2977(6), Cu3-P8 2.2946(6), Cu3-P6 2.2704(5), Cu4-P5 2.2904(5), Cu4-P7 2.2777(6), Cu4-P62.2684(5), P3-Cu1-P1 125.965(17), P4-Cu2-P1 120.437(17), P8-Cu3-P5 119.393(18), P7-Cu4-P5 121.716(17).

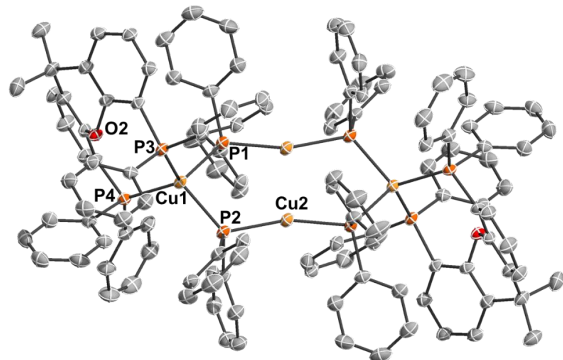


Figure S18. X-ray solid-state structure of **3**. Thermal ellipsoids were drawn at the 50% probability level; H atoms and solvent molecule have been omitted for clarity. Selected bond lengths (Å) and angles [deg]: Cu1-P1 2.3418(12), Cu1-P2 2.3651(8), Cu2-P2 2.2500(12), Cu2-P1 2.2492(11), Cu1-P3 2.3569(8), Cu1-P4 2.3449(9), P1-Cu1-P2 99.13(3), P2-Cu2-P1 161.11(3).

Table S1. Crystal data and structure refinement for **1–3**.

Identification code	1	2	3
CCDC number	2379891	2379892	2379890
Empirical formula	C _{61.25} H ₅₆ Cu ₂ P ₄	C ₅₄ H ₅₂ Cu ₂ O _{0.5} P ₄	C _{64.33} H _{54.66} Cu ₂ O _{1.33} P ₄
Formula weight	1043.02	959.91	1100.08
Temperature [K]	100		
Crystal system	monoclinic	triclinic	triclinic
Space group	P2 ₁ /c	P-1	P-1
a [Å]	12.9339(4)	15.1047(3)	13.1205(3)
b [Å]	20.5583(7)	17.2117(4)	16.3246(5)
c [Å]	21.1058(6)	19.5900(5)	17.9182(5)
α [°]	90	88.7840(10)	63.7060(10)
β [°]	105.8690(10)	83.3650(10)	68.7360(10)
γ [°]	90	82.1340(10)	78.9980(10)
Volume [Å ³]	5398.1(3)	5011.2(2)	3204.41(16)
Z	4	4	4
ρ _{calc} [g/cm ³]	1.283	1.272	1.140
μ [mm ⁻¹]	0.944	1.011	0.800
F(000)	2166.0	1992.0	1139.0
Crystal size [mm ³]	0.336 × 0.2 × 0.156	0.284 × 0.255 × 0.168	0.136 × 0.102 × 0.069
Radiation type	MoKα (λ = 0.71073)		
2θ range for data collection [°]	3.826 to 54.996	4.736 to 50.284	4.832 to 53.998
Index ranges	-16 ≤ h ≤ 16, -23 ≤ k ≤ 26, -27 ≤ l ≤ 27	-18 ≤ h ≤ 17, -20 ≤ k ≤ 20, -23 ≤ l ≤ 23	-16 ≤ h ≤ 14, -20 ≤ k ≤ 20, -22 ≤ l ≤ 22
Reflections collected	47760	104787	75490
Independent reflections	12340 [R _{int} = 0.0287, R _{sigma} = 0.0270]	17871 [R _{int} = 0.0269, R _{sigma} = 0.0170]	13933 [R _{int} = 0.0976, R _{sigma} = 0.0650]
Data/restraints/parameters	12340/142/624	17871/0/1090	13933/75/678
Goodness-of-fit on F ² ^(a)	1.037	1.038	1.029
Final R indexes [I ≥ 2σ(I)] ^(b)	R ₁ = 0.0354, wR ₂ = 0.0970	R ₁ = 0.0241, wR ₂ = 0.0655	R ₁ = 0.0507, wR ₂ = 0.1442
Final R indexes [all data] ^(b)	R ₁ = 0.0414, wR ₂ = 0.1004	R ₁ = 0.0266, wR ₂ = 0.0669	R ₁ = 0.0744, wR ₂ = 0.1590
Largest diff. peak/hole [e/Å ⁻³]	0.69/-0.55	0.35/-0.28	1.13/-0.42

^(a) GooF = S = $[\sum w(F_o^2 - F_c^2)^2 / (m - n)]^{1/2}$, where m = number of reflexes and n = number of parameters; ^(b) R₁ = $\sum |F_o| - |F_c| / \sum |F_o|$; wR₂ = $[\sum [w(F_o^2 - F_c^2)^2] / \sum [(wF_o^2)^2]]^{1/2}$; w = $1 / [\sigma^2(F_o^2) + (aP)^2 + bP]$, where P = $(F_o^2 + 2F_c^2) / 3$

6. Structural details of 1-3

Table S2. Structural Details of Compounds 1–6 at 100 K

Compd.	1	2	3
Geometry at Cu centre	Distorted triangular planar	Distorted triangular planar	Flattened tetrahedron (Cu1) Distorted linear (Cu2)
Cu–Cu (Å)	Cu1–Cu2 3.0008(4) ^a	Cu1–Cu2 3.7166(5) ^a Cu3–Cu4 3.6458(5) ^a	Cu2–Cu2 2.8470(5) ^a Cu1–Cu2 3.9655(7)^a
Cu–P (Å)	Cu1–P 2.2514(6) Cu2–P 2.2797(6)	Cu1–P 2.2818(6) Cu2–P 2.2804(5) Cu3–P 2.2840(6) Cu4–P 2.2794(5)	Cu1–P 2.3534(10) Cu2–P 2.2496(12)
Cu–P (Å) (phosphide)	Cu–P 2.2698(6)	Cu–P 2.2568(6)^c Cu–P 2.2861(6)^d	Cu–P 2.3509(9)
Dihedral angle (°)	β : 109.9 α : 40.8	β : 105.1, 102.9 α : 28.1, 33.7	88.8
β_n (°) ^b	71.70	97.70	107.12
β_n (°)	-	-	P3–Cu1–P4 107.97(3)
P–Cu–P (°) (phosphide)	P2–Cu–P1 124.25(2)	P1–Cu–P2 119.947(17) P5–Cu–P6 123.445(17)	P1–Cu1–P2 99.13(3) P1–Cu2–P2 161.11(3)
P–Cu–P (°) (phosphide and phosphine)	P1–Cu–P 105.52(2) P2–Cu–P 129.51(2)	P3–Cu1–P 118.560(17) P2–Cu2–P 120.802(17) P8–Cu3–P 119.347(18) P7–Cu4–P 116.995(17)	P–Cu1–P4 116.00(3) P–Cu1–P3 108.61(3)
Cu–P–Cu (°) (phosphide)	Cu1–P2–Cu2 115.97(2) Cu1–P1–Cu2 82.957(19)	Cu1–P1–Cu2 122.876(19) Cu1–P2–Cu2 109.910(18) Cu3–P5–Cu4 126.39(2) Cu3–P6–Cu4 106.882(18)	Cu1–P–Cu2 118.96(4)

^aDistance between two Cu centres. ^bbite angle from ref 6. ^cwith Cu1 and Cu2 centres. ^dwith Cu3 and Cu4 centres. Mean values written in bold font.

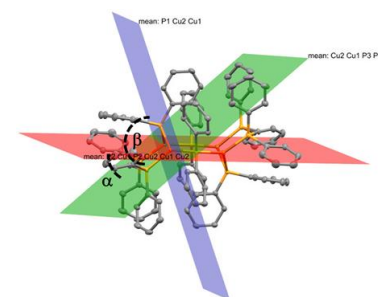


Figure S19. Dihedral angle in **1** ($\alpha = 40.85^\circ$ & $\beta = 109.93^\circ$). Red: Cu₄P₄(phosphide), green: Cu₂P₂(phosphine), and blue:Cu₂P (phosphide).

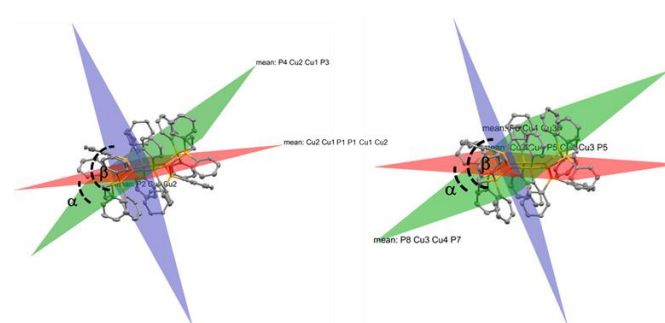


Figure S20. Dihedral angle in **2a** (left) ($\alpha = 28.05^\circ$ & $\beta = 105.16^\circ$) and in **2b** (right) ($\alpha = 33.75^\circ$ & $\beta = 102.92^\circ$). Red: Cu₄P₄(phosphide), green: Cu₂P₂(phosphine), and blue:Cu₂P (phosphide).

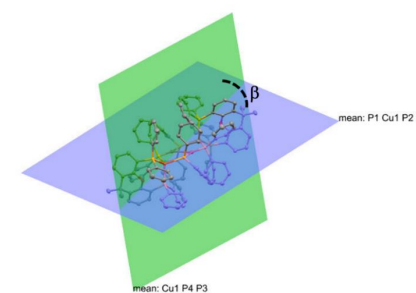


Figure S21. Dihedral angle in **3** ($\beta = 88.79^\circ$). Green: Cu₂P₂(phosphine), and blue:Cu₂P (phosphide).

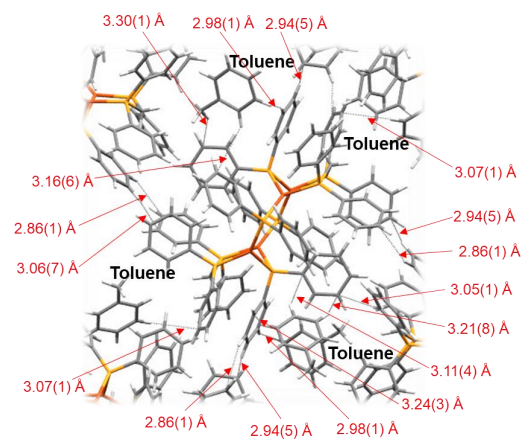


Figure S22. Molecular C–H··· π interactions of **1**.

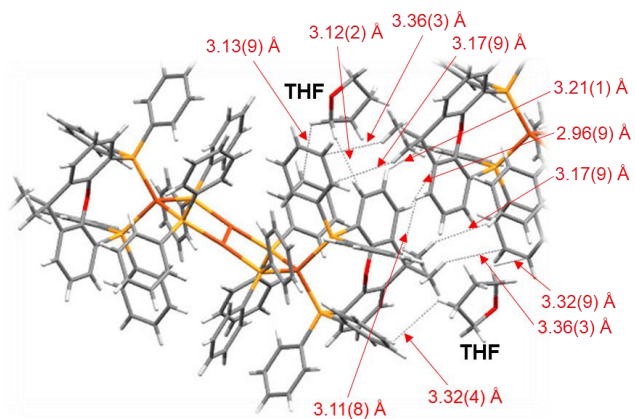


Figure S23. Molecular C–H··· π interactions of **3**.

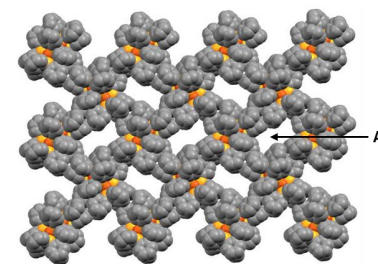


Figure S24. Packing diagram of **1**, view along the crystallographic a-axis. Channel A has a cuboid/cylindrical shape with approximately length 1.21 nm and breadth/diameter 0.74 nm. H atoms and solvent molecules omitted for clarity.

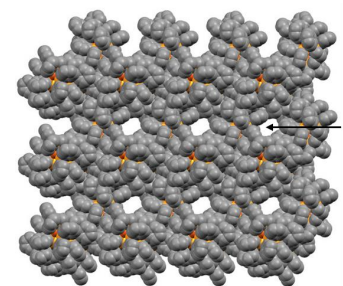


Figure S25. Packing diagram of **2**, view along the crystallographic a-axis. Channel A has a cuboid/cylindrical shape with approximately length 1.16 nm and breadth/diameter 0.89 nm. H atoms and solvent molecule omitted for clarity.

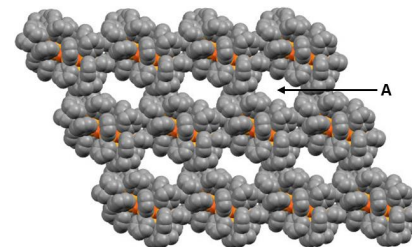


Figure S26. Packing diagram of **3**, view along the crystallographic a-axis. Channel A has a cuboid/cylindrical shape with approximately length 1.32 nm and breadth/diameter 0.91 nm. H atoms and solvent molecule omitted for clarity.

7. Photophysical Measurements

All photophysical measurements were performed in solid-state were in single-crystalline form under argon. Excitation and emission spectra were recorded on an Edinburgh Instrument FLS1000 spectrometer, equipped with a 450 W Xenon arc lamp, double monochromators for the excitation and emission pathways, and a red-sensitive photomultiplier (PMT-980) as a detector. For NIR measurements liquid N₂-cooled PMT-1400, range up to 1400 nm was used. The excitation and emission spectra were corrected using the standard corrections supplied by the manufacturer for the excitation source's spectral power and the detector's sensitivity. Quantum yields of solid samples were measured using an integrating cryosphere (Microstat N2) from Oxford Instruments. The luminescence lifetimes were measured using a μ F2 pulsed 60 W Xenon microsecond flashlamp, with a repetition rate of 100 Hz, a multichannel scaling (MCS) module or VPLED (271.8 nm with 0.3 mW or 383.8 nm with 1.1 mW or 449.6 nm with 37 mW), with 48.4 ns or 48.1 ns or 59.8 ns minimum pulse width respectively and an MCS module, depending on the time range. The low temperature experiments were performed using a 4 K cryostat (CS204SI-FMX-1SS) from Advanced Research System equipped with a closed cycle water-cooled helium compressor. The emission was collected at a right angle to the excitation source.

8. Emission Studies

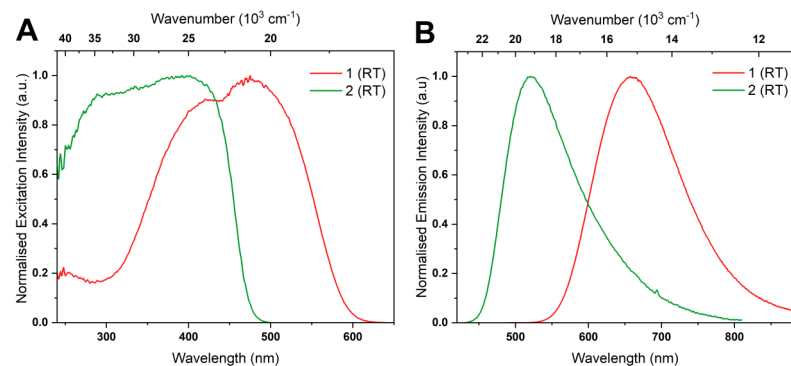


Figure S27. Normalized excitation (A) and emission (B) spectra of compound **1** (red) and **2** (green) at room temperature in solid state.

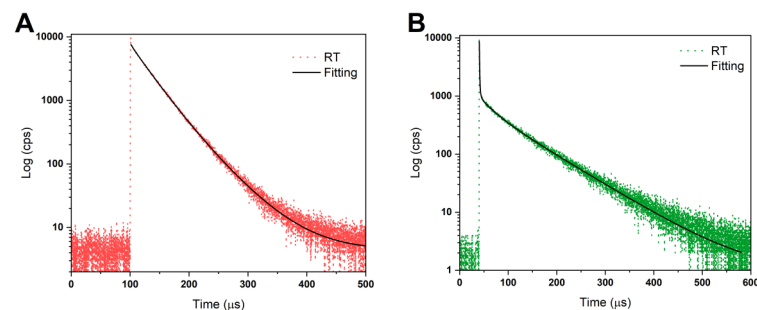


Figure S28. Emission decays of compound **1** (A) and **2** (B) at room temperature in solid state.

Table S3. Selected photophysical data of compound **1** and **2** at RT.

	λ_{em}^{max} (nm) [λ_{ex} (nm)]	Stokes Shift (cm ⁻¹)	FWHM (cm ⁻¹)	τ (μ s) ^a	$\langle \tau \rangle_{amp}$ (μ s)	Φ	k_r (s ⁻¹) ^b
1	660 [490]	6125	3117	31(82), 53 (18)	34	0.38	1.1×10^4
2	520 [410]	5461	4011	0.56 (83), 2 (8), 27 (3) 85 (6)	7	0.44	6.3×10^4

(a) For lifetimes fitted with two or multi exponentials, the pre-exponential factors are given in parentheses. (b) k_r was calculated using amplitude-weighted averaged lifetimes.

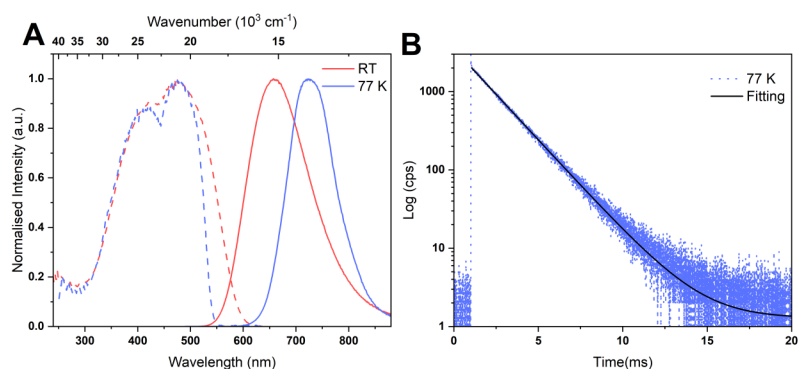


Figure S29. Normalized excitation and emission spectra (A) of **1** at room temperature (red) and at 77 K (blue) in solid state (solid lines for emission spectra and dash lines for excitation spectra). Emission decay (B) of **1** at 77 K in solid state.

Table S4. Selected photophysical data for **1** at RT and 77 K.

	λ_{em}^{max} (nm) [λ_{ex} (nm)]	Stokes Shift (cm ⁻¹)	FWHM (cm ⁻¹)	τ (μ s) ^a	$\langle \tau \rangle_{amp}$ (μ s)	Φ	k_r (s ⁻¹) ^b
RT	660 [490]	6125	3117	31(82), 53 (18)	34	0.38	1.1×10^4
77 K	720 [490]	6944	2000	1864 (100)	1864	0.29	1.5×10^2

(a) For lifetimes fitted with two or multi exponentials, the pre-exponential factors B are given in parentheses. (b) k_r was calculated using amplitude-weighted averaged lifetimes.

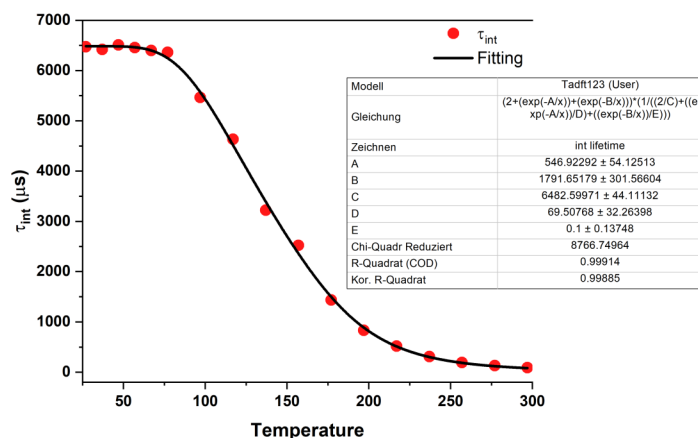


Figure S30. Radiative lifetimes of **1** at various temperatures with three-level fit. Intrinsic lifetimes (τ_{int}) are calculated by dividing amplitude-weighted averaged lifetimes by quantum yields.

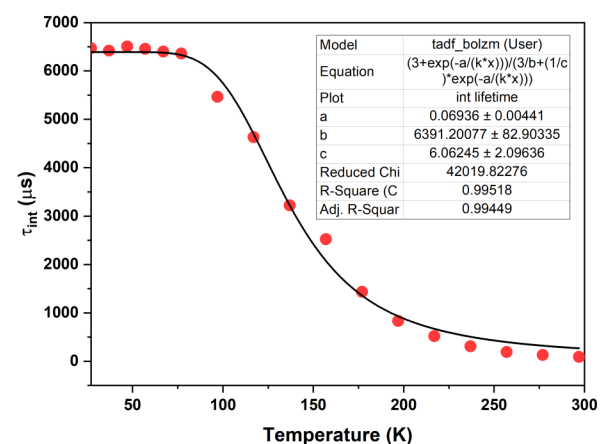


Figure S31. Radiative lifetimes of **1** at various temperatures with two-level fit. Intrinsic lifetimes (τ_{int}) are calculated by dividing amplitude-weighted averaged lifetimes by quantum yields.

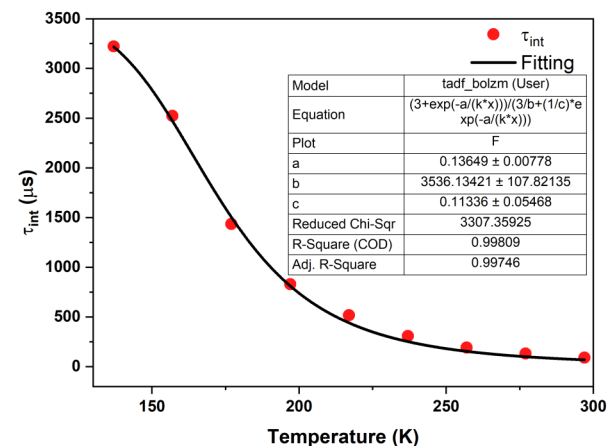


Figure S32. Radiative lifetimes of **1** at various temperatures with two-level fit for temperature >137 °C. Intrinsic lifetimes (τ_{int}) are calculated by dividing amplitude-weighted averaged lifetimes by quantum yields.

$$\text{Three-level fitting equation: } \tau_{r,av}(T) = \frac{\left(2 + e^{-\frac{\Delta E(T_1^I - T_1^{II,III})}{k_B T}} + e^{-\frac{\Delta E(S_1 - T_1^{II,III})}{k_B T}} \right)}{\left(\frac{2}{\tau_r(T_1^{II,III})} + \frac{e^{-\frac{\Delta E(T_1^I - T_1^{II,III})}{k_B T}}}{\tau_r(T_1^I)} + \frac{e^{-\frac{\Delta E(S_1 - T_1^{II,III})}{k_B T}}}{\tau_r(S_1)} \right)}$$

$$\text{Two-level fitting equation: } \tau_{r,av}(T) = \frac{3 + \exp\left[-\frac{\Delta E(S_1 - T_1)}{k_B T}\right]}{\frac{3}{\tau(T_1)} + \left[\frac{1}{\tau(S_1)}\right] \exp\left[-\frac{\Delta E(S_1 - T_1)}{k_B T}\right]}$$

Table S5. Temperature dependent life-times details for compound 1.

Temp (K)	τ_1 (μ s)	τ_2 (μ s)	τ <amp;gt; (μ s)	τ <int> (μ s)	χ^2	Φ	τ <intrinsic>
27	1021.77 (10)	1998.89 (90)	1896.38	1943.65	1.09	0.29	6470.09
37	1217.27 (17)	2017.04 (83)	1881.44	1929.30	1.09	0.2	6419.10
47	1906.92 (100)		1906.92	1906.92	1.16	0.29	6506.04
57	1892.20 (100)		1892.20	1892.20	1.06	0.29	6455.82
67	1874.82 (100)		1874.81	1874.81	1.13	0.29	6396.50
77	1863.87 (100)		1863.87	1863.87	1.09	0.29	6359.16
97	1810.93 (99)	4844.36 (1)	1831.76	1866.02	1.17	0.33	5464.68
117	1719.77 (99)	4388.52 (1)	1737.45	1764.45	1.19	0.37	4631.98
137	1389.32 (100)		1389.32	1389.32	1.17	0.43	3221.98
157	1066.56 (98)	2189.02 (2)	1084.56	1102.89	1.16	0.42	2522.82
177	638.94 (96)	1176.29 (4)	657.94	672.91	1.11	0.45	1436.24
197	371.25 (98)	791.09 (2)	380.84	391.18	1.15	0.45	831.00
217	207.94 (95)	386.24 (5)	217.36	224.67	1.10	0.41	517.77
237	123.65 (93)	224.75 (7)	130.87	136.05	1.01	0.42	308.73
257	66.89 (73)	106.96(27)	77.64	81.70	1.09	0.40	192.70
277	47.23 (88)	83.74 (12)	51.39	54.00	1.18	0.39	131.77
297	30.77 (82)	52.71 (18)	33.70	36.74	1.20	0.38	90.79

τ <amp;gt;: amplitude-weighted averaged lifetimes; τ <int>: intensity-weighted averaged lifetimes.

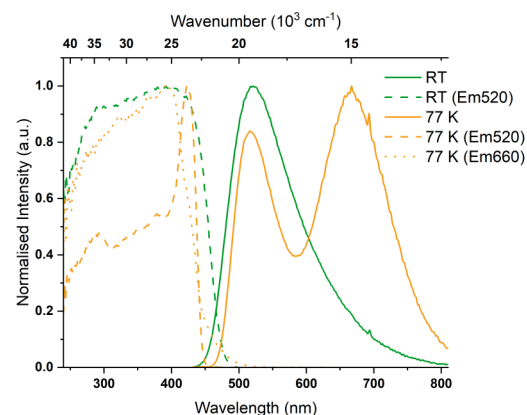


Figure S33. Normalized excitation and emission spectra of **2** at room temperature (green) and at 77 K (yellow) in solid state. Solid lines for emission spectra and dash/dot lines for excitation spectra.

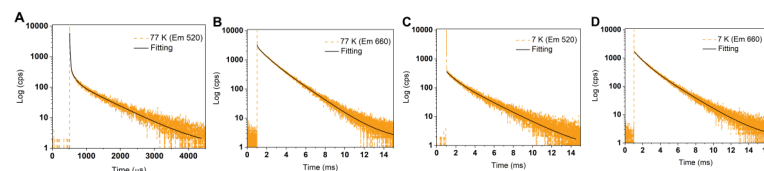


Figure S34. Emission decays of compound **2** (A: 77 K, Em 520 nm; B: 77 K, Em 660 nm; C: 7 K, Em 520 nm; D: 7 K, Em 660 nm).

Table S6. Selected photophysical data for **2** at 77 K and 7 K.

Temperature	λ_{em}^{max} (nm) [λ_{ex} (nm)]	τ (μ s) ^a	$\langle \tau \rangle_{amp}$ (μ s)	Φ	k_r (s^{-1}) ^b	
2	RT	520 [410]	0.56 (83), 2 (8), 27 (3) 85 (6)	7	0.44	6.3×10^4
	77 K	520 [410] HE, 660 [410] LE	2 (66), 15 (29), 128 (3), 787 (2) 72 (17), 819 (34), 1891 (49)	24	0.38	-
	7 K	520 [410] HE 660 [410] LE	769 (44), 2569 (56) 912 (52), 2276 (48)	1773		

(a) For lifetimes fitted with two or multi exponentials, the pre-exponential factors B are given in parentheses. (b) k_r was calculated using amplitude-weighted averaged lifetimes.

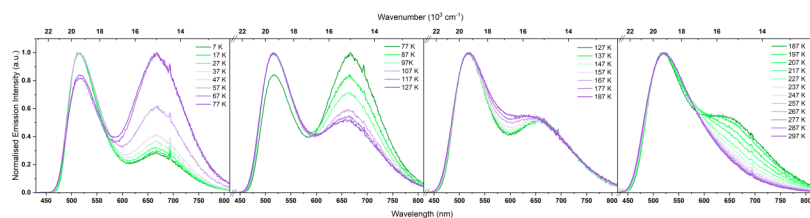


Figure S35. Normalized emission spectra of **2** at various temperatures. Left-to-right: 7 K-77 K, 77 K-127 K, 127 K-187 K and 187 K-297 K. Low temperatures in green lines and high temperatures in purple line.

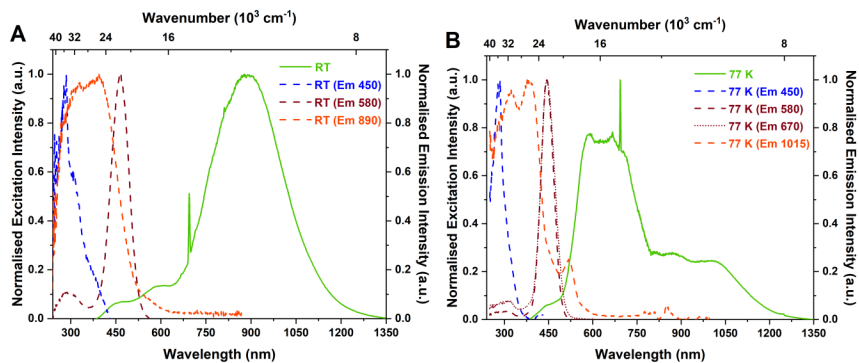


Figure S36. Normalized excitation and emission spectra of compound **3** at room temperature (**A**) and at 77 K (**B**) in solid state. Solid lines for emission spectra and dash/dot lines for excitation spectra.

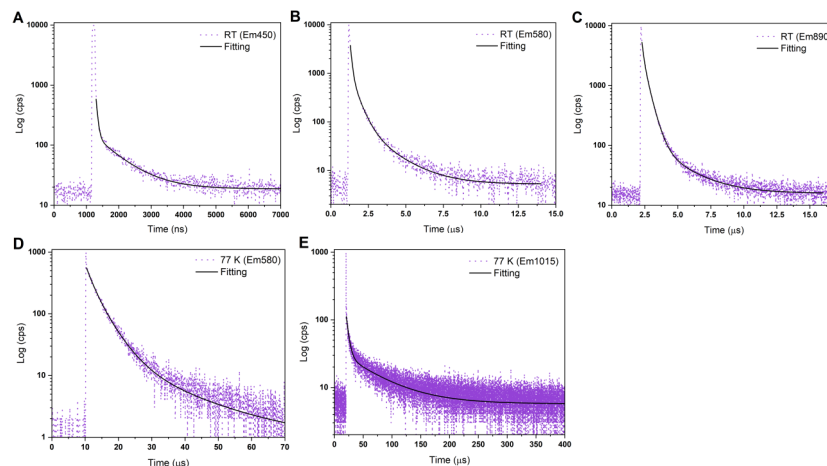


Figure S37. Emission decays of compound **3** (**A**: Room Temperature(RT), Em 450 nm; **B**: RT, Em 580 nm; **C**: RT, Em 890 nm; **D**: 77 K, Em 580 nm; **E**: 77 K, Em 1015 nm).

Table S7. Selected photophysical data of compound **3** at RT and 77 K.

Temperature	λ_{em}^{max} (nm) [λ_{ex} (nm)]	τ (μ s) ^a	$\langle \tau \rangle_{amp}$ (μ s)	Φ	
3	RT	450 [365] HE,	0.05(82), 0.79(18)	0.2	< 0.01
		580 [365] LE,	0.10(80), 0.46(20)	0.2	
		890 [365] LE	0.12(44), 0.43(56)	0.3	
77 K	450 [365] HE,	n.d.	n.d.	0.02	
		580 [365] LE,	2(43), 4.5(53), 18(4)	4	
		1015[365] LE	4.3(79), 62(21)	17	

(a) For lifetimes fitted with two or multi exponentials, the pre-exponential factors B are given in parentheses. (b) Emission maxima written in bold.

9. Thermal stability of compound 1-3

Thermal stability of the compounds were checked using TA SDT 650 simultaneous thermal analyzer under continuous flow of argon.

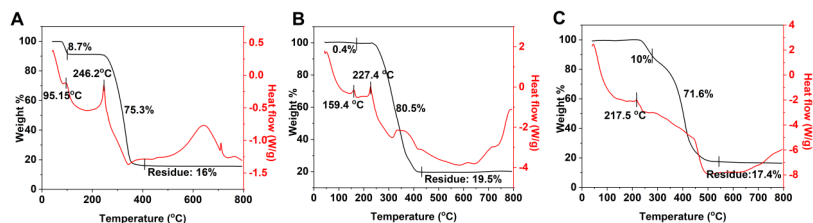


Figure S38. TG/DTA data of compound 1 (A), 2 (B) and 3 (C).

All three compounds shows thermal stability up to 200 °C. Compound 1 undergo weight loss of 8.7% around 95 °C which is the removal of toluene molecules present in the unit cell. Similarly, compound 2 undergo weight loss of 0.4% at 159 °C which is the removal of THF molecules present in the unit cell. Around 400 °C, approximately 20% weight still remains in the melt for all the three compounds which indicates the presence of CuP(phosphide) units.

10. TD-DFT calculations

DFT calculations for compound 1 were performed with the ORCA 5.0.3 software package.^[7] Geometry optimization with tight convergence criteria was carried out using PBE0 functional^[8] with def2-TZVP basis set^[9] and Grimme-D3BJ empirical dispersion correction.^[10] To accelerate calculations, the SARC/J^[11] auxiliary basis set was used together with RI approximation. Solvents effects (1: CH₂Cl₂, $\epsilon = 9.08$) were accounted for by implicit solvent model CPCM.^[12] Relativistic effects were accounted for by employing the ZORA method.^[13] Electronic transition differences at isovalues of 0.003 were prepared using the orca plot module as implemented in ORCA 5.0.3. software and USCF Chimera.^[14]

Table S8. XYZ coordinates of optimized molecule 1.

Cu	2.659241	8.741882	8.680621
Cu	1.722410	11.567772	10.949827
P	1.002249	9.975049	9.553566
P	3.177632	13.163380	10.388758
P	3.977745	12.181893	13.781882
P	1.028264	12.109938	13.005061
C	-0.037066	10.820164	8.294044
C	3.622858	13.541401	8.668421
C	-0.205491	8.854202	10.371067
C	0.193148	7.565893	10.758149
H	1.191471	7.219527	10.488381
C	-1.497489	9.281028	10.720766
H	-1.832301	10.279392	10.435912
C	4.132742	12.741055	6.429754
H	4.236249	11.911486	5.735087
C	-1.942271	7.172517	11.827242
H	-2.613007	6.526442	12.394311

C	0.218398	12.163506	7.973701
H	0.974938	12.707399	8.541748
C	0.266883	10.934773	14.185219
C	4.381683	14.045961	5.995963
H	4.676072	14.233199	4.963039
C	-2.358640	8.447938	11.432851
H	-3.357048	8.801546	11.693934
C	-1.027422	10.141824	7.562923
H	-1.249168	9.098990	7.792869
C	2.323844	12.977782	14.002417
H	2.437503	13.970758	13.542778
H	2.038915	13.121346	15.052418
C	-0.272825	13.374180	12.768345
C	4.098217	10.918291	15.103870
C	3.870654	14.851482	8.221728
H	3.775512	15.685376	8.916839
C	3.757123	12.487872	7.745618
H	3.561318	11.458612	8.060406
C	4.245706	15.100016	6.900290
H	4.433283	16.126059	6.579894
C	1.761713	15.495028	11.131433
H	0.908235	15.040218	10.628367
C	0.275593	9.576364	13.861570
H	0.702059	9.249514	12.913953
C	2.993174	14.823529	11.145301

C	5.251767	10.120125	15.103130
H	6.002461	10.247959	14.321935
C	-0.660571	6.736638	11.488599
H	-0.320037	5.743812	11.786105
C	4.079227	15.430808	11.794757
H	5.045138	14.927635	11.795429
C	5.141682	13.453078	14.407680
C	-0.483020	14.459686	13.626215
H	0.137793	14.592776	14.512296
C	-1.729693	10.782845	6.542437
H	-2.492315	10.235288	5.986965
C	3.129768	10.718510	16.094297
H	2.218025	11.310664	16.113589
C	4.871759	14.232245	15.539187
H	3.944134	14.092960	16.095446
C	5.436971	9.147883	16.083891
H	6.337576	8.534750	16.065687
C	6.345046	13.632943	13.714938
H	6.548018	13.027660	12.828375
C	3.933015	16.656097	12.446089
H	4.785897	17.100338	12.960836
C	-1.454484	12.116453	6.224121
H	-2.001077	12.614566	5.422922
C	-0.475532	12.802852	6.945557
H	-0.250239	13.844498	6.712594

C	-1.066028	13.240731	11.619251
H	-0.884269	12.410593	10.933441
C	-1.475355	15.397968	13.337951
H	-1.627973	16.245336	14.006663
C	-0.301182	11.355323	15.397618
H	-0.328262	12.415205	15.655317
C	1.613306	16.726377	11.772314
H	0.645380	17.227847	11.761252
C	-0.253252	8.638509	14.751910
H	-0.230958	7.581212	14.490859
C	2.695181	17.303883	12.441059
H	2.574794	18.258614	12.953999
C	5.790833	15.192730	15.960920
H	5.573394	15.802038	16.838449
C	-2.261639	15.260384	12.191978
H	-3.030329	15.999527	11.965491
C	4.463016	8.946557	17.065364
H	4.600834	8.174753	17.822847
C	-0.827224	10.419754	16.285166
H	-1.261471	10.750921	17.228772
C	-0.797827	9.057299	15.964497
H	-1.207343	8.325388	16.661148
C	3.308552	9.730532	17.065399
H	2.538097	9.576129	17.821220
C	-2.056722	14.178255	11.332324

H	-2.658794	14.068964	10.430102
C	6.988110	15.373509	15.262136
H	7.703855	16.126027	15.593765
C	7.267629	14.588910	14.141666
H	8.199132	14.725144	13.591942
Cu	4.503543	11.816279	11.621111
Cu	5.440655	8.990393	9.351515
P	6.160448	10.582719	10.748390
P	3.985582	7.394541	9.912311
P	3.184678	8.377036	6.519613
P	6.134441	8.448877	7.295990
C	7.199529	9.737559	12.008098
C	3.540761	7.015843	11.632615
C	7.368401	11.703647	9.931282
C	6.970036	12.992238	9.544855
H	5.971952	13.338837	9.815196
C	8.659976	11.276391	9.580542
H	8.994452	10.277679	9.864579
C	3.032796	7.815110	13.872104
H	2.930205	8.644313	14.567344
C	9.105106	13.385298	8.474952
H	9.775855	14.031411	7.907942
C	6.944118	8.394189	12.328337
H	6.187642	7.850294	11.760207
C	6.896421	9.624204	6.116374

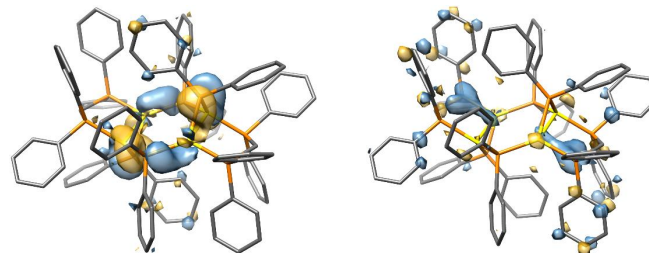
C	2.783056	6.510119	14.305177
H	2.489096	6.322435	15.338141
C	9.521130	12.109492	8.868469
H	10.519301	11.755644	8.606805
C	8.189917	10.415860	12.739218
H	8.411702	11.458685	12.509275
C	4.838715	7.581632	6.298303
H	4.725286	6.588323	6.757275
H	5.123465	7.438780	5.248153
C	7.435177	7.184210	7.532430
C	3.063311	9.641016	5.198064
C	3.292483	5.705636	12.078675
H	3.386753	4.872101	11.383014
C	3.407762	8.068880	12.556164
H	3.604018	9.098216	12.241904
C	2.917927	5.456531	13.400143
H	2.729836	4.430413	13.719997
C	5.401443	5.063315	9.168237
H	6.255065	5.518030	9.671150
C	6.892312	10.981990	6.442755
H	6.469080	11.308141	7.392071
C	4.169877	5.734646	9.155172
C	1.910393	10.440093	5.200677
H	1.160774	10.312716	5.982989
C	7.823743	13.821520	8.814420

H	7.483507	14.814675	8.517670
C	3.083751	5.127680	8.505547
H	2.117834	5.630846	8.505244
C	2.020948	7.105720	5.893688
C	7.644860	6.098683	6.674463
H	7.023974	5.965952	5.788379
C	8.892297	9.774763	13.759577
H	9.654988	10.322270	14.315001
C	4.030522	9.840348	4.206336
H	4.941806	9.247539	4.185615
C	2.290824	6.326958	4.761892
H	3.218336	6.466571	4.205531
C	1.724505	11.412691	4.220401
H	0.824467	12.026619	4.240145
C	0.817570	6.925673	6.586361
H	0.614569	7.530748	7.473059
C	3.229800	3.902553	7.853871
H	2.376819	3.458493	7.339137
C	8.617191	8.441096	14.077743
H	9.163928	7.942895	14.878789
C	7.638226	7.754731	13.356298
H	7.412929	6.713079	13.589230
C	8.227985	7.316810	8.681893
H	8.046410	8.146790	9.367946
C	8.637100	5.160191	6.962365

H	8.789449	4.312915	6.293476
C	7.460135	9.204519	4.901650
H	7.483286	8.145124	4.641583
C	5.549601	3.831973	8.527289
H	6.517536	3.330509	8.537968
C	7.421854	11.920119	5.553115
H	7.403286	12.976945	5.816388
C	4.467594	3.254692	7.858561
H	4.587807	2.300003	7.345503
C	1.371973	5.366256	4.340165
H	1.589462	4.757138	3.462518
C	9.423457	5.297306	8.108344
H	10.191991	4.557936	8.334613
C	2.697180	11.613481	3.237549
H	2.558908	12.385647	2.480518
C	7.986925	10.140362	4.014831
H	8.417815	9.809881	3.069448
C	7.962321	11.502233	4.338381
H	8.372466	12.234361	3.642330
C	3.851100	10.828701	3.235733
H	4.620532	10.982619	2.478771
C	9.218599	6.379087	8.968450
H	9.820498	6.487825	9.870853
C	0.174857	5.185025	5.039105
H	-0.540677	4.432281	4.707530

C	-0.104726	5.969388	6.159726
H	-1.036270	5.833053	6.709356

Figure S39. HOMO (left) and LUMO (right) orbitals for compound 1.



11. References

- [1] W. L. F. Armarego, *Purification of laboratory Chemicals*, Butterworth Heinemann,

Oxford; Boston, 1996.

[2] T. H. Lemmen, G. V. Goeden, J. C. Huffman, R. L. Geerts, and K. G. Caulton, *Inorg. Chem.*, 1990, **29**, 3680.

[3] G. M. Sheldrick, *Acta Crystallogr. C*, 2015, **71**, 3.

[4] O. V. Dolomanov, L. J. Bourhis, R. J. Gildea, J. A. K. Howard, and H. Puschmann, *J. Appl. Crystallogr.* 2009, **42**, 339.

[5] A. L. Spek, *Acta Crystallogr. C*, 2015, **71**, 9.

[6] P. Dierkes, and P. W. N. M. van Leeuwen, *J. Chem. Soc., Dalton Trans.*, 1999, 1519.

[7] F. Neese, *WIREs Comput. Mol. Sci.*, 2012, **2**, 73.

[8] a) C. Adamo, and V. Barone, *J. Chem. Phys.*, 1999, **110**, 6158; b) J. P. Perdew, K. Burke, and M. Ernzerhof, *Phys. Rev. Lett.*, 1996, **77**, 3865; c) J. P. Perdew, K. Burke, and M. Ernzerhof, *Phys. Rev. Lett.* 1997, **78**, 1396; d) C. Cardoso, A. T. Costa, A. H. MacDonald, and J. Fernández-Rossier, *Phys. Rev. B Condens. Matter.*, 1996, **105**, 9982; e) M. Ernzerhof, and G. E. Scuseria, *J. Chem. Phys.*, 1999, **110**, 5029; f) J. Tao, J. P. Perdew, V. N. Staroverov, and G. E. Scuseria, *Phys. Rev. Lett.*, 2003, **91**, 146401; g) J. P. Perdew, J. Tao, V. N. Staroverov, and G. E. Scuseria, *J. Chem. Phys.*, 2004, **120**, 6898.

[9] a) A. Schäfer, H. Horn, and R. Ahlrichs, *J. Chem. Phys.*, 1992, **97**, 2571; b) F. Weigend, and R. Ahlrichs, *Phys. Chem. Chem. Phys.*, 2005, **7**, 3297.

[10] a) S. Grimme, J. Antony, S. Ehrlich, and H. Krieg, *J. Chem. Phys.*, 2010, **132**, 154104; b) S. Grimme, S. Ehrlich, and L. Goerigk, *J. Comput. Chem.*, 2011, **32**, 1456.

[11] a) F. Weigend, *Phys. Chem. Chem. Phys.*, 2006, **8**, 1057; b) D. A. Pantazis, and F. Neese, *J. Chem. Theory Comput.*, 2009, **5**, 2229; c) D. A. Pantazis, and F. Neese, *Theor. Chem. Acc.*, 2012, **131**, 1292; d) D. A. Pantazis, and F. Neese, *J. Chem. Theory Comput.*, 2011, **7**, 677.

[12] V. Barone, and M. Cossi, *J. Phys. Chem. A*, 1998, **102**, 1995.

[13] D. A. Pantazis, X. Y. Chen, C. R. Landis, and F. Neese, *J. Chem. Theory Comput.*, 2008, **4**, 908.

[14] E. F. Pettersen, T. D. Goddard, C. C. Huang, G. S. Couch, D. M. Greenblatt, E. C. Meng, and T. E. Ferrin, *J. Comput. Chem.*, 2004, **13**, 1605.

Supporting Information

Hetero-di/multi-nuclear Copper(I) Diphenylphosphides Displaying Thermally Activated Delayed Fluorescence (TADF) in the Visible to Near NIR

Sabyasachi Maity, Ondřej Mrózek, Konstantinos P. Zois, Andrey Belyaev, Benjamin Hupp, Andreas Steffen

Table of Contents

1. General Procedures	S1
2. Characterization Data	S2
3. NMR spectra	S4
4. ATR-IR	S10
5. X-ray characterization data	S12
6. Structural details of 1-3	S16
7. Photophysical Measurements	S20
8. Emission Studies	S21
9. Thermal stability of compound 1-3	S28
10. TD-DFT calculations	S29
11. References	S44

1. General Procedures

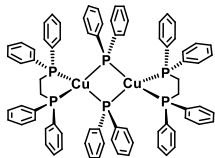
All manipulations were carried out under an inert atmosphere of argon using standard Schlenk link^[1] or glovebox techniques (GS MEGA E-Line, <0.5 ppm of H₂O and O₂). All reagents were used as supplied. Solvents such as tetrahydrofuran (THF), toluene, and pentane were used at HPLC grade purity from commercial sources (VWR and Fisher Chemicals) and dried using PureSolv MD 7 drying system. After being dried, diethyl ether was kept in 4 Å molecular sieves.

NMR spectra were recorded on a Bruker Avance III HD NanoBay 400 MHz; ¹H and chemical shifts (δ) are given in ppm relative to TMS, coupling constants (J) in Hz. The solvent signals were used as references, and the chemical shifts were converted to the TMS scale. ATR-IR spectra were measured on a Bruker Alpha-II IR Spectrometer, and CHN elemental analyses were performed on a Micro cube (Elementar).

Copper(I) *tert*-butanolate and [Cu(PPh)₂]₈ were synthesised according to literature procedures.^[2]

2. Characterization Data

Synthesis of 1

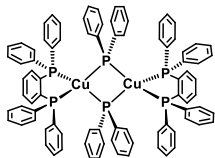


[Cu(PPh)₂]₈ (80 mg, 0.3 mmol) and 1,2-bis (diphenylphosphino) ethane (128 mg, 0.3 mmol) were added to a 20 mL scintillation vial, and 6 mL anhydrous THF was added to the reaction mixture inside the glovebox. After stirring for 24 hours the reaction mixture was filtered over a pipette containing celite and basic aluminium oxide. A yellow transparent filtrate was obtained which was then co-crystallized with n-pentane in the ratio of 2:1 (THF:n-pentane). Yellow-green crystals were obtained which were washed with 2 mL pentane. Yield: 20% (84 mg). **EA** calc. for [C₇₆H₆₈Cu₂P₆] C, 70.53; H, 5.30. Found: C, 70.7; H, 5.3. **IR (ATR)** [cm⁻¹]: $\tilde{\nu}$ = 3041.36, 1574.25, 1469.17, 1430.02, 1096.21, 1024.09, 999.36, 873.67, 818.03, 729.43, 690.28, 659.37, 519.25, 473.92, 414.17.

On measuring the ¹H-NMR spectra at room temperature, the number of protons were more than the expected structure and also the aromatic peaks were merged. In the ³¹P{¹H} NMR at room temperature shows multiple peaks indicating presence of multiple species in solution. On cooling down to -80 °C, ¹H-NMR spectra shows better resolution in the aromatic as well as in the aliphatic part, yet number of protons were more than the expected structure. ³¹P{¹H} NMR shows less peaks at -80 °C, but when warmed up to room temperature shows the extra peaks which were missing. This indicates the presence of multiple species in solution which are at equilibrium to one another and can't be separated even at low temperatures.

¹H-NMR (d₈-THF, 400 MHz, 298 K): 7.32 - 6.42 (m, Ar-H), 2.13 (s), 2.04 - 1.99 (bs); ³¹P {¹H} NMR (d₈-THF, 400 MHz, 298 K): 27.71, 27.25, 27.08, 17.28, -0.37, -5.57, -12.71, -21.07.

Synthesis of 2



[Cu(PPh)₂]₈ (40 mg, 0.1 mmol) and 1,2-bis (diphenylphosphino) benzene (72 mg, 0.1 mmol) were taken. Compound **2** was obtained using similar procedure to that reported for compound **1** as orange crystals were obtained on recrystallisation with a mixture of n-pentane/cyclohexane (2:0.8/0.2). Yield: 22% (50 mg). **EA** calc. for [C₈₄H₆₈Cu₂P₆] C, 72.56; H, 4.93. Found: C, 72.2; H, 5.1. **IR (ATR)** [cm⁻¹]: $\tilde{\nu}$ = 3045.48, 1574.25, 1471.23, 1427.95, 1090.02, 1024.09, 995.24, 760.34, 729.43, 690.28, 515.13, 473.92, 436.83, 416.23.

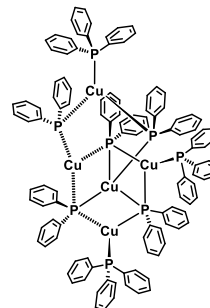
On measuring the ¹H-NMR spectra at room temperature, the number of protons were more than the expected structure and also the aromatic peaks were merged. In the ³¹P{¹H} NMR at room temperature shows multiple peaks indicating presence of multiple species in solution.

On cooling down to -80 °C, ¹H-NMR spectra shows better resolution in the aromatic as well as the aliphatic part, yet number of protons were more than the expected structure. ³¹P{¹H} NMR shows less peaks at -80 °C, but when warmed up to room temperature shows the extra peaks which were missing. This indicates the presence of multiple species in solution which are at equilibrium to one another and can't be separated even at low temperatures.

¹H-NMR (d₈-THF, 400 MHz, 298 K): 7.70 - 6.30 (m, Ar-H), 1.33 - 1.24 (m, n-pentane), 0.88 (t, n-pentane); ³¹P {¹H} NMR (d₈-THF, 400 MHz, 298 K): 27.60, 26.18, 18.20, -11.45, -14.01.

The orange crystals of compound **2** were redissolved in THF and co-crystallised with a mixture of n-pentane and cyclohexane over a month resulted in orange crystals of compound **2** along with very few yellow crystals of compound **4** (decomposition product). The reaction conditions were optimized, yet the isolation of compound **4** was not possible.

Synthesis of 3



[Cu(PPh)₂]₈ (80 mg, 0.3 mmol) and triphenylphosphine (51 mg, 0.2 mmol) were taken. Compound **3** was obtained using similar procedure to that reported for compound **1** as orange crystals were obtained on recrystallisation with pentane (1:1). Yield: 34% (45 mg). **EA** calc. for [C₁₁₄H₉₅Cu₅P₈] C, 67.43; H, 4.72. Found: C, 67.6; H, 5.0. **IR (ATR)** [cm⁻¹]: $\tilde{\nu}$ = 3045.48, 1576.31, 1473.29, 1430.02, 1092.09, 1063.24, 1024.09, 997.30, 731.49, 690.28, 616.10, 502.77, 475.98, 434.77.

On measuring the ¹H-NMR spectra at room temperature, the number of protons were more than the expected structure and also the aromatic peaks were merged. In the ³¹P{¹H} NMR at room temperature shows multiple peaks indicating presence of multiple species in solution. On cooling down to -80 °C, ¹H-NMR spectra shows better resolution in the aromatic part, yet number of protons were more than the expected structure. ³¹P{¹H} NMR shows less peaks at -80 °C, but when warmed up to room temperature shows the extra peaks which were missing. This indicates the presence of multiple species in solution which are at equilibrium to one another and can't be separated even at low temperatures.

¹H-NMR (d₈-THF, 400 MHz, 298 K): 7.71 - 5.99 (m, Ar-H), 1.31 - 1.22 (m, n-pentane), 0.88 (t, n-pentane); ³¹P {¹H} NMR (d₈-THF, 400 MHz, 298 K): 23.26, 21.00, 16.17, -5.23, -31.66.

3. NMR spectra

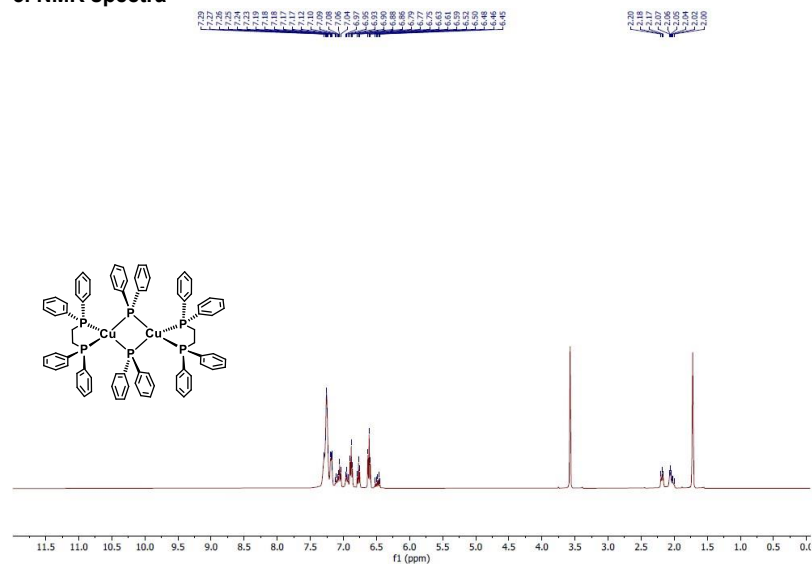


Figure S1. $^1\text{H-NMR}$ (400 MHz, THF-d_8 , 298 K) of **1**.

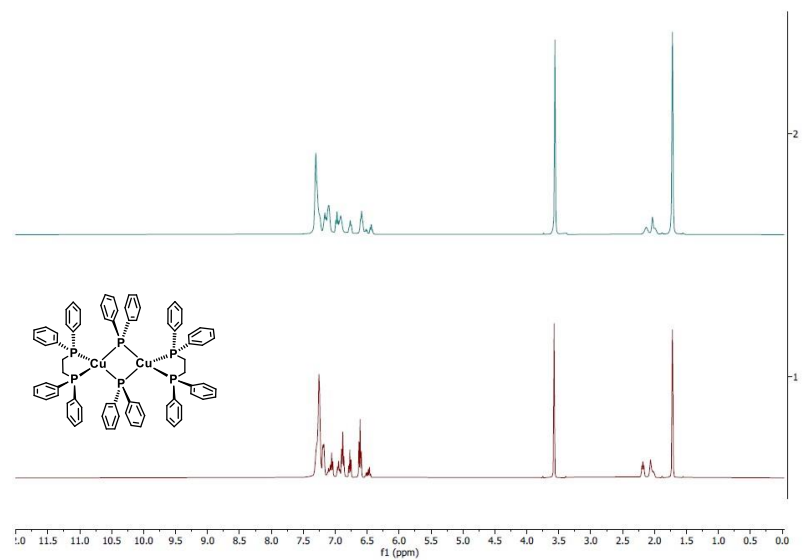


Figure S2. $^1\text{H-NMR}$ (400 MHz, THF-d_8 , top: 298 K, bottom: 193 K) of **1**.

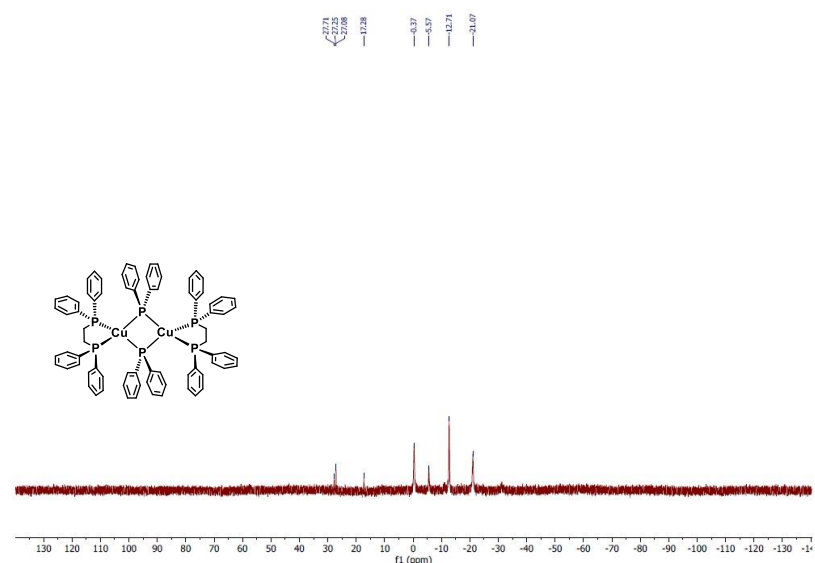


Figure S3. $^{31}\text{P-NMR}$ (400 MHz, THF-d_8 , 298 K) of **1**.

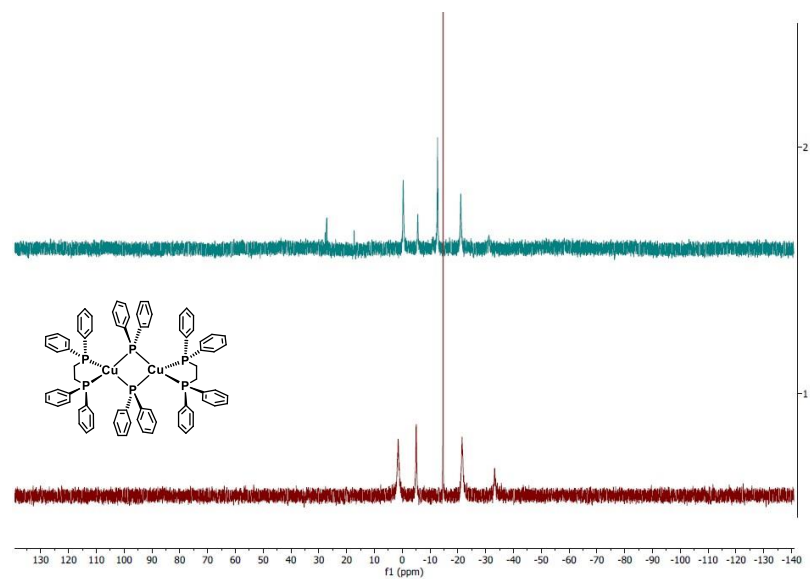
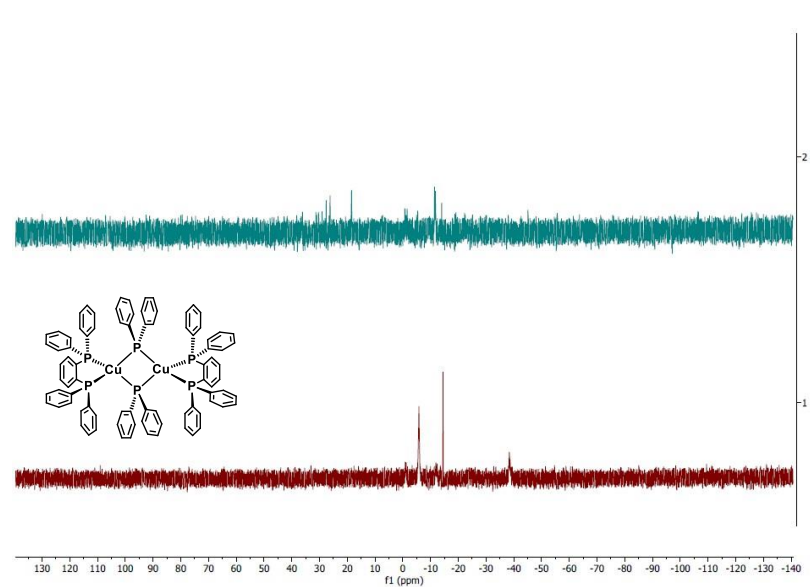
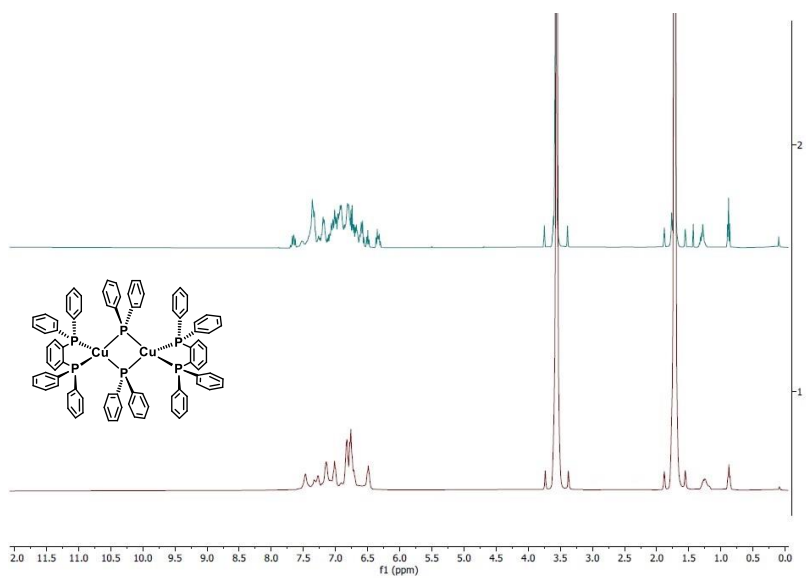
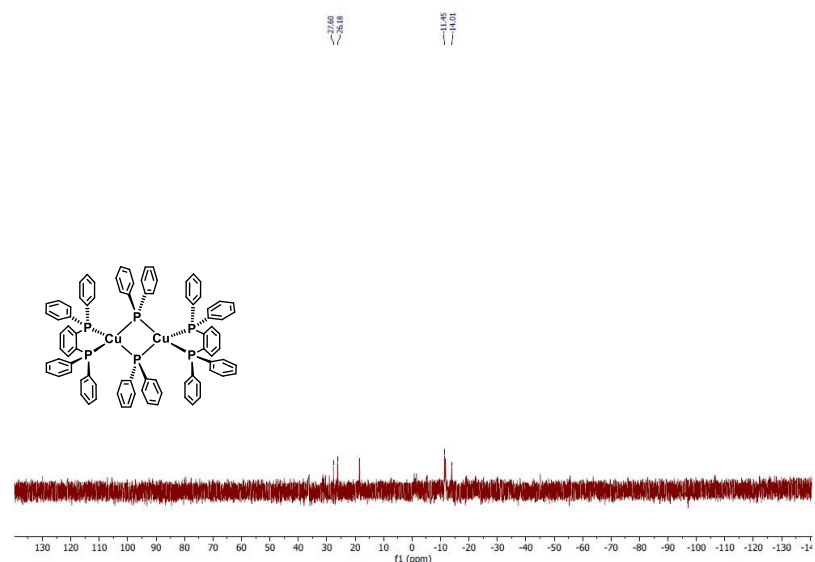
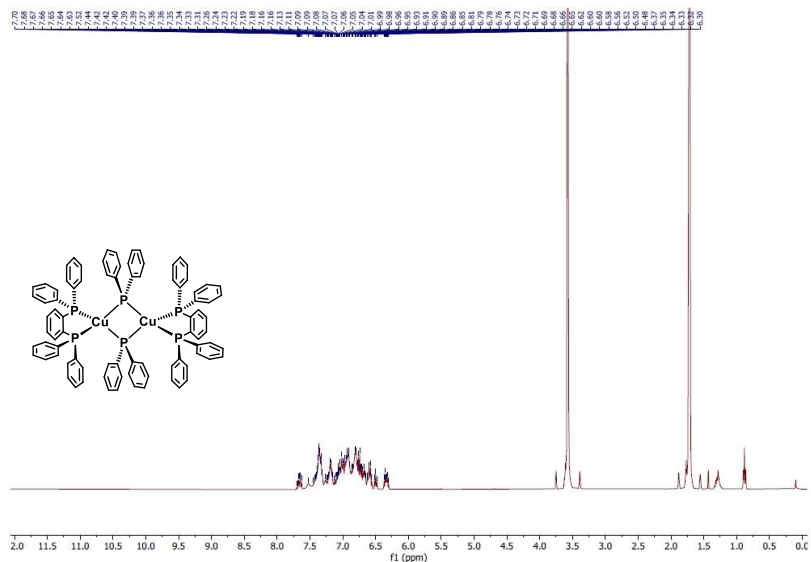


Figure S4. $^{31}\text{P-NMR}$ (400 MHz, THF-d_8 , top: 298 K, bottom: 193 K) of **1**.



4. ATR-IR

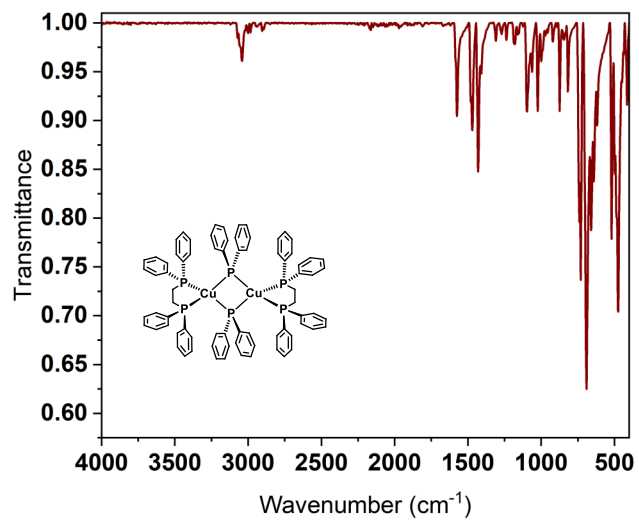


Figure S13. ATR-IR spectrum of 1.

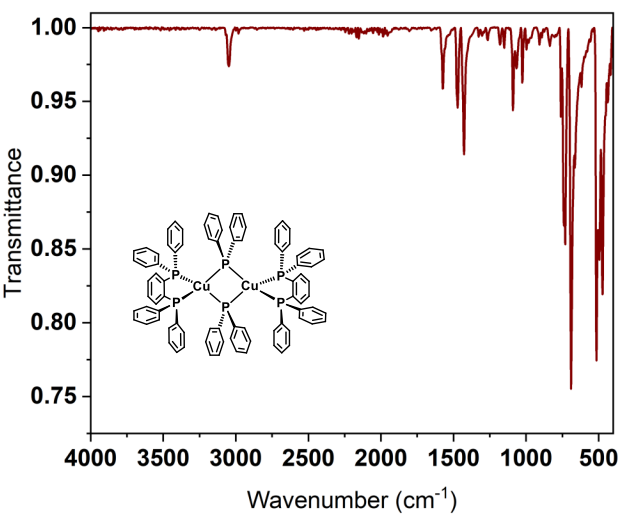


Figure S14. ATR-IR spectrum of 2.

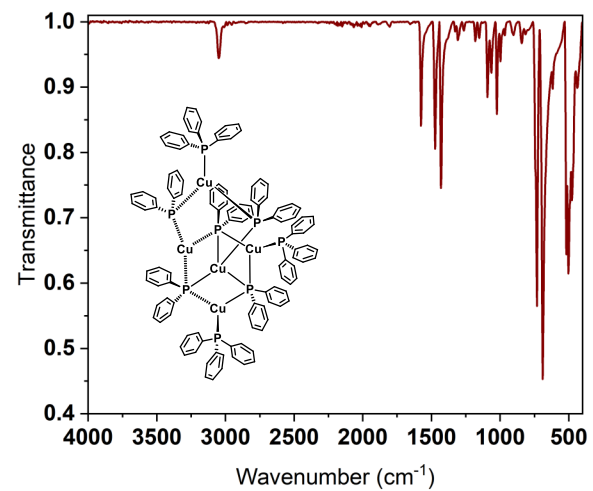


Figure S15. ATR-IR spectrum of 3.

5. X-ray characterization data

General part

X-ray diffraction determination

The single crystals of **1–4** were immersed in a film of NVH or perfluoropolyether oil, mounted on a polyimide microloop (MiTeGen) and transferred to a stream of cold nitrogen (Bruker Kryoflex2), and measured at a temperature of 100 K. The X-ray diffraction data were collected on a Bruker D8 diffractometer with a CMOS Photon 100 and multilayer optics monochromated MoK α (0.71073Å) radiation (INCOATEC microfocuss sealed tube). The frames were integrated with the Bruker SAINT software package using a narrow-frame algorithm. The APEX3 v2018.7-0 program package was used for cell refinements and data reductions. The structure was solved using the intrinsic phasing method,^[3] refined and visualized with the OLEX2-1.5 program.^[4] A semiempirical absorption correction (SADABS) was applied to all data. All non-hydrogen atoms were refined anisotropically. Hydrogen atoms were included in structure factors calculations. All Hydrogen atoms were assigned to idealized geometric positions. Unit cells of the **4** contain disordered solvent molecules treated as a diffuse contribution to the overall scattering without specific atom positions by SQUEEZE/PLATON.^[5] Crystallographic data of the **3** and **4** contains alerts of level B (see check CIF reports), this is a result of limited diffraction of the samples associated with reflections omitted by the beam stopper and possible deficiencies in the correction absorption model. The crystallographic details are summarized in **Table S1**. CCDC **2384013–2384016** contains the supplementary crystallographic data for this paper.

X-ray Structures

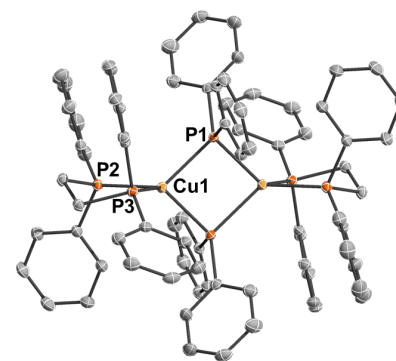


Figure S16. X-ray solid-state structure of **1**. Thermal ellipsoids were drawn at the 50% probability level; H atoms have been omitted for clarity. Selected bond lengths (Å) and angles [deg]: Cu1-P1 2.3501(4), Cu1-P2 2.3075(3), Cu1-P3 2.2773(4), P1-Cu1-P1 87.92(1), P2-Cu1-P3 88.51(1).

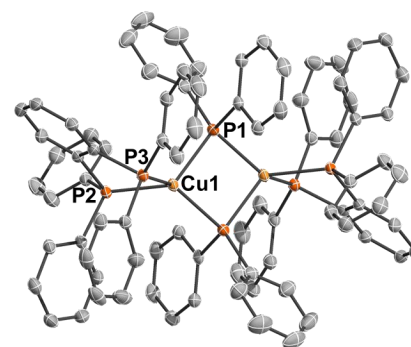


Figure S17. X-ray solid-state structure of **2**. Thermal ellipsoids were drawn at the 50% probability level; H atoms have been omitted for clarity. Selected bond lengths (Å) and angles [deg]: Cu1-P1 2.3364(5), Cu1-P2 2.3111(6), Cu1-P3 2.2793(5), P1-Cu1-P1 87.17(2), P2-Cu1-P3 85.19(2).

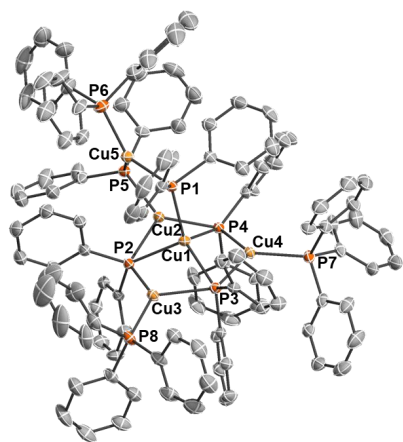


Figure S18. X-ray solid-state structure of **3**. Thermal ellipsoids were drawn at the 50% probability level; H atoms and solvent molecule have been omitted for clarity. Selected bond lengths (Å): Cu1-P1 2.268(1), Cu1-P2 2.5012(9), Cu1-P3 2.321(1), Cu1-P4 2.6955(9), Cu2-P2 2.367(1), Cu2-P4 2.3146(9), Cu2-P5 2.235(1), Cu3-P2 2.3403(9), Cu3-P3 2.3763(9), Cu3-P8 2.262(1), Cu4-P3 2.354(1), Cu4-P4 2.3175(9), Cu4-P7 2.2760(9), Cu5-P1 2.331(1), Cu5-P5 2.3115(9), Cu5-P6 2.274(1).

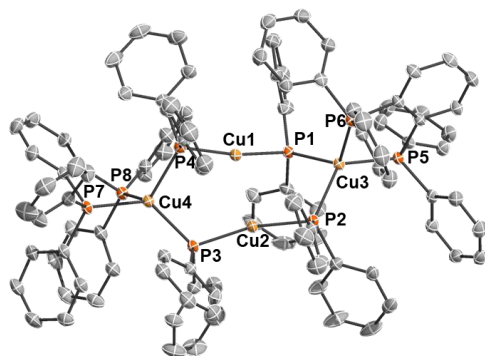


Figure S19. X-ray solid-state structure of **4**. Thermal ellipsoids were drawn at the 50% probability level; H atoms and solvent molecule have been omitted for clarity. Selected bond lengths (Å) and angles [deg]: Cu4-P3 2.3013(5), Cu4-P4 2.3406(6), Cu4-P7 2.2981(6), Cu4-P8 2.3012(5), Cu3-P1 2.3215(5), Cu3-P2 2.3186(6), Cu3-P5 2.2811(6), Cu3-P6 2.2630(6), Cu1-P1 2.2255(6), Cu1-P4 2.2244(6), Cu2-P2 2.2227(6), Cu2-P3 2.2248(6), P1-Cu1-P4 168.64(2), P2-Cu2-P3 163.13(2), P3-Cu4-P4 100.81(2), P7-Cu4-P8 84.06(2), P1-Cu3-P2 91.82(2), P5-Cu3-P6 89.54(2).

Table S1. Crystal data and structure refinement for **1-3**.

Identification code	1	2	3	4
CCDC number	2384013	2384014	2384015	2384016
Empirical formula	C ₇₆ H ₆₈ Cu ₂ P ₆	C ₄₂ H ₃₄ CuP ₃	C ₂₃₃ H ₂₀₀ Cu ₁₀ P ₁₆	C ₁₁₁ H ₉₄ Cu ₄ P ₈
Formula weight	1294.20	695.14	4130.84	1929.78
Temperature [K]	100			
Crystal system	triclinic	triclinic	monoclinic	triclinic
Space group	P-1	P-1	P2 ₁	P-1
a [Å]	12.0545(3)	11.6992(3)	13.4937(3)	14.4287(5)
b [Å]	12.1466(3)	11.7418(3)	17.2806(5)	16.0646(5)
c [Å]	12.9951(3)	13.6414(4)	21.3461(6)	21.9752(7)
α [°]	101.3900(10)	107.1790(10)	90	87.0740(10)
β [°]	114.3490(10)	105.9810(10)	97.0430(10)	83.4680(10)
γ [°]	104.5500(10)	98.9700(10)	90	83.2500(10)
Volume [Å ³]	1577.09(7)	1662.72(8)	4939.9(2)	5021.9(3)
Z	1	2	1	2
ρ _{calc} [g/cm ³]	1.363	1.388	1.389	1.276
μ [mm ⁻¹]	0.871	0.832	1.238	1.009
F(000)	672.0	720.0	2128.0	1992.0
Crystal size [mm ³]	0.278 × 0.244 × 0.116	0.14 × 0.099 × 0.081	0.274 × 0.123 × 0.091	0.103 × 0.098 × 0.077
Radiation type	MoKα (λ = 0.71073)			
2θ range for data collection [°]	5.522 to 65.19	5.396 to 55.998	5.81 to 57.128	5.374 to 57.156
Index ranges	-18 ≤ h ≤ 18, -18 ≤ k ≤ 14, -19 ≤ l ≤ 19	-15 ≤ h ≤ 14, -15 ≤ k ≤ 15, -18 ≤ l ≤ 18	-18 ≤ h ≤ 17, -23 ≤ k ≤ 23, -28 ≤ l ≤ 28	-19 ≤ h ≤ 19, -21 ≤ k ≤ 21, -27 ≤ l ≤ 29
Reflections collected	44918	36527	166401	114619
Independent reflections	11439 [R _{int} = 0.0250, R _{sigma} = 0.0243]	8008 [R _{int} = 0.0347, R _{sigma} = 0.0290]	25085 [R _{int} = 0.0543, R _{sigma} = 0.0378]	25484 [R _{int} = 0.0323, R _{sigma} = 0.0273]
Data/restraints/parameters	11439/0/379	8008/0/415	25085/92/1192	25484/113/1135
Goodness-of-fit on F ² _(a)	1.023	1.028	1.047	1.036
Final R indexes [I ≥ 2σ(I)] ^(b)	R ₁ = 0.0260, wR ₂ = 0.0667	R ₁ = 0.0343, wR ₂ = 0.0804	R ₁ = 0.0323, wR ₂ = 0.0827	R ₁ = 0.0331, wR ₂ = 0.0979
Final R indexes [all data] ^(b)	R ₁ = 0.0302, wR ₂ = 0.0686	R ₁ = 0.0411, wR ₂ = 0.0837	R ₁ = 0.0366, wR ₂ = 0.0856	R ₁ = 0.0393, wR ₂ = 0.1017
Largest diff. peak/hole [e/Å ⁻³]	0.45/-0.28	0.65/-0.31	1.05/-0.42	1.08/-0.52
Flack parameter			0.010(7)	

^(a) GooF = S = $[\sum w(F_o^2 - F_c^2)^2] / (m - n)]^{1/2}$, where m = number of reflexes and n = number of parameters;

^(b) R₁ = $\sum ||F_o| - |F_c|| / \sum |F_o|$; wR₂ = $[\sum w(F_o^2 - F_c^2)^2 / \sum (wF_o^2)]^{1/2}$; w = $1/[\sigma^2(F_o^2) + (aP)^2 + bP]$, where P = $(F_o^2 + 2F_c^2) / 3$

6. Structural details of 1-3

Table S2. Structural Details of Compounds **1–3** at 100 K

Compd.	1	2	3
Geometry at Cu centre	Flattened tetrahedron	Flattened tetrahedron	Distorted tetrahedron(Cu1) Distorted triangular planar (Cu3/Cu4/Cu5)
Cu–Cu (Å)	Cu1–Cu1 3.3935(3) ^a	Cu1–Cu1 3.4108(3) ^a	Cu1–Cu 2.5254(7)^b Cu2–Cu5 3.0821(7)
Cu–P (Å) (phosphide)	Cu1–P 2.3572(3)	Cu1–P 2.3543(5)	Cu1–P 2.5055(12)^c Cu–P 2.3447(12)^c Cu–P 2.2866(12)^d
Cu–P (Å) (phosphine)	Cu–P 2.2925(5)	Cu–P 2.2952(13)	Cu–P 2.2708(13)
Dihedral angle α (°)	81.890(14)	81.606(18)	65.64
β_n (°) ^e	85.03	83.04	145 ^g
β_n (°)	P2–Cu1–P3 88.514(10)	P2–Cu1–P3 85.191(18)	-
P–Cu–P (°) (phosphide)	P1–Cu1–P1 87.924(10)	P1–Cu1–P1 87.171(17)	P–Cu1–P1 114.26(4) P–Cu2–P5 123.98(4)
P–Cu–P (°) (phosphide and phosphine)	P1–Cu1–P3 117.283(10)	P1–Cu1–P3 126.228(19)	P–Cu–P 122.08(5)
Cu–P–Cu (°) (phosphide)	Cu1–P1–Cu1 92.077(9)	Cu1–P1–Cu1 92.829(17)	Cu1–P–Cu 62.60(3)^f Cu2–P5–Cu5 83.34(4) Cu1–P1–Cu5 113.78(5)

^aDistances between two *Cu* centres. ^bbond length between two *Cu* centres (in the hexagonal plane). ^cbond length in the hexagonal plane. ^dbond length not in the hexagonal plane. ^egeneral bite angle from ref 6. ^fbond angle in the hexagonal plane. ^gCone angle. Mean values written in bold font.

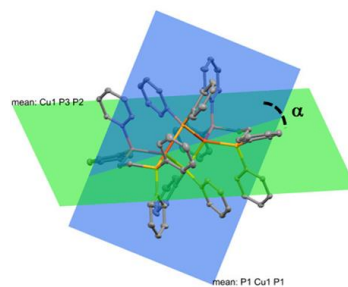


Figure S20. Dihedral angle in **1** ($\alpha = 81.89^\circ$). Green: Cu₁P₂(phosphine), and blue:Cu₁P₂(phosphide).

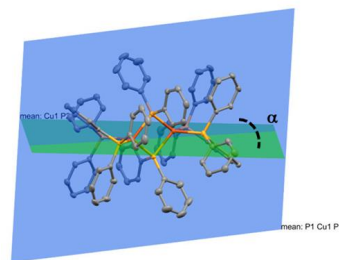


Figure S21. Dihedral angle in **2** ($\alpha = 81.61^\circ$). Green: Cu₁P₂(phosphine), and blue:Cu₁P₂(phosphide).

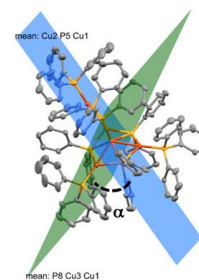


Figure S22. Dihedral angle in **3** ($\alpha = 65.64^\circ$). Green: Cu₂P(phosphine), and blue:Cu₂P₁(phosphide).

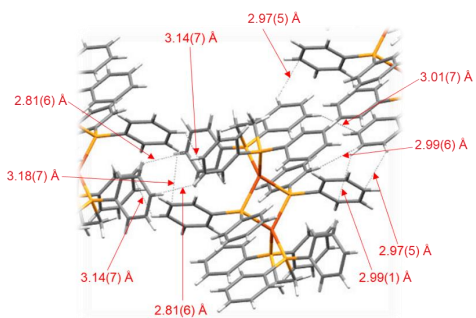


Figure S23. Molecular C–H··· π interactions of **1**.

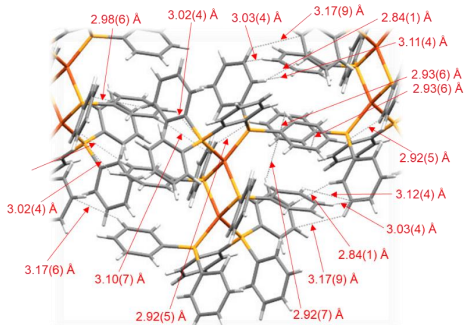


Figure S24. Molecular C–H··· π interactions of **2**.

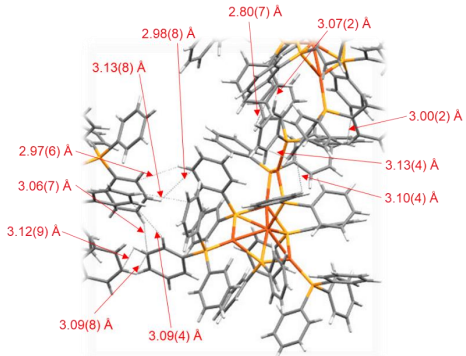


Figure S25. Molecular C–H··· π interactions of **3**.

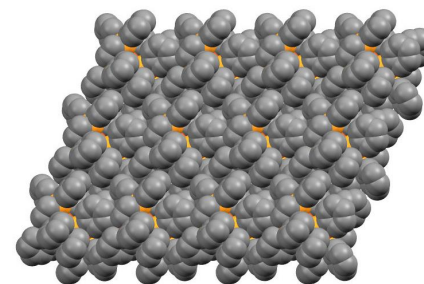


Figure S26. Packing diagram of **1**, view along the crystallographic c-axis. No channel present. H atoms omitted for clarity.

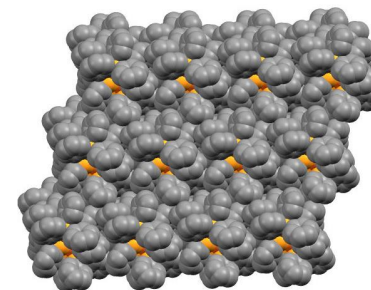


Figure S27. Packing diagram of **2**, view along the crystallographic a-axis. No channel present. H atoms omitted for clarity.

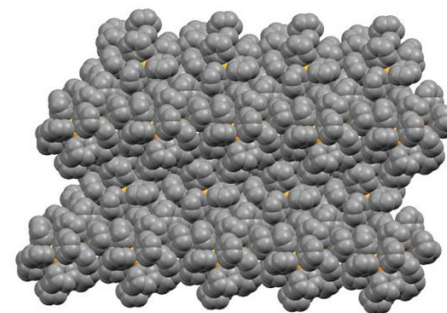


Figure S28. Packing diagram of **3**, view along the crystallographic b-axis. No channel present. H atoms omitted for clarity.

7. Photophysical Measurements

All photophysical measurements were performed in solid-state were in single-crystalline form under argon. Excitation and emission spectra were recorded on an Edinburgh Instrument FLS1000 spectrometer, equipped with a 450 W Xenon arc lamp, double monochromators for the excitation and emission pathways, and a red-sensitive photomultiplier (PMT-980) as a detector. The excitation and emission spectra were corrected using the standard corrections supplied by the manufacturer for the excitation source's spectral power and the detector's sensitivity. Quantum yields of solid samples were measured using an integrating cryosphere (Microstat N2) from Oxford Instruments. The luminescence lifetimes were measured using a μ F2 pulsed 60 W Xenon microsecond flashlamp, with a repetition rate of 100 Hz, a multichannel scaling (MCS) module or VPLED (271.8 nm with 0.3 mW or 383.8 nm with 1.1 mW or 449.6 nm with 37 mW), with 48.4 ns or 48.1 ns or 59.8 ns minimum pulse width respectively and an MCS module, depending on the time range. The low temperature experiments were performed using a 4 K cryostat (CS204SI-FMX-1SS) from Advanced Research System equipped with a closed cycle water-cooled helium compressor. The emission was collected at a right angle to the excitation source.

8. Emission Studies

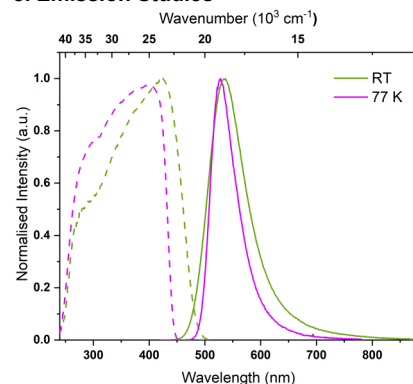


Figure S29. Normalized excitation (dash lines) and emission (solid lines) spectra of compound **1** in solid state at room temperature (green) and at 77 K (purple) at room temperature in solid state.

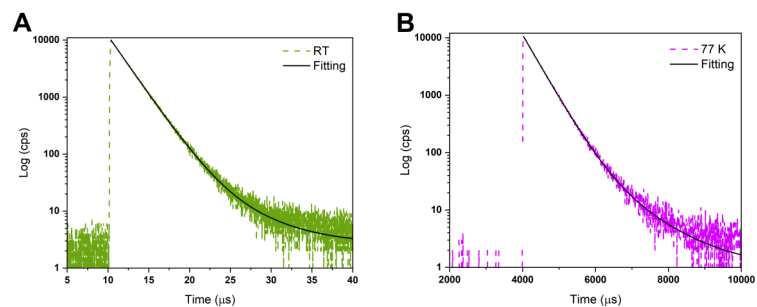


Figure S30. Emission decays of compound **1** at room temperature (**A**) and at 77 K (**B**) in solid state.

Table S3. Selected photophysical data of compound **1** at RT and 77 K.

		λ_{em}^{max} (nm)	Stokes Shift (cm^{-1})	FWHM (cm^{-1})	τ (μs) ^a	$\langle \tau \rangle_{amp}$ (μs)	Φ	k_r (s^{-1}) ^b
1	RT	535 [400]	4838	2679	2.14 (100)	2.1	0.32	1.5×10^5
	77 K	525 [400]	5952	749	403.46 (100)	403.4	0.38	9.4×10^2

(a) The pre-exponential factors B are given in parentheses. (b) k_r was calculated using amplitude-weighted averaged lifetimes.

Two-level fitting equation:
$$\tau_{r,av}(T) = \frac{3 + \exp\left[-\frac{\Delta E(S_1 - T_1)}{k_B T}\right]}{\frac{3}{\tau(T_1)} + \left[\frac{1}{\tau(S_1)}\right] \exp\left[-\frac{\Delta E(S_1 - T_1)}{k_B T}\right]}$$

Table S4. Temperature dependent life-times details for compound 1.

Temp (K)	τ_1 (μ s)	τ_2 (μ s)	τ_3 (μ s)	τ <ampgt; (μ s)	τ <int> (μ s)	χ^2	ϕ	τ <intrinsic>
7	576.14 (12)	1333.80 (80)	2780.44 (8)	1355.58	1521.44	1.11	0.37	3613.93
17	1259.11 (90)	2517.67 (10)		1380.75	1480.91	1.13	0.37	3681.03
27	1251.02 (89)	2290.54 (11)		1378.26	1688.32	1.10	0.37	3674.40
37	1253.42 (89)	2210.73 (11)		1360.86	1453.54	1.09	0.37	3627.99
47	1207.28 (91)	2194.91 (9)		1308.17	1549.38	1.06	0.37	3487.52
57	1870.51 (10)	1002.36 (90)		1282.05	36449.01	1.01	0.37	3417.90
67	659.35 (94)	1322.80 (6)		706.41	850.06	0.97	0.37	1883.26
77	403.46 (100)			403.46	403.46	1.00	0.37	1075.61
87	219.09 (100)			219.09	219.09	1.19	0.37	591.67
97	113.18 (97)	247.07 (3)		117.46	122.18	1.08	0.36	325.10
107	66.71 (96)	137.99 (4)		69.26	71.79	1.04	0.36	191.38
117	14.24 (8)	44.88 (92)		44.23	47.56	1.15	0.36	122.10
127	16.40 (12)	31.69 (88)		30.62	32.42	1.26	0.35	85.15
137	19.76 (71)	28.32 (29)		25.47	920.28	1.15	0.35	71.54
147	15.79 (91)	25.81 (9)		16.77	17.72	1.06	0.35	47.16
157	13.00 (100)			13.00	13.00	1.15	0.36	35.59
167	9.93 (97)	20.61 (3)		10.27	10.62	1.09	0.36	27.93
177	8.01 (96)	15.87 (4)		8.29	8.55	1.15	0.37	22.37
197	5.845(100)			5.84	5.84	1.24	0.38	15.23
227	3.73 (95)	6.37 (5)		3.89	4.25	1.16	0.37	10.29
237	3.51(100)			3.51	3.51	1.14	0.37	9.47
267	2.68 (100)			2.68	2.68	1.09	0.35	7.50
297	2.14 (100)			2.14	2.14	1.14	0.3188	6.71

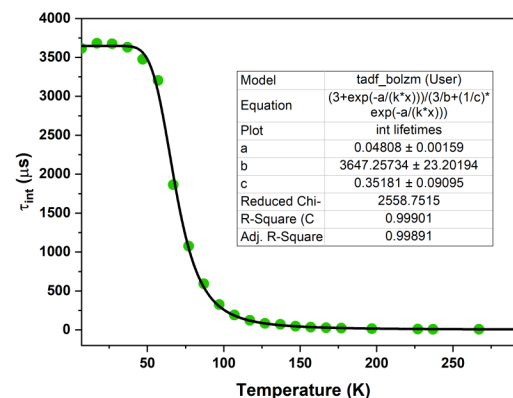


Figure S31. Radiative lifetimes of **1** at various temperatures with two-level fit. Intrinsic lifetimes (τ_{int}) are calculated by dividing amplitude-weighted averaged lifetimes by quantum yields.

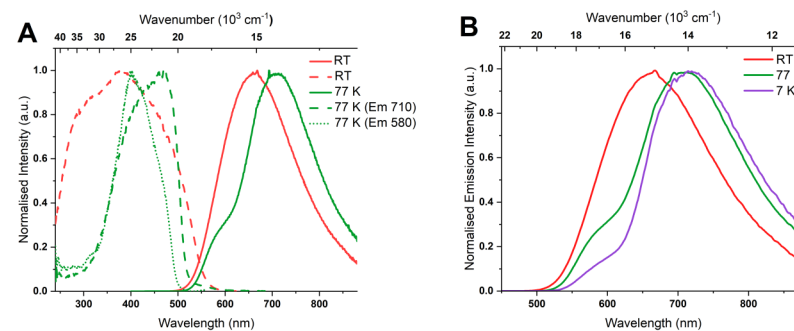


Figure S32. (A) : Normalised emission (solid lines) and excitation (dash/dot lines) spectra of **2** at room temperature (red) and at 77 K (green) in solid state. (B) : Normalised emission spectra of **2** at room temperature (red), 77 K (green) and 7 K (violet) in solid state.

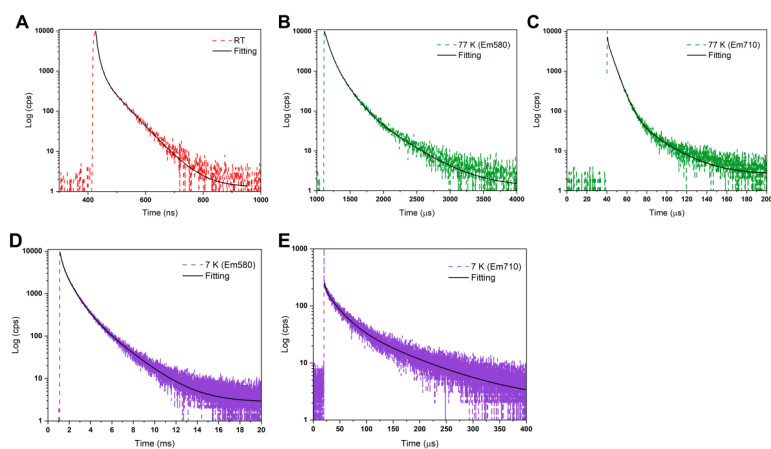


Figure S33. Emission decays of compound **2** at room temperature (**A**), at 77 K (**B** : Em 580 nm; **C** : Em 710 nm), and at 7 K (**D** : Em 580 nm; **E** : Em 710 nm) in solid state.

Table S5. Selected photophysical data of compound **2** at RT, 77 K and 7 K.

Temp	λ_{em}^{max} [nm]	Stokes shift (cm ⁻¹)	FWHM (cm ⁻¹)	τ (μ s) ^a	$\langle \tau \rangle_{amp}$ (μ s)	Φ	k_r (s ⁻¹) ^b
2 RT	660 [380]	11164	4098	0.04(54), 0.1(38), 0.6(8)	0.1	0.03	3×10^5
77 K	710 [380] LE,	7421	-	0.5(30), 5.8(70), 24(2)	4.6	0.21	-
77 K	580 [380] HE	7758	-	58(65), 146(32), 404(3)	97	-	-
7 K	710 [380] LE,	-	-	3.8 (24), 25 (54), 102 (22)	37	-	-
7 K	580 [380] HE	-	-	207 (47), 807 (44), 2181 (9)	644	-	-

(a) For lifetimes fitted with two or multi exponentials, the pre-exponential factors B are given in parentheses. (b) k_r was calculated using amplitude-weighted averaged lifetimes.

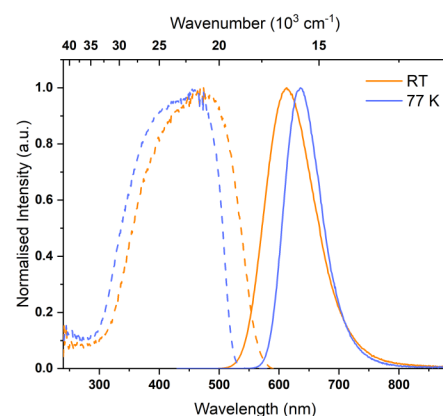


Figure S34. Normalized excitation (dash lines) and emission (solid lines) spectra of compound **3** in solid state at room temperature (orange) and at 77 K (blue) at room temperature in solid state.

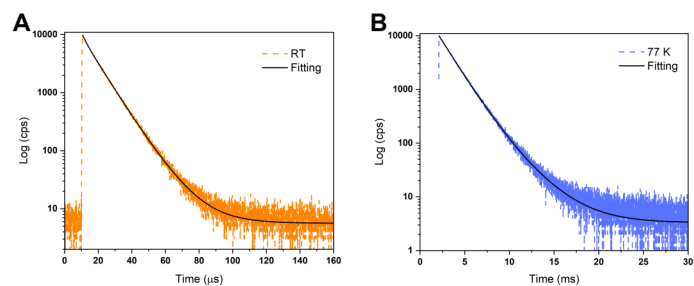


Figure S35. Emission decays of compound **3** at room temperature (**A**) and at 77 K (**B**) in solid state.

Table S6. Selected photophysical data of compound **3** at RT and 77 K.

	Temp	λ_{em}^{max} [nm]	Stokes Shift (cm ⁻¹)	FWHM (cm ⁻¹)	τ (μ s) ^a	$\langle \tau \rangle_{amp}$ (μ s)	Φ	k_r (s ⁻¹) ^b
3	RT	610 [485]	4659	2565	2.29(11), 9.07(83), 15(6)	8.7	0.24	2.7×10^4
	77 K	635 [485]	5991	1736	1599.07 (94), 3119.96 (6)	1697.0	0.28	1.6×10^2

(a) For lifetimes fitted with two or multi exponentials, the pre-exponential factors B are given in parentheses. (b) k_r was calculated using amplitude-weighted averaged lifetimes.

Two-level fitting equation:
$$\tau_{r,av}(T) = \frac{3 + \exp\left[-\frac{\Delta E(S_1 - T_1)}{k_B T}\right]}{\frac{3}{\tau(T_1)} + \left[\frac{1}{\tau(S_1)}\right] \exp\left[-\frac{\Delta E(S_1 - T_1)}{k_B T}\right]}$$

Table S7. Temperature dependent life-times details for compound **3**.

Temp (K)	τ_1 (μ s)	τ_2 (μ s)	τ_3 (μ s)	τ <amp;gt; (μ s)	τ <int> (μ s)	χ^2	Φ	τ <intrinsic>
27	1642.05 (94)	2947.35 (6)		1720.77	1776.88	1.23	0.27	6250.53
47	1637.60 (95)	2994.44 (5)		1707.37	1759.96	1.23	0.27	6201.86
67	1609.96 (95)	3074.80 (5)		1677.28	1733.37	1.20	0.27	6092.57
77	1599.07 (94)	3119.96 (6)		1697.01	1779.14	1.21	0.27	6164.24
97	1276.46 (98)	2829.71 (2)		1309.17	1347.16	1.14	0.25	5232.51
117	723.46 (98)	1577.33 (2)		743.30	765.57	1.15	0.23	3163.00
137	337.92 (96)	672.44 (4)		350.22	361.53	1.13	0.23	1520.72
157	162.96 (92)	271.51 (8)		172.17	177.48	1.03	0.24	699.60
177	25.43 (16)	89.92 (84)		84.09	92.71	1.13	0.25	334.09
197	12.96 (10)	53.44 (84)	90.61 (6)	51.30	56.08	1.17	0.25	198.31
217	10.37 (14)	36.20 (86)		33.54	36.70	1.16	0.26	126.19
237	11.45 (21)	26.74 (79)		23.48	25.15	1.14	0.26	88.24
257	4.36 (12)	17.29 (82)	27.82 (6)	16.46	18.04	1.12	0.25	63.71
277	3.28 (12)	12.67 (82)	21.01 (6)	12.02	13.18	1.17	0.29	41.41
297	2.29 (11)	9.07 (83)	15.00 (6)	8.66	9.48	1.08	0.23	36.6992

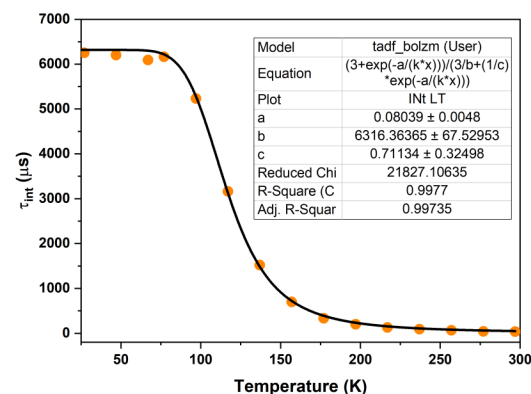


Figure S36. Radiative lifetimes of **3** at various temperatures with two-level fit. Intrinsic lifetimes (τ_{int}) are calculated by dividing amplitude-weighted averaged lifetimes by quantum yields.

9. Thermal stability of compound 1-3

Thermal stability of the compounds were checked using TA SDT 650 simultaneous thermal analyzer under continuous flow of argon.

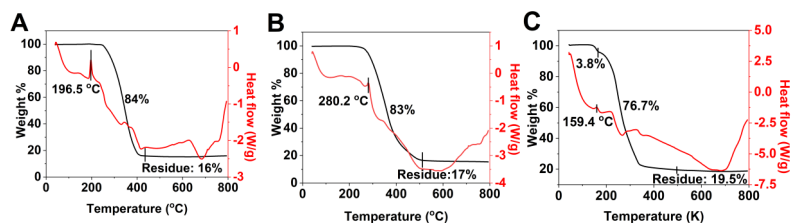


Figure S37. TG/DTA data of compound **1** (A), **2** (B) and **3** (C).

All three compounds shows high thermal stability. Compound **1** and **2** undergo steady decomposition from 196 and 280 °C respectively. For compound **3** weight loss of 3.8% around 159 °C might be the removal of one PPh₃ unit. Around 400 °C, approximately 20% weight still remains in the melt for all the three compounds which indicates the presence of CuP(phosphide) units.

10. TD-DFT calculations

DFT calculations for compounds **1**, and **2** were performed with the ORCA 5.0.3 software package.^[7] Geometry optimization with tight convergence criteria was carried out using PBE0 (**1** and **2**) functional^[8] with def2-TZVP basis set^[9] and Grimme-D3BJ empirical dispersion correction.^[10] To accelerate calculations, the SARC/J^[11] auxiliary basis set was used together with RI approximation. Solvents effects (**1** and **2**: CH₂Cl₂, $\epsilon = 9.08$) were accounted for by implicit solvent model CPCM.^[12] Relativistic effects were accounted for by employing the ZORA method.^[13] The same level of theory (PBE0 functional for **1** and **2** compounds) was used for TD-DFT calculation of the first 50 (**1** and **2**) singlet and triplet excited states. Electronic transition differences at isovalues of 0.003 were prepared using the orca plot module as implemented in ORCA 5.0.3. software and USCF Chimera.^[14]

Table S8. Singlet excitations calculated for **1** in the ground state geometry.

State	Energy [cm ⁻¹]	λ [nm]	f_{osc}
1	23186.1	431.3	0.00232209
2	23314.0	428.9	0.07288507
3	23460.5	426.2	0.02717621
4	23955.4	417.4	0.00123901
5	24199.2	413.2	0.03357893
6	24809.7	403.1	0.01208048
7	25366.1	394.2	0.00640034
8	25817.0	387.3	0.02642138
9	26104.5	383.1	0.01284119
10	26275.3	380.6	0.07241241
11	26387.0	379	0.02905901
12	26617.4	375.7	0.00394938
13	26736.2	374	0.02166967
14	26820.3	372.9	0.01874251
15	26979.1	370.7	0.04938752
16	27192.2	367.8	0.0068806
17	27222.9	367.3	0.00965934
18	27332.7	365.9	0.01571698
19	27556.1	362.9	0.01084567
20	27720.8	360.7	0.02250234
21	28036.6	356.7	0.00935109

22	28302.0	353.3	0.0355592	4	23609.9	423.6	0.012477618
23	28488.4	351	0.01462202	5	23785.6	420.4	0.000000731
24	28885.8	346.2	0.03445336	6	23962.1	417.3	0.106104712
25	29025.5	344.5	0.03800212	7	24536.7	407.6	0.000039770
26	29046.5	344.3	0.0254672	8	24549.7	407.3	0.006599342
27	29334.0	340.9	0.0008672	9	24905.2	401.5	0.028269731
28	29495.0	339	0.00662568	10	25257.5	395.9	0.000000159
29	29745.6	336.2	0.01529405	11	25682.0	389.4	0.000006996
30	29884.4	334.6	0.02163188	12	25892.8	386.2	0.021957144
31	30004.4	333.3	0.02880632	13	26207.0	381.6	0.000000649
32	30250.0	330.6	0.03551985	14	26541.1	376.8	0.000052660
33	30332.2	329.7	0.01012068	15	26571.8	376.3	0.103298091
34	30390.3	329.1	0.00429185	16	27119.4	368.7	0.018035619
35	30735.6	325.4	0.01416715	17	27287.5	366.5	0.016926338
36	30854.4	324.1	0.03724564	18	27415.9	364.8	0.000001056
37	30918.0	323.4	8.7378E-05	19	27935.8	358.0	0.000083765
38	31369.0	318.8	0.00319264	20	27962.0	357.6	0.058945728
39	31528.2	317.2	0.00161556	21	28405.9	352.0	0.034374022
40	31545.5	317	0.04756355	22	28472.1	351.2	0.000012280
41	31807.7	314.4	0.05312015	23	28654.9	349.0	0.040106383
42	31845.7	314	0.0100191	24	28690.7	348.5	0.000006373
43	32009.7	312.4	0.00715673	25	28834.6	346.8	0.056381135
44	32156.5	311	0.02693581	26	28892.0	346.1	0.089703174
45	32284.0	309.8	0.03737595	27	28896.3	346.1	0.001015530
46	32362.1	309	0.17612319	28	28970.4	345.2	0.000003222
47	32458.1	308.1	0.01040755	29	29125.8	343.3	0.095761045
48	32599.1	306.8	0.10076803	30	29152.8	343.0	0.000106867
49	32720.3	305.6	0.01448012	31	29348.4	340.7	0.055618276
50	32888.8	304.1	0.00699175	32	29357.6	340.6	0.000002209
				33	29670.1	337.0	0.000008072
				34	29686.3	336.9	0.028340126
				35	29820.1	335.3	0.037661344
				36	29864.4	334.8	0.000019797
				37	29955.1	333.8	0.009105626
				38	30020.9	333.1	0.000003401

Table S9. Singlet excitations calculated for **2** in the ground state geometry.

State	Energy [cm ⁻¹]	λ [nm]	f_{osc}
1	22201.9	450.4	0.000000205
2	22367.4	447.1	0.020396327
3	23445.0	426.5	0.000005532

39	30029.0	333.0	0.001243708
40	30198.2	331.1	0.000010954
41	30324.5	329.8	0.000001274
42	30601.2	326.8	0.000057281
43	30632.2	326.5	0.129800114
44	30861.4	324.0	0.000001937
45	30975.1	322.8	0.044047800
46	31072.6	321.8	0.043861312
47	31166.1	320.9	0.000008141
48	31224.2	320.3	0.010401965
49	31226.7	320.2	0.010228220
50	31332.3	319.2	0.008057801

21	27282.8	366.5
22	27599.7	362.3
23	27841.4	359.2
24	28017.4	356.9
25	28159.1	355.1
26	28296.2	353.4
27	28746.0	347.9
28	28905.0	346
29	29106.1	343.6
30	29308.3	341.2
31	29468.0	339.4
32	29609.5	337.7
33	29632.9	337.5
34	29733.9	336.3
35	29817.4	335.4
36	29917.3	334.3
37	29952.7	333.9
38	30034.1	333
39	30132.8	331.9
40	30192.1	331.2
41	30310.3	329.9
42	30363.0	329.3
43	30380.6	329.2
44	30522.9	327.6
45	30798.0	324.7
46	31122.0	321.3
47	31139.7	321.1
48	31199.7	320.5
49	31448.1	318
50	31627.7	316.2

Table S10. Triplet excitations calculated for **1** in the ground state geometry.

State	Energy [cm ⁻¹]	λ [nm]
1	22374.5	446.9
2	22566.1	443.1
3	22926.1	436.2
4	23436.0	426.7
5	23541.8	424.8
6	23848.4	419.3
7	24299.8	411.5
8	24600.2	406.5
9	24896.9	401.7
10	25126.1	398
11	25391.1	393.8
12	25952.7	385.3
13	25980.9	384.9
14	26373.3	379.2
15	26378.0	379.1
16	26622.3	375.6
17	26831.7	372.7
18	26879.6	372
19	26982.7	370.6
20	27093.9	369.1

Table S11. Triplet excitations calculated for **2** in ground state geometry.

State	Energy [cm ⁻¹]	λ [nm]
1	21778.2	459.2

2	21972.4	455.1	37	29215.9	342.3
3	22712.9	440.3	38	29329.1	341.0
4	23194.8	431.1	39	29398.5	340.2
5	23377.0	427.8	40	29449.7	339.6
6	23487.9	425.8	41	29552.6	338.4
7	24018.3	416.3	42	29640.8	337.4
8	24153.4	414.0	43	29733.4	336.3
9	24273.6	412.0	44	29757.6	336.0
10	24409.4	409.7	45	29874.2	334.7
11	24596.2	406.6	46	29899.8	334.5
12	24625.1	406.1	47	30023.8	333.1
13	24957.0	400.7	48	30213.2	331.0
14	25336.9	394.7	49	30275.0	330.3
15	25865.3	386.6	50	30736.7	325.3
16	26212.6	381.5			
17	26579.6	376.2			
18	26631.5	375.5			
19	26808.4	373.0			
20	27065.8	369.5			
21	27243.2	367.1			
22	27574.3	362.7			
23	27700.1	361.0			
24	27809.6	359.6			
25	27999.0	357.2			
26	28049.0	356.5			
27	28258.2	353.9			
28	28307.5	353.3			
29	28493.3	351.0			
30	28639.5	349.2			
31	28852.5	346.6			
32	28964.0	345.3			
33	28966.1	345.2			
34	28988.8	345.0			
35	29096.0	343.7			
36	29196.9	342.5			

Table S12. XYZ coordinates of optimized molecule 1.

Cu	-3.40646	4.089322	6.900145
P	-2.82816	4.28021	4.646748
P	-2.37098	2.831575	8.525721
P	-2.90177	5.985334	8.076356
C	-1.44807	3.293908	3.960806
C	-1.10047	1.54003	8.291418
C	-4.22557	0.388923	11.316
H	-4.02112	-0.54896	11.84162
C	-3.29441	0.882942	10.40131
H	-2.36724	0.330463	10.22393
C	-3.54505	2.076505	9.713726
C	0.335113	1.665281	4.302148
H	0.907416	1.031416	4.987355
C	-0.6879	2.47322	4.804645
H	-0.90489	2.472839	5.876176
C	-1.4813	0.380365	7.59785
H	-2.51986	0.262441	7.273377
C	-4.74549	2.759669	9.952028
H	-4.97549	3.661201	9.378381
C	-0.5536	-0.61687	7.31339
H	-0.87232	-1.51421	6.774099
C	-5.40802	1.087776	11.56463
H	-6.13476	0.698922	12.2844
C	-5.66432	2.276884	10.88115
H	-6.59615	2.824299	11.05285

C	-1.17205	6.406173	3.669997
H	-0.35188	5.687	3.593131
C	0.236128	1.681601	8.684977
H	0.568065	2.568521	9.229314
C	0.625005	1.674595	2.938629
H	1.426692	1.045739	2.539128
C	1.169318	0.685769	8.387313
H	2.210439	0.812998	8.699226
C	-1.95639	8.691461	3.449502
H	-1.76931	9.738589	3.193304
C	-3.21853	8.281434	3.886661
H	-4.03601	9.005633	3.968618
C	-0.93975	7.740792	3.337049
H	0.05674	8.043778	2.998388
C	-0.39655	5.9596	6.894377
H	-0.62984	4.905175	6.712649
C	-1.52212	4.095891	9.592091
H	-1.2797	3.664767	10.57847
H	-0.57064	4.350905	9.094373
C	-2.43391	5.978488	4.114439
C	-3.45014	6.945631	4.200247
H	-4.45007	6.625167	4.506112
C	0.779395	-0.46513	7.703696
H	1.513214	-1.24339	7.473544
C	-1.36004	6.784466	7.492649
C	-4.01448	7.377473	8.476423
C	-2.37419	5.34942	9.741485
H	-1.82287	6.129147	10.29452
H	-3.29384	5.121159	10.30815
C	1.096203	7.843302	6.653291
H	2.053561	8.258949	6.324436
C	-1.15178	3.279935	2.585966
H	-1.74007	3.900403	1.901447
C	-4.5943	8.07067	7.403268
H	-4.31769	7.804846	6.379592
C	0.129915	8.676362	7.219985
H	0.327956	9.74625	7.337124
C	-0.12301	2.488871	2.082122
H	0.087962	2.492508	1.007941
C	0.830436	6.483042	6.492591
H	1.572382	5.826493	6.028132
C	-1.0903	8.1497	7.645471
H	-1.83717	8.808244	8.098658
C	-4.38836	7.720652	9.781963
H	-3.95519	7.203891	10.64148
C	-5.51803	9.087634	7.626678

H	-5.95649	9.616937	6.775307
C	-5.89326	9.416951	8.931365
H	-6.62897	10.20679	9.110059
C	-5.32638	8.731168	10.00502
H	-5.61165	8.984227	11.03069
Cu	-5.009961	3.625906	4.193782
P	-5.54752	3.310644	6.441873
P	-6.38106	4.95905	2.979232
P	-5.36147	1.918953	2.704455
C	-7.00193	4.094215	7.230821
C	-7.71945	5.946642	3.725597
C	-5.51641	8.114239	0.43341
H	-5.97974	9.050232	0.106293
C	-6.18314	7.295006	1.345577
H	-7.16446	7.593478	1.727117
C	-5.59477	6.101969	1.780447
C	-9.40486	4.363097	7.539861
H	-10.4253	4.038138	7.312201
C	-8.32458	3.703316	6.957101
H	-8.51319	2.866488	6.27724
C	-7.43234	6.626692	4.917975
H	-6.44551	6.524525	5.379771
C	-4.32989	5.744946	1.293692
H	-3.84519	4.841413	1.678865
C	-8.40219	7.409477	5.539145
H	-8.15993	7.929331	6.469836
C	-4.2645	7.742832	-0.06084
H	-3.74412	8.388317	-0.775
C	-3.67395	6.552321	0.367008
H	-2.68593	6.262376	-0.00362
C	-6.62233	0.995276	7.76609
H	-7.31934	1.649561	8.296155
C	-9.00693	6.042847	3.180598
H	-9.25827	5.518751	2.254408
C	-9.19159	5.443614	8.400623
H	-10.0416	5.965459	8.851011
C	-9.9839	6.811678	3.814442
H	-10.9878	6.874152	3.383374
C	-5.76687	-1.24074	7.366847
H	-5.79555	-2.31678	7.563031
C	-4.84485	-0.70743	6.461054
H	-4.14132	-1.36505	5.938794
C	-6.65069	-0.37723	8.016828
H	-7.37286	-0.77588	8.73731
C	-7.54437	0.979789	4.118918
H	-7.50367	1.977025	4.569101

C	-7.24693	3.775355	1.839027
H	-7.73561	4.313002	1.008892
H	-8.03465	3.273922	2.430146
C	-5.70997	1.544177	6.850947
C	-4.82026	0.661239	6.21275
H	-4.09943	1.077337	5.50099
C	-9.68165	7.501549	4.989233
H	-10.4494	8.104388	5.483621
C	-6.57462	0.62817	3.172407
C	-4.02766	0.968559	1.897068
C	-6.24373	2.760406	1.300716
H	-6.7392	2.016402	0.653775
H	-5.47909	3.278011	0.694977
C	-8.50936	-1.22887	3.981306
H	-9.25862	-1.9588	4.302725
C	-6.80935	5.179945	8.097424
H	-5.78827	5.504598	8.314668
C	-3.1876	0.201664	2.71962
H	-3.35377	0.182282	3.800343
C	-7.5405	-1.58924	3.042129
H	-7.5322	-2.60048	2.623664
C	-7.887	5.852041	8.674887
H	-7.69948	6.699217	9.342694
C	-8.5137	0.060621	4.515236
H	-9.26026	0.346739	5.262484
C	-6.57924	-0.66427	2.633878
H	-5.82263	-0.9542	1.898503
C	-3.78373	0.990666	0.51834
H	-4.42027	1.574375	-0.15088
C	-2.13983	-0.53522	2.177358
H	-1.49434	-1.12349	2.836028
C	-1.90207	-0.50541	0.801498
H	-1.07151	-1.07556	0.374602
C	-2.72312	0.261004	-0.02377
H	-2.54398	0.290619	-1.10291

Table S13. XYZ coordinates of optimized molecule 2.

C	4.613064	0.930009	6.133645
C	4.775875	-0.44754	6.35652
H	4.057753	-0.98555	6.975761
C	5.83303	-1.14945	5.770254
H	5.931276	-2.22062	5.954179
C	6.747319	-0.49651	4.941521
H	7.564343	-1.04829	4.476207

C	6.607852	0.879369	4.726698
H	7.315502	1.410795	4.088528
C	5.564438	1.58062	5.322441
H	5.469206	2.653782	5.150322
C	2.329463	0.819601	7.881208
C	2.96377	0.413386	9.069572
H	4.004307	0.693655	9.24358
C	2.275356	-0.31401	10.03832
H	2.785834	-0.61251	10.95499
C	0.92889	-0.6432	9.845467
H	0.386885	-1.20401	10.60746
C	0.283746	-0.24195	8.675042
H	-0.76677	-0.4891	8.516173
C	0.979613	0.481634	7.702462
H	0.463225	0.811279	6.800522
C	5.329836	3.425979	10.2322
C	6.191978	2.759097	11.11008
H	7.221621	2.55865	10.81565
C	5.738258	2.326866	12.35665
H	6.417509	1.796981	13.02466
C	4.418656	2.568438	12.74275
H	4.058723	2.224387	13.71252
C	3.560384	3.263133	11.89055
H	2.536591	3.470155	12.20211
C	4.006198	3.696288	10.63756
C	1.264068	4.438053	10.14613
C	0.562688	3.284684	9.772585
H	1.034987	2.55205	9.119702
C	-0.74172	3.075543	10.21668
H	-1.27498	2.174038	9.913803
C	-1.36393	4.02372	11.03328
H	-2.38749	3.865838	11.37415
C	-0.67041	5.175714	11.40816
H	-1.14859	5.91992	12.04564
C	0.639017	5.38249	10.96968
H	1.169233	6.286197	11.26717
C	3.339487	6.391399	9.97392
C	4.125226	6.717045	11.08602
H	4.524331	5.929726	11.72457
C	4.411569	8.051979	11.37776
H	5.032368	8.293848	12.24083
C	3.908754	9.071588	10.56773
H	4.135797	10.11338	10.79554
C	3.120371	8.751537	9.459301
H	2.728699	9.541403	8.817758
C	2.84433	7.418775	9.159059

H	2.247388	7.175206	8.28009
C	7.209283	2.902226	8.088956
C	7.157623	1.525453	8.352097
H	6.305517	1.101625	8.883179
C	8.194586	0.689998	7.941038
H	8.146847	-0.37588	8.163542
C	9.280862	1.212403	7.235149
H	10.08791	0.556378	6.908441
C	9.321295	2.575659	6.938961
H	10.15966	2.990252	6.378538
C	8.293122	3.417672	7.364955
H	8.339545	4.482378	7.135173
C	6.630885	5.604276	8.869062
C	7.711341	5.738909	9.751558
H	8.114518	4.86324	10.26174
C	8.275469	6.993267	9.97928
H	9.11385	7.09352	10.66918
C	7.768399	8.120089	9.323948
H	8.213162	9.099551	9.502164
C	6.690972	7.991264	8.446996
H	6.287296	8.866542	7.938081
C	6.119988	6.736474	8.227107
H	5.258012	6.629027	7.568424
Cu	3.835404	4.030343	7.45671
P	3.183994	1.922436	6.694209
P	2.957599	4.665716	9.482868
P	5.814382	3.992579	8.543507
C	1.499297	5.996438	6.120627
C	1.338661	7.375097	5.903113
H	2.059251	7.914947	5.288357
C	0.28048	8.075661	6.489124
H	0.183908	9.147698	6.309401
C	-0.63713	7.420164	7.312142
H	-1.45517	7.970802	7.777033
C	-0.49987	6.043222	7.521434
H	-1.21037	5.509771	8.154722
C	0.54459	5.343357	6.92589
H	0.638195	4.269387	7.09382
C	3.782328	6.108344	4.372581
C	3.147987	6.513051	3.183726
H	2.107939	6.231189	3.009358
C	3.835946	7.240582	2.214752
H	3.325591	7.537551	1.297519
C	5.181889	7.5717	2.408038
H	5.723652	8.132307	1.645736
C	5.826966	7.172204	3.579089

H	6.877165	7.420553	3.738145
C	5.131695	6.448038	4.55165
H	5.647916	6.120282	5.454374
C	0.783469	3.500786	2.021521
C	-0.07863	4.167458	1.143444
H	-1.10848	4.367377	1.437504
C	0.375247	4.599691	-0.10307
H	-0.30408	5.129088	-0.7714
C	1.694967	4.358356	-0.48892
H	2.05492	4.702139	-1.45878
C	2.553189	3.663808	0.363452
H	3.577021	3.456777	0.052021
C	2.107209	3.230639	1.616379
C	4.849243	2.488245	2.108399
C	5.551146	3.64093	2.483049
H	5.078941	4.373447	3.136115
C	6.856219	3.849131	2.040489
H	7.390017	4.749905	2.3446
C	7.47848	2.900787	1.224125
H	8.502674	3.057756	0.884749
C	6.784355	1.749585	0.847931
H	7.262688	1.005108	0.210884
C	5.474428	1.543545	1.285251
H	4.943601	0.640625	0.986452
C	2.773357	0.535426	2.279741
C	1.987468	0.210171	1.167633
H	1.588446	0.997705	0.529293
C	1.700684	-1.12464	0.875747
H	1.079764	-1.36619	0.012675
C	2.203239	-2.1445	1.685611
H	1.975979	-3.18621	1.457614
C	2.991768	-1.82483	2.794042
H	3.383358	-2.61492	3.435363
C	3.268305	-0.4922	3.094409
H	3.865168	-0.24892	3.973503
C	-1.09639	4.024218	4.164515
C	-1.04574	5.400713	3.899705
H	-0.19434	5.824401	3.367368
C	-2.08303	6.235992	4.310287
H	-2.03627	7.301568	4.086142
C	-3.16846	5.713789	5.017629
H	-3.97588	6.369644	5.343737
C	-3.20775	4.350897	5.315669
H	-4.0456	3.936427	5.87696
C	-2.17949	3.50895	4.889759
H	-2.22487	2.44457	5.121256

C	-0.51732	1.322244	3.38451
C	-1.59768	1.187443	2.501931
H	-2.00107	2.06309	1.991879
C	-2.16121	-0.06709	2.273709
H	-2.99943	-0.1675	1.583636
C	-1.65364	-1.19392	2.928641
H	-2.09792	-2.17353	2.750026
C	-0.57631	-1.06493	3.805684
H	-0.17226	-1.94021	4.314302
C	-0.0059	0.190041	4.026043
H	0.855991	0.297639	4.684812
Cu	2.277779	2.896932	4.796933
P	2.928805	5.004824	5.559663
P	3.155466	2.260939	2.771122
P	0.298767	2.934125	3.710196

Figure S38. HOMO (left) and LUMO (right) orbitals for compound 1.

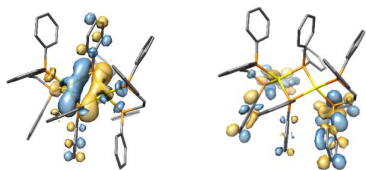


Figure S39. Electron density differences for compound 1.

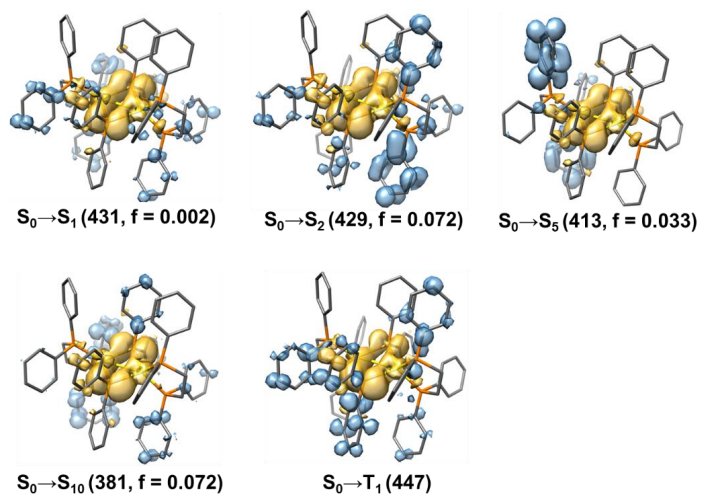


Figure S40. HOMO (left) and LUMO (right) orbitals for compound 2.

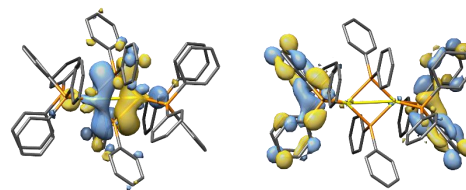
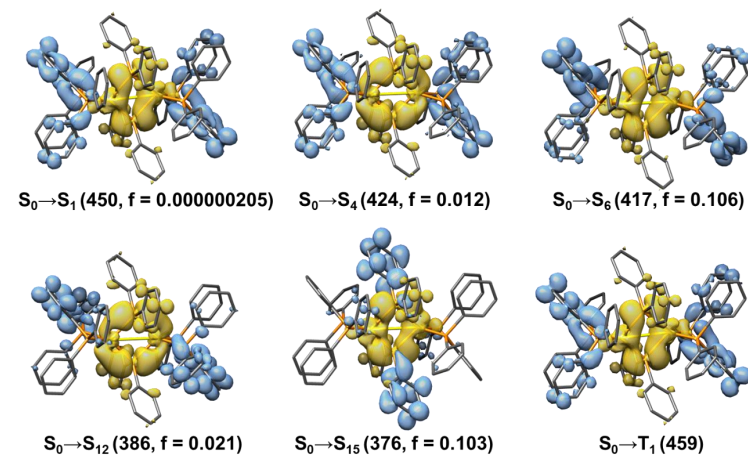


Figure S41. Electron density differences for compound 2.



11. References

- [1] W. L. F. Armarego, *Purification of laboratory Chemicals*, Butterworth Heinemann, Oxford; Boston, 1996.
- [2] T. H. Lemmen, G. V. Goeden, J. C. Huffman, R. L. Geerts, and K. G. Caulton, *Inorg. Chem.*, 1990, **29**, 3680.
- [3] G. M. Sheldrick, *Acta Crystallogr. C*, 2015, **71**, 3.
- [4] O. V. Dolomanov, L. J. Bourhis, R. J. Gildea, J. A. K. Howard, and H. Puschmann, *J. Appl. Crystallogr.* 2009, **42**, 339.
- [5] A. L. Spek, *Acta Crystallogr. C*, 2015, **71**, 9.
- [6] P. Dierkes, and P. W. N. M. van Leeuwen, *J. Chem. Soc., Dalton Trans.*, 1999, 1519.
- [7] F. Neese, *WIREs Comput. Mol. Sci.*, 2012, **2**, 73.
- [8] a) C. Adamo, and V. Barone, *J. Chem. Phys.*, 1999, **110**, 6158; b) J. P. Perdew, K. Burke, and M. Ernzerhof, *Phys. Rev. Lett.*, 1996, **77**, 3865; c) J. P. Perdew, K. Burke, and M. Ernzerhof, *Phys. Rev. Lett.* 1997, **78**, 1396; d) C. Cardoso, A. T. Costa, A. H. MacDonald, and J. Fernández-Rossier, *Phys. Rev. B Condens. Matter.*, 1996, **105**, 9982; e) M. Ernzerhof, and G. E. Scuseria, *J. Chem. Phys.*, 1999, **110**, 5029; f) J. Tao, J. P. Perdew, V. N. Staroverov, and G. E. Scuseria, *Phys. Rev. Lett.*, 2003, **91**, 146401; g) J. P. Perdew, J. Tao, V. N. Staroverov, and G. E. Scuseria, *J. Chem. Phys.*, 2004, **120**, 6898.
- [9] a) A. Schäfer, H. Horn, and R. Ahlrichs, *J. Chem. Phys.*, 1992, **97**, 2571; b) F. Weigend, and R. Ahlrichs, *Phys. Chem. Chem. Phys.*, 2005, **7**, 3297.
- [10] a) S. Grimme, J. Antony, S. Ehrlich, and H. Krieg, *J. Chem. Phys.*, 2010, **132**, 154104; b) S. Grimme, S. Ehrlich, and L. Goerigk, *J. Comput. Chem.*, 2011, **32**, 1456.
- [11] a) F. Weigend, *Phys. Chem. Chem. Phys.*, 2006, **8**, 1057; b) D. A. Pantazis, and F. Neese, *J. Chem. Theory Comput.*, 2009, **5**, 2229; c) D. A. Pantazis, and F. Neese, *Theor. Chem. Acc.*, 2012, **131**, 1292; d) D. A. Pantazis, and F. Neese, *J. Chem. Theory Comput.*, 2011, **7**, 677.
- [12] V. Barone, and M. Cossi, *J. Phys. Chem. A*, 1998, **102**, 1995.
- [13] D. A. Pantazis, X. Y. Chen, C. R. Landis, and F. Neese, *J. Chem. Theory Comput.*, 2008, **4**, 908.
- [14] E. F. Pettersen, T. D. Goddard, C. C. Huang, G. S. Couch, D. M. Greenblatt, E. C. Meng, and T. E. Ferrin, *J. Comput. Chem.*, 2004, **13**, 1605.

Supporting Information

A [2.2]Isoindolinophanyl-Based Carbene (iPC) Ligand: Synthesis, Electronic and Photophysical Properties, and Application in Photocatalysis

*S. Maity, A. M. T. Muthig, I. Sen, O. Mrózek, A. Belyaev, B. Hupp, A. Steffen**

Table of Contents

1. General Procedures.....	S-1
2. Characterization Data	S-2
3. NMR spectra.....	S-7
4. X-ray characterization data.....	S-22
5. IR-spectroscopy.....	S-28
6. Photophysical Measurements	S-29
7. UV-Visible Spectroscopy.....	S-30
8. Emission Studies	S-31
9. Photostability of the Au(I) complex 5.....	S-35
10. Steric Properties	S-37
11. TD-DFT calculations.....	S-39
12. References.....	S-57

1. General Procedures

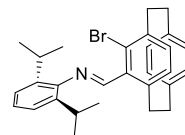
All manipulations were carried out under an inert atmosphere of argon using standard Schlenk link^[1] or glovebox techniques (GS MEGA E-Line, <0.5 ppm of H₂O and O₂). All reagents were used as supplied. Solvents such as tetrahydrofuran (THF), dichloromethane (DCM), toluene, and pentane were used at HPLC grade purity from commercial sources (VWR and Fisher Chemicals) and dried using PureSolv MD 7 drying system. After being dried, diethyl ether was kept in 4 Å molecular sieves.

NMR spectra were recorded on a Bruker Avance III HD NanoBay 500 or 600 MHz; H and chemical shifts (δ) are given in ppm relative to TMS, coupling constants (J) in Hz. The solvent signals were used as references, and the chemical shifts were converted to the TMS scale. ATR-IR spectra were measured on a Bruker Alpha-II IR Spectrometer, CHN elemental analyses were performed on a Micro cube (Elementar) and ESI-MS in Finnigan MAT 95, accurate mass determinations in Bruker APEX III FT-MS (7 T magnet).

4-Bromo-5-formyl[2.2]paracyclophane was synthesised according to literature procedures.^[2]

2. Characterization Data

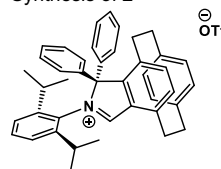
Synthesis of 1



4-Bromo-5-formyl[2.2]paracyclophane (1.2 g, 3.81 mmol, 1.00 equiv.) was dissolved in 100 mL dry dichloromethane. 2,6-diisopropylaniline (0.7 mL, 3.67 mmol, 1.01 equiv.) and triethylamine (1 mL, 7.21 mmol, 2.06 equiv.) were added subsequently and cooled to 0 °C for 30 minutes. Titanium(IV) chloride (0.2 mL, 1.82 mmol, 0.51 equiv.) was added to the solution and stirred at room temperature overnight, poured into 100 mL water, and stirred for another 2 hours. The aqueous phase was extracted with 100 mL dichloromethane and the combined organic phases were dried over Na₂SO₄ and concentrated under reduced pressure. The crude product was purified via column chromatography (the column was made basic by running triethylamine and then running eluent i.e. n-pentane/ethyl acetate) to obtain **5** as a yellow oil which was kept at -35 °C to get a yellow solid (1.2 g, 2.53 mmol, 66 %).

¹H-NMR (CDCl₃, 600 MHz, 298 K): 8.27 (s, 1H, CHN), 7.24 – 7.20 (m, 2H, Ar-H), 7.15 (dd, J = 8.4, 6.9 Hz, 1H, Ar-H), 6.99 (dd, J = 7.9, 2 Hz, 1H, Ar-H), 6.69 – 6.65 (m, 2H, Ar-H), 6.60 – 6.57 (m, 3H, Ar-H), 4.26 (ddd, J = 12.8, 10.2, 2.6 Hz, 1H), 3.59 – 3.52 (m, 1H), 3.23 – 3.16 (m, 5H), 3.12 – 3.08 (m, 1H), 2.99 – 2.89 (m, 2H), 1.29 (d, J = 6.9 Hz, 6H), 1.24 (d, J = 6.9 Hz, 6H); ¹³C {¹H} NMR (CDCl₃, 151 MHz, 298 K): 164.13 (CHN), 149.83 (Ar-CH), 143.32 (Ar-CH), 140.21 (Ar-CH), 140.04 (Ar-CH), 139.20 (Ar-CH), 137.77 (Ar-CH), 136.13 (Ar-CH), 134.52 (Ar-CH), 134.43 (Ar-CH), 133.28 (Ar-CH), 132.99 (Ar-CH), 131.14 (Ar-CH), 130.98 (Ar-CH), 128.59 (Ar-CH), 124.43 (Ar-CH), 123.24 (Ar-CH), 35.92 (CH₂), 35.33 (CH₂), 34.59 (CH₂), 33.46 (CH₂), 28.11 (CH), 24.10 (CH₃), 23.91 (CH₃).

Synthesis of 2



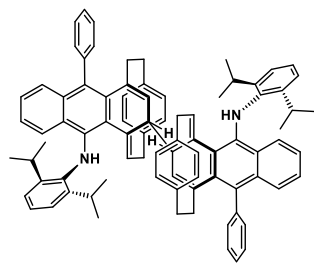
Preparation of isoindolium salt i.e. (HiPC)(OTf) (**2**) was conducted similarly to an earlier published route.^[3]

4-Bromo-5-formyl[2.2]paracyclophane-N-(2,6-diisopropylphenyl)methanimine **1** (1.2 g, 2.53 mmol, 1.00 equiv.) was dissolved in 20 mL diethyl ether. ⁿBuLi (1.2 mL, 3.03 mmol, 1.20 equiv., 2.5 M in *n*-hexane) was added dropwise at -78 °C, and the resulting mixture was stirred at the same temperature for 2 hours. Subsequently, a solution of diphenyl ketone (0.5 g, 2.66 mmol, 1.05 equiv.) in diethyl ether (5 mL) was added and the mixture was warmed to room temperature and stirred for 1 hour. Then trifluoromethanesulfonic anhydride (0.4 mL, 2.66 mmol, 1.05 equiv.) was added dropwise at -78 °C. The reaction mixture was stirred at room temperature for 12 hours. After filtration, the solid was washed with diethyl ether (5 × 10 mL), and extracted with dichloromethane (20 mL).

The organic solvent was removed by evaporation to give the corresponding isoindolium salt **2** (0.7 g, 1.25 mmol, 49 %) as a yellow solid showing green photoluminescence upon irradiation. Suitable crystals were grown by dissolving the powder in THF and slowly diffusing diethyl ether.

¹H-NMR (CD₂Cl₂, 600 MHz, 298 K): 9.66 (s, 1H, CHN), 8.11 (br, 1H, Ar-H), 7.71 (br, 1H, Ar-H), 7.60 – 7.54 (m, 1H, Ar-H), 7.48 (br, 1H, Ar-H), 7.40 – 7.27 (m, 4H, Ar-H), 7.26 – 7.10 (m, 2H, Ar-H), 7.06 (br, 1H, Ar-H), 6.94 (dd, J = 7.7, 2.0 Hz, 2H, Ar-H), 6.86 (dd, J = 7.7, 2.0 Hz, 1H, Ar-H), 6.84 – 6.81 (m, 2H, Ar-H), 6.79 (dd, J = 7.6, 1.0 Hz, 1H, Ar-H), 6.64 – 6.59 (m, 1H, Ar-H), 5.30 (dd, J = 8.2, 2.0 Hz, 1H, Ar-H), 4.00 (ddd, J = 13.8, 10.4, 5.5 Hz, 1H), 3.76 (ddd, J = 13.0, 10.0, 2.2 Hz, 1H), 3.61 – 3.53 (m, 1H), 3.35 – 3.28 (m, 1H), 3.18 (ddd, J = 13.3, 10.9, 5.5 Hz, 1H), 2.98 (ddd, J = 13.8, 10.6, 2.5 Hz, 1H), 2.79 (ddd, J = 13.5, 10.6, 5.3 Hz, 1H), 2.61 (ddd, J = 14.2, 10.2, 5.4 Hz, 1H), 2.41 (ddd, J = 13.1, 10.2, 2.5 Hz, 1H), 1.32 (d, J = 6.7 Hz, 3H), 0.87 (p, J = 6.7 Hz, 1H), 0.72 (d, J = 6.8 Hz, 3H), 0.50 (d, J = 6.7 Hz, 3H), -0.11 (d, J = 6.6 Hz, 3H); **¹³C {¹H} NMR** (CD₂Cl₂, 151 MHz, 298 K): 174.37 (CHN), 148.98 (Ar-CH), 147.63 (Ar-CH), 147.20 (Ar-CH), 147.10 (Ar-CH), 143.69 (Ar-CH), 141.03 (Ar-CH), 139.28 (Ar-CH), 138.28 (Ar-CH), 137.49 (Ar-CH), 134.02 (Ar-CH), 133.43 (Ar-CH), 133.12 (Ar-CH), 132.41 (Ar-CH), 132.29 (Ar-CH), 131.98 (Ar-CH), 131.58 (Ar-CH), 131.23 (Ar-CH), 130.95 (Ar-CH), 130.58 (Ar-CH), 130.46 (Ar-CH), 129.18 (Ar-CH), 127.05 (Ar-CH), 125.15 (Ar-CH), 122.90 (Ar-CH), 96.09, 35.54 (CH₂), 34.91 (CH₂), 33.23 (CH₂), 31.50 (CH₂), 30.23 (CH), 30.20 (CH), 26.65 (CH₃), 25.82 (CH₃), 23.33 (CH₃), 22.09 (CH₃); **¹⁹F-NMR** (CD₂Cl₂, 565 MHz, 298 K): -78.54 (s, OTf); **¹⁵N-NMR** (CD₂Cl₂, 60.8 MHz, 298 K): -165.2; **HR-MS-ESI(+)** calc. for [C₄₂H₄₂N⁺][M]⁺ 560.3317; found 560.3322; **EA** calc. for [C₄₃H₄₂F₃NO₃S] C, 72.76; H, 5.96; N, 1.97; found C: 72.8; H: 6.2; N: 1.9.

Synthesis of 3

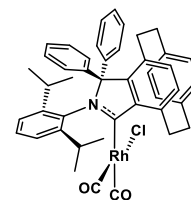


(HiPC)(OTf) (**2**) (200 mg, 0.28 mmol, 1.00 equiv.) and Se (50 mg, 0.63 mmol, 2.25 equiv.) in THF were stirred at -78 °C for 20 mins. Subsequently, a solution of KHMDS (59 mg, 0.30 mmol, 1.05 equiv.) in 5 mL THF was added to the mixture and stirred for 24 hrs. The solvent was removed under reduced pressure and the crude was brought inside the glovebox, dissolved in DCM, and filtered over basic aluminium oxide. Evaporation of the filtrate yielded a yellow powder which was washed with n-pentane (60 mg, 0.05 mmol, 19%). Crystals were obtained by dissolving the powder in DCM and slowly diffusing n-pentane at -35 °C.

¹H-NMR (CD₂Cl₂, 600 MHz, 298 K): 7.79 (d, J = 7.5 Hz, 2H, NH), 7.69 – 7.66 (m, 2H, Ar-H), 7.55 (td, J = 7.4, 1.8 Hz, 2H, Ar-H), 7.45 – 7.39 (m, 4H, Ar-H), 7.35 – 7.29 (m, 4H, Ar-H), 7.22 (t, J = 7.7 Hz, 2H, Ar-H), 7.18 (ddd, J = 8.3, 6.6, 1.3 Hz, 2H, Ar-H), 7.14 – 7.06 (m, 2H, Ar-H), 7.00 (dd, J = 7.7, 1.6 Hz, 2H, Ar-H), 6.91 (ddd, J = 8.6, 6.6, 1.3 Hz, 2H, Ar-H), 6.68 (dd, J = 8.1, 1.8 Hz, 2H, Ar-H), 6.63 (s, 2H, Ar-H), 6.51 (dd, J = 8.2, 1.9 Hz, 2H, Ar-H), 6.16 (dd, J =

7.4, 1.8 Hz, 2H, Ar-H), 5.75 (dd, J = 7.4, 1.9 Hz, 2H, CH(sp²)), 5.74 – 5.71 (m, 2H, Ar-H), 5.26 (dt, J = 4.4, 1.8 Hz, 2H), 4.05 (h, J = 6.9 Hz, 2H), 3.69 – 3.60 (m, 4H), 2.57 – 2.53 (m, 2H, CH(sp³)), 2.52 (dd, J = 4.7, 2.3 Hz, 2H), 2.38 (dd, J = 13.2, 9.2 Hz, 2H), 2.14 – 2.07 (m, 2H), 1.60 – 1.55 (m, 2H), 1.48 (d, J = 6.8 Hz, 6H), 1.39 (d, J = 6.8 Hz, 6H), 1.37 – 1.32 (m, 2H), 1.02 (d, J = 6.8 Hz, 6H), 0.02 (d, J = 6.6 Hz, 6H); **¹³C {¹H} NMR** (CD₂Cl₂, 151 MHz, 298 K): 145.17 (Ar-CH), 144.78 (Ar-CH), 141.21 (Ar-CH), 140.74 (Ar-CH), 140.57 (Ar-CH), 140.10 (Ar-CH), 139.58 (Ar-CH), 138.63 (Ar-CH), 137.39 (Ar-CH), 134.37 (Ar-CH), 134.11 (Ar-CH), 134.04 (Ar-CH), 132.97 (Ar-CH), 131.61 (Ar-CH), 131.04 (Ar-CH), 131.02 (Ar-CH), 130.44 (Ar-CH), 128.75 (Ar-CH), 128.01 (Ar-CH), 127.53 (Ar-CH), 127.50 (Ar-CH), 126.98 (Ar-CH), 126.14 (Ar-CH), 126.07 (Ar-CH), 125.87 (Ar-CH), 125.72 (Ar-CH), 125.48 (Ar-CH), 124.85 (Ar-CH), 123.99 (Ar-CH), 123.20 (Ar-CH), 123.00 (Ar-CH), 117.16 (CH, sp²), 50.41 (CH₂), 38.10 (CH, sp³), 36.43 (CH₂), 32.55 (CH₂), 29.65 (CH, dipp), 27.93 (CH, dipp), 26.56 (CH₃), 24.62 (CH₃), 22.88 (CH₃), 21.88 (CH₃); **HR-MS-ESI(+)** calc. (for monomeric unit) C₆₂H₄₄N⁺[M+H]⁺ 559.3238; found 559.3228; **EA** calc. for [C₆₈H₈₀N₂] C, 90.28; H, 7.22; N, 2.51; found C: 88.2; H: 7.2; N: 2.5.

Synthesis of 4



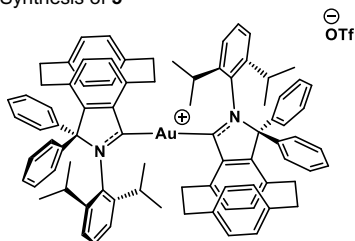
(HiPC)(OTf) (**2**) (180 mg, 0.25 mmol, 2.00 equiv.) and Rh₂Cl₂(CO)₄ (50 mg, 0.13 mmol, 1.02 equiv.) in THF were stirred at -78 °C for 20 mins. Subsequently, a solution of KHMDS (53 mg, 0.27 mmol, 2.10 equiv.) in 5 mL THF was added to the mixture and stirred for 48 hrs. The solvent was removed under reduced pressure and the crude product was subjected to column chromatography (DCM/EtOAc). The brown oil was brought inside the glovebox and was dissolved in 10 mL n-pentane and kept at -35 °C for 24 hours. The solution was filtered and solvent was removed, yielding a yellow powder (35 mg, 0.05 mmol, 37%). Crystals were grown by dissolving the powder in DCM and layering with an excess of n-pentane at -35 °C.

The product was kept inside the glovebox.

¹H-NMR (d₈-THF, 600 MHz, 298 K): 7.87 (d, J = 7.5 Hz, 1H, Ar-H), 7.70 (dd, J = 8.6, 1.3 Hz, 1H, Ar-H), 7.57 (td, J = 7.5, 1.5 Hz, 1H, Ar-H), 7.44 (tt, J = 7.5, 1.3 Hz, 1H, Ar-H), 7.40 (td, J = 7.8, 1.4 Hz, 2H, Ar-H), 7.32 (dd, J = 7.8, 1.6 Hz, 1H, Ar-H), 7.24 – 7.19 (m, 1H, Ar-H), 7.17 (ddt, J = 7.3, 3.4, 1.4 Hz, 2H, Ar-H), 7.05 (dd, J = 7.7, 1.6 Hz, 1H, Ar-H), 6.91 (ddd, J = 8.6, 6.6, 1.3 Hz, 1H, Ar-H), 6.80 (s, 1H, Ar-H), 6.71 (dd, J = 8.0, 1.8 Hz, 1H, Ar-H), 6.52 (dd, J = 8.2, 1.8 Hz, 1H, Ar-H), 6.17 (dd, J = 7.4, 1.8 Hz, 1H, Ar-H), 5.85 – 5.79 (m, 2H, Ar-H), 5.37 (dt, J = 4.3, 1.7 Hz, 1H, Ar-H), 4.14 (p, J = 6.8 Hz, 1H), 2.67 (p, J = 6.9 Hz, 1H), 2.64 – 2.60 (m, 1H), 2.42 – 2.35 (m, 1H), 2.19 (dd, J = 13.1, 9.3 Hz, 1H), 1.61 – 1.56 (m, 1H), 1.51 (d, J = 6.8 Hz, 3H), 1.46 (d, J = 5.5 Hz, 1H), 1.41 (d, J = 6.8 Hz, 3H), 1.39 – 1.37 (m, 1H), 1.36 (d, J = 5.9 Hz, 2H), 1.09 (d, J = 6.8 Hz, 3H), 0.10 (d, J = 6.7 Hz, 3H); **¹³C {¹H} NMR** (d₈-THF, 151 MHz, 298 K): 244.63 (d, ¹J_{CRh} = 39.2 Hz, CRh), 188.13 (d, ¹J_{CRh} = 51.2 Hz, RhCO), 185.94 (d, ¹J_{CRh} = 77.1 Hz, RhCO), 149.79 (Ar-CH), 148.45 (Ar-CH), 148.05 (Ar-CH), 147.92 (Ar-CH), 145.67 (Ar-CH), 143.61 (Ar-CH), 142.09 (Ar-CH), 139.81 (Ar-CH), 138.70 (Ar-CH), 138.35 (Ar-CH), 137.31 (Ar-CH), 134.71 (Ar-CH), 134.55 (Ar-CH), 133.87 (Ar-CH), 133.03 (Ar-CH), 132.65 (Ar-CH), 131.88 (Ar-CH), 129.82 (Ar-CH), 129.29 (Ar-CH), 128.86 (Ar-CH),

127.62 (Ar-CH), 127.22 (Ar-CH), 126.00 (Ar-CH), 125.28 (Ar-CH), 96.03, 35.85 (CH₂), 35.49 (CH₂), 34.43 (CH₂), 31.86 (CH₂), 31.02 (CH), 30.78 (CH), 27.68 (CH₃), 26.81 (CH₃), 24.07 (CH₃), 22.37(CH₃); **IR (ATR)** [cm⁻¹]: $\tilde{\nu}$ = 2958.11, 2922.91, 2856.49, 2077.28, 1995.53, 1587.21, 1492.10, 1445.93, 1410.56, 1379.46, 1321.40, 1259.31, 1177.91, 1100.87, 1055.33, 800.50, 774.65, 754.87, 742.13, 723.56, 702.54, 675.64, 608.73, 581.77, 513.89, 428.88; **HR-MS-ESI(+)** calc. C₄₄H₄₁NO₂Rh⁺[M-Cl]⁻ 718.2192; found 718.2192; C₄₃H₄₁NORh⁺[M-Cl-CO]⁺ 690.2243; found 690.2240; **EA** calc. for [C₄₄H₄₁ClNO₂Rh] C, 70.07; H, 5.48; N, 1.86; found C: 70.4; H: 5.5; N: 2.0.

Synthesis of 5



(HiPC)(OTf) (**2**) (300 mg, 0.42 mmol, 1.00 equiv.) and AuCl.SMe₂ (124 mg, 0.42 mmol, 1.00 equiv.) in THF were stirred at -78 °C for 20 mins. Subsequently, a solution of KHMDS (89 mg, 0.45 mol, 1.05 equiv.) in 5 mL THF was added to the mixture and stirred for 48 hrs. The solvent was removed under reduced pressure and the crude product was dissolved in DCM and filtered over a PTFE syringe filter. Removing the solvent yielded a yellow powder which was washed with THF (3 x 3 ml) resulting in a white powder (225 mg, 153.52 μmol, 36%).

Dissolving the powder in DCM and slowly diffusing *n*-pentane and cyclohexane mixture at -35 °C provided crystals of (R,S) conformer of the compound **5** crystallized as 1:1 with DCM. ¹H and ¹³C-NMR of this crystalline material show two species were present (a minor one approximately 25%). The crystals were then dissolved in a mixture of DCM and 1,2-Difluorobenzene and slowly diffusing *n*-pentane provided crystals of (R,R) conformer (with (S,S) conformer present in the unit cell) of the compound **5**. Although, ¹H and ¹³C-NMR of this batch also show the presence of both (R,S) and (R,R) conformers. Further this crystalline mixture was also subjected to column chromatography but individual conformers isolation was not possible.

The crystalline mixture in solid state is stable under ambient conditions.

¹H-NMR of major conformer (CD₂Cl₂, 600 MHz, 298 K): 7.82 – 7.72 (m, 1H, Ar-H), 7.54 (d, *J* = 7.8 Hz, 2H, Ar-H), 7.52 (s, 2H, Ar-H), 7.51 (d, *J* = 1.8 Hz, 2H, Ar-H), 7.50 (d, *J* = 1.2 Hz, 2H, Ar-H), 7.48 – 7.45 (m, 2H, Ar-H), 7.40 – 7.38 (m, 2H, Ar-H), 7.38 – 7.36 (m, 1H, Ar-H), 7.33 (dd, *J* = 7.5, 1.9 Hz, 1H, Ar-H), 7.32 – 7.30 (m, 2H, Ar-H), 7.27 – 7.21 (m, 1H, Ar-H), 7.04 (ddd, *J* = 7.6, 4.8, 2.8 Hz, 1H, Ar-H), 6.98 (ddt, *J* = 7.2, 5.2, 2.1 Hz, 4H, Ar-H), 6.94 (dd, *J* = 7.5, 1.8 Hz, 2H, Ar-H), 6.92 – 6.89 (m, 1H, Ar-H), 6.75 (d, *J* = 1.2 Hz, 4H, Ar-H), 6.45 (dd, *J* = 7.6, 0.9 Hz, 2H, Ar-H), 6.36 (d, *J* = 7.7 Hz, 2H, Ar-H), 6.32 – 6.27 (m, 1H, Ar-H), 5.79 (d, *J* = 8.0 Hz, 1H, Ar-H), 5.32 – 5.29 (m, 2H, Ar-H), 4.33 (d, *J* = 8.1 Hz, 2H), 3.66 (p, *J* = 6.9 Hz, 2H), 2.93 (dd, *J* = 13.8, 10.7 Hz, 2H), 2.77 (dd, *J* = 9.5, 5.3 Hz, 4H), 2.68 – 2.64 (m, 4H), 2.51 – 2.47 (m, 2H), 2.42 (ddd, *J* = 12.5, 10.0, 1.8 Hz, 2H), 1.88 (d, *J* = 6.8 Hz, 6H), 1.10 (p, *J* = 6.6 Hz, 2H), 0.93 (d, *J* = 6.7 Hz, 6H), 0.63 (d, *J* = 6.7 Hz, 6H), -0.10 (d, *J* = 6.5 Hz, 6H); **¹³C {¹H} NMR** of major conformer (CD₂Cl₂, 126 MHz, 298 K): 229.76 (CCu), 149.37 (Ar-CH),

145.51 (Ar-CH), 145.05 (Ar-CH), 144.32 (Ar-CH), 139.70 (Ar-CH), 139.39 (Ar-CH), 136.03 (Ar-CH), 135.59 (Ar-CH), 133.10 (Ar-CH), 132.78 (Ar-CH), 131.97 (Ar-CH), 131.73 (Ar-CH), 131.41 (Ar-CH), 131.07 (Ar-CH), 130.66 (Ar-CH), 130.31 (Ar-CH), 129.70 (Ar-CH), 129.53 (Ar-CH), 129.42 (Ar-CH), 128.78 (Ar-CH), 127.61 (Ar-CH), 127.38 (Ar-CH), 126.26 (Ar-CH), 125.08 (Ar-CH), 95.50, 36.60 (CH₂), 34.33 (CH₂), 33.20 (CH₂), 30.80 (CH₂), 30.69 (CH), 29.68 (CH), 26.76 (CH₃), 26.14 (CH₃), 22.60 (CH₃), 21.77 (CH₃); **¹⁹F-NMR** (CD₂Cl₂, 565 MHz, 298 K): -78.89 (s, OTf); **HR-MS-ESI(+)** calc. C₈₄H₈₂AuN₂⁺[M]⁺ 1315.61; found 1315.6095; **EA** calc. for [C₈₅H₈₂AuF₃N₂O₃S.CH₂Cl₂] C, 66.62; H, 5.46; N, 1.81; found C: 66.3; H: 5.4; N: 1.8.

[2+2] cycloaddition of (E,E')-dicinnamyl ether

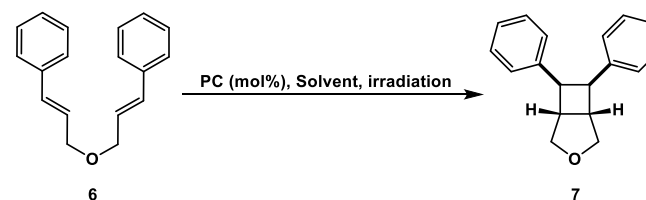


Table S1. Photocatalysis reaction details.

Conditions	Conversion	Duration
No light and no catalyst	0	2 h
No catalyst	0	2 h
No light	0	2 h
[Au(iPC) ₂] ⁺ OTf ⁻ (1 mol%)	100	2 h
[Au(iPC) ₂] ⁺ OTf ⁻ (5 mol%)	100	2 h

In a J. Young's NMR tube, ((1*E*,1'*E*)-oxybis(prop-1-ene-3,1-diyl))dibenzene (**6**) (20 mg, 79.9 μmol, 1 equiv.) and Au⁺-(iPC)₂(OTf) **5** (1 mg, 1 mol%) were dissolved in DCM (0.1 M) inside the glovebox. The tube was bought outside and was sonicated in an ultrasonic bath for 30 minutes. Later it was brought inside the UV chamber/box and irradiated at 405 nm (2W LED). The conversion from **6** to **7** was completed in 2 hours and was monitored via ¹H-NMR. No conversion could be found in the absence of **5** or light or both.

¹H-NMR (CD₂Cl₂, 600 MHz, 298 K): 7.12 – 7.04 (m, 4H), 7.03 – 6.96 (m, 6H), 4.06 (d, *J* = 9.8 Hz, 2H), 3.74 (d, *J* = 4.4 Hz, 2H), 3.70 – 3.66 (m, 2H), 3.33 – 3.28 (m, 2H); **¹³C {¹H} NMR** (CD₂Cl₂, 151 MHz, 298 K): 141.58, 128.58, 127.98, 125.83, 74.19, 47.64, 42.62.

3. NMR spectra

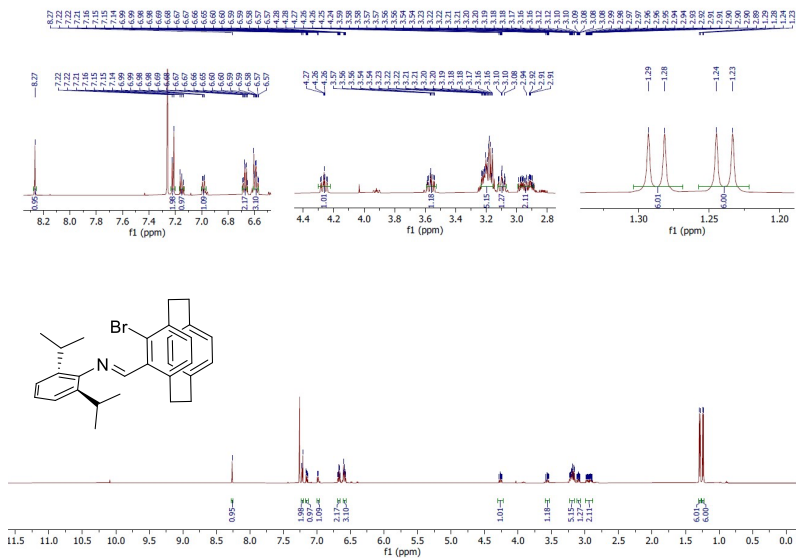


Figure S1. ¹H-NMR (600 MHz, CDCl₃, 298 K) of 1.

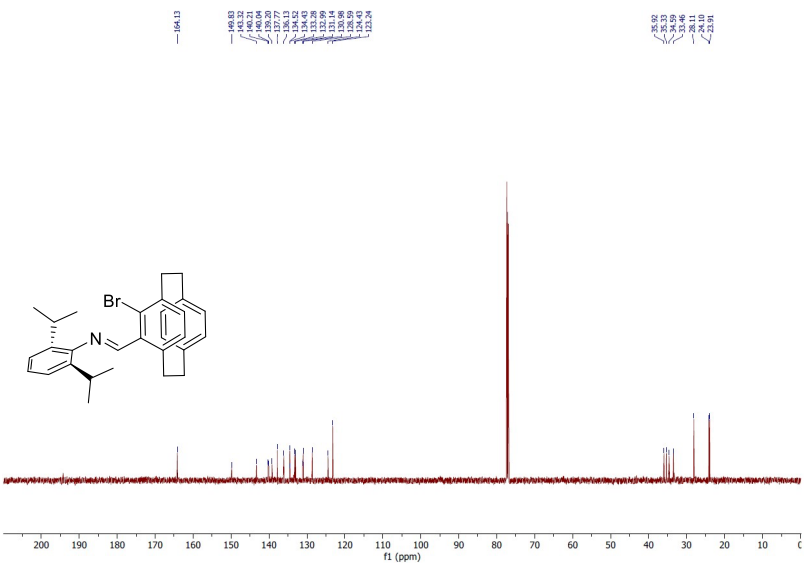


Figure S2. ¹³C-NMR (151 MHz, CDCl₃, 298 K) of 1.

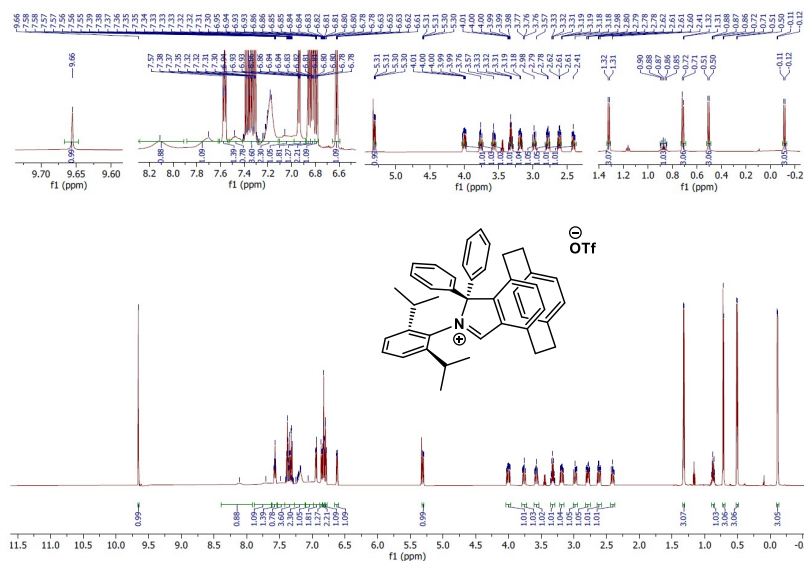


Figure S3. ¹H-NMR (600 MHz, CD₂Cl₂, 298 K) of 2.

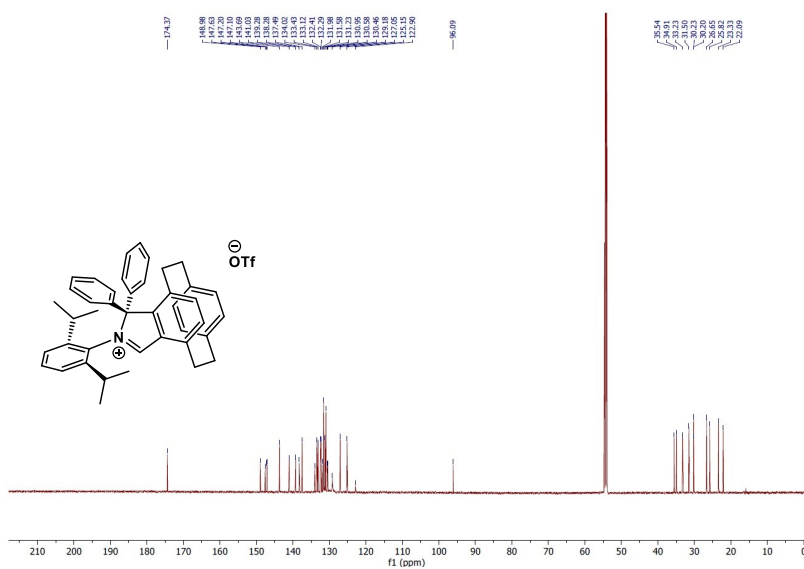


Figure S4. ¹³C-NMR (151 MHz, CD₂Cl₂, 298 K) of 2.

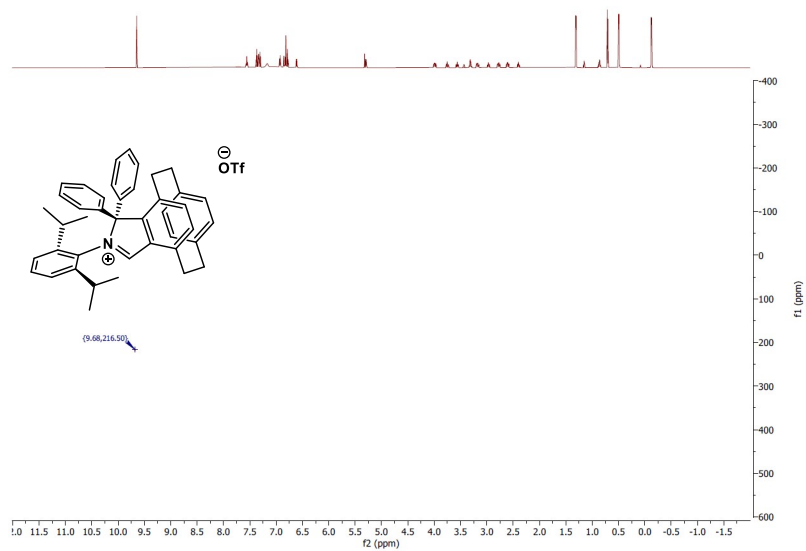


Figure S5. $^1\text{H}/^{15}\text{N}$ HMBC (600/60.8 MHz, CD_2Cl_2 , 298 K) of **2**.

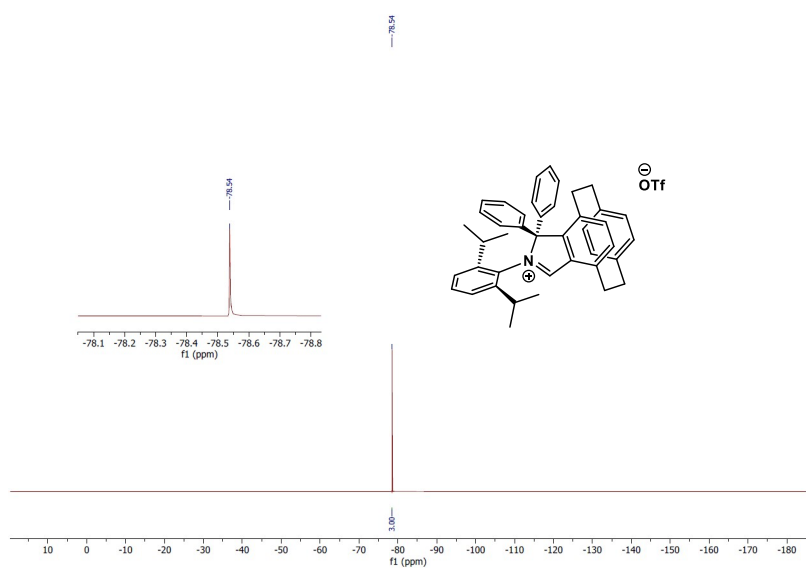


Figure S6. ^{19}F -NMR (565 MHz, CD_2Cl_2 , 298 K) of **2**.

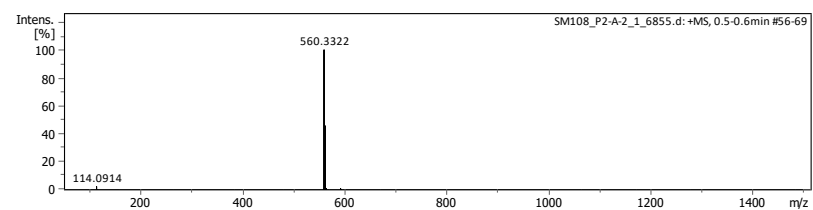


Figure S7. HR-MS-ESI of **2**.

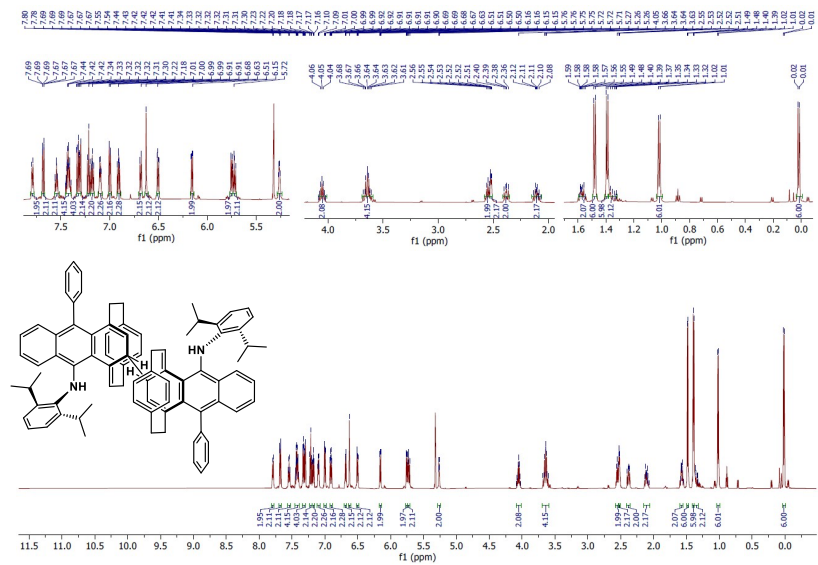


Figure S8. ^1H -NMR (600 MHz, CD_2Cl_2 , 298 K) of **3**.

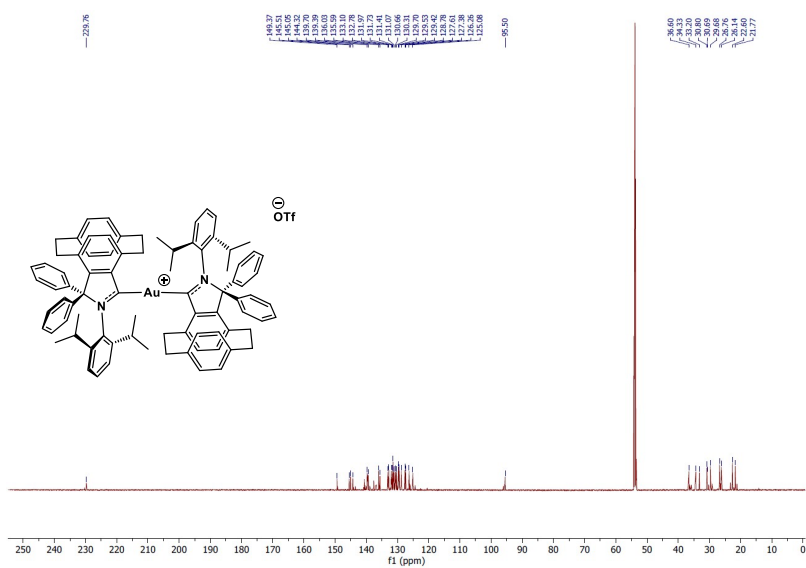


Figure S17. ^{13}C -NMR (151 MHz, CD_2Cl_2 , 298 K) of 5 (major conformer).

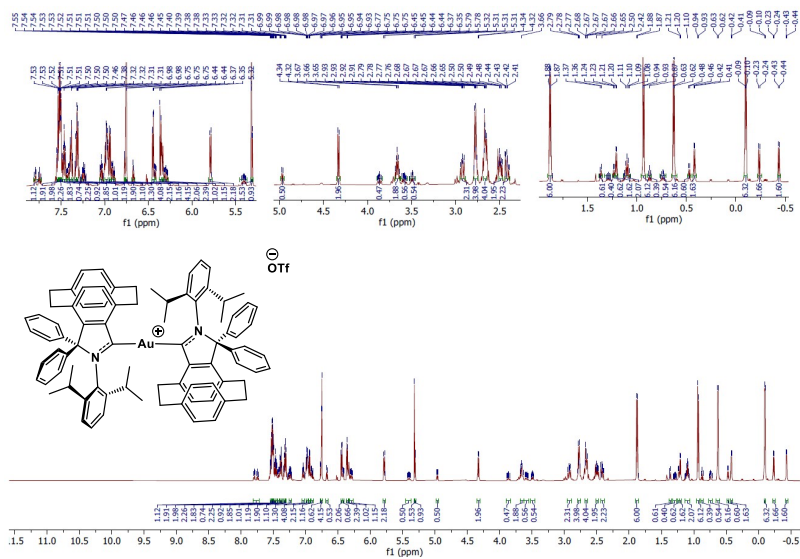


Figure S18. ^1H -NMR (600 MHz, CD_2Cl_2 , 298 K) of 5 (Both conformers; minor one ~ 25%).

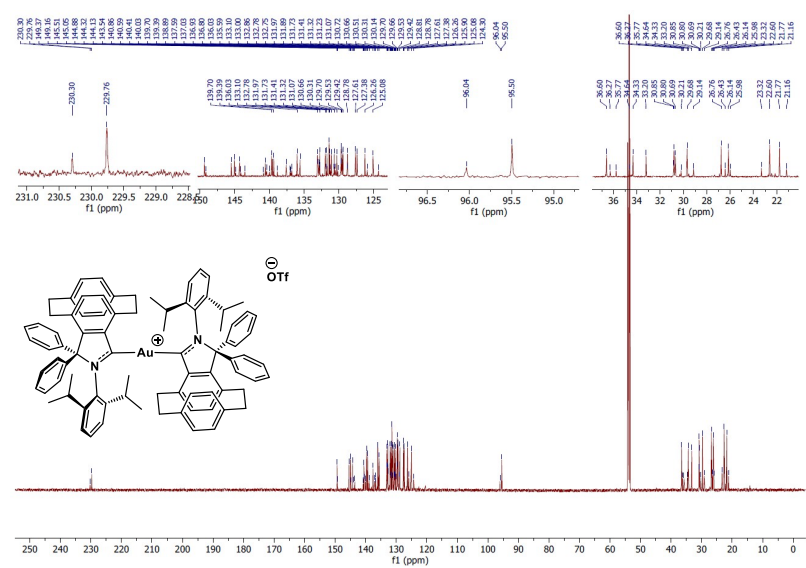


Figure S19. ^{13}C -NMR (151 MHz, CD_2Cl_2 , 298 K) of 5 (Both conformers; minor one ~ 25%).

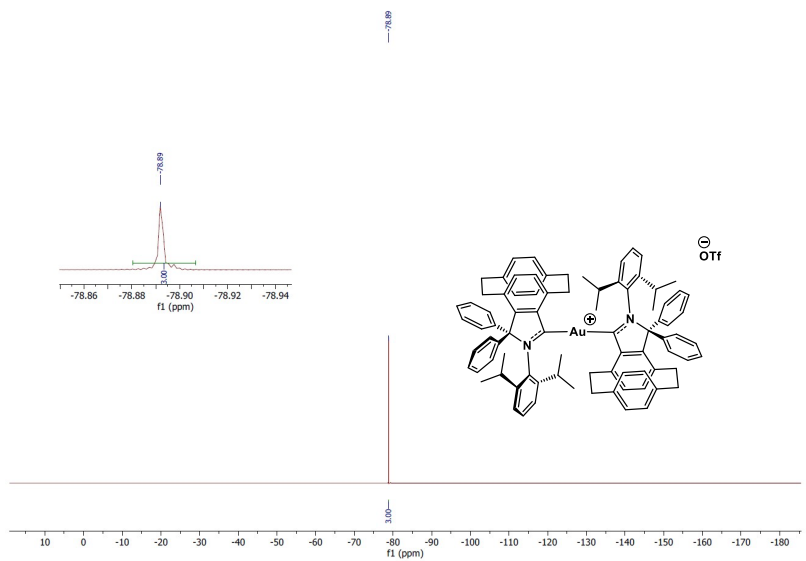


Figure S20. ^{19}F -NMR (565 MHz, CD_2Cl_2 , 298 K) of 5 (both conformers mixture).

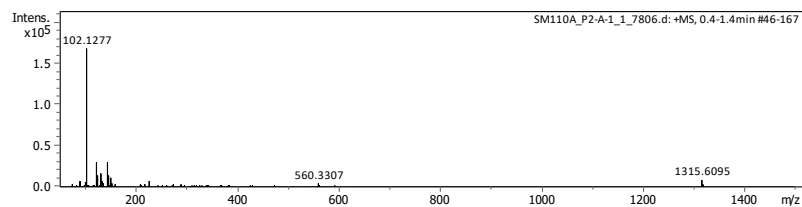


Figure S21. HR-MS-ESI of 5 (both conformers mixture).

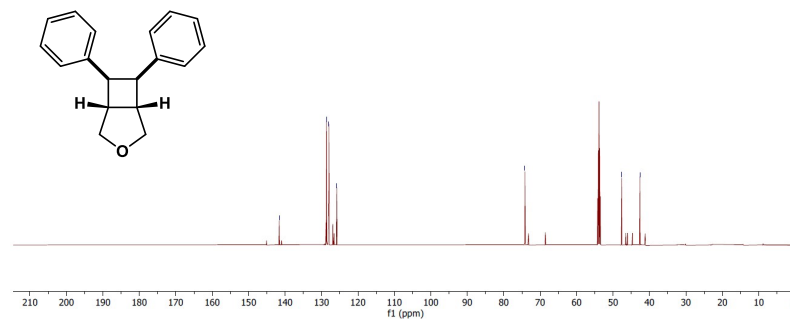


Figure S23. ¹³C-NMR (151 MHz, CD₂Cl₂, 298 K) of 7 (after 2 hours).

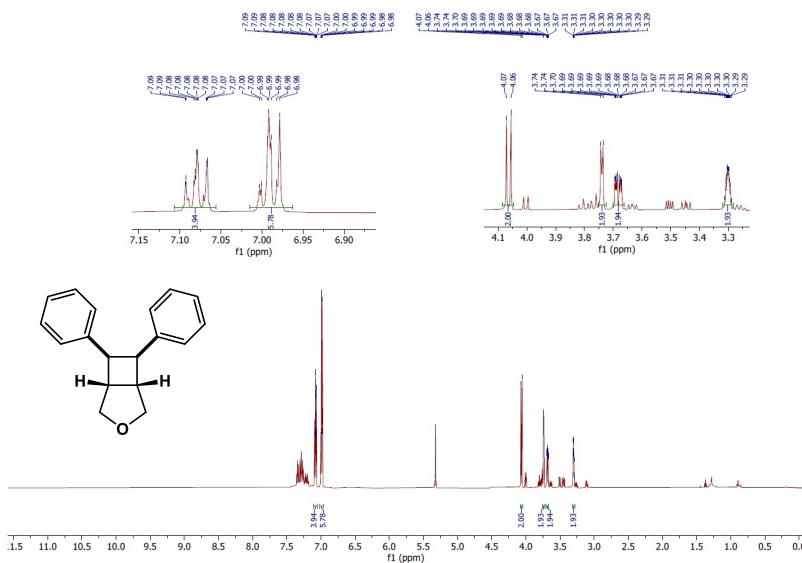


Figure S22. ¹H-NMR (600 MHz, CD₂Cl₂, 298 K) of 7 (after 2 hours).

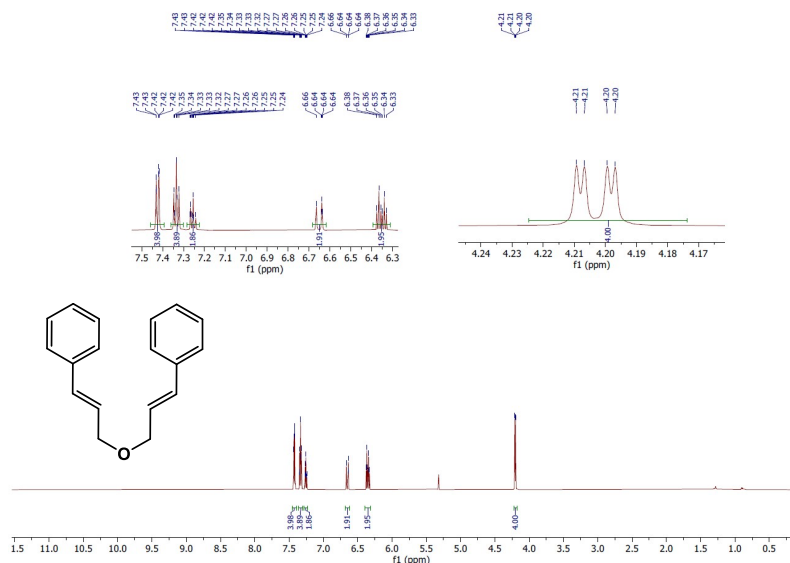


Figure S24. ¹H-NMR (600 MHz, CD₂Cl₂, 298 K) of 6 (no light and no catalyst).

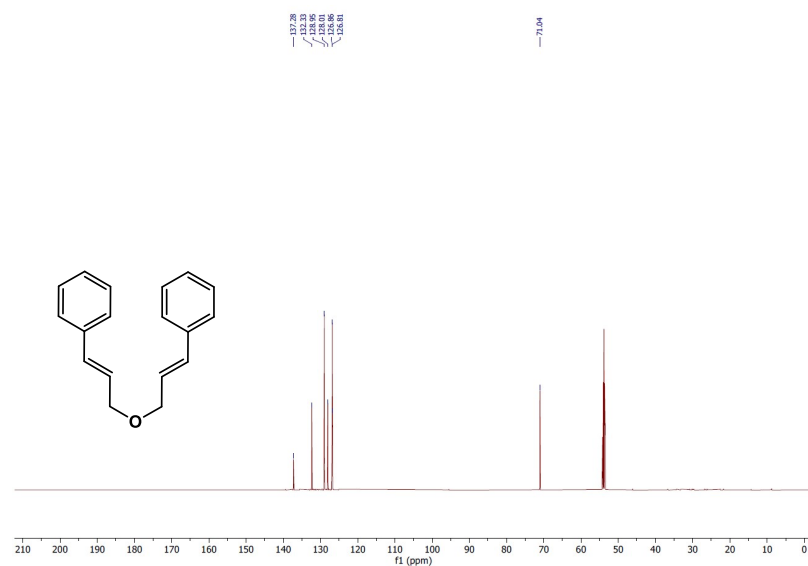


Figure S29. ¹³C-NMR (151 MHz, CD₂Cl₂, 298 K) of **6** (no catalyst).

4. X-ray characterization data

General part

X-ray diffraction determination

The crystals of **6–9** were immersed in a film of NVH or perfluoropolyether oil, mounted on a polyimide microloop (MiTeGen) and transferred to a stream of cold nitrogen (Bruker Kryoflex2), and measured at a temperature of 100 K. The X-ray diffraction data were collected on a Bruker D8 diffractometer with a CMOS Photon 100 and multilayer optics monochromated MoK α (0.71073Å) radiation (INCOATEC microfocus sealed tube). The frames were integrated with the Bruker SAINT software package using a narrow-frame algorithm. The APEX3 v2018.7-0 program package was used for cell refinements and data reductions. The structure was solved using the intrinsic phasing method,^[4] refined and visualized with the OLEX2-1.5 program.^[5] A semiempirical absorption correction (SADABS) was applied to all data. All non-hydrogen atoms were refined anisotropically. Hydrogen atoms were included in structure factors calculations. All Hydrogen atoms were assigned to idealized geometric positions. The unit cells of the **2** contain disordered solvent molecules which have been treated as a diffuse contribution to the overall scattering without specific atom positions by SQUEEZE/PLATON.^[6] The crystallographic details are summarized in Table 1. CCDC **2271625–2271627** and **2349442** (R,S-conformer) contains the supplementary crystallographic data for this paper.

The crystal quality of **5** (R,R-conformer) was sufficient to confirm the connectivity.

X-ray Structures

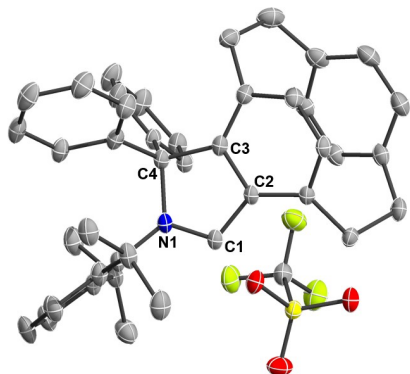


Figure S30. X-ray solid-state structure of **2 (S-isomer)**. Thermal ellipsoids were drawn at the 50% probability level; H atoms, solvent molecule and R-isomer have been omitted for clarity. Selected bond lengths (Å) and angles [deg]: C1-C2 1.423(2), C2-C3 1.414(2), C3-C4 1.528(3), C4-N1 1.541(2), N1-C1 1.305(2), C2-C1-N1 112.6(1).

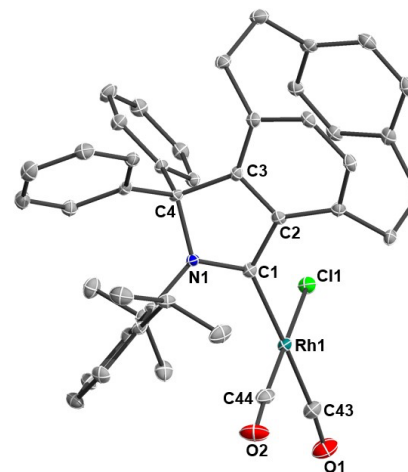


Figure S32. X-ray solid-state structure of **4 (S-isomer)**. Thermal ellipsoids were drawn at the 50% probability level; H atoms, solvent molecule and R-isomer have been omitted for clarity. Selected bond lengths (Å) and angles [deg]: C1-C2 1.463(4), C2-C3 1.414(3), C3-C4 1.533(3), C4-N1 1.543(3), N1-C1 1.331(3), Rh1-C1 2.078(3), Rh1-C11 2.3682(8), Rh1-C43 1.914(3), Rh1-C44 1.833(3), C2-C1-N1 107.0(2), C1-Rh1-C43 172.3(1), C1-Rh1-C44 97.4(1), C1-Rh1-C11 86.94(8), C43-Rh1-C44 86.99(9), C43-Rh1-C44 88.4(1).

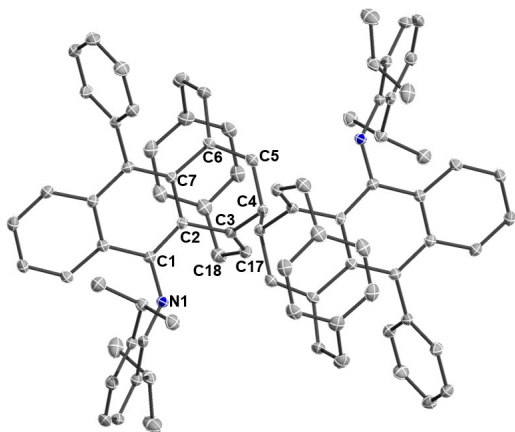


Figure S31. X-ray solid-state structure of **3**. Thermal ellipsoids were drawn at the 50% probability level; H atoms and solvent molecules have been omitted for clarity. Selected bond lengths (Å) and angles [deg]: C4-C4 1.548(2), C4-C3 1.509(2), C3-C2 1.486(2), C3-C17 1.343(2), C17-C18 1.529(2), C1-N1 1.393(2), C2-C3-C4 112.0(1), C3-C17-C18 126.4(1).

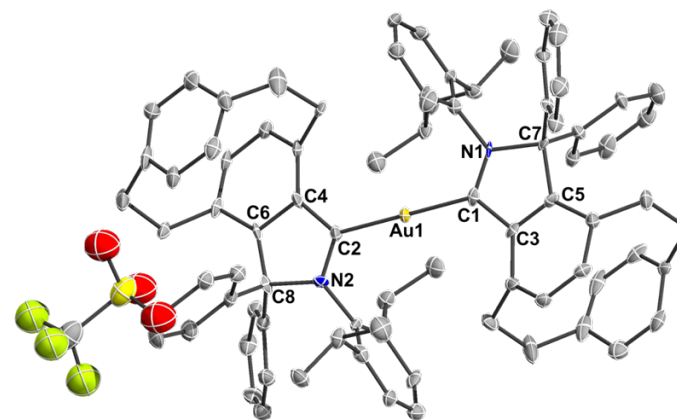


Figure S33. X-ray solid-state structure of **5 (R,S-conformer)**. Thermal ellipsoids were drawn at the 50% probability level; H atoms and solvent molecule have been omitted for clarity. Selected bond lengths (Å) and angles [deg]: C1-C3 1.46(1), C3-C5 1.38(2), C5-C7 1.55(1), C7-N1 1.54(2), N1-C1 1.30(1), C1-Au1 2.03(1), C3-C1-N1 106.3(8), C1-Au1-C2 179.5(4).

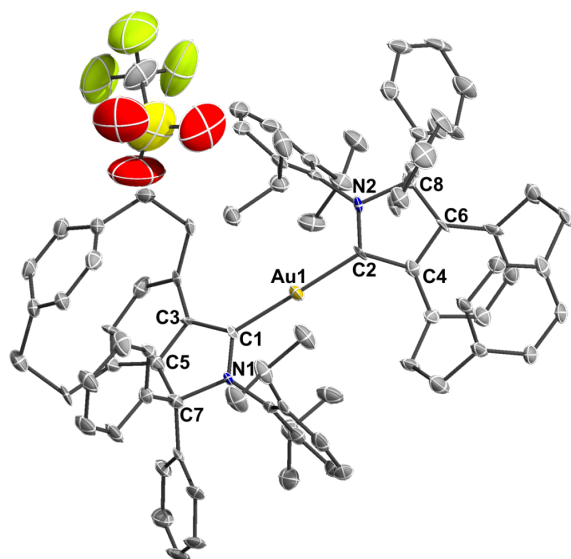


Figure S34. X-ray solid-state structure of **5 (R,R-conformer)**. Thermal ellipsoids were drawn at the 50% probability level; H atoms, solvent molecule and S,S-conformer have been omitted for clarity. Selected bond lengths (Å) and angles [deg]: C1-C3 1.45(1), C3-C5 1.42(2), C5-C7 1.52(1), C7-N1 1.55(1), N1-C1 1.34(4), C1-Au1 2.025(9), C3-C1-N1 108.2(8), C1-Au1-C2 179.2(4).

Table S2. Crystal data and structure refinement for **2–5 (R,S-conformer)**.

Identification code	2	3	4	5 (R,S-conformer)
CCDC number	2271625	2271626	2271627	2349442
Empirical formula	C ₄₃ H ₄₂ F ₃ NO ₃ S	C ₄₄ H ₄₄ Cl ₄ N	C ₄₅ H ₄₃ Cl ₃ NO ₂ Rh	C ₈₆ H ₈₄ AuCl ₂ F ₃ N ₂ O ₃ S
Formula weight	709.83	728.60	839.06	1551.47
Temperature/K	100.00	100.00	100.00	100.00
Crystal system	monoclinic	monoclinic	triclinic	triclinic
Space group	C2/c	P2 ₁ /c	P-1	P1
a/Å	39.1326(17)	12.3827(3)	10.6973(5)	11.9902(6)
b/Å	11.1427(4)	20.4942(4)	12.2998(5)	12.8137(6)
c/Å	22.6859(8)	14.5949(3)	16.1099(7)	14.3004(6)
α/°	90	90	86.248(2)	64.780(2)
β/°	118.8000(10)	92.8350(10)	72.965(2)	75.969(2)
γ/°	90	90	67.280(2)	89.653(2)
Volume/Å ³	8668.4(6)	3699.27(14)	1866.66(14)	1916.49(16)
Z	8	4	2	1
ρ _{calc} /cm ⁻³	1.088	1.308	1.493	1.343
μ/mm ⁻¹	0.122	0.353	0.713	2.073
F(000)	2992.0	1532.0	864.0	794.0
Crystal size/mm ³	0.13 × 0.096 × 0.088	0.211 × 0.17 × 0.129	0.199 × 0.16 × 0.12	0.11 × 0.08 × 0.06
Radiation	MoKα (λ = 0.71073)			
2θ range for data collection/°	4.618 to 60.086	3.846 to 57.99	4.314 to 57.99	5.912 to 60.116
Index ranges	-53 ≤ h ≤ 54, -15 ≤ k ≤ 15, -31 ≤ l ≤ 31	-16 ≤ h ≤ 16, -27 ≤ k ≤ 27, -19 ≤ l ≤ 17	-14 ≤ h ≤ 14, -16 ≤ k ≤ 16, -21 ≤ l ≤ 21	-16 ≤ h ≤ 16, -18 ≤ k ≤ 18, -20 ≤ l ≤ 20
Reflections collected	45418	71443	59397	125977
Independent reflections	12618 [R _{int} = 0.0447, R _{sigma} = 0.0474]	9818 [R _{int} = 0.0633, R _{sigma} = 0.0353]	9911 [R _{int} = 0.0691, R _{sigma} = 0.0466]	22195 [R _{int} = 0.0504, R _{sigma} = 0.0345]
Data/restraints/parameters	12618/0/464	9818/0/446	9911/0/473	22195/189/843
Goodness-of-fit on F ²	1.034	1.031	1.076	1.072
Final R indexes [I ≥ 2σ(I)]	R ₁ = 0.0514, wR ₂ = 0.1356	R ₁ = 0.0442, wR ₂ = 0.0999	R ₁ = 0.0424, wR ₂ = 0.1035	R ₁ = 0.0353, wR ₂ = 0.0974
Final R indexes [all data]	R ₁ = 0.0696, wR ₂ = 0.1462	R ₁ = 0.0611, wR ₂ = 0.1090	R ₁ = 0.0521, wR ₂ = 0.1091	R ₁ = 0.0357, wR ₂ = 0.0978
Largest diff. peak/hole / e Å ⁻³	0.32/-0.44	0.42/-0.51	1.78/-1.22	1.76/-1.23

^(a) $R_1 = \frac{\sum ||F_o| - |F_c||}{\sum |F_o|}$; $wR_2 = \frac{[\sum w(F_o^2 - F_c^2)^2 / \sum (wF_o^2)^2]}{1/[\sigma^2(F_o^2) + (aP)^2 + bP]}$, where $P = (F_o^2 + 2F_c^2)/3$ ^(b) $Goof = S = \frac{[\sum w(F_o^2 - F_c^2)^2]}{(m-n)^{1/2}}$, where m = number of reflexes and n = number of parameters

Table S3. Crystal data and structure refinement for **5 (R,R-conformer)**.

Identification code	5 (R,R-conformer)
Empirical formula	C ₈₈ H ₈₄ AuF ₄ N ₂ O ₅ S
Formula weight	1522.59
Temperature/K	100.00
Crystal system	triclinic
Space group	P-1
a/Å	14.728(3)
b/Å	15.943(3)
c/Å	16.773(3)
α/°	101.479(6)
β/°	99.532(8)
γ/°	92.547(7)
Volume/Å ³	3794.1(12)
Z	2
ρ _{calc} /cm ⁻³	1.333
μ/mm ⁻¹	2.026
F(000)	1562.0
Crystal size/mm ³	0.07 × 0.06 × 0.03
Radiation	MoKα (λ = 0.71073)
2θ range for data collection/°	3.684 to 66.284
Index ranges	-22 ≤ h ≤ 22, -24 ≤ k ≤ 24, -25 ≤ l ≤ 25
Reflections collected	287458
Independent reflections	28929 [R _{int} = 0.1879, R _{sigma} = 0.1003]
Data/restraints/parameters	28929/329/937
Goodness-of-fit on F ²	1.875
Final R indexes [I>=2σ(I)]	R ₁ = 0.1766, wR ₂ = 0.4416
Final R indexes [all data]	R ₁ = 0.2001, wR ₂ = 0.4575
Largest diff. peak/hole / e Å ⁻³	40.65/-4.24

^(a) $R_1 = \sum ||F_o| - |F_c|| / \sum |F_o|$; $wR_2 = [\sum [w(F_o^2 - F_c^2)^2] / \sum [(wF_o^2)^2]]^{1/2}$; $w = 1/[\sigma^2(F_o^2) + (aP)^2 + bP]$, where $P = (F_o^2 + 2F_c^2)/3$ ^(b) $\text{Goof} = S = [\sum w(F_o^2 - F_c^2)^2 / (m-n)]^{1/2}$, where m = number of reflexes and n = number of parameters

5. IR-spectroscopy

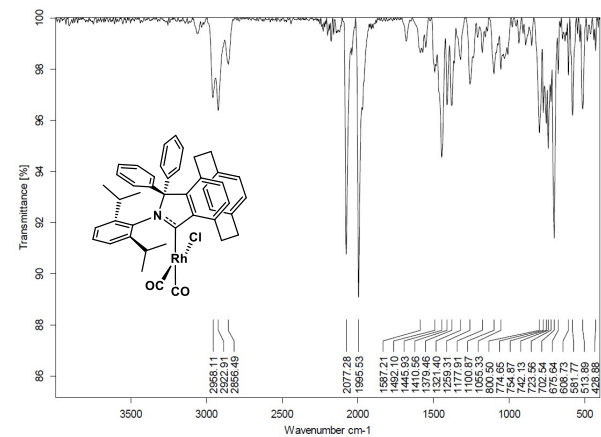


Figure S35. ATR-IR spectrum of **4** (measured as solid).

Table S4. v_{av} and TEP for **4**.

	IR ν (CO)	v_{av} (CO)	TEP [cm ⁻¹]
[RhCl(CO) ₂ (iPC)]	2077/1996	2037	2050

* (TEP = 0.8001 v_{av} + 420 cm⁻¹)

6. Photophysical Measurements

All photophysical measurements were performed in dry and deaerated solutions. The solid-state measurements were performed either in single-crystalline form (sample denoted as 'crystals') or, to remove co-crystallized molecules of solvent, single-crystals were ground and dried under vacuum for 24 h (sample denoted as 'solid'). Optical absorption spectroscopy was performed using an Agilent Cary 5000 spectrophotometer using standard 1 cm path length quartz cells. Excitation and emission spectra were recorded on an Edinburgh Instrument FLS1000 spectrometer, equipped with a 450 W Xenon arc lamp, double monochromators for the excitation and emission pathways, and a red-sensitive photomultiplier (PMT-980) as a detector. The excitation and emission spectra were corrected using the standard corrections supplied by the manufacturer for the excitation source's spectral power and the detector's sensitivity. Quantum yields in solution were measured using an FLS1000 spectrometer equipped with an integrating sphere (N-M01), or Quantaaurus-QY Absolute PL quantum yield spectrometer (C11347- 11 Series: Standard type) from Hamamatsu and the quantum yield of solid samples were measured using an integrating cryosphere (Microstat N2) from Oxford Instruments. The luminescence lifetimes were measured using a μ F2 pulsed 60 W Xenon microsecond flashlamp, with a repetition rate of 100 Hz, and a time-correlated single photon counting (TCSPC) module or EPLED (365 nm with 1.7 μ W), with 50 ns pulse width and an TCSPC module, depending on the time range. The emission was collected at a right angle to the excitation source.

7. UV-Visible Spectroscopy

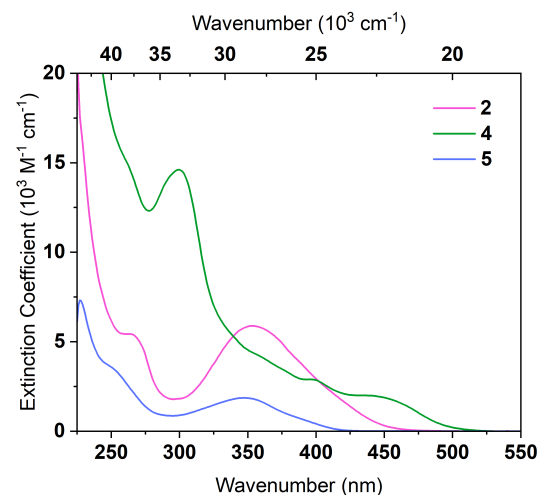


Figure S36. UV-Vis absorption spectra of ligand salt **2**, Rh(I) complex **4** and Au(I) complex **5** in THF.

8. Emission Studies

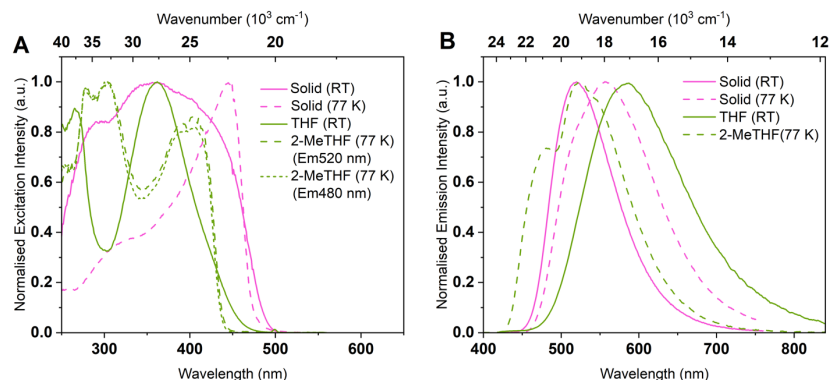


Figure S37. Normalized excitation (A) and emission (B) spectra of ligand salt **2** in grinded Solid (pink) and in THF (green). Solid lines for room temperature measurements and dash/short dash lines for 77 K measurements.

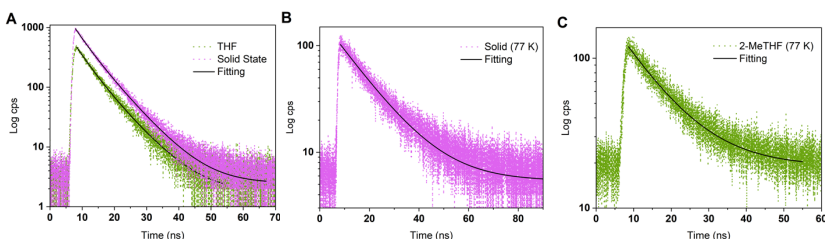


Figure S38. Emission decays of ligand salt **2** (A: Room Temperature, B: Solid 77 K and C: 2-MeTHF 77K).

Table S5. Selected photophysical data of iPC ligand salt **2** at RT.

	Medium	λ_{max} (nm)	τ (ns) ^a	ϕ	k_r (10^5 s^{-1}) ^b
2	Solid (grinded) (RT)	520	3.9 (40.8)/ 7.4 (59.2)	0.32	533
	Solid (grinded) (77 K)	560	13.6 (100)	-	-
	THF	585	3.9 (47.4)/7.7 (52.6)	0.01	17
	2-MeTHF (77 K)	525	10.8 (100)	-	-

(a) For lifetimes fitted with two exponentials, the pre-exponential factors B are given in parentheses. (b) k_r was calculated using amplitude-weighted averaged lifetimes.

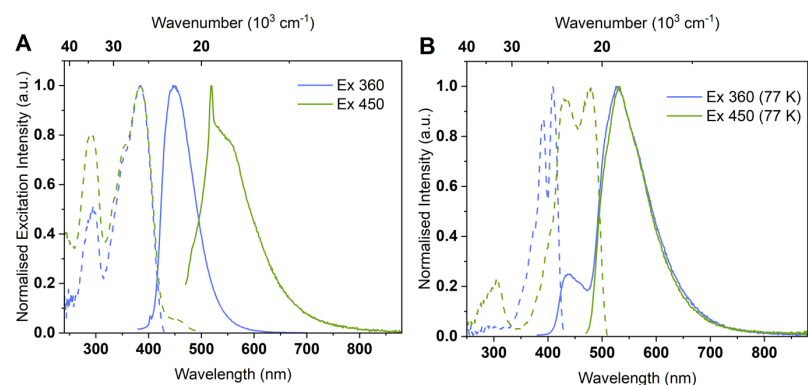


Figure S39. Normalized excitation and emission (A) spectra of Rh(I) complex **4** in THF at room temperature and normalized excitation and emission (B) spectra of Rh(I) complex **4** in 2-MeTHF at 77 K. The sharp peak around 520 nm in (B) is Raman scattering.

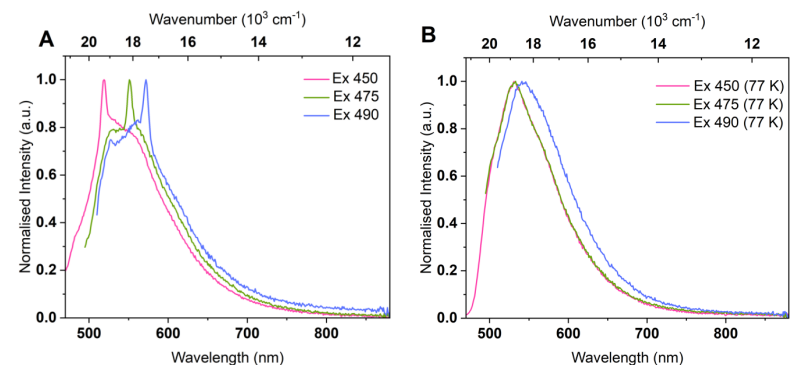


Figure S40. Emission map (A) of Rh(I) complex **4** in THF at room temperature and emission map (B) of Rh(I) complex **4** in 2-MeTHF at 77 K. The sharp peaks around 520, 552 and 572 nm in (A) are Raman scattering.

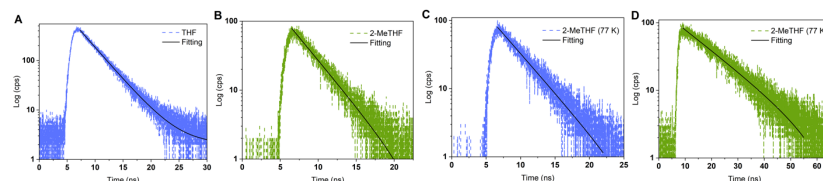


Figure S41. Emission decays of Rh(I) complex **4** at room temperature in THF(A) and in 2-MeTHF (B). Emission decays of Rh(I) complex **4** at 77 K in 2-MeTHF (C and D), ($\lambda_{\text{em}} = 450$ nm, blue; $\lambda_{\text{em}} = 530$ nm, green).

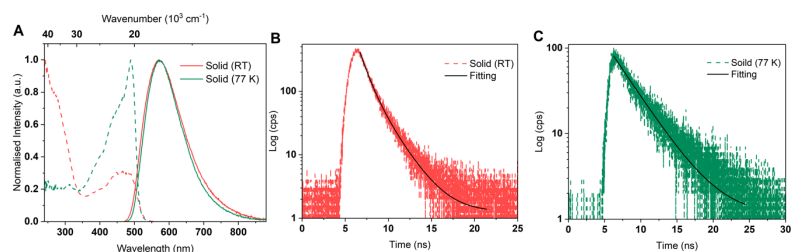


Figure S42. Normalized excitation and emission (A) spectra of Rh(I) complex **4** in solid state at room temperature (red) and at 77 K (green). Emission decays of Rh(I) complex **4** at room temperature (B) and at 77 K (C) in solid state.

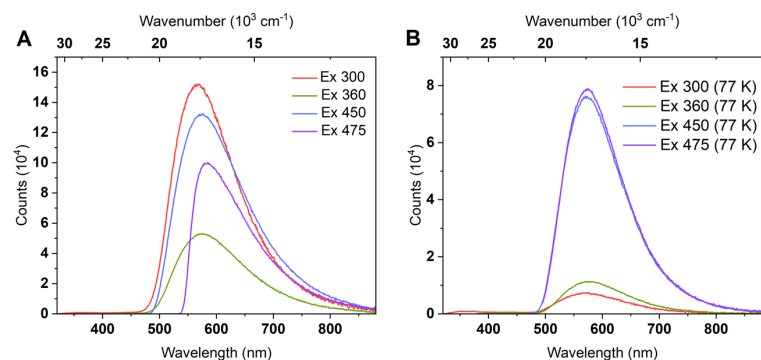


Figure S43. Emission map (A) of Rh(I) complex **4** in solid state at room temperature and emission map (B) of Rh(I) complex **4** in solid state at 77 K.

Table S6. Selected photophysical data of Rh(I) complex **4** at RT.

	Medium	λ_{\max} (nm)	τ (ns) ^a	ϕ	k_r (10^5 s^{-1}) ^b
4	Solid (grinded) (RT)	575	0.8 (64.1)/2.0 (35.9)	-	-
	Solid (grinded) (77 K)	575	3.2	-	-
	THF (RT)	450	3.3	0.026	79
	2-MeTHF (RT)	530	3.3	-	-
	2-MeTHF (77 K)	450	3.7	-	-
	2-MeTHF (77 K)	530	14.4	-	-

(a) For lifetimes fitted with two exponentials, the pre-exponential factors B are given in parentheses. (b) k_r was calculated using amplitude-weighted averaged lifetimes.

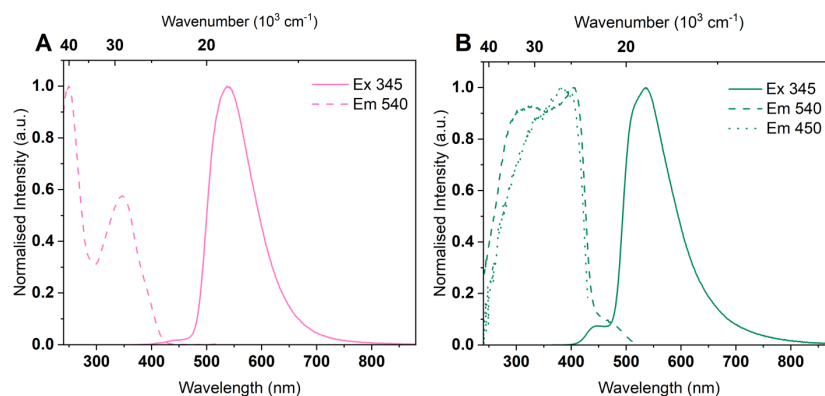


Figure S44. Normalized excitation and emission (A) spectra of Au(I) complex **5** in DCM (pink) and normalized excitation and emission (B) spectra of Au(I) complex **5** in solid state (green).

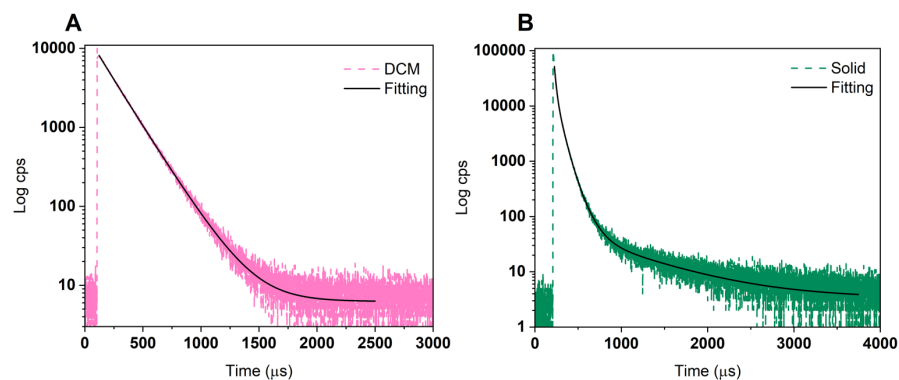


Figure S45. Emission decays of Au(I) complex **5** in DCM ($\lambda_{\text{em}} = 540 \text{ nm}$; pink) and in solid state ($\lambda_{\text{em}} = 540 \text{ nm}$; green).

Table S7. Selected photophysical data of Au(I) complex **5** at RT.

	Medium	λ_{\max} (nm)	τ (μs) ^a	ϕ	k_r (10^5 s^{-1}) ^b
5	Solid (grinded)	535	17.9 (64.6)/57.7 (29.9)/112.6 (5.5)	0.025	0.0071
	DCM	540	172.9 (81.2)/230.4 (18.8)	0.12	0.0065

(a) For lifetimes fitted with two/three exponentials, the pre-exponential factors B are given in parentheses. (b) k_r was calculated using amplitude-weighted averaged lifetimes.

9. Photostability of the Au(I) complex 5

Photostability of the Au(I) complex **5** for the cycloaddition reaction was checked via UV-Visible spectroscopy and $^1\text{H-NMR}$ spectroscopy.

The Au(I) complex **5** (18 mg, 12.22 μmol , 1.02 equiv.) and (E,E')-dicinnamyl ether (3 mg, 11.98 μmol , 1.00 equiv.) were added in 3 mL DCM and stirred for 30 minutes. This reaction mixture was diluted to 6×10^{-5} M and irradiated for 4 hours inside the UV chamber/box. UV-Vis absorption spectra was recorded after every 15 minutes irradiation interval.

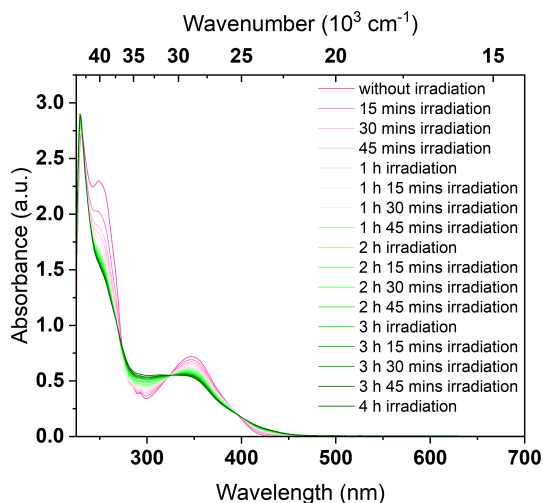


Figure S46. UV-Vis absorption spectra of Au(I) complex **5** and (E,E')-dicinnamyl ether upon irradiation till 4 hours.

Further, Au(I) complex **5** (18 mg, 12.22 μmol , 1.02 equiv.) and (E,E')-dicinnamyl ether (3 mg, 11.98 μmol , 1.00 equiv.) were added in 0.7 mL CD_2Cl_2 and sonicated in an ultrasonic bath for 2 hours. This reaction mixture was irradiated inside a non-optimised setup (self-made dark box without mirrors). $^1\text{H-NMR}$ spectra after every 15 minutes irradiation interval was recorded.

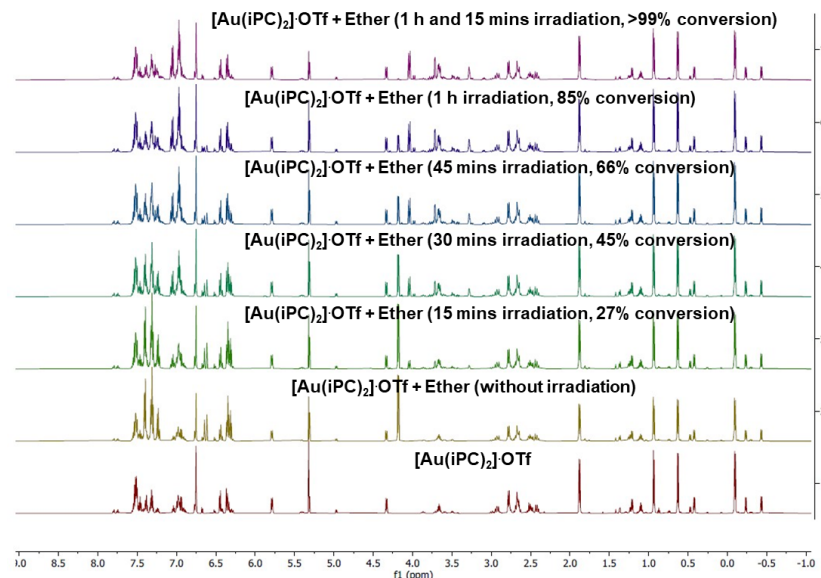


Figure S47. $^1\text{H-NMR}$ spectra of Au(I) complex **5** and (E,E')-dicinnamyl ether upon irradiation till 1 hour and 15 minutes.

From the $^1\text{H-NMR}$, it can be concluded that the Au(I) complex **5** is responsible for the photocatalysis reaction.

10. Steric Properties

Figure S48. Topographic steric map of [(CAArC)CuCl].^[7,8]

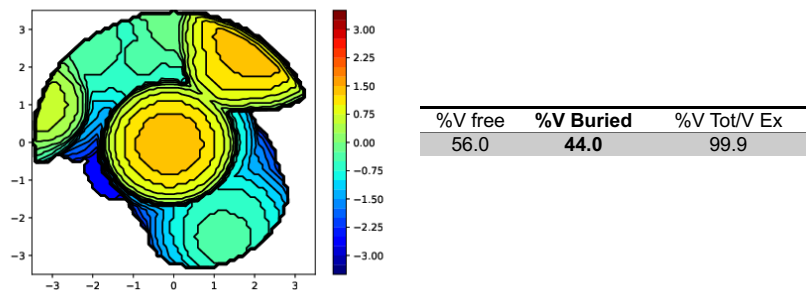


Table S8. Distribution of volume in different quadrants.

Quadrant	V f	V b	V t	%V f	%V b
SW	32.6	12.3	44.9	72.6	27.4
NW	22.1	22.8	44.9	49.2	50.8
NE	18.7	26.2	44.9	41.7	58.3
SE	27.0	17.8	44.9	60.1	39.8

Figure S50. Topographic steric map of ((iPC)₂Au(OTf))₅.

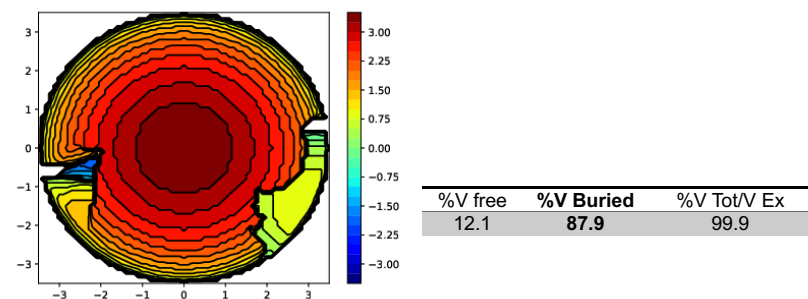


Table S10. Distribution of volume in different quadrants.

Quadrant	V f	V b	V t	%V f	%V b
SW	5.8	39.1	44.9	12.9	87.1
NW	5.1	39.8	44.9	11.3	88.7
NE	5.8	39.1	44.9	12.9	87.1
SE	5.1	39.8	44.9	11.3	88.7

Figure S49. Topographic steric map of [(iPC)CuCl].

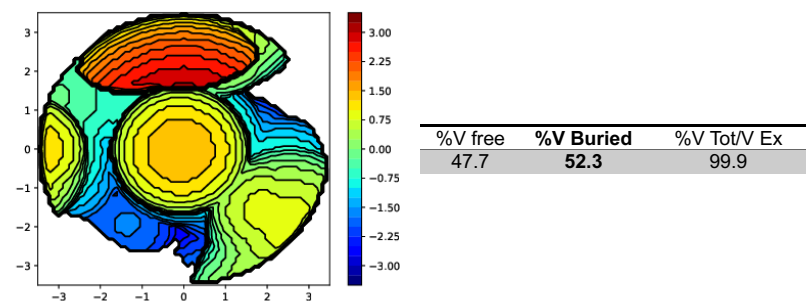


Table S9. Distribution of volume in different quadrants.

Quadrant	V f	V b	V t	%V f	%V b
SW	28.2	16.7	44.9	62.8	37.2
NW	15.9	29.0	44.9	35.4	64.6
NE	22.4	22.5	44.9	49.9	50.1
SE	19.2	25.7	44.9	42.8	57.2

11. TD-DFT calculations

DFT calculations for compounds **2**, **4**, and **5** were performed with the ORCA 5.0.3 software package.^[9] Geometry optimization with tight convergence criteria was carried out using BP86 (**2** and **4**) or PBE0 (**5**) functional^[10] with def2-TZVP basis set^[11] and Grimme-D3BJ empirical dispersion correction.^[12] To accelerate calculations, the SARC/J^[13] auxiliary basis set was used together with RI approximation. Solvents effects (**2** and **4**: CH₂Cl₂, $\epsilon = 9.08$; **5**: THF, $\epsilon = 7.25$) were accounted for by implicit solvent model CPCM.^[14] Relativistic effects were accounted for by employing the ZORA method.^[15] The same level of theory (PBE0 functional for all compounds) was used for TD-DFT calculation of the first 50 (**2** and **4**) and 20 (**5**) singlet and triplet excited states. Electronic transition differences at isovalues of 0.003 were prepared using the orca_plot module as implemented in ORCA 5.0.3. software and USCF Chimera.^[16]

Table S11. Singlet excitations calculated for **2** in the ground state geometry.

State	Energy [cm ⁻¹]	λ [nm]	f _{osc}
1	24431.5	409.3	0.032089823
2	27421.6	364.7	0.072761986
3	29160.8	342.9	0.126504841
4	29399.2	340.1	0.007976549
5	31049.9	322.1	0.004283742
6	31362.9	318.8	0.109700295
7	31944.1	313.0	0.020168068
8	33231.6	300.9	0.018433678
9	34474.7	290.1	0.009580648
10	34895.3	286.6	0.012575773
11	35745.6	279.8	0.004239361
12	37927.3	263.7	0.085877933
13	38093.4	262.5	0.057167441
14	38715.7	258.3	0.006180336
15	39036.2	256.2	0.064414252
16	40070.7	249.6	0.007118958
17	40873.9	244.7	0.008503911
18	41055.6	243.6	0.023247734
19	41150.4	243.0	0.023342632
20	41445.6	241.3	0.028549111
21	41629.1	240.2	0.013464676
22	41800.1	239.2	0.012494774
23	42032.7	237.9	0.060428643
24	42244.5	236.7	0.001820358
25	42495.0	235.3	0.017051980
26	42890.4	233.2	0.018263348
27	43183.3	231.6	0.013721169
28	43411.5	230.4	0.013258856
29	43504.4	229.9	0.012098119
30	43714.1	228.8	0.016861974
31	43741.9	228.6	0.003520980
32	43995.1	227.3	0.009266508
33	44088.7	226.8	0.001004503
34	44350.7	225.5	0.000412968
35	44550.0	224.5	0.032962372
36	44655.9	223.9	0.029262198
37	44731.8	223.6	0.012273937
38	44764.4	223.4	0.003664580
39	44930.5	222.6	0.007498324
40	45009.2	222.2	0.043352204

41	45144.6	221.5	0.000193053
42	45266.6	220.9	0.029813401
43	45389.8	220.3	0.014578411
44	45509.8	219.7	0.011980836
45	45618.5	219.2	0.038223647
46	45676.9	218.9	0.026697122
47	45820.1	218.2	0.024360185
48	45871.7	218.0	0.035980139
49	45934.1	217.7	0.006111596
50	46084.7	217.0	0.010256489

Table S12. Singlet excitations calculated for **4** in the ground state geometry.

State	Energy [cm ⁻¹]	λ [nm]	f _{osc}
1	25216.4	396.6	0.032296818
2	27248.2	367.0	0.014943752
3	28182.6	354.8	0.038879066
4	29351.8	340.7	0.059202151
5	30891.1	323.7	0.015144667
6	31476.9	317.7	0.073893146
7	31597.6	316.5	0.087511557
8	32123.5	311.3	0.000333393
9	32811.8	304.8	0.022832287
10	33363.4	299.7	0.034066371
11	34243.5	292.0	0.006142122
12	34761.5	287.7	0.020630698
13	34939.6	286.2	0.001114146
14	35236.3	283.8	0.013845003
15	35677.7	280.3	0.020564981
16	35876.4	278.7	0.002243215
17	36121.0	276.8	0.007401416
18	36504.5	273.9	0.000888696
19	36638.2	272.9	0.010076055
20	36813.7	271.6	0.003467099
21	37668.3	265.5	0.011078387
22	37852.5	264.2	0.032736299
23	38045.8	262.8	0.005595758
24	38313.4	261.0	0.003513425
25	38451.6	260.1	0.019994422
26	38636.1	258.8	0.005532071
27	38733.2	258.2	0.004677159
28	38910.3	257.0	0.014452862
29	39086.9	255.8	0.049024493
30	39259.3	254.7	0.010300282
31	39417.0	253.7	0.038023823
32	39555.5	252.8	0.011188598
33	39805.5	251.2	0.069223629
34	40166.8	249.0	0.018375608
35	40369.5	247.7	0.018834195
36	40421.3	247.4	0.006869063
37	40561.6	246.5	0.001134377
38	40783.6	245.2	0.000587386
39	40824.8	244.9	0.039330540
40	41101.1	243.3	0.010657672
41	41125.9	243.2	0.005524259
42	41358.8	241.8	0.003479594
43	41475.9	241.1	0.004537909
44	41618.8	240.3	0.004725296
45	41715.6	239.7	0.011438162
46	41830.6	239.1	0.001244659
47	41953.7	238.4	0.008390597
48	42071.8	237.7	0.014323651
49	42208.0	236.9	0.008933428
50	42334.5	236.2	0.015749505

Table S13. Singlet excitations calculated for R,R-5 in the ground state geometry.

State	Energy [cm ⁻¹]	λ [nm]	f _{osc}
1	25411.8	393.5	0.003414746
2	25485.5	392.4	0.060647450
3	26824.8	372.8	0.002865354
4	27817.4	359.5	0.156407540
5	28202.6	354.6	0.006804713
6	29139.5	343.2	0.002648361
7	29702.0	336.7	0.025587580
8	29722.5	336.4	0.046160808
9	29946.0	333.9	0.015798089
10	30288.9	330.2	0.059611215
11	30326.7	329.7	0.014579007
12	30584.6	327.0	0.002085971
13	31209.1	320.4	0.062424993
14	31572.6	316.7	0.007480244
15	32209.0	310.5	0.044248339
16	32403.3	308.6	0.001014742
17	32446.0	308.2	0.016392218
18	32532.2	307.4	0.006161575
19	32804.1	304.8	0.055406401
20	33111.7	302.0	0.000033043

6	3.693760000	10.545110000	17.220381000
1	3.424313000	11.599713000	17.315967000
6	5.044526000	10.178591000	17.145014000
6	5.331377000	8.805791000	17.113467000
1	6.371095000	8.484996000	17.153732000
6	4.338106000	7.869287000	16.848376000
1	4.614280000	6.830096000	16.660612000
6	6.140912000	11.159507000	16.798980000
1	7.030711000	10.990581000	17.422444000
1	5.796694000	12.185796000	16.984151000
6	6.808978000	11.040361000	15.270799000
1	6.844296000	12.054417000	14.847967000
1	7.627094000	10.640185000	15.240239000
6	2.067561000	7.405148000	15.847160000
1	1.048617000	7.809466000	15.910460000
1	2.054006000	6.376690000	16.231972000
6	2.482809000	7.306510000	14.304171000
1	2.845280000	6.291227000	14.105128000
1	1.578840000	7.468036000	13.700011000
6	8.080563000	7.938811000	14.857530000
6	7.598402000	7.000815000	15.777848000
1	6.673265000	6.457638000	15.585795000
6	8.293730000	6.744046000	16.959144000
1	7.908903000	5.996251000	17.653300000
6	9.461822000	7.450253000	17.256426000
1	10.003265000	7.253382000	18.182654000
6	9.926744000	8.415024000	16.360777000
1	10.830842000	8.983213000	16.583443000
6	9.243036000	8.655253000	15.165444000
1	9.623597000	9.406582000	14.475435000
6	8.105627000	8.981662000	12.528067000
6	9.331433000	8.441205000	12.105807000
1	9.684965000	7.499204000	12.521564000
6	10.117971000	9.109360000	11.168950000
1	11.065721000	8.671405000	10.853666000
6	9.699297000	10.337665000	10.647437000
1	10.318240000	10.864415000	9.919856000
6	8.482644000	10.881054000	11.061168000
1	8.140704000	11.834743000	10.657242000
6	7.687300000	10.202723000	11.988962000
1	6.735578000	10.634375000	12.292816000
6	7.464596000	6.102233000	12.001565000
6	8.323724000	5.061807000	12.400671000
6	9.034866000	4.389931000	11.396183000
1	9.716884000	3.587643000	11.679870000
6	8.874241000	4.714391000	10.052856000
1	9.439527000	4.177414000	9.289535000
6	7.973275000	5.709846000	9.681084000
1	7.828876000	5.940201000	8.625568000
6	7.251541000	6.428213000	10.640688000
6	8.480551000	4.606706000	13.836785000
1	7.753906000	5.158540000	14.441539000
6	9.885722000	4.909939000	14.376223000
1	10.651596000	4.377578000	13.792688000
1	9.966013000	4.584924000	15.423056000
1	10.108577000	5.985014000	14.338592000
6	8.141578000	3.114771000	13.984232000
1	7.130112000	2.901236000	13.614235000
1	8.180718000	2.829789000	15.044807000
1	8.855850000	2.481830000	13.437545000
6	6.254400000	7.461234000	10.185585000
1	6.028337000	8.143196000	11.031681000
6	6.807168000	8.372278000	9.064689000
1	7.785025000	8.789014000	9.336154000
1	6.115969000	9.207254000	8.883055000
1	6.914354000	7.817678000	8.121584000
6	4.936832000	6.814435000	9.748248000
1	5.109098000	6.158563000	8.820040000
1	4.201597000	7.580078000	9.461494000
1	4.500626000	6.202442000	10.549718000
7	6.757594000	6.907529000	12.977991000
6	5.106721000	3.468412000	17.283519000
9	4.925376000	4.512010000	18.130893000
9	4.550098000	2.372146000	17.851913000
9	6.441136000	3.250347000	17.180210000

Table S14. Singlet excitations calculated for S,R-5 in the ground state geometry.

State	Energy [cm ⁻¹]	λ [nm]	f _{osc}
1	25122.7	398.0	0.053490626
2	25247.9	396.1	0.000001193
3	26038.0	384.1	0.017303993
4	27485.4	363.8	0.000032814
5	27551.6	363.0	0.148405376
6	29060.8	344.1	0.000000264
7	29282.7	341.5	0.008280243
8	29439.4	339.7	0.000002222
9	29534.3	338.6	0.139140836
10	30209.9	331.0	0.000000070
11	30628.6	326.5	0.000015882
12	30646.9	326.3	0.026668053
13	31090.9	321.6	0.000000262
14	31232.6	320.2	0.071690942
15	31818.7	314.3	0.000000354
16	31918.1	313.3	0.012751419
17	32290.3	309.7	0.000000043
18	32643.7	306.3	0.033087561
19	32826.3	304.6	0.038435058
20	32856.0	304.4	0.000001705

Table S15. XYZ coordinates of optimized molecule 2.

6	5.452779000	6.812476000	13.146251000
1	4.921002000	5.936837000	12.785557000
6	4.892532000	7.993699000	13.699502000
6	5.955577000	8.907434000	13.936945000
6	7.279589000	8.237520000	13.574718000
6	3.540516000	8.314453000	13.949854000
6	3.291646000	9.684580000	14.080499000
1	2.262159000	10.037354000	14.148042000
6	4.330921000	10.576060000	14.336809000
1	4.085170000	11.613735000	14.568892000
6	5.678507000	10.171994000	14.461439000
6	3.007468000	8.276708000	16.647196000
6	2.685226000	9.598339000	16.986286000
1	1.648142000	9.933386000	16.909482000

Table S16. XYZ coordinates of optimized molecule 4.

45	11.439932000	8.161514000	9.148040000
17	13.106917000	7.230051000	10.599306000
8	9.758379000	9.926129000	7.429309000
7	9.419470000	8.363100000	11.382958000
8	13.806091000	8.775156000	7.328695000
6	9.713484000	5.005204000	10.069657000
6	8.789903000	7.623138000	12.577496000
6	8.801064000	3.985236000	10.370309000
1	8.777107000	3.092811000	9.743350000
6	9.997214000	7.536404000	10.507262000
6	8.769412000	6.211220000	12.005446000
6	11.168238000	7.537440000	13.519190000
1	11.544667000	7.397823000	12.506751000
6	9.547260000	6.190944000	10.815482000
6	10.876660000	4.692601000	9.174508000
1	11.340394000	5.620948000	8.803373000
1	10.524753000	4.120097000	8.305250000
6	8.075222000	3.997421000	11.556762000
1	7.489921000	3.116124000	11.825953000
6	9.145002000	9.740806000	11.045686000
6	7.447916000	8.215153000	12.994395000
6	12.083402000	7.553324000	14.570205000
1	13.147759000	7.454441000	14.351680000
6	8.196815000	5.035340000	12.502303000
6	11.730285000	4.403097000	12.361846000
1	12.342079000	5.289368000	12.187178000
6	12.551402000	11.059541000	11.324780000
1	12.556686000	10.661209000	10.299687000
1	13.489451000	10.759180000	11.813440000
1	12.529472000	12.158015000	11.274656000
6	10.048867000	10.764144000	11.378687000
6	9.721986000	12.070851000	10.990305000
1	10.403591000	12.885120000	11.239987000
6	6.259516000	7.479068000	12.950076000
1	6.264001000	6.466407000	12.551369000
6	10.326380000	9.176808000	8.107564000
6	11.315266000	11.035617000	13.542213000
1	12.262802000	10.814014000	14.054225000
1	10.503996000	10.572079000	14.121103000
1	11.165365000	12.125819000	13.552449000
6	7.687221000	11.302738000	9.942163000
1	6.783655000	11.522131000	9.373265000
6	11.352792000	10.500017000	12.103762000
1	11.485195000	9.413735000	12.154859000
6	9.797859000	7.679074000	13.756283000
6	10.895970000	2.278612000	11.639185000
1	10.839243000	1.475809000	10.900040000
6	5.058603000	8.031779000	13.402839000
1	4.145581000	7.436152000	13.363440000
6	7.202970000	8.344752000	8.504477000
1	6.426488000	7.602359000	8.268799000
1	8.178890000	7.853171000	8.401162000
1	7.143426000	9.155556000	7.765076000
6	10.955642000	4.318681000	13.513394000
1	10.980632000	5.135965000	14.234861000
6	6.985632000	8.871556000	9.931960000
1	7.161461000	8.022697000	10.602360000
6	9.354346000	7.787414000	15.080536000
1	8.291734000	7.880860000	15.298681000
6	7.404827000	9.529369000	13.487631000
1	8.319052000	10.117535000	13.550180000
6	7.887923000	4.733674000	13.950608000
1	6.833141000	4.447629000	14.075478000
1	8.049826000	5.629599000	14.559099000
6	12.897796000	8.568491000	8.006033000
6	5.524194000	9.299937000	10.122336000
1	5.220175000	10.039235000	9.366984000
1	5.358405000	9.732001000	11.117234000
1	4.866430000	8.426102000	10.013506000
6	7.956479000	9.981853000	10.316696000
6	5.025715000	9.338568000	13.891254000
1	4.087937000	9.772559000	14.241122000
6	11.605883000	3.449598000	11.336551000
6	11.638009000	7.677664000	15.886920000

1	12.351205000	7.686253000	16.714247000
6	10.268831000	7.781624000	16.138831000
1	9.900635000	7.866873000	17.162463000
6	8.554719000	12.340521000	10.280870000
1	8.322226000	13.363876000	9.981406000
6	11.995113000	3.822897000	9.925031000
1	12.180933000	2.921106000	9.326135000
1	12.914511000	4.423095000	9.936702000
6	8.788281000	3.546933000	14.523311000
1	9.065285000	3.818860000	15.552696000
1	8.182314000	2.632097000	14.577553000
6	10.009167000	3.295573000	13.668429000
6	10.098437000	2.206055000	12.790051000
1	9.426351000	1.354033000	12.919132000
6	6.204712000	10.089610000	13.923275000
1	6.194834000	11.113705000	14.298848000
8	5.100811000	4.999861000	15.154216000
8	4.601960000	2.593435000	14.843350000
8	2.933403000	4.076773000	15.924251000
16	4.342271000	3.819401000	15.604511000

Table S17. XYZ coordinates of optimized molecule R,R-5.

Au	3.072564	2.954549	3.436676
C	2.801172	2.445245	5.380156
C	3.462435	3.468970	1.514343
C	2.195608	3.177052	6.478646
C	3.326837	2.712961	0.281899
C	2.250486	2.381242	7.662348
C	3.721762	3.531699	-0.819437
C	3.074865	1.131584	7.364668
C	4.314889	4.824698	-0.267002
C	1.552005	4.443108	6.469159
C	0.661639	4.655368	7.539007
H	0.021702	5.545554	7.534766
C	0.717420	3.869279	8.695964
H	0.099016	4.153721	9.556295
C	1.661760	2.824805	8.859422
C	2.071443	2.420223	10.263541
H	2.844688	1.638579	10.208886
H	1.219679	1.977156	10.812176
C	2.628105	3.653967	11.109188
H	1.852490	3.993892	11.817919
H	3.475554	3.286523	11.716514
C	3.041768	4.804165	10.211747
C	2.269414	5.974951	10.072752
H	1.526584	6.228810	10.841010
C	2.312405	6.727038	8.882451
H	1.609335	7.559825	8.747584
C	3.115889	6.311169	7.802127
C	4.083024	5.317048	8.068270
H	4.797774	5.046219	7.282470
C	4.057524	4.586724	9.258800
H	4.748149	3.748005	9.393632
C	2.824981	6.686042	6.366299
H	3.765767	6.791895	5.803727
H	2.312031	7.661768	6.313912
C	1.934097	5.603226	5.584244
H	1.028398	6.109237	5.208368
H	2.491460	5.248348	4.699016
C	3.423377	0.101523	4.995979
C	2.290090	-0.677571	4.635138
C	2.518831	-1.888972	3.956957
H	1.665187	-2.518424	3.682359
C	3.817868	-2.313241	3.649556
H	3.977410	-3.275889	3.149316
C	4.909838	-1.487165	3.943653
H	5.920088	-1.798729	3.650653
C	4.735501	-0.251832	4.598210
C	0.865656	-0.208094	4.908804
H	0.898173	0.513526	5.743264
C	0.305277	0.537966	3.679131

H	0.216182	-0.144992	2.814565
H	0.956296	1.380475	3.375607
H	-0.698210	0.943825	3.898770
C	-0.074040	-1.349154	5.331794
H	-1.038768	-0.936326	5.675158
H	0.356963	-1.940318	6.155288
H	-0.294714	-2.032626	4.491772
C	6.391152	1.189335	3.388661
H	5.547865	1.665479	2.854865
H	6.781000	0.367560	2.760191
H	7.193436	1.941229	3.501036
C	5.923223	0.681476	4.676415
H	5.567744	1.560743	5.322857
C	7.066762	0.052679	5.577995
H	7.492827	-0.830121	5.067567
H	6.718791	-0.263322	6.576836
H	7.883397	0.781534	5.724148
C	4.499705	1.327297	7.950407
C	5.336832	2.332330	7.429139
H	4.980591	2.964524	6.609923
C	6.612390	2.561563	7.960622
H	7.244820	3.346580	7.529484
C	7.065633	1.803654	9.054126
H	8.060600	1.982904	9.477770
C	6.226758	0.822844	9.604957
H	6.560913	0.231539	10.465640
C	4.953974	0.583253	9.055792
H	4.316852	-0.191955	9.493332
C	2.450070	-0.197365	7.789147
C	1.186901	-0.263976	8.406584
H	0.608750	0.652031	8.562387
C	0.655941	-1.495837	8.824545
H	-0.326377	-1.523891	9.310603
C	1.372387	-2.683469	8.611351
H	0.957929	-3.645162	8.936195
C	2.623815	-2.631310	7.972605
C	3.190969	-3.551800	7.791739
C	3.159746	-1.399966	7.571084
H	4.144726	-1.374174	7.092950
C	2.818573	1.402162	0.082001
C	2.358221	1.146371	-1.224100
H	1.825194	0.210878	-1.430146
C	2.739540	1.957987	-2.299467
H	2.469115	1.646621	-3.315894
C	3.606141	3.069040	-2.141548
C	4.437753	3.529047	-3.324904
H	5.092221	4.356395	-3.009713
H	3.795146	3.930422	-4.130307
C	5.332404	2.354670	-3.929811
H	4.870863	1.980955	-4.860794
H	6.308614	2.790588	-4.211034
C	5.493937	1.213563	-2.944772
C	4.804900	-0.008196	-3.079461
H	4.387822	-0.290998	-4.055423
C	4.491963	-0.784598	-1.946477
H	3.843256	-1.663372	-2.060742
C	4.848305	-0.345402	-0.655903
C	5.776388	0.716034	-0.574333
H	6.162688	1.012746	0.407908
C	6.105156	1.473775	-1.701168
H	6.739044	2.359519	-1.591003
C	4.107577	-0.776831	0.590832
H	4.806166	-0.884581	1.436054
H	3.640259	-1.765018	0.438551
C	2.970575	0.257660	1.053473
H	2.020158	-0.295272	1.145725
H	3.214770	0.638731	2.061347
C	3.755967	5.845014	2.063658
C	4.823191	6.274561	2.888383
C	4.685572	7.515810	3.540771
H	5.510605	7.886967	4.161251
C	3.513167	8.272422	3.422056
H	3.432129	9.240963	3.929722
C	2.429868	7.771136	2.688960
H	1.499050	8.346261	2.636782

C	2.524707	6.552287	1.992239
C	6.051878	5.419784	3.154696
H	5.955458	4.512215	2.541412
C	7.359778	6.118098	2.750253
H	8.221707	5.444574	2.900905
H	7.537540	7.029935	3.348970
H	7.342770	6.406164	1.684842
C	6.065534	4.958130	4.625778
H	6.181465	5.809956	5.320594
H	6.900663	4.257341	4.806619
H	5.121650	4.436383	4.869242
C	1.319815	6.000707	1.237456
H	1.690478	5.306091	0.463651
C	0.508017	7.090619	0.518277
H	-0.038141	7.732730	1.233064
H	-0.246299	6.625993	-0.140573
H	1.153703	7.733586	-0.101260
C	0.417704	5.186485	2.189996
H	0.978420	4.375638	2.692502
H	-0.418896	4.729727	1.632215
H	-0.007758	5.837323	2.975123
C	5.863125	4.714546	-0.322227
C	6.627651	5.491362	-1.213170
H	6.137123	6.233108	-1.851605
C	8.022726	5.327248	-1.288505
H	8.599478	5.943165	-1.988544
C	8.673279	4.389359	-0.472212
H	9.761338	4.268104	-0.526842
C	7.913982	3.598502	0.407563
H	8.401825	2.843851	1.035785
C	6.523243	3.753334	0.466355
H	5.941477	3.095434	1.118955
C	3.803539	6.121957	-0.891910
C	2.830149	6.127303	-1.908495
H	2.392766	5.183002	-2.247052
C	2.409356	7.333713	-2.492983
H	1.656325	7.314692	-3.289590
C	2.941300	8.555658	-2.053342
H	2.612058	9.497406	-2.508172
C	3.895737	8.563849	-1.020999
H	4.313163	9.511472	-0.661287
C	4.326785	7.358411	-0.450534
H	5.083886	7.378055	0.340301
N	3.183182	1.246981	5.839694
N	3.895398	4.696749	1.202546

Table S18. XYZ coordinates of optimized molecule S,R-5.

Au	10.414297	12.475241	9.079030
C	11.422631	14.106539	9.740229
C	8.021668	8.957078	8.231307
C	13.742009	14.102074	12.159640
H	13.491289	13.483895	11.291191
N	11.155039	14.665494	10.927390
C	15.595682	13.843132	7.955111
C	10.908942	6.806192	4.724483
H	11.437200	6.859914	3.765465
C	11.260430	18.247333	10.971865
H	11.768234	18.290385	10.003647
C	8.393420	10.041760	9.080119
C	6.152584	12.044207	10.955208
H	5.758233	12.268764	11.961197
H	6.225402	13.007493	10.421300
C	13.507963	16.162806	13.406807
H	13.054706	17.149444	13.545458
C	8.007172	15.077719	8.885195
H	6.959836	14.850053	9.156953
H	8.532806	14.115857	8.720778
H	8.001173	15.630973	7.929275
C	16.388512	16.156130	9.410336
C	10.576086	19.379620	11.445387
H	10.564577	20.295315	10.842602

C	9.947780	14.402836	11.676594
C	8.688590	15.911539	9.991629
H	9.716443	16.133012	9.655497
C	11.303215	17.061508	11.729505
N	9.672738	10.286136	7.229816
C	13.928555	17.003570	8.094088
H	14.510187	17.832788	7.672853
C	12.055889	9.850513	6.878114
C	13.735291	16.960351	9.496369
C	12.091831	15.834743	11.264695
C	10.879994	10.548731	6.480579
C	16.323649	14.872283	7.324516
H	16.468369	14.847795	6.236213
C	12.818639	9.869255	9.271761
H	13.866158	10.097332	9.001068
H	12.823996	9.314595	10.226867
H	12.292915	10.830881	9.437235
C	13.192394	9.967363	6.055336
H	14.105438	9.425621	6.326545
C	12.978944	14.773330	7.771487
C	7.967292	17.258000	10.175555
H	8.070696	17.869772	9.262223
H	8.385350	17.829261	11.018722
H	6.885400	17.121205	10.354866
C	16.188763	17.505716	10.076129
H	16.586543	18.303972	9.424574
H	16.737364	17.575413	11.033534
C	7.640848	11.474847	11.121805
H	8.358462	12.244158	10.786778
H	7.827255	11.317308	12.196151
C	10.074965	13.813984	5.377212
H	10.382391	13.930602	6.432443
H	9.206185	14.473647	5.201629
H	10.903111	14.172269	4.738570
C	13.188068	13.475042	7.036313
H	13.004779	13.633084	5.961498
H	12.468811	12.706276	7.369072
C	13.171210	10.746660	4.891312
H	14.058526	10.797489	4.248794
C	7.849340	10.176777	10.385994
C	14.649801	17.783921	10.385154
H	14.443810	17.541174	11.438989
H	14.457189	18.866870	10.269749
C	9.960110	13.528349	12.790234
C	13.560164	15.945926	7.254309
H	13.877914	15.966103	6.205409
C	6.125549	11.308902	5.086689
H	5.659627	12.290317	5.234568
C	9.702119	12.350487	5.066200
H	8.891849	12.082797	5.757753
C	12.028351	11.488030	4.570644
H	12.034875	12.141979	3.689973
C	12.138083	9.037032	8.163611
H	11.110044	8.814881	8.498723
C	11.126436	12.602578	13.092075
H	11.936877	12.870917	12.400988
C	7.656460	14.204685	13.265658
H	6.789042	14.153724	13.908022
C	13.115621	15.352080	12.324919
C	8.799646	13.464086	13.586941
H	8.793296	12.810578	14.467940
C	10.213640	7.929941	5.192095
H	10.199737	8.840111	4.583914
C	8.771479	15.099924	11.280260
C	10.868006	11.424000	5.367542
C	9.162380	12.179913	3.637353
H	8.278396	12.822340	3.480553
H	8.856673	11.136222	3.447151
H	9.915846	12.460176	2.878772
C	10.612105	17.023821	12.962348
H	10.625975	16.114341	13.571566
C	4.878075	9.954833	8.075525
H	5.032923	9.921309	6.992255
C	5.281372	11.083136	8.794541
H	5.735937	11.930171	8.265271

C	5.748676	10.501661	3.999654
H	4.994330	10.852342	3.285779
C	12.434767	14.908945	9.077261
C	14.484970	15.717660	14.315607
H	14.776060	16.364604	15.151527
C	7.635006	14.983185	12.101105
H	6.721577	15.523937	11.829212
C	7.711116	9.602038	5.832811
C	7.092383	7.990895	8.659873
C	14.702475	13.647255	13.072882
H	15.169647	12.866325	12.925729
C	15.547042	13.868358	9.365946
H	15.092675	13.022004	9.896471
C	16.708944	16.020597	8.044148
H	17.139386	16.873012	7.501338
C	4.118879	8.929007	10.112972
H	3.688330	8.075820	10.654475
C	10.754563	11.138940	12.780570
H	9.926445	10.780059	13.418917
H	11.623661	10.479704	12.956186
H	10.447448	11.022509	11.725215
C	9.904917	19.336089	12.676771
H	9.370515	20.218834	13.047274
C	6.177908	7.167689	7.770779
H	6.369721	6.084699	7.887015
H	6.384685	7.409681	6.716938
C	10.920328	5.617184	5.474860
H	11.454348	4.734703	5.103178
C	7.267774	9.004051	10.902517
H	6.950064	8.983346	11.951419
C	8.735281	9.117681	6.891815
C	11.665458	12.773212	14.521171
H	11.970656	13.817010	14.711615
H	12.549642	12.131134	14.678272
H	10.911823	12.492538	15.279429
C	15.078284	14.455753	14.159353
H	15.832843	14.106429	14.873671
C	15.950394	14.997713	10.083279
H	15.795733	15.032733	11.166533
C	12.859739	7.690974	7.978117
H	13.941739	7.828242	7.799819
H	12.442411	7.120955	7.133747
H	12.755778	7.077745	8.890410
C	9.523120	7.891111	6.425231
C	10.249659	5.572482	6.706476
H	10.261191	4.656130	7.308261
C	9.566016	6.704506	7.181637
H	9.058596	6.660540	8.150015
C	6.340586	9.239231	3.842324
H	6.048643	8.593255	3.005953
C	6.899159	7.946949	10.062171
H	6.317574	7.117482	10.482981
C	4.504347	10.076172	10.834350
H	4.359475	10.089123	11.922667
C	4.638783	7.446954	8.078718
H	4.091202	7.379720	7.120565
H	4.239553	6.647827	8.728297
C	9.916305	18.147897	13.428437
H	9.387745	18.095108	14.387341
C	9.405645	10.844314	8.417465
C	12.806018	15.994303	9.925387
C	4.439490	8.795504	8.746645
C	5.232400	11.106250	10.205400
C	14.675100	12.903979	7.207272
H	14.599870	11.943126	7.745180
H	15.070318	12.674601	6.202716
C	7.086016	10.852540	5.999163
H	7.338239	11.470297	6.867480
C	7.317594	8.792520	4.750353
H	7.770113	7.805698	4.610571

Table S19. XYZ coordinates of optimized molecule S,R-5 in the T₁ state

Au	10.437862	12.402287	9.115669
C	11.417852	14.065756	9.786692
C	8.059913	8.903605	8.198128
C	13.721488	14.119956	12.238320
H	13.401349	13.436285	11.470119
N	11.162576	14.653378	10.977655
C	15.702233	13.798119	8.314296
C	10.686396	6.924069	4.437775
H	11.156014	7.030321	3.470869
C	11.233080	18.191266	10.927594
H	11.660671	18.206601	9.939071
C	8.434202	9.954144	9.054479
C	6.207459	11.902173	10.928694
H	5.816813	12.150861	11.912640
H	6.288623	12.837636	10.380500
C	13.622957	16.266364	13.278310
H	13.213740	17.260285	13.355437
C	8.030892	15.090802	8.839245
H	6.989485	14.902321	9.099888
H	8.515310	14.130936	8.672912
H	8.047246	15.644315	7.901061
C	16.282565	16.307924	9.397631
C	10.585334	19.330727	11.389789
H	10.538622	20.208230	10.761397
C	9.935316	14.437505	11.690192
C	8.726903	15.891686	9.941315
H	9.744991	16.080741	9.615638
C	11.323655	17.048087	11.713961
N	9.690726	10.235833	7.223165
C	13.757134	16.933702	7.935770
H	14.170041	17.822733	7.484604
C	12.032442	9.749843	6.810711
C	13.621773	16.900670	9.408575
C	12.089522	15.805203	11.271556
C	10.891698	10.501978	6.476359
C	16.310570	14.775511	7.530154
H	16.426446	14.618361	6.466137
C	12.791924	9.549038	9.184729
H	13.831202	9.758329	8.932929
H	12.761515	8.918804	10.073061
H	12.308697	10.491820	9.433366
C	13.163868	9.886560	6.014840
H	14.045520	9.308076	6.243781
C	13.073621	14.621924	7.821656
C	8.040892	17.244676	10.113721
H	8.192391	17.855199	9.224866
H	8.432988	17.786842	10.966993
H	6.966180	17.133215	10.248479
C	15.985356	17.712174	9.862907
H	16.263758	18.419658	9.084796
H	16.554932	17.981950	10.751513
C	7.675365	11.329851	11.120350
H	8.384653	12.103956	10.844821
H	7.825730	11.132936	12.177544
C	10.278563	13.860969	5.425443
H	10.674966	13.977009	6.432189
H	9.447918	14.556066	5.309531
H	11.055109	14.154748	4.720377
C	13.458918	13.293706	7.241756
H	13.515964	13.428140	6.164536
H	12.687974	12.548005	7.416098
C	13.172043	10.736912	4.922323
H	14.050805	10.807221	4.297010
C	7.910127	10.059601	10.354389
C	14.465107	17.858949	10.199947
H	14.309356	17.687631	11.257904
H	14.148830	18.884295	9.995558
C	9.893842	13.609378	12.819277
C	13.518449	15.813002	7.204366
H	13.794216	15.786198	6.159114
C	6.149682	11.463462	5.254975
H	5.746720	12.447671	5.446171
C	9.802155	12.429024	5.180646
H	9.022402	12.236728	5.902737

C	12.065643	11.520269	4.656127
H	12.094596	12.221501	3.835068
C	12.090697	8.841892	8.023656
H	11.074955	8.624932	8.338915
C	11.048247	12.732632	13.245374
H	11.845484	12.888828	12.535246
C	7.585035	14.244520	13.155158
H	6.677799	14.191848	13.739996
C	13.146180	15.384431	12.312783
C	8.710565	13.549561	13.551970
H	8.672353	12.934634	14.439253
C	10.067252	8.017021	5.019019
H	10.053131	8.953336	4.484854
C	8.777428	15.096389	11.231872
C	10.917268	11.443690	5.441349
C	9.199586	12.267561	3.788854
H	8.365864	12.954002	3.653571
H	8.824737	11.258113	3.635146
H	9.932624	12.479294	3.011347
C	10.706783	17.062181	12.967043
H	10.752990	16.190684	13.600262
C	4.893059	9.858137	8.085459
H	5.028991	9.836836	7.016023
C	5.288361	10.971269	8.801808
H	5.717693	11.814198	8.280658
C	5.674032	10.708392	4.191427
H	4.906803	11.102458	3.541247
C	12.414185	14.821970	9.136508
C	14.625348	15.881673	14.161155
H	14.975551	16.583039	14.904498
C	7.615321	14.984770	11.986052
H	6.721673	15.494177	11.659019
C	7.678471	9.690748	5.870559
C	7.158262	7.928900	8.620415
C	14.708056	13.725472	13.125761
H	15.129108	12.732934	13.053008
C	15.688478	13.996817	9.692844
H	15.333424	13.205300	10.333404
C	16.591600	16.023047	8.068491
H	16.919794	16.819623	7.414616
C	4.203938	8.810073	10.101416
H	3.811545	7.955031	10.635985
C	10.680471	11.251783	13.163675
H	9.882915	10.992057	13.858716
H	11.545708	10.638854	13.413550
H	10.356112	10.982013	12.160606
C	9.993210	19.336389	12.641493
H	9.488553	20.220471	13.003289
C	6.236426	7.109340	7.747948
H	6.436518	6.043974	7.861180
H	6.421874	7.345827	6.706908
C	10.691588	5.695845	5.088062
H	11.162748	4.838338	4.629801
C	7.359115	8.885877	10.851339
H	7.049988	8.844088	11.885102
C	8.729700	9.126905	6.851183
C	11.575308	13.104951	14.627561
H	11.889390	14.145960	14.664459
H	12.437441	12.492181	14.884540
H	10.818373	12.952381	15.396007
C	15.165774	14.607147	14.095569
H	15.937575	14.304824	14.788098
C	15.977331	15.235523	10.232325
H	15.833656	15.403713	11.288856
C	12.766803	7.506109	7.732202
H	13.840182	7.621652	7.589599
H	12.355343	7.035060	6.845779
H	12.624543	6.828485	8.572384
C	9.450656	7.916112	6.268623
C	10.091594	5.584157	6.331004
H	10.095152	4.638866	6.853936
C	9.486384	6.688284	6.919836
H	9.040586	6.579391	7.893902
C	6.188695	9.439099	3.980697
H	5.823301	8.832373	3.164967

C	6.996388	7.853333	10.004757
H	6.431656	7.027119	10.412454
C	4.585551	9.939834	10.820726
H	4.474197	9.941051	11.896970
C	4.712492	7.367785	8.069369
H	4.161739	7.298256	7.131988
H	4.338812	6.571462	8.710270
C	10.045255	18.189061	13.424195
H	9.577608	18.172946	14.397734
C	9.444680	10.763176	8.404654
C	12.771961	15.933626	9.918113
C	4.495980	8.698740	8.745412
C	5.278266	10.972118	10.196028
C	14.834181	12.718204	7.732113
H	14.649398	11.960022	8.489240
H	15.305911	12.215319	6.889730
C	7.128191	10.950260	6.088284
H	7.451902	11.537476	6.930888
C	7.183525	8.936242	4.811257
H	7.567600	7.947433	4.622622

C	0.085075	-1.538520	5.429356
H	-0.867015	-1.178948	5.816620
H	0.578793	-2.100716	6.215482
H	-0.138770	-2.221189	4.610951
C	6.432991	1.155809	3.347660
H	5.620504	1.575176	2.757357
H	6.862068	0.323007	2.792196
H	7.203984	1.918526	3.452444
C	5.919256	0.720993	4.719994
H	5.546045	1.610789	5.206836
C	7.036114	0.148100	5.585491
H	7.461250	-0.752232	5.143428
H	6.675061	-0.101640	6.580849
H	7.840089	0.873375	5.699904
C	4.523798	1.441139	7.917562
C	5.292542	2.466835	7.373033
H	4.920934	3.018679	6.527546
C	6.522839	2.806501	7.906935
H	7.098597	3.602217	7.456336
C	7.005618	2.137192	9.024426
H	7.964200	2.399268	9.447843
C	6.239427	1.133219	9.594460
H	6.596085	0.607335	10.468190
C	5.008172	0.788439	9.046396
H	4.435506	-0.000224	9.506508
C	2.582685	-0.198541	7.803966
C	1.334083	-0.325452	8.402999
H	0.689123	0.531864	8.501251
C	0.885514	-1.554021	8.871868
H	-0.085516	-1.623015	9.340177
C	1.671403	-2.685277	8.725765
H	1.323520	-3.641951	9.087695
C	2.906948	-2.579643	8.098926
H	3.525985	-3.454633	7.964570
C	3.357308	-1.350008	7.649145
H	4.326689	-1.287299	7.181001
C	2.692828	1.501722	0.013312
C	2.233841	1.285820	-1.280138
H	1.669554	0.391306	-1.497843
C	2.668692	2.072203	-2.331664
H	2.408393	1.776637	-3.338055
C	3.580352	3.116945	-2.159642
C	4.438078	3.520533	-3.335517
H	5.127357	4.299163	-3.030091
H	3.826711	3.947719	-4.130014
C	5.260832	2.310823	-3.936006
H	4.784250	1.972204	-4.853838
H	6.244256	2.687392	-4.214750
C	5.365774	1.158397	-2.969679
C	4.619805	-0.006880	-3.110023
H	4.186043	-0.253541	-4.070181
C	4.265308	-0.759811	-1.992930
H	3.569830	-1.580429	-2.110062
C	4.639719	-0.350709	-0.717541
C	5.624025	0.634475	-0.632730
H	6.020098	0.900809	0.336150
C	5.990960	1.368496	-1.743495
H	6.660756	2.205424	-1.631847
C	3.869733	-0.729363	0.518790
H	4.548120	-0.843665	1.357318
H	3.382706	-1.691954	0.379433
C	2.765066	0.330093	0.951063
H	1.801912	-0.174086	0.977177
H	2.974246	0.654485	1.965838
C	3.827000	5.816226	2.060609
C	4.888598	6.169600	2.901368
C	4.784729	7.358215	3.621176
H	5.603631	7.662816	4.256378
C	3.652222	8.146465	3.546030
H	3.597104	9.072151	4.100808
C	2.574449	7.729049	2.785320
H	1.675893	8.326211	2.765881
C	2.634594	6.561183	2.034001
C	6.108583	5.303113	3.117295
H	5.985704	4.411464	2.520209

Table S20. XYZ coordinates of optimized molecule R,R-5 in the T₁ state

Au	3.002832	2.938176	3.382674
C	2.725469	2.382235	5.331042
C	3.426591	3.503222	1.463737
C	2.147260	3.088952	6.402914
C	3.264300	2.767147	0.227004
C	2.241512	2.344491	7.592729
C	3.703228	3.562997	-0.846812
C	3.130033	1.139944	7.324187
C	4.341677	4.820139	-0.278109
C	1.569772	4.453168	6.455782
C	0.600255	4.637487	7.480497
H	-0.049056	5.501581	7.448806
C	0.585492	3.827495	8.567241
H	-0.101233	3.999861	9.381420
C	1.622159	2.792961	8.745855
C	1.948772	2.361038	10.148447
H	2.728332	1.609766	10.120634
H	1.071629	1.879639	10.585418
C	2.391706	3.547645	11.072374
H	1.576035	3.818789	11.738742
C	3.208468	3.197344	11.702010
C	2.792684	4.749715	10.256159
C	2.004029	5.894970	10.194573
H	1.241421	6.062262	10.943376
C	2.056905	6.720785	9.080700
H	1.332510	7.517463	8.977717
C	2.887318	6.403893	8.009929
C	3.878873	5.444642	8.222523
H	4.605939	5.245447	7.447998
C	3.834735	4.630585	9.336476
H	4.531790	3.812598	9.427328
C	2.560092	6.835110	6.606163
H	3.390397	7.350799	6.129652
H	1.728636	7.537337	6.629790
C	2.195984	5.605328	5.719003
H	1.550852	5.933286	4.902232
H	3.096241	5.240312	5.230598
C	3.457447	0.072332	4.997492
C	2.365843	-0.745621	4.655022
C	2.621042	-1.928058	3.970021
H	1.800667	-2.580242	3.713215
C	3.911285	-2.293575	3.628657
H	4.092640	-3.228424	3.117865
C	4.962549	-1.439969	3.905944
H	5.961050	-1.705112	3.589583
C	4.755199	-0.231929	4.566923
C	0.932891	-0.359401	4.962926
H	0.945881	0.368151	5.767658
C	0.284087	0.312345	3.752313
H	0.228792	-0.380227	2.913047
H	0.842138	1.187764	3.429690
H	-0.730233	0.627289	3.994320

C	7.393868	5.991358	2.671099
H	8.244465	5.322629	2.789154
H	7.589708	6.886522	3.260029
H	7.344105	6.279091	1.623631
C	6.190537	4.845975	4.572604
H	6.334101	5.683686	5.254072
H	7.025950	4.160350	4.708547
H	5.278403	4.326633	4.856995
C	1.406011	6.117990	1.264726
H	1.713664	5.396411	0.514854
C	0.719698	7.267870	0.533749
H	0.208630	7.934816	1.226490
H	-0.032813	6.878279	-0.149562
H	1.426794	7.854134	-0.043889
C	0.418977	5.414496	2.197796
H	0.874709	4.565807	2.704367
H	-0.439428	5.051269	1.634572
H	0.050286	6.102459	2.958658
C	5.877040	4.666653	-0.352125
C	6.657163	5.428189	-1.216747
H	6.203747	6.186721	-1.833079
C	8.030296	5.225786	-1.302809
H	8.613122	5.832404	-1.980624
C	8.648331	4.259822	-0.525050
H	9.715983	4.108136	-0.587719
C	7.876133	3.481315	0.327057
H	8.335294	2.708188	0.926423
C	6.508528	3.678309	0.396828
H	5.925331	3.036515	1.033726
C	3.873764	6.130160	-0.900593
C	2.927523	6.170406	-1.918703
H	2.459722	5.262005	-2.258498
C	2.570198	7.373654	-2.515227
H	1.839793	7.375680	-3.311166
C	3.139769	8.561423	-2.088084
H	2.864117	9.497206	-2.552219
C	4.065373	8.539106	-1.051841
H	4.511579	9.458002	-0.700683
C	4.429843	7.337002	-0.469402
H	5.166063	7.339979	0.318349
N	3.202846	1.215494	5.821986
N	3.914422	4.690180	1.169225

Figure S51. Electron density differences for compound 2.

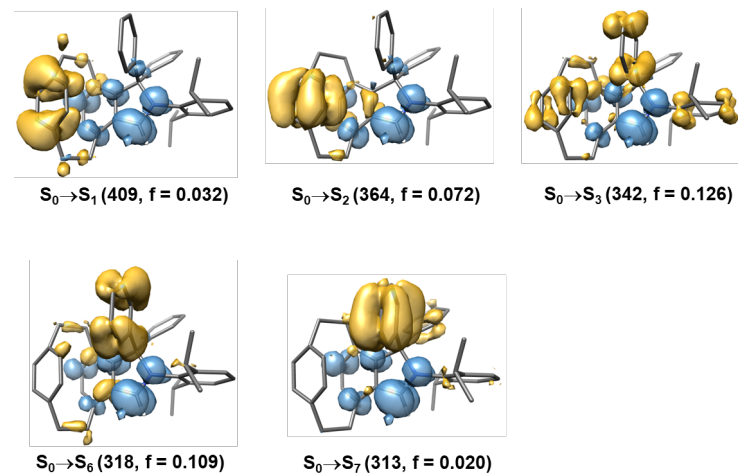


Figure S52. Electron density differences for compound 4.

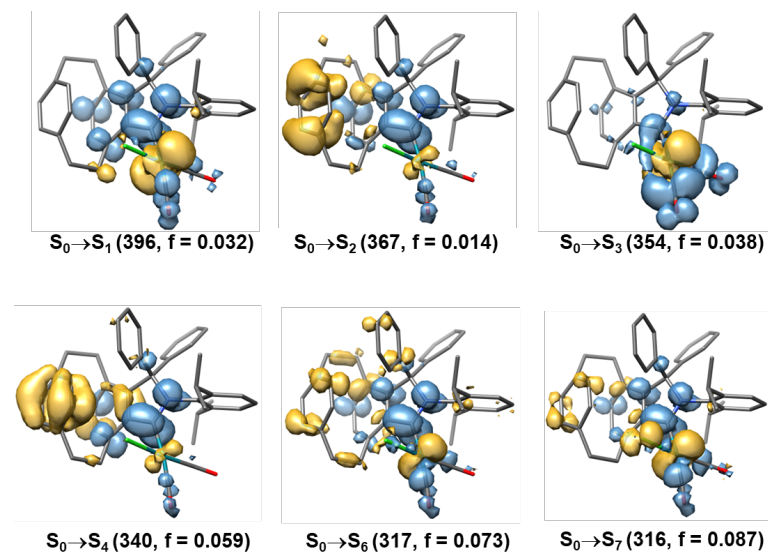


Figure S53. Electron density differences for compound S,R-5.

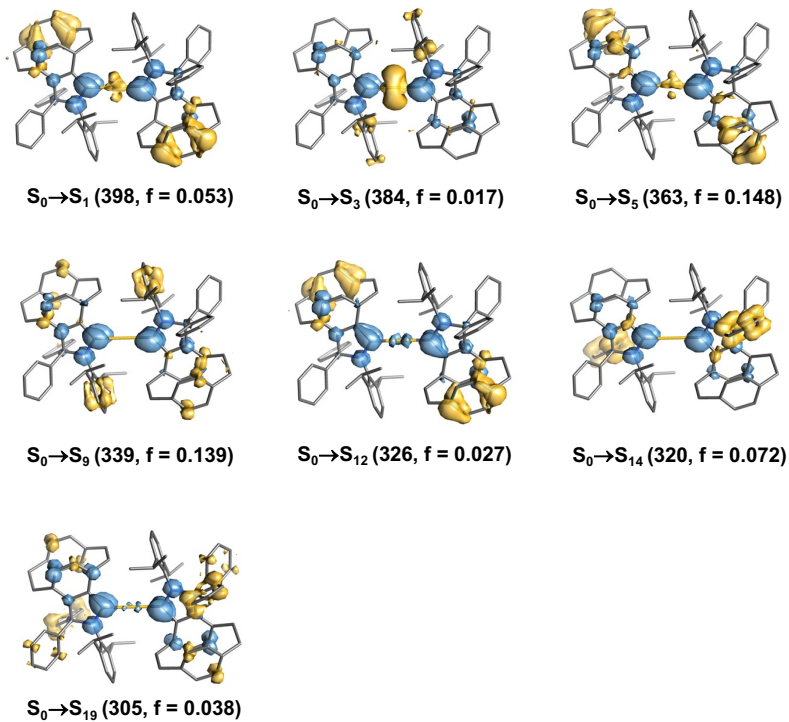


Figure S54. Electron density differences for compound R,R-5.

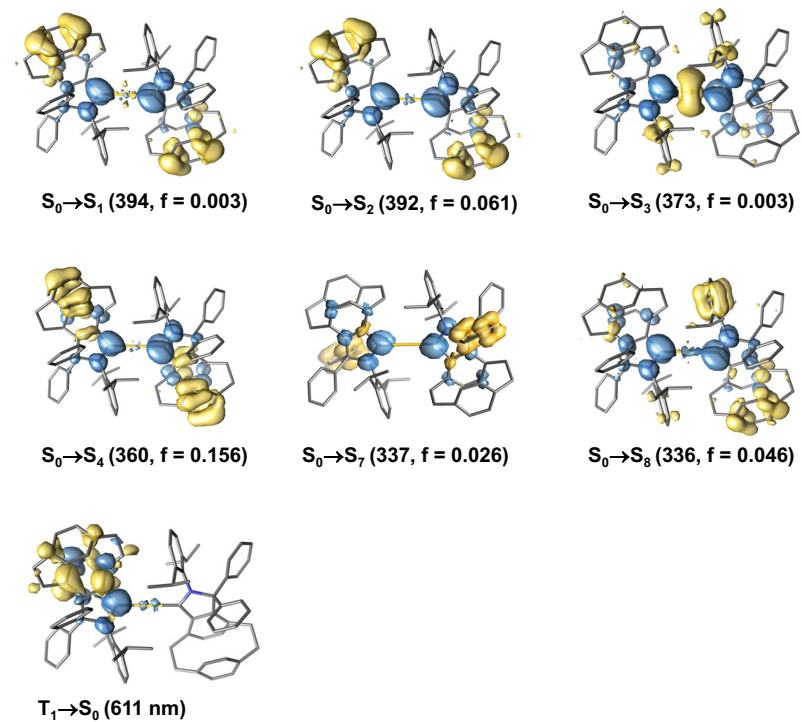
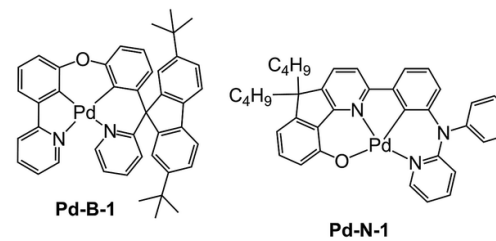


Figure S55. Graphical sketch of the photocatalysts Pd-B-1 and Pd-N-1 in Scheme 1 of the main text.



12. References

- [1] W. L. F. Armarego, *Purification of laboratory Chemicals*, Butterworth Heinemann, Oxford; Boston, **1996**.
- [2] C. J. Friedmann, S. Ay, S. Bräse, *J. Org. Chem.* **2010**, *75*, 4612.
- [3] J. J. P. Kramer, C. Yildiz, M. Nieger, S. Bräse, *Eur. J. Org. Chem.* **2014**, *2014*, 1287.
- [4] G. M. Sheldrick, *Acta Crystallogr. C* **2015**, *71*, 3.
- [5] O. V. Dolomanov, L. J. Bourhis, R. J. Gildea, J. A. K. Howard, H. Puschmann, *J. Appl. Crystallogr.* **2009**, *42*, 339.
- [6] A. L. Spek, *Acta Cryst.* **2015**, *71*, 9.
- [7] J. Lorkowski, M. Krahfuß, M. Kubicki, U. Radius, C. Pietraszuk, *Chem. Eur. J.* **2019**, *25*, 11365.
- [8] a) L. Falivene, Z. Cao, A. Petta, L. Serra, A. Poater, R. Oliva, V. Scarano, L. Cavallo, *Nat. Chem.* **2019**, *11*, 872; b) A. Poater, F. Ragone, S. Giudice, C. Costabile, R. Dorta, S. P. Nolan, L. Cavallo, *Organometallics* **2008**, *27*, 2679; c) A. Poater, F. Ragone, R. Mariz, R. Dorta, L. Cavallo, *Chem. Eur. J.* **2010**, *16*, 14348.
- [9] F. Neese, *WIREs Comput. Mol. Sci.* **2012**, *2*, 73.
- [10] a) C. Adamo, V. Barone, *J. Chem. Phys.* **1999**, *110*, 6158; b) J. P. Perdew, K. Burke, M. Ernzerhof, *Phys. Rev. Lett.* **1996**, *77*, 3865; c) J. P. Perdew, K. Burke, M. Ernzerhof, *Phys. Rev. Lett.* **1997**, *78*, 1396; d) C. Cardoso, A. T. Costa, A. H. MacDonald, J. Fernández-Rossier, *Phys. Rev. B Condens. Matter.* **1996**, *105*, 9982; e) M. Ernzerhof; G. E. Scuseria, *J. Chem. Phys.* **1999**, *110*, 5029; f) J. Tao, J. P. Perdew, V. N. Staroverov, G. E. Scuseria, *Phys. Rev. Lett.* **2003**, *91*, 146401; g) J. P. Perdew, J. Tao, V. N. Staroverov, G. E. Scuseria, *J. Chem. Phys.* **2004**, *120*, 6898.
- [11] a) A. Schäfer, H. Horn, R. Ahlrichs, *J. Chem. Phys.* **1992**, *97*, 2571; b) F. Weigend, R. Ahlrichs, *Phys. Chem. Chem. Phys.* **2005**, *7*, 3297.
- [12] a) S. Grimme, J. Antony, S. Ehrlich, H. Krieg, *J. Chem. Phys.* **2010**, *132*, 154104; b) S. Grimme, S. Ehrlich, L. Goerigk, *J. Comput. Chem.* **2011**, *32*, 1456.
- [13] a) F. Weigend, *Phys. Chem. Chem. Phys.* **2006**, *8*, 1057; b) D. A. Pantazis, F. Neese, *J. Chem. Theory Comput.* **2009**, *5*, 2229; c) D. A. Pantazis, F. Neese, *Theor. Chem. Acc.* **2012**, *131*, 1292; d) D. A. Pantazis, F. Neese, *J. Chem. Theory Comput.* **2011**, *7*, 677.
- [14] V. Barone, M. Cossi, *J. Phys. Chem. A* **1998**, *102*, 1995.
- [15] D. A. Pantazis, X. Y. Chen, C. R. Landis, F. Neese, *J. Chem. Theory Comput.* **2008**, *4*, 908.
- [16] E. F. Pettersen, T. D. Goddard, C. C. Huang, G. S. Couch, D. M. Greenblatt, E. C. Meng, T. E. Ferrin, *J. Comput. Chem.* **2004**, *13*, 1605.

Supporting Information

Highly Efficient Mechanochromic TADF in the Deep Red to Near-IR in Copper(I) [2.2]Isoindolinophanyl-Carbene Carbazolates

André M. T. Muthig, Sabyasachi Maity, Justin Krieger, Andrei Belyaev, Benjamin Hupp, Björn Ewald, Jens Pflaum, Andreas Steffen

Table of Contents

1. General Procedures	1
2. Characterization Data	2
3. NMR spectra	8
4. X-ray characterization data	14
5. Structural Details	20
6. Photophysical Measurements	25
7. UV-Visible Spectroscopy	26
8. Emission Studies	27
9. TD-DFT calculations	36
10. References	40

1. General Procedures

All manipulations were carried out under an inert atmosphere of argon using standard Schlenk link⁽¹⁾ or glovebox techniques (GS MEGA E-Line, <0.5 ppm of H₂O and O₂). All reagents were used as supplied. Solvents such as tetrahydrofuran (THF), dichloromethane (DCM), cyclohexane, diethyl ether and n-pentane were used at HPLC grade purity from commercial sources (VWR and Fisher Chemicals) and dried using PureSolv MD 7 drying system.

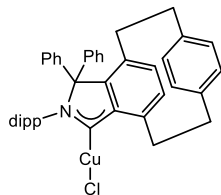
NMR spectra were recorded on a Bruker Avance III HD NanoBay 400 or 600 MHz; δ and chemical shifts (δ) are given in ppm relative to TMS, coupling constants (J) in Hz. The solvent signals were used as references, and the chemical shifts were converted to the TMS scale. CHN elemental analyses were performed on a Micro cube (Elementar).

(HiPC)(OTf), 1-Methyl-9H-carbazole and 1-Methoxy-9H-carbazole were synthesised according to literature procedures.^[2,3]

The potassium salts of 9H-carbazole, 3,6-ditert-butyl-9H-carbazole, 1-Methyl-9H-carbazole, and 1-Methoxy-9H-carbazole were prepared by deprotonating the respective carbazoles with KHMDS in a 1:1 ratio in diethyl ether. After 24 hours, the respective potassium salt precipitated from the solution and was washed twice with 4 ml of diethyl ether. The spectroscopic data matches the reported literature.

2. Characterization Data

Synthesis of 1

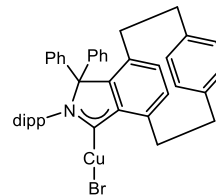


At -85°C, a solution of 69 mg (0.43 mmol, 1.00 equiv.) KHMDS in 2 ml THF was slowly added to a suspension of 300 mg (423 μmol, 1.00 equiv.) (HiPC)(OTf) and 70 mg copper(I) chloride dimethyl sulfide complex (0.44 mmol, 1.05 equiv.) in 20 ml THF. The yellow-orange suspension was warmed to room temperature and stirred overnight. All volatile components of the yellow-green suspension were removed under reduced pressure. After extraction with DCM and filtration over basic aluminum oxide, the filtrate was reduced to one-third volume, and the crude product was precipitated by the addition of n-pentane and washed twice with 2 ml n-pentane. The product was obtained by vapour diffusion of n-pentane into a THF/cyclohexane solution as orange crystals of compound **1** crystallized as 2:3 with THF (112 mg, 170 μmol, 40%).

The product slowly decomposes, and yellow-green crystals of (HiPC)(OTf) can be isolated from the decomposed mixture. To minimize the decomposition process, compound **1** was kept at -35°C inside the glovebox.

¹H-NMR (THF-*d*₈, 600 MHz, 298 K): 7.86 – 7.76 (m, 1H, Ar–H), 7.70 – 7.61 (m, 1H, Ar–H), 7.43 (tt, *J* = 7.3, 1.2 Hz, 1H, Ar–H), 7.37 – 7.30 (m, 1H, Ar–H), 7.27 – 7.21 (m, 4H, Ar–H), 7.17 – 6.97 (br, 2H, Ar–H), 6.94 (d, *J* = 8.1 Hz, 1H, Ar–H), 6.90 (dd, *J* = 7.7, 2.0 Hz, 1H, Ar–H), 6.78 (dd, *J* = 7.7, 1.9 Hz, 1H, Ar–H), 6.73 (dd, *J* = 5.4, 3.8 Hz, 1H, Ar–H), 6.66 (d, *J* = 7.6 Hz, 1H, Ar–H), 6.59 – 6.55 (m, 1H, Ar–H), 6.37 (dd, *J* = 8.2, 2.0 Hz, 1H, Ar–H), 5.00 (dd, *J* = 8.2, 2.0 Hz, 1H, Ar–H), 4.80 (ddd, *J* = 13.7, 10.4, 4.9 Hz, 1H, Ar–H), 3.54 (q, *J* = 6.7 Hz, 1H), 3.51 – 3.44 (m, 1H), 3.38 (q, *J* = 7.0 Hz, 1H), 3.22 (ddd, *J* = 13.3, 10.8, 4.9 Hz, 1H), 2.97 – 2.89 (m, 1H), 2.70 (ddd, *J* = 13.3, 10.2, 6.0 Hz, 1H), 2.53 (ddd, *J* = 14.1, 10.0, 6.0 Hz, 1H), 2.40 (ddd, *J* = 12.7, 9.9, 2.0 Hz, 1H), 1.35 (d, *J* = 6.7 Hz, 3H), 1.10 (dt, *J* = 13.0, 6.8 Hz, 2H), 0.48 (d, *J* = 6.7 Hz, 3H), 0.80 (d, *J* = 6.7 Hz, 3H), -0.20 (d, *J* = 6.7 Hz, 3H); **¹³C {¹H} NMR** (THF-*d*₈, 151 MHz, 298 K): 229.60 (CCu), 149.78 (Ar–CH), 146.03 (Ar–CH), 144.98 (Ar–CH), 143.28 (Ar–CH), 143.25 (Ar–CH), 140.54 (Ar–CH), 139.79 (Ar–CH), 139.49 (Ar–CH), 139.10 (Ar–CH), 136.55 (Ar–CH), 136.24 (Ar–CH), 134.89 (Ar–CH), 133.70 (Ar–CH), 133.05 (Ar–CH), 133.00 (Ar–CH), 132.77 (Ar–CH), 131.73 (Ar–CH), 131.13 (Ar–CH), 130.48 (Ar–CH), 129.65 (Ar–CH), 129.37 (Ar–CH), 128.43 (Ar–CH), 126.04 (Ar–CH), 124.52 (Ar–CH), 96.02, 35.78 (CH₂), 35.02 (CH₂), 34.57 (CH₂), 30.76 (CH₂), 30.49 (CH), 30.05 (CH), 27.25 (CH₃), 26.37 (CH₃), 23.35 (CH₃), 21.53 (CH₃); **EA** calc. for [(C₄₂H₄₁ClCuN)₂·((CH₂)₄O)₃] C, 75.17; H, 6.97; N, 1.83; found C: 75.1; H: 6.9; N: 1.9.

Synthesis of 2



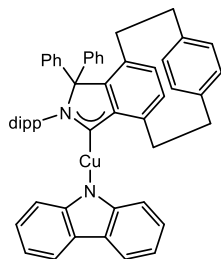
At -85°C, a solution of 69 mg (0.43 mmol, 1.00 equiv.) KHMDS in 2 ml THF was slowly added to a suspension of 300 mg (423 μmol, 1.00 equiv.) (HiPC)(OTf) and 87 mg copper(I) bromide dimethyl sulfide complex (0.43 mmol, 1.05 equiv.) in 20 ml THF. The yellow-orange suspension was warmed to room temperature and stirred overnight. All volatile components of the yellow-green suspension were removed under reduced pressure. After extraction with DCM and filtration over basic aluminum oxide, the filtrate was reduced to one-third volume, and the crude product was precipitated by the addition of n-pentane and washed twice with 2 ml n-pentane. The product was obtained by vapour diffusion of n-pentane into a THF/cyclohexane solution as orange crystals of compound **2** (21 mg, 30 μmol, 7%).

Low yield was observed for **2** in comparison to **1**, maybe due to incorporation of air or moisture during the reaction process.

The product slowly decomposes, and yellow-green crystals of (HiPC)(OTf) can be isolated from the decomposed mixture. To minimize the decomposition process, compound **2** was kept at -35°C inside the glovebox.

¹H-NMR (THF-*d*₈, 400 MHz, 298 K): 7.88 – 7.78 (br, 1H, Ar–H), 7.70 – 7.61 (br, 1H, Ar–H), 7.43 (tt, *J* = 7.3, 1.1 Hz, 1H, Ar–H), 7.36 – 7.29 (br, 1H, Ar–H), 7.28 – 7.19 (m, 4H, Ar–H), 7.15 – 7.03 (br, 2H, Ar–H), 6.97 – 6.91 (br, 1H, Ar–H), 6.90 (dd, *J* = 7.7, 2.0 Hz, 1H, Ar–H), 6.78 (dd, *J* = 7.7, 2.0 Hz, 1H, Ar–H), 6.73 (dd, *J* = 5.5, 3.8 Hz, 1H, Ar–H), 6.66 (dd, *J* = 7.6, 0.9 Hz, 1H, Ar–H), 6.57 (dd, *J* = 7.6, 0.9 Hz, 1H, Ar–H), 6.38 (dd, *J* = 8.2, 2.0 Hz, 1H, Ar–H), 5.01 (dd, *J* = 8.2, 2.0 Hz, 1H, Ar–H), 4.81 (ddd, *J* = 13.5, 10.3, 4.8 Hz, 1H, Ar–H), 3.55 – 3.50 (m, 1H), 3.49 – 3.44 (m, 1H), 3.38 (q, *J* = 7.0 Hz, 1H), 3.22 (ddd, *J* = 13.2, 10.7, 4.9 Hz, 1H), 2.93 (dd, *J* = 13.9, 10.4 Hz, 1H), 2.70 (ddd, *J* = 13.1, 10.2, 5.9 Hz, 1H), 2.53 (ddd, *J* = 13.7, 9.8, 5.8 Hz, 1H), 2.48 – 2.35 (m, 1H), 1.35 (d, *J* = 6.7 Hz, 3H), 1.17 – 1.03 (m, 2H), 0.81 (d, *J* = 6.7 Hz, 3H), 0.47 (d, *J* = 6.7 Hz, 3H), -0.21 (d, *J* = 6.7 Hz, 3H); **EA** calc. for [C₄₂H₄₁BrCuN] C, 71.73; H, 5.88; N, 1.99; found C: 71.4; H: 6.0; N: 1.8.

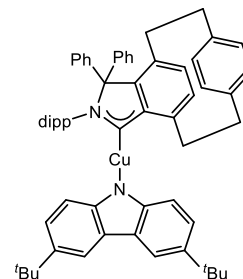
Synthesis of 3



In a 20 ml scintillation vial, 16 mg (78 μmol , 1.03 equiv.) KCz (potassium salt of 9H-carbazole) was added to a solution of 50 mg (76 μmol , 1.0 equiv.) [CuCl(iPC)] **1** in 4 ml THF and stirred overnight. The deep red suspension was mixed with 2 ml diethyl ether and filtered over basic aluminum oxide and concentrated to one-fourth of the volume under reduced pressure. The product was obtained by vapour diffusion of a mixture of cyclohexane and n-pentane into the solution as yellow crystals of compound **3** crystallized as 2:3 with THF (45 mg, 57 μmol , 75%).

¹H-NMR (THF-*d*₈, 600 MHz, 298 K): 7.96 (d, *J* = 8.2 Hz, 1H, Ar-H), 7.83 (dt, *J* = 7.5, 1.4 Hz, 2H, Ar-H), 7.67 (t, *J* = 7.8 Hz, 1H, Ar-H), 7.49 (t, *J* = 7.8 Hz, 1H, Ar-H), 7.46 – 7.42 (m, 1H, Ar-H), 7.41 – 7.34 (m, 2H, Ar-H), 7.29 (t, *J* = 7.1 Hz, 1H, Ar-H), 7.17 (br, 2H, Ar-H), 7.00 (d, *J* = 8.2 Hz, 1H, Ar-H), 6.97 (d, *J* = 1.4 Hz, 1H, Ar-H), 6.96 (q, *J* = 1.6 Hz, 2H, Ar-H), 6.96 – 6.93 (m, 2H, Ar-H), 6.81 (q, *J* = 2.2 Hz, 1H, Ar-H), 6.79 (d, *J* = 1.0 Hz, 1H, Ar-H), 6.78 (d, *J* = 0.8 Hz, 1H, Ar-H), 6.77 (d, *J* = 1.1 Hz, 1H, Ar-H), 6.74 (q, *J* = 1.0 Hz, 1H, Ar-H), 6.73 – 6.70 (m, 2H, Ar-H), 6.64 – 6.58 (m, 1H, Ar-H), 6.50 (dd, *J* = 8.1, 2.2 Hz, 1H, Ar-H), 5.15 – 5.12 (m, 1H, Ar-H), 5.11 – 5.08 (m, 1H), 3.89 (dd, *J* = 13.7, 10.6 Hz, 1H), 3.74 – 3.67 (m, 1H), 3.66 – 3.63 (m, 1H), 3.37 (dtd, *J* = 9.2, 7.2, 5.3 Hz, 1H), 2.97 (dd, *J* = 14.0, 10.6 Hz, 1H), 2.73 (tdd, *J* = 10.0, 7.1, 4.2 Hz, 1H), 2.60 (ddd, *J* = 14.8, 10.0, 5.9 Hz, 1H), 2.42 (t, *J* = 11.6 Hz, 1H), 1.28 – 1.21 (m, 1H), 1.13 (d, *J* = 6.9 Hz, 3H), 0.87 (d, *J* = 8.2 Hz, 3H), 0.50 (d, *J* = 6.7 Hz, 3H), -0.16 (d, *J* = 6.7 Hz, 3H); **¹³C {¹H} NMR** (THF-*d*₈, 151 MHz, 298 K): 231.03 (CCu), 151.14 (Ar-CH), 150.52 (Ar-CH), 146.54 (Ar-CH), 144.87 (Ar-CH), 143.52 (Ar-CH), 140.41 (Ar-CH), 140.04 (Ar-CH), 139.62 (Ar-CH), 136.53 (Ar-CH), 136.46 (Ar-CH), 135.10 (Ar-CH), 133.80 (Ar-CH), 133.23 (Ar-CH), 133.09 (Ar-CH), 132.80 (Ar-CH), 131.25 (Ar-CH), 130.68 (Ar-CH), 129.77 (Ar-CH), 129.49 (Ar-CH), 126.64 (Ar-CH), 125.55 (Ar-CH), 125.27 (Ar-CH), 123.66 (Ar-CH), 119.56 (Ar-CH), 115.78 (Ar-CH), 115.22 (Ar-CH), 96.17, 35.84 (CH₂), 35.23 (CH₂), 35.06 (CH₂), 30.99 (CH₂), 30.57 (CH), 30.24 (CH), 27.01 (CH₃), 26.37 (CH₃), 23.41 (CH₃), 21.89 (CH₃); **EA** calc. for [(C₅₄H₄₉CuN₂)₂·((CH₂)₄O)₃] C, 80.28; H, 6.85; N, 3.12; found C: 79.9; H: 6.9; N: 3.3.

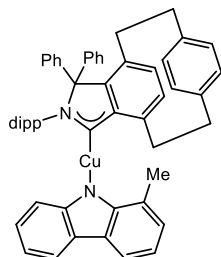
Synthesis of 4



In a 20 ml scintillation vial, 28 mg (77 μmol , 1.00 equiv.) [KCz^{tBu} · (Et₂O)_{2/3}] (potassium salt of 3,6-ditert-butyl-9H-carbazole) was added to a solution of 50 mg (76 μmol , 1.00 equiv.) [CuCl(iPC)] **1** in 4 ml THF and stirred overnight. The deep red suspension was mixed with 2 ml diethyl ether and filtered over basic aluminum oxide and concentrated to one-fourth of the volume under reduced pressure. The product was obtained by vapour diffusion of a mixture of cyclohexane and n-pentane into the solution as deep yellow crystals of compound **4** crystallised as 4:5 with THF (51 mg, 57 μmol , 75%).

¹H-NMR (*d*₈-THF, 600 MHz, 298 K): 7.94 (d, *J* = 8.2 Hz, 1H, Ar-H), 7.90 (d, *J* = 2.0 Hz, 2H, Ar-H), 7.66 (t, *J* = 7.8 Hz, 1H, Ar-H), 7.49 (t, *J* = 7.8 Hz, 1H, Ar-H), 7.43 (tt, *J* = 7.4, 1.1 Hz, 1H, Ar-H), 7.39 (d, *J* = 1.5 Hz, 1H, Ar-H), 7.37 (d, *J* = 1.5 Hz, 1H, Ar-H), 7.35 – 7.30 (br, 1H, Ar-H), 7.30 – 7.25 (m, 1H, Ar-H), 7.23 – 7.10 (br, 2H, Ar-H), 7.09 (d, *J* = 2.1 Hz, 1H, Ar-H), 7.07 (d, *J* = 2.1 Hz, 1H, Ar-H), 7.05 – 6.98 (m, 1H, Ar-H), 6.98 – 6.96 (m, 1H, Ar-H), 6.96 (d, *J* = 1.5 Hz, 1H, Ar-H), 6.90 (dd, *J* = 7.6, 1.9 Hz, 1H, Ar-H), 6.76 (dd, *J* = 7.7, 1.9 Hz, 1H, Ar-H), 6.68 (d, *J* = 8.4 Hz, 2H, Ar-H), 6.63 – 6.58 (m, 1H, Ar-H), 6.55 – 6.51 (m, 1H, Ar-H), 6.47 (dd, *J* = 8.2, 2.0 Hz, 1H, Ar-H), 5.13 – 5.10 (m, 1H, Ar-H), 5.09 (d, *J* = 5.8 Hz, 1H), 3.82 (ddd, *J* = 13.6, 10.6, 2.9 Hz, 1H), 3.67 (ddd, *J* = 13.9, 10.7, 3.2 Hz, 1H), 3.28 (ddd, *J* = 13.2, 10.7, 5.1 Hz, 1H), 2.94 (ddd, *J* = 13.7, 10.3, 2.2 Hz, 1H), 2.69 (ddd, *J* = 13.1, 10.2, 5.9 Hz, 1H), 2.58 (ddd, *J* = 13.9, 9.9, 5.9 Hz, 1H), 2.41 (ddd, *J* = 12.7, 10.0, 1.8 Hz, 1H), 1.40 (s, 18H), 1.27 – 1.18 (m, 2H), 1.12 (d, *J* = 7.0 Hz, 3H), 0.84 (d, *J* = 6.7 Hz, 3H), 0.49 (d, *J* = 6.7 Hz, 3H), -0.17 (d, *J* = 6.6 Hz, 3H); **¹³C {¹H} NMR** (*d*₈-THF, 151 MHz, 298 K): 231.18 (CCu), 150.47 (Ar-CH), 149.81 (Ar-CH), 146.50 (Ar-CH), 144.85 (Ar-CH), 143.50 (Ar-CH), 143.35 (Ar-CH), 140.42 (Ar-CH), 140.02 (Ar-CH), 139.96 (Ar-CH), 139.55 (Ar-CH), 137.73 (Ar-CH), 136.58 (Ar-CH), 136.37 (Ar-CH), 135.15 (Ar-CH), 133.86 (Ar-CH), 133.20 (Ar-CH), 133.06 (Ar-CH), 132.82 (Ar-CH), 131.19 (Ar-CH), 130.58 (Ar-CH), 129.72 (Ar-CH), 129.43 (Ar-CH), 126.60 (Ar-CH), 125.45 (Ar-CH), 125.20 (Ar-CH), 121.26 (Ar-CH), 115.47 (Ar-CH), 114.70 (Ar-CH), 96.06, 35.82 (CH₂), 35.19 (CH₂), 35.06 (CH₂), 35.02 (CH₂), 32.79, 30.96 (CH), 30.23 (CH), 27.06 (CH₃), 26.37 (CH₃), 23.40 (CH₃), 23.20 (CH₃(Cz^{tBu})), 21.88 (CH₃); **EA** calc. for [(C₆₂H₆₅CuN₂)₄·((CH₂)₄O)₅] C, 81.13; H, 7.62; N, 2.82; found C: 81.0; H: 7.3; N: 3.1.

Synthesis of 5

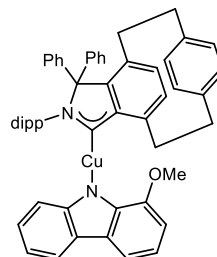


In a 20 ml scintillation vial, 17 mg (78 μmol , 1.00 equiv.) $\text{K}^{\text{Me}}\text{Cz}$ (potassium salt of 1-Methyl-9H-carbazole) was added to a solution of 50 mg (76 μmol , 1.00 equiv.) $[\text{CuCl}(\text{iPC})]$ **1** in 4 ml THF and stirred overnight. The deep red suspension was mixed with 2 ml diethyl ether and filtered over basic aluminum oxide and concentrated to one-fourth of the volume under reduced pressure. The product was obtained by vapour diffusion of a mixture of cyclohexane and n-pentane into the solution as deep yellow crystals of compound **5** crystallised as 2:3 with THF (48 mg, 60 μmol , 79%).

The crystals obtained from the above procedure have poor reflections and thus poor data quality in SC-XRD measurements. The crystals were then dissolved in DCM, and vapour diffusion of the mixture of n-pentane and cyclohexane gave yellow crystals of **5** with much better data quality for SC-XRD measurements.

$^1\text{H-NMR}$ (THF- d_6 , 600 MHz, 298 K): 7.95 (d, $J = 8.1$ Hz, 1H, Ar-H), 7.87 (dd, $J = 7.7, 0.7$ Hz, 1H, Ar-H), 7.78 (dd, $J = 7.8, 0.6$ Hz, 1H, Ar-H), 7.74 (t, $J = 7.6$ Hz, 1H, Ar-H), 7.66 – 7.51 (br, 1H, Ar-H), 7.48 (tt, $J = 7.3, 1.2$ Hz, 1H, Ar-H), 7.39 (t, $J = 7.8$ Hz, 2H, Ar-H), 7.29 (td, $J = 7.5, 3.8$ Hz, 3H, Ar-H), 7.25 – 7.19 (m, 2H, Ar-H), 7.02 (ddd, $J = 8.1, 5.5, 1.3$ Hz, 3H, Ar-H), 6.93 (dt, $J = 7.0, 1.1$ Hz, 1H, Ar-H), 6.90 (dd, $J = 7.6, 2.0$ Hz, 1H, Ar-H), 6.86 (dd, $J = 7.7, 1.6$ Hz, 1H, Ar-H), 6.84 – 6.81 (m, 1H, Ar-H), 6.81 – 6.76 (m, 2H, Ar-H), 6.69 (dd, $J = 7.5, 0.9$ Hz, 1H, Ar-H), 6.61 (dd, $J = 7.6, 0.9$ Hz, 1H, Ar-H), 6.40 (dd, $J = 8.1, 2.0$ Hz, 1H, Ar-H), 5.06 (dd, $J = 8.1, 2.0$ Hz, 1H, Ar-H), 4.97 (ddd, $J = 13.2, 10.4, 4.8$ Hz, 1H), 3.53 (ddd, $J = 13.4, 10.7, 3.5$ Hz, 1H), 3.18 (ddd, $J = 13.2, 10.7, 4.8$ Hz, 1H), 3.03 – 2.95 (m, 1H), 2.74 (ddd, $J = 13.0, 10.2, 5.8$ Hz, 1H), 2.68 – 2.62 (m, 1H), 2.61 (s, 3H), 2.42 (ddd, $J = 12.8, 9.9, 2.3$ Hz, 1H), 1.29 – 1.22 (m, 2H), 1.12 (d, $J = 7.0$ Hz, 1H), 1.09 (d, $J = 6.7$ Hz, 3H), 0.94 (d, $J = 6.7$ Hz, 3H), 0.47 (d, $J = 6.7$ Hz, 3H), -0.13 (d, $J = 6.7$ Hz, 3H); **^{13}C (^1H) NMR** (THF- d_6 , 151 MHz, 298 K): 231.57 (CCu), 151.34 (Ar-CH), 149.96 (Ar-CH), 149.79 (Ar-CH), 146.10 (Ar-CH), 145.00 (Ar-CH), 143.72 (Ar-CH), 140.46 (Ar-CH), 140.13 (Ar-CH), 139.89 (Ar-CH), 139.68 (Ar-CH), 136.70 (Ar-CH), 136.56 (Ar-CH), 135.25 (Ar-CH), 133.92 (Ar-CH), 133.19 (Ar-CH), 132.90 (Ar-CH), 132.87 (Ar-CH), 131.93 (Ar-CH), 131.13 (Ar-CH), 130.77 (Ar-CH), 129.74 (Ar-CH), 129.55 (Ar-CH), 129.52 (Ar-CH), 128.35 (Ar-CH), 126.49 (Ar-CH), 126.03 (Ar-CH), 125.46 (Ar-CH), 125.02 (Ar-CH), 124.80 (Ar-CH), 123.42 (Ar-CH), 121.67 (Ar-CH), 119.69 (Ar-CH), 117.76 (Ar-CH), 116.01 (Ar-CH), 115.93 (Ar-CH), 115.83 (Ar-CH), 96.26, 35.92 (CH_2), 35.06 (CH_2), 34.78 (CH_2), 31.01 (CH_2), 30.70 (CH), 30.38 (CH), 27.13 (CH_3), 26.37 (CH_3), 23.67 (CH_3), 21.89 (CH_3), 21.06 ($\text{CH}_3^{\text{Me}}\text{Cz}$); **EA** calc. for $[(\text{C}_{55}\text{H}_{51}\text{CuN}_2)_2 \cdot ((\text{CH}_2)_4\text{O})_3]$ C, 80.36; H, 6.97; N, 3.07; found C: 80.4; H: 6.9; N: 3.3.

Synthesis of 6



In a 20 ml scintillation vial, 20 mg (76 μmol , 1.00 equiv.) $[\text{K}^{\text{OMe}}\text{Cz} \cdot (\text{Et}_2\text{O})_{1/3}]$ (potassium salt of 1-Methoxy-9H-carbazole) was added to a solution of 50 mg (76 μmol , 1.00 equiv.) $[\text{CuCl}(\text{iPC})]$ **1** in 4 ml THF and stirred overnight. The deep red suspension was mixed with 2 ml diethyl ether and filtered over basic aluminum oxide and concentrated to one-fourth of the volume under reduced pressure. The product was obtained by vapour diffusion of a mixture of cyclohexane and n-pentane into the solution as deep yellow crystals of compound **6** crystallises as 1:1 with THF (46 mg, 56 μmol , 74%).

$^1\text{H-NMR}$ (THF- d_6 , 600 MHz, 298 K): 8.01 (d, $J = 8.1$ Hz, 1H, Ar-H), 7.80 (ddd, $J = 7.7, 1.4, 0.7$ Hz, 1H, Ar-H), 7.73 (t, $J = 7.7$ Hz, 1H, Ar-H), 7.55 (dd, $J = 7.6, 1.0$ Hz, 1H, Ar-H), 7.47 (tt, $J = 7.3, 1.1$ Hz, 1H, Ar-H), 7.38 (t, $J = 7.5$ Hz, 1H, Ar-H), 7.27 (ddd, $J = 7.3, 6.2, 1.8$ Hz, 2H, Ar-H), 7.25 – 7.21 (m, 2H, Ar-H), 7.20 – 7.07 (m, 1H, Ar-H), 7.06 – 6.89 (m, 2H, Ar-H), 6.87 (ddd, $J = 7.7, 3.3, 1.6$ Hz, 2H, Ar-H), 6.83 (dt, $J = 8.2, 0.9$ Hz, 1H, Ar-H), 6.81 (d, $J = 1.2$ Hz, 1H, Ar-H), 6.80 – 6.79 (m, 2H, Ar-H), 6.78 (d, $J = 1.8$ Hz, 1H, Ar-H), 6.74 (ddt, $J = 7.7, 5.9, 1.0$ Hz, 2H, Ar-H), 6.67 (dt, $J = 7.5, 1.2$ Hz, 1H, Ar-H), 6.60 – 6.56 (m, 1H, Ar-H), 6.39 (dd, $J = 8.1, 1.9$ Hz, 1H, Ar-H), 5.02 (ddd, $J = 13.6, 10.4, 5.0$ Hz, 1H, Ar-H), 4.96 – 4.91 (m, 1H), 4.05 (s, 3H), 3.70 (p, $J = 6.8$ Hz, 1H), 3.56 – 3.51 (m, 1H), 3.44 (ddd, $J = 13.4, 10.4, 3.1$ Hz, 1H), 3.13 (ddd, $J = 12.8, 10.9, 4.9$ Hz, 1H), 3.01 – 2.94 (m, 1H), 2.72 (ddd, $J = 12.9, 10.2, 6.0$ Hz, 1H), 2.62 (ddd, $J = 13.9, 9.9, 6.1$ Hz, 1H), 2.48 – 2.41 (m, 1H), 1.33 – 1.29 (m, 1H), 1.27 (d, $J = 6.7$ Hz, 3H), 0.98 (d, $J = 6.7$ Hz, 3H), 0.52 (d, $J = 6.7$ Hz, 3H), -0.14 (d, $J = 6.7$ Hz, 3H); **^{13}C (^1H) NMR** (THF- d_6 , 151 MHz, 298 K): 232.14 (CCu), 150.63 (Ar-CH), 149.95 (Ar-CH), 148.35 (Ar-CH), 146.17 (Ar-CH), 145.61 (Ar-CH), 143.94 (Ar-CH), 143.39 (Ar-CH), 141.26 (Ar-CH), 140.60 (Ar-CH), 139.80 (Ar-CH), 139.72 (Ar-CH), 139.60 (Ar-CH), 136.53 (Ar-CH), 136.04 (Ar-CH), 135.38 (Ar-CH), 133.92 (Ar-CH), 133.08 (Ar-CH), 132.91 (Ar-CH), 132.80 (Ar-CH), 131.84 (Ar-CH), 131.11 (Ar-CH), 130.48 (Ar-CH), 129.65 (Ar-CH), 129.40 (Ar-CH), 128.25 (Ar-CH), 126.82 (Ar-CH), 126.20 (Ar-CH), 125.63 (Ar-CH), 124.79 (Ar-CH), 123.25 (Ar-CH), 119.56 (Ar-CH), 116.35 (Ar-CH), 115.69 (Ar-CH), 115.59 (Ar-CH), 113.32 (Ar-CH), 103.88 (Ar-CH), 96.16, 55.70 ($\text{CH}_3\text{O}^{\text{OMe}}\text{Cz}$), 36.02 (CH_2), 35.03 (CH_2), 34.93 (CH_2), 30.95 (CH_2), 30.70 (CH), 30.29 (CH), 27.08 (CH_3), 25.78 (CH_3), 23.54 (CH_3), 21.88 (CH_3); **EA** calc. for $[(\text{C}_{55}\text{H}_{51}\text{CuN}_2)_2 \cdot ((\text{CH}_2)_4\text{O})_3]$ C, 79.47; H, 6.67; N, 3.14; found C: 79.4; H: 6.3; N: 3.4.

3. NMR spectra

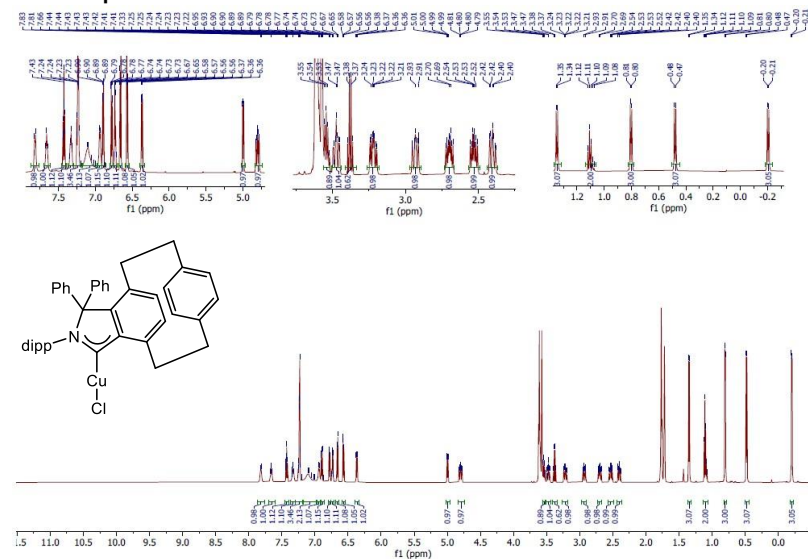


Figure S1. ¹H-NMR (600 MHz, THF-d₈, 298 K) of 1.

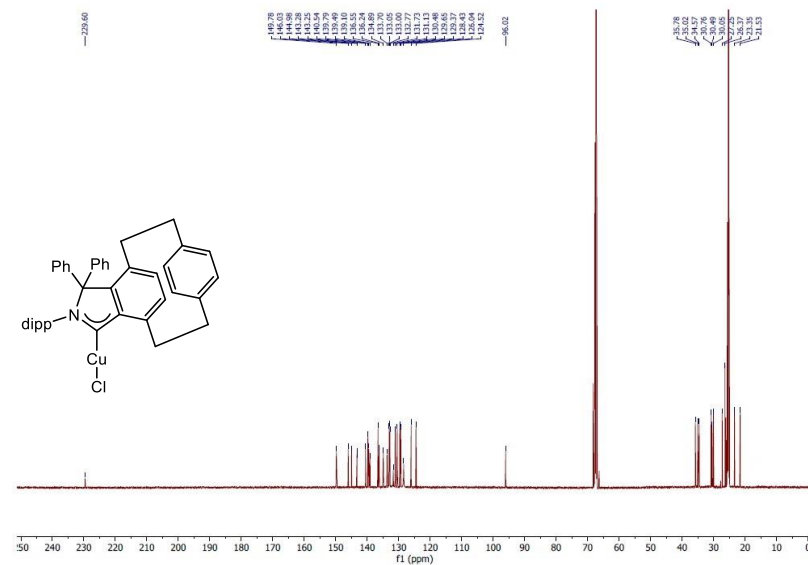


Figure S2. ¹³C-NMR (151 MHz, THF-d₈, 298 K) of 1.

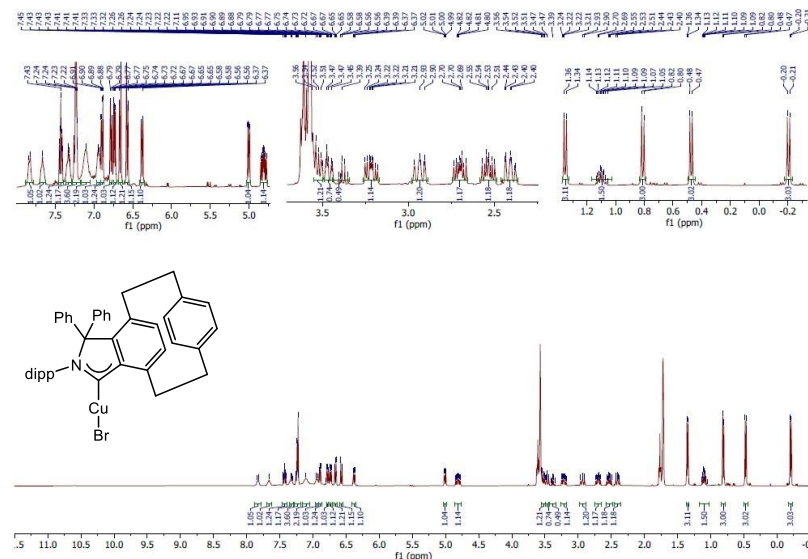
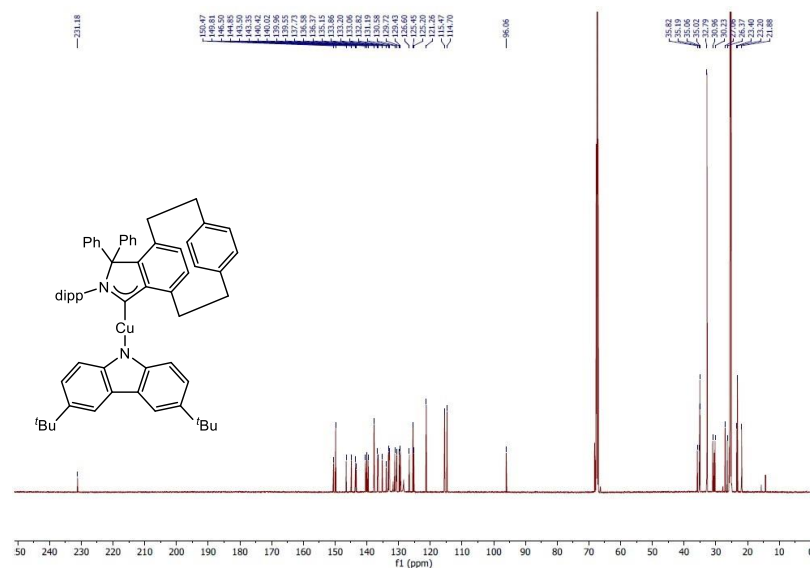
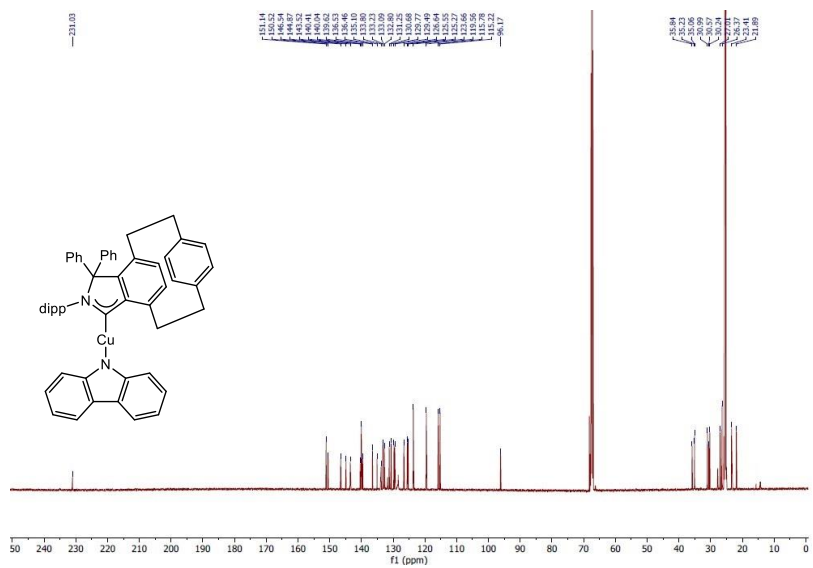
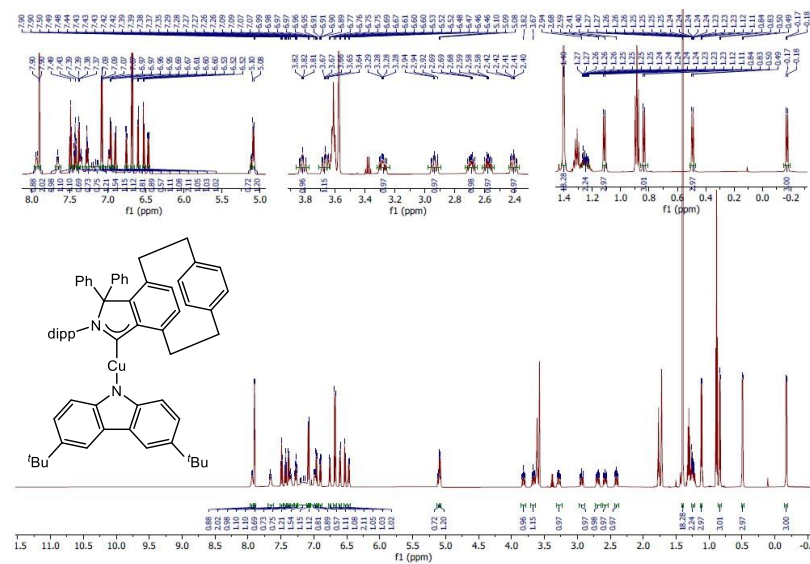
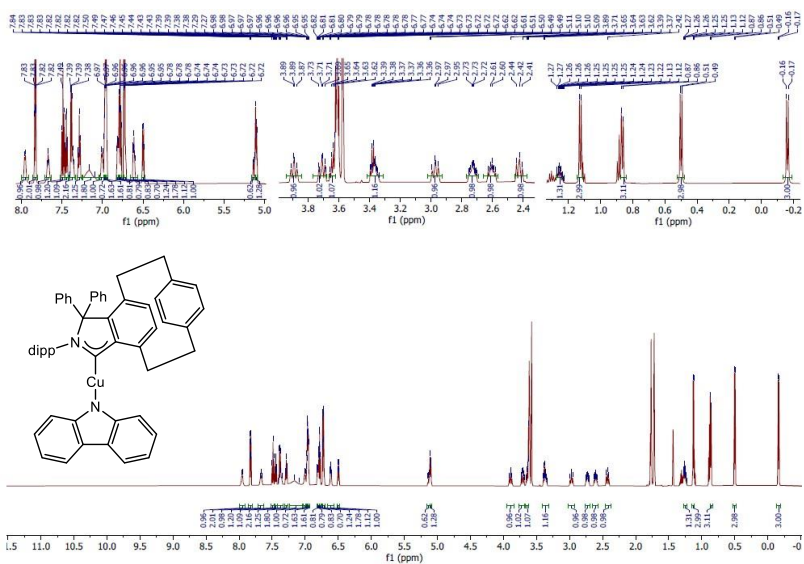
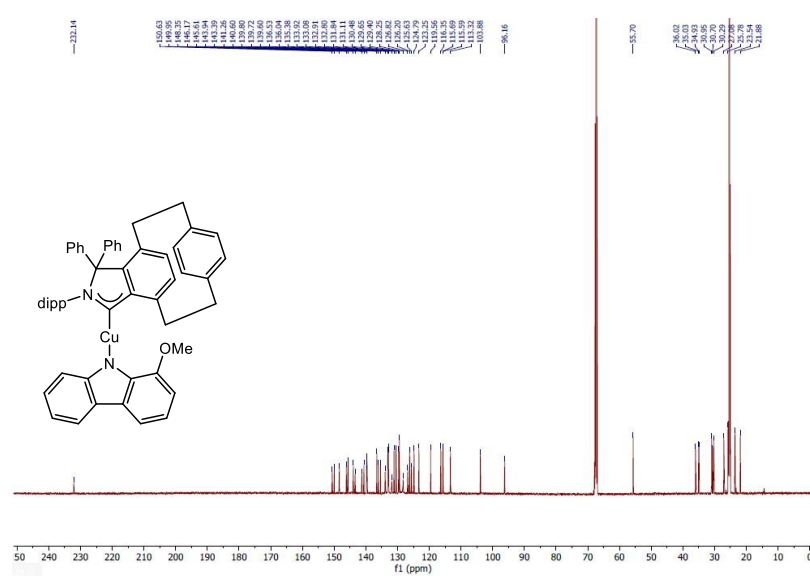
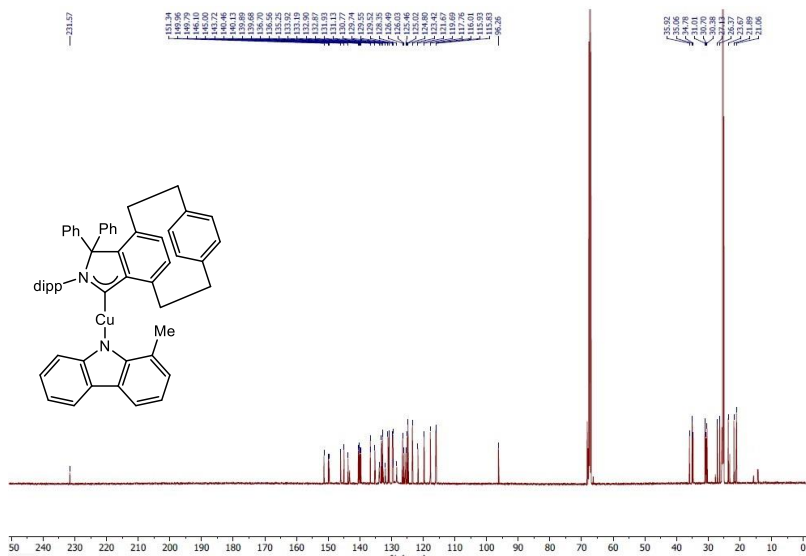
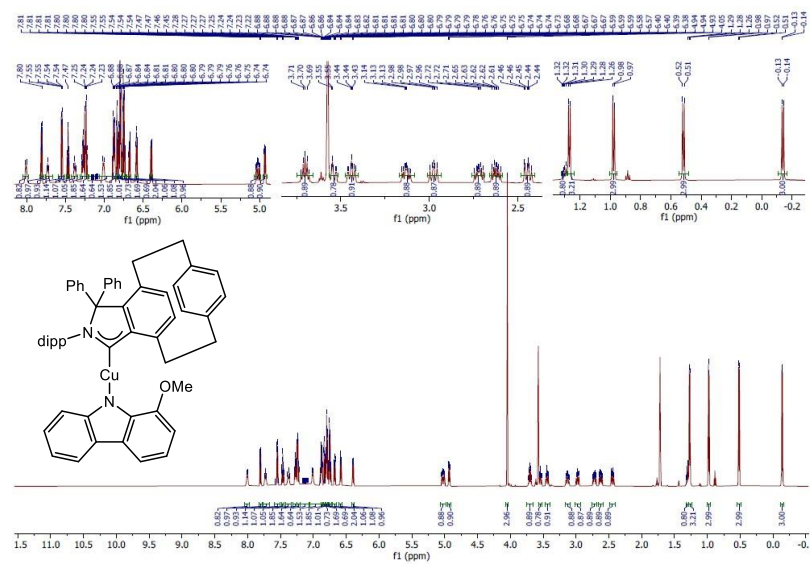
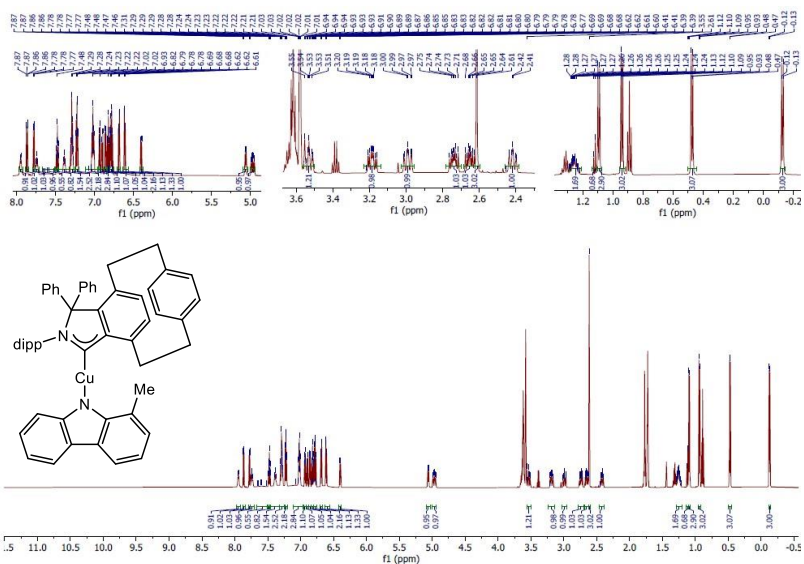


Figure S3. ¹H-NMR (400 MHz, THF-d₈, 298 K) of 2.





4. X-ray characterization data

General part

X-ray diffraction determination

The crystals of **1–6** were immersed in a film of NVH or perfluoropolyether oil, mounted on a polyimide microloop (MiTeGen) and transferred to a stream of cold nitrogen (Bruker Kryoflex2), and measured at a temperature of 100 or 109 K. The X-ray diffraction data were collected on a Bruker D8 diffractometer with a CMOS Photon 100 and multilayer optics monochromated MoK α (0.71073Å) radiation (INCOATEC microfocuss sealed tube). The frames were integrated with the Bruker SAINT software package using a narrow-frame algorithm. The APEX3 v2018.7-0 program package was used for cell refinements and data reductions. The structure was solved using the intrinsic phasing method,^[4] refined and visualized with the OLEX2-1.5 program.^[5] A semiempirical absorption correction (SADABS) was applied to all data. All non-hydrogen atoms were refined anisotropically. Hydrogen atoms were included in structure factors calculations. All Hydrogen atoms were assigned to idealized geometric positions. The unit cells of the **3** and **4** contain disordered solvent molecules which have been treated as a diffuse contribution to the overall scattering without specific atom positions by SQUEEZE/PLATON.^[6] The crystallographic details are summarized in Tables 1 and 2. CCDC **2271628**, **2386570-2386573**, and **2386579** numbers contain the supplementary crystallographic data for this paper.

The crystal quality of **2** [Cu(Br)(iPC)] was sufficient to confirm the connectivity.

X-ray Structures

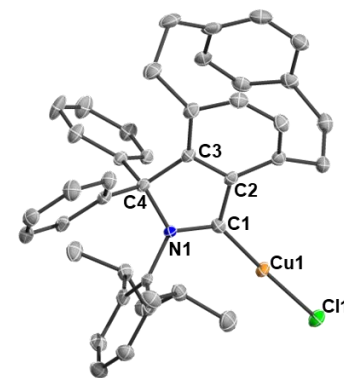


Figure S12. X-ray solid-state structure of **1** [CuCl(iPC)] (**S-isomer**). Thermal ellipsoids were drawn at the 50% probability level; H atoms, solvent molecule and R-isomer have been omitted for clarity. Selected bond lengths (Å) and angles [deg]: C1-N1 1.323(4), C1-Cu1 1.882(2), Cu1-Cl1 2.1236(9), C1-Cu1-Cl1 174.77(6).

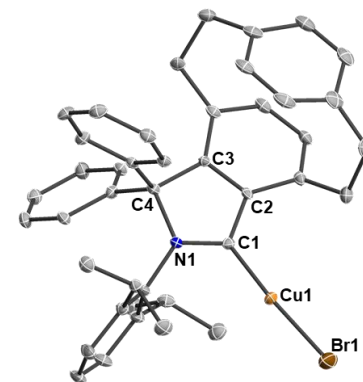


Figure S13. X-ray solid-state structure of **2** [CuBr(iPC)] (**R-isomer**). Thermal ellipsoids were drawn at the 50% probability level; H atoms and S-isomer have been omitted for clarity. Selected bond lengths (Å) and angles [deg]: C1-N1 1.316(4), C1-Cu1 1.897(3), Cu1-Br1 2.2478(6), C1-Cu1-Br1 174.43(9).

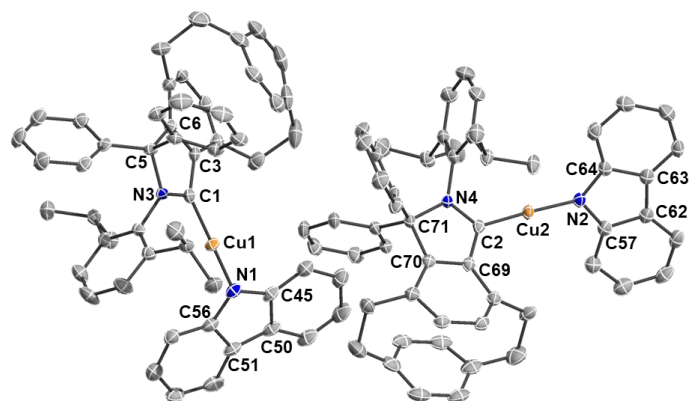


Figure S14. X-ray solid-state structure of **3** [Cu(Cz)(iPC)] (**R-isomers**). Thermal ellipsoids were drawn at the 50% probability level; H atoms, and S-isomers have been omitted for clarity. Selected bond lengths (Å) and angles [deg]: C1-N3 1.330(3), C1-Cu1 1.871(2), Cu1-N1 1.855(2), C1-Cu1-N1 174.87(9), C2-N4 1.325(3), C2-Cu2 1.873(2), Cu2-N2 1.858(2), C2-Cu2-N2 175.13(1).

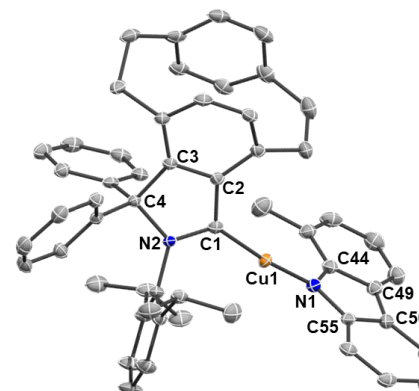


Figure S16. X-ray solid-state structure of **5** [Cu(^{Me}Cz)(iPC)] (**R,S-conformer**). Thermal ellipsoids were drawn at the 50% probability level; H atoms, solvent molecules and S,R-conformer have been omitted for clarity. Selected bond lengths (Å) and angles [deg]: C1-N2 1.325(2), C1-Cu1 1.872(2), Cu1-N1 1.859(2), C1-Cu1-N1 170.34(9).

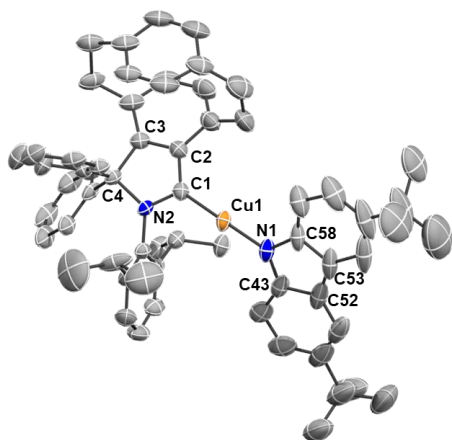


Figure S15. X-ray solid-state structure of **4** [Cu(Cz^{Bu})(iPC)] (**R-isomer**). Thermal ellipsoids were drawn at the 50% probability level; H atoms and S-isomer have been omitted for clarity. Selected bond lengths (Å) and angles [deg]: C1-N2 1.332(3), C1-Cu1 1.874(2), Cu1-N1 1.852(2), C1-Cu1-N1 178.10(9).

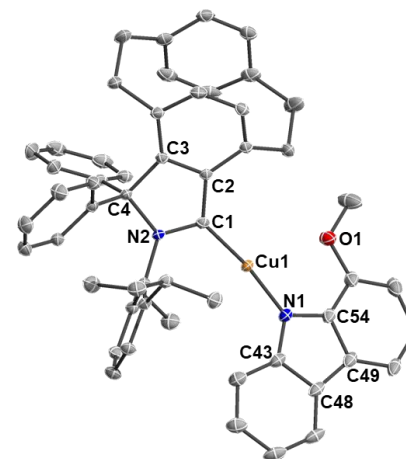


Figure S17. X-ray solid-state structure of **6** [Cu(^{OMe}Cz)(iPC)] (**S,R-conformer**). Thermal ellipsoids were drawn at the 50% probability level; H atoms, solvent molecules and R,S-conformer have been omitted for clarity. Selected bond lengths (Å) and angles [deg]: C1-N2 1.331(2), C1-Cu1 1.878(1), Cu1-N1 1.867(1), C1-Cu1-N1 171.27(7).

Table S1. Crystal data and structure refinement for 1, 3–6.

Identification code	1 [CuCl(iPC)]	3 [Cu(Cz)(iPC)]	4 [Cu(Cz ^{Bu})(iPC)]	5 [Cu ^{(Me)Cz} (iPC)]	6 [Cu ^{(OMe)Cz} (iPC)]
CCDC number	2271628	2386570	2386571	2386572	2386573
Empirical formula	C ₄₆ H ₄₉ ClCuNO	C ₅₄ H ₄₉ CuN ₂	C ₆₂ H ₆₅ CuN ₂	C ₅₉ H ₅₉ Cl ₂ CuN ₂	C ₆₂ H ₅₉ CuN ₂ O
Formula weight	730.85	789.49	901.70	930.52	911.65
Temperature [K]	100.00				
Crystal system	triclinic	triclinic	monoclinic	triclinic	monoclinic
Space group	P-1	P-1	P2 ₁ /n	P-1	C2/c
a [Å]	9.770(2)	14.5590(5)	19.7377(7)	12.6764(4)	20.6394(6)
b [Å]	15.193(4)	16.8310(6)	17.5008(5)	14.4116(5)	14.7201(4)
c [Å]	15.794(4)	19.7336(7)	20.3020(7)	15.3308(5)	31.6213(11)
α [°]	63.057(7)	89.1390(10)	90	69.3780(10)	90
β [°]	79.152(8)	84.7080(10)	102.2620(10)	74.5390(10)	97.1470(10)
γ [°]	86.052(8)	79.8220(10)	90	64.5130(10)	90
Volume [Å ³]	2052.4(9)	4739.2(3)	6852.8(4)	2344.15(14)	9532.4(5)
Z	2	4	4	2	8
ρ _{calc} [g/cm ³]	1.183	1.107	0.874	1.318	1.270
μ [mm ⁻¹]	0.630	0.496	0.349	0.622	0.504
F(000)	772.0	1664.0	1920.0	980.0	3856.0
Crystal size [mm ³]	0.2 × 0.05 × 0.05	0.177 × 0.12 × 0.101	0.092 × 0.078 × 0.034	0.201 × 0.097 × 0.054	0.144 × 0.111 × 0.08
Radiation type	MoKα (λ = 0.71073)				
2θ range for data collection [°]	5.38 to 50	5.244 to 53.554	4.654 to 60.094	5.642 to 60.178	4.132 to 60.04
Index ranges	-11 ≤ h ≤ 11, -18 ≤ k ≤ 18, -18 ≤ l ≤ 18	-18 ≤ h ≤ 18, -21 ≤ k ≤ 21, -24 ≤ l ≤ 24	-27 ≤ h ≤ 27, -21 ≤ k ≤ 24, -28 ≤ l ≤ 28	-17 ≤ h ≤ 17, -20 ≤ k ≤ 20, -21 ≤ l ≤ 21	-29 ≤ h ≤ 28, -20 ≤ k ≤ 20, -44 ≤ l ≤ 37
Reflections collected	47616	96378	122818	67750	49424
Independent reflections	7214 [R _{int} = 0.1267, R _{sigma} = 0.0739]	20172 [R _{int} = 0.0893, R _{sigma} = 0.0637]	19975 [R _{int} = 0.0710, R _{sigma} = 0.0483]	13722 [R _{int} = 0.0792, R _{sigma} = 0.0635]	13861 [R _{int} = 0.0311, R _{sigma} = 0.0316]
Data/restraint s/parameters	7214/6/455	20172/0/1035	19975/202/621	13722/138/597	13861/308/665
Goodness-of-fit on F ² (a)	1.025	1.036	1.041	1.024	1.055
Final R indexes [I >= 2σ (I)] (b)	R ₁ = 0.0576, wR ₂ = 0.1511	R ₁ = 0.0456, wR ₂ = 0.1198	R ₁ = 0.0724, wR ₂ = 0.1919	R ₁ = 0.0508, wR ₂ = 0.1180	R ₁ = 0.0449, wR ₂ = 0.1191
Final R indexes [all data] (b)	R ₁ = 0.0769, wR ₂ = 0.1670	R ₁ = 0.0702, wR ₂ = 0.1310	R ₁ = 0.0986, wR ₂ = 0.2092	R ₁ = 0.0803, wR ₂ = 0.1318	R ₁ = 0.0527, wR ₂ = 0.1241
Largest diff. peak/hole [e/Å ³]	0.98/-0.62	0.54/-0.38	0.86/-0.54	1.33/-1.00	1.52/-0.44

^{a)} Goof = S = [Σw(F_o²-F_c²)/(m-n)]^{1/2}, where m = number of reflexes and n = number of parameters; ^(b) R₁ = Σ||F_o-|F_c||/Σ|F_o|; wR₂ = [Σ[w(F_o²-F_c²)²]/Σ[(wF_o²)²]^{1/2}; w = 1/(σ²(F_o²)+(aP)²+bP), where P = (F_o²+2F_c²)/3

Table S2. Crystal data and structure refinement for 2.

Identification code	2 [CuBr(iPC)]
CCDC number	2386579
Empirical formula	C ₄₂ H ₄₁ BrCuN
Formula weight	703.21
Temperature [K]	109.00
Crystal system	monoclinic
Space group	P2 ₁ /n
a [Å]	12.3719(6)
b [Å]	14.6658(6)
c [Å]	18.0296(9)
α [°]	90
β [°]	90.052(2)
γ [°]	90
Volume [Å ³]	3271.4(3)
Z	4
ρ _{calc} [g/cm ³]	1.428
μ [mm ⁻¹]	1.921
F(000)	1456.0
Crystal size [mm ³]	0.302 × 0.084 × 0.072
Radiation type	MoKα (λ = 0.71073)
2θ range for data collection [°]	4.308 to 60.116
Index ranges	-17 ≤ h ≤ 17, -20 ≤ k ≤ 20, -25 ≤ l ≤ 25
Reflections collected	54326
Independent reflections	7113 [R _{int} = 0.0796, R _{sigma} = 0.0687]
Data/restraint s/parameters	7113/0/410
Goodness-of-fit on F ² (a)	1.084
Final R indexes [I >= 2σ (I)] (b)	R ₁ = 0.0601, wR ₂ = 0.1657
Final R indexes [all data] (b)	R ₁ = 0.0835, wR ₂ = 0.1931
Largest diff. peak/hole [e/Å ³]	0.70/-1.69

^{a)} Goof = S = [Σw(F_o²-F_c²)/(m-n)]^{1/2}, where m = number of reflexes and n = number of parameters; ^(b) R₁ = Σ||F_o-|F_c||/Σ|F_o|; wR₂ = [Σ[w(F_o²-F_c²)²]/Σ[(wF_o²)²]^{1/2}; w = 1/(σ²(F_o²)+(aP)²+bP), where P = (F_o²+2F_c²)/3

5. Structural Details

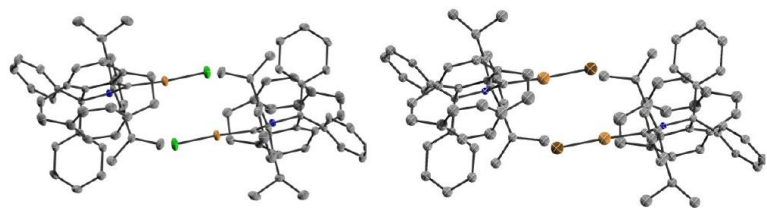


Figure S18. Aggregation of the complexes *rac*-[CuCl(iPC)] **1** (left) and *rac*-[CuBr(iPC)] **2** (right) in a single crystal at 100 K. Hydrogen atoms are omitted for clarity.

Table S3. Selected bond distances (in Å) and bond angles (in °) compounds **1** and **2** (X = Cl and Br).

	Cu-C _{carbene}	Cu-X	C1-N1	C _{carbene} -Cu-X	X-Cu-X'	Cu-Cu'	Cu-X'
1	1.887(2)	2.1233(9)	1.321(4)	174.77(10)	94.82(4)	3.7551(9)	3.2812(13)
2^a	1.897(3)	2.2478(6)	1.316(4)	174.43(9)	90.70	4.18(1)	5.06(8)

^aApproximate values are given for complex **2** due to poor data quality of crystal structure.

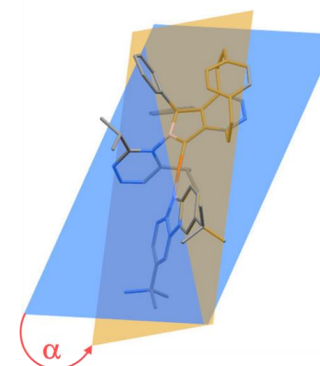


Figure S20. Dihedral angle $\alpha = 42.9(5)^\circ$ between blue plane (mean: N2C1C2) and yellow plane (mean: N1C43C58) in **4**.

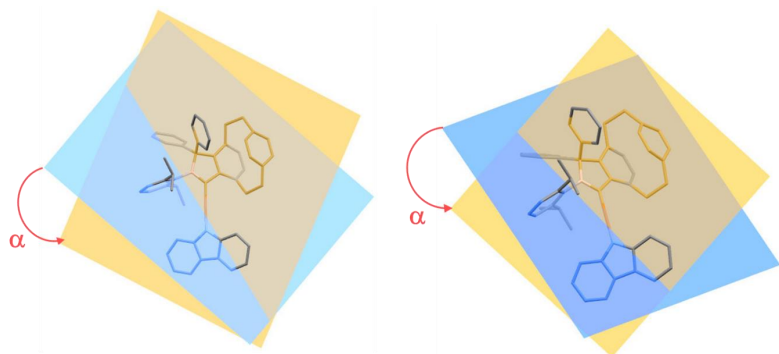


Figure S19. Dihedral angle in **3**. Right : Dihedral angle $\alpha = 46.4(2)^\circ$ between blue plane (mean: N3C1C3) and yellow plane (mean: N1C45C56). Left : Dihedral angle $\alpha = 52.2(4)^\circ$ between blue plane (mean: N4C2C69) and yellow plane (mean: N2C57C64).

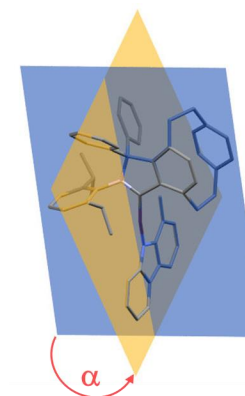


Figure S21. Dihedral angle $\alpha = 77.0(5)^\circ$ between blue plane (mean: N2C1C2) and yellow plane (mean: N1C44C55) in **5**.

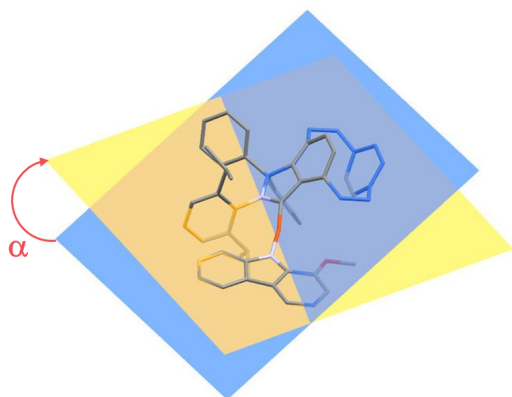


Figure S22. Dihedral angle $\alpha = 32.3(8)^\circ$ between blue plane (mean: N2C1C2) and yellow plane (mean: N1C43C54) in **6**.

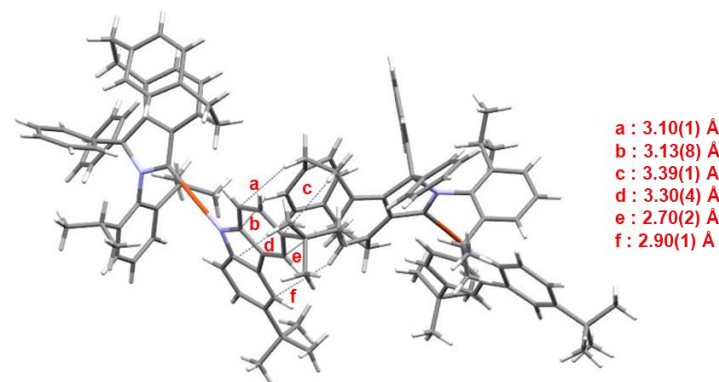


Figure S24. Intermolecular C–H \cdots π interactions between the Cz^{tBu} and iPC ligands in **4**.

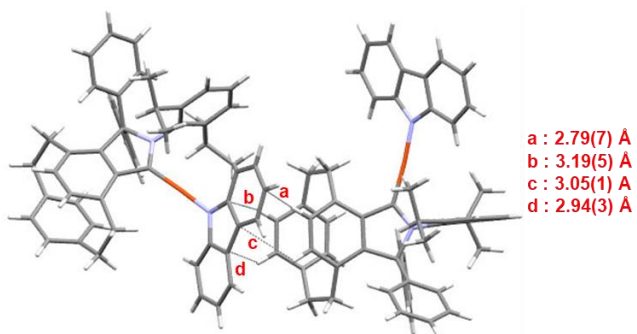


Figure S23. Intermolecular C–H \cdots π interactions between the Cz and iPC ligands in **3**.

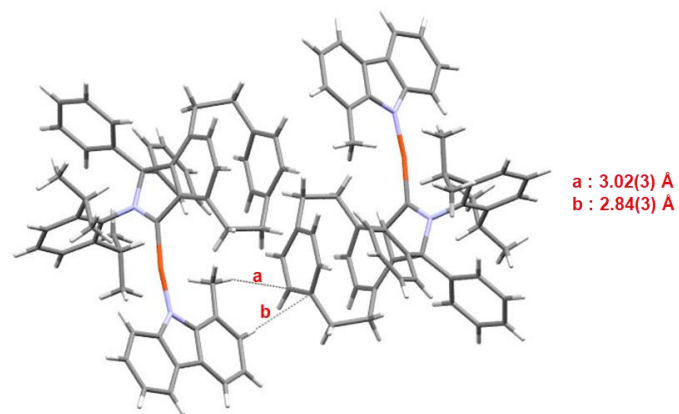


Figure S25. Intermolecular C–H \cdots π interactions between the MeCz and iPC ligands in **5**.

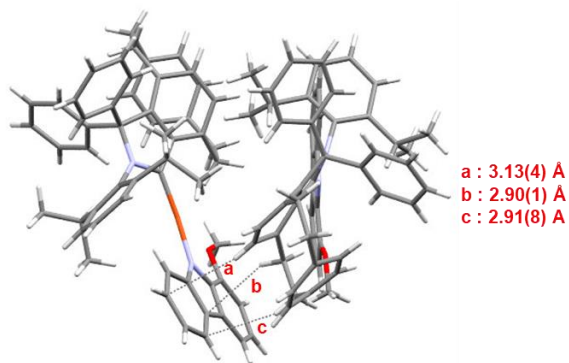


Figure S26. Intermolecular C–H··· π interactions between the ^{OMe}Cz and iPC ligands in **6**.

6. Photophysical Measurements

All photophysical measurements were performed in dry and deaerated solutions. The solid-state measurements were performed either in single-crystalline form (sample denoted as 'crystals') or, to remove co-crystallized molecules of solvent, single-crystals were ground and dried under vacuum for 24 h (sample denoted as 'solid'). Optical absorption spectroscopy was performed using an Agilent Cary 5000 spectrophotometer using standard 1 cm path length quartz cells. Excitation and emission spectra were recorded on an Edinburgh Instrument FLS1000 spectrometer, equipped with a 450 W Xenon arc lamp, double monochromators for the excitation and emission pathways, and a red-sensitive photomultiplier (PMT-980) as a detector. For NIR measurements liquid N₂-cooled PMT-1400, range up to 1400 nm was used. The excitation and emission spectra were corrected using the standard corrections supplied by the manufacturer for the excitation source's spectral power and the detector's sensitivity. Quantum yields in solution were measured using an FLS1000 spectrometer equipped with an integrating sphere (N-M01), or Quantaurus-QY Absolute PL quantum yield spectrometer (C11347- 11 Series: Standard type) from Hamamatsu and the quantum yield of solid samples were measured using an integrating cryosphere (Microstat N2) from Oxford Instruments. The luminescence lifetimes were measured using a μ F2 pulsed 60 W Xenon microsecond flashlamp, with a repetition rate of 100 Hz, and a time-correlated single photon counting (TCSPC) module or EPLED (365 nm with 1.7 μ W), with 50 ns pulse width and a TCSPC module, depending on the time range and a multichannel scaling (MCS) module or VPLED (383.8 nm with 1.1 mW or 449.6 nm with 37 mW), with 48.1 ns or 59.8 ns minimum pulse width respectively and an MCS module, depending on the time range. The emission was collected at a right angle to the excitation source.

7. UV-Visible Spectroscopy

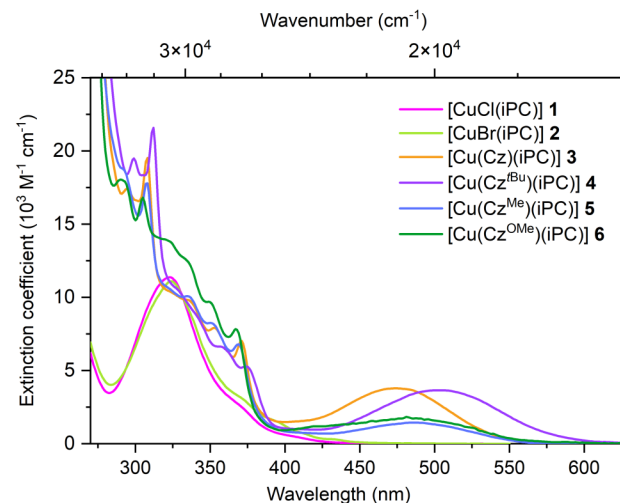


Figure S27. UV-Vis absorption spectra of compounds **1-6** in THF.

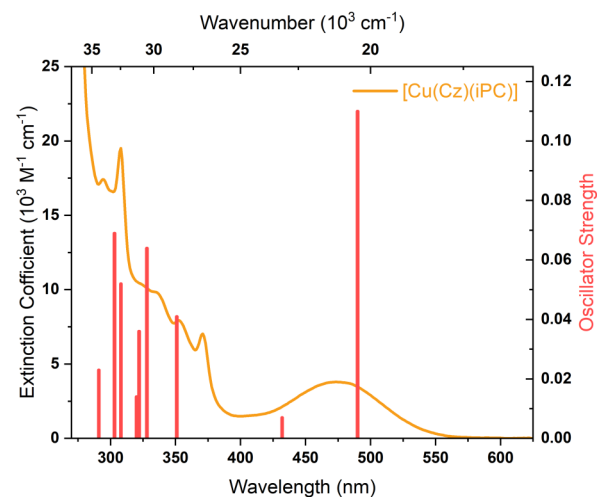


Figure S28. UV-Vis absorption spectra in THF and TD-DFT calculated oscillator strength of **3**.

8. Emission Studies

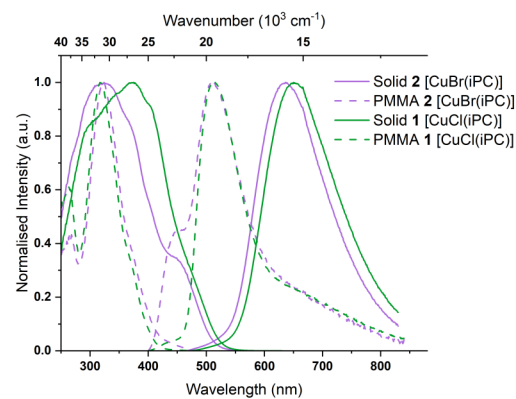


Figure S29. Normalized excitation and emission spectra of compounds **1** (green) and **2** (purple) at room temperature. Solid lines for solid state (ground) measurements and dash lines for measurements in PMMA matrix (1 wt% of the compound in DCM).

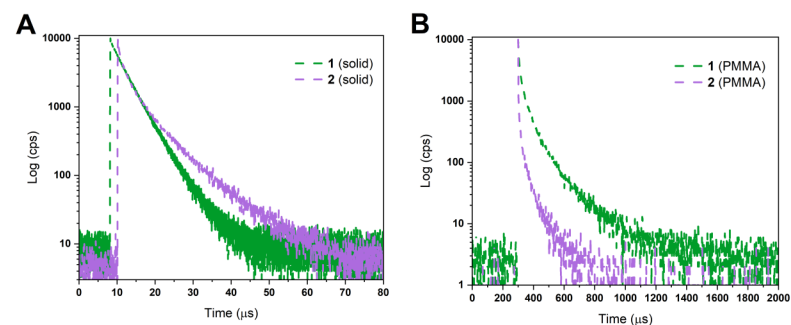


Figure S30. Emission decays of compound **1** (green) and **2** (purple) at room temperature (**A**: Solid state, **B**: PMMA).

Table S4. Selected photophysical data of compound **1** and **2** at RT.

	Medium	λ_{\max} (nm)	τ (μs) ^a	ϕ	k_r (10^5 s^{-1}) ^b
1	Solid (ground)	650	2.8 (38.7)/ 4.8 (61.3)	0.13	0.31
	PMMA	510	13 (50.0)/ 50 (42.3)/ 159 (8.7)	0.03	0.0062
2	Solid (ground)	635	1.2 (40.4)/ 4.4 (42.6)/ 9.9 (16.9)	0.03	0.064
	PMMA	510	14 (78.7)/ 73 (21.3)	0.02	0.0089

(a) For lifetimes fitted with two or multi exponentials, the pre-exponential factors are given in parentheses. (b) k_r was calculated using amplitude-weighted averaged lifetimes.

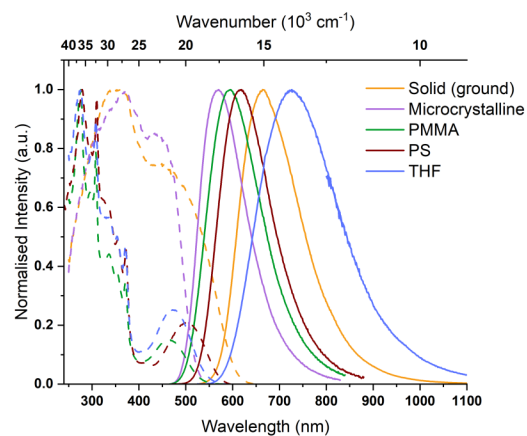


Figure S31. Normalized excitation and emission spectra of compound **3** in solid state (orange), microcrystalline state (purple), PMMA matrix (green; 1 wt% of the compound in DCM), PS matrix (brown; 1 wt% of the compound in DCM) and THF (blue) at room temperature. Solid lines for emission spectra and dash lines for excitation spectra.

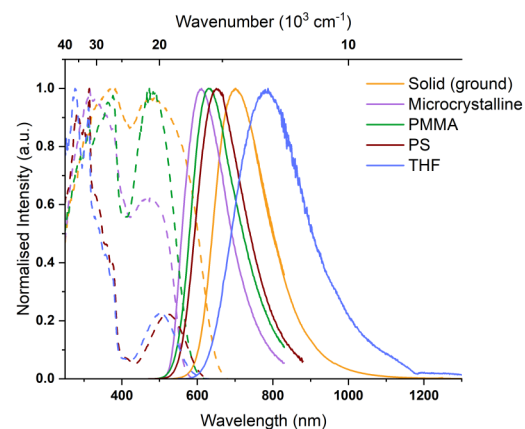


Figure S33. Normalized excitation and emission spectra of compound **4** in solid state (ground; orange), microcrystalline state (purple), PMMA matrix (green; 1 wt% of the compound in DCM), PS matrix (brown; 1 wt% of the compound in DCM) and THF (blue) at room temperature. Solid lines for emission spectra and dash lines for excitation spectra.

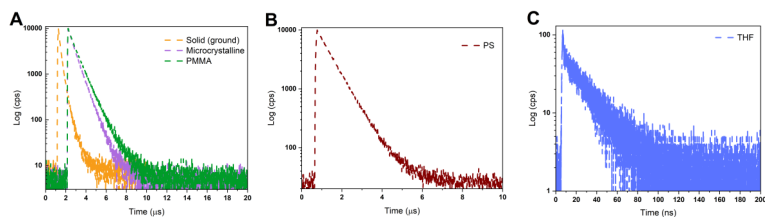


Figure S32. Emission decays of compound **3** at room temperature in solid state (ground; orange), microcrystalline state (purple), PMMA matrix (green), PS matrix (brown) and THF (blue).

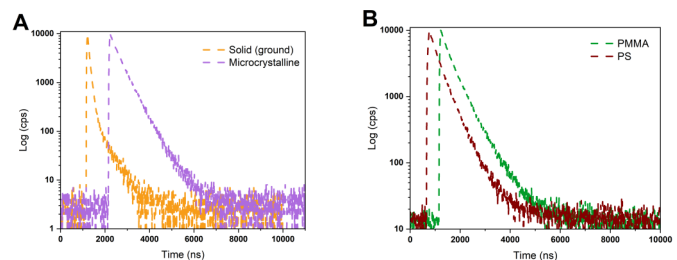


Figure S34. Emission decays of compound **4** at room temperature in solid state (ground; orange), microcrystalline state (purple), PMMA matrix (green) and PS matrix (brown).

Table S5. Selected photophysical data of compound **3** at RT.

	Medium	λ_{max} (nm)	τ (μs) ^a	ϕ	k_r (10^5 s^{-1}) ^b
3	Solid(ground)	665	0.18 (66.3)/ 0.33 (33.7)	0.22	9.8
	Microcrystalline	570	0.46 (62.1)/ 0.77 (37.9)	0.80	14
	PMMA	595	0.56 (59.4)/ 0.96 (40.6)	0.58	8.1
	PS	615	0.69 (98.7)/ 1.62 (1.2)	0.62	8.7
	THF	725	0.021	0.01	4.8

(a) For lifetimes fitted with two exponentials, the pre-exponential factors B are given in parentheses. (b) k_r was calculated using amplitude-weighted averaged lifetimes.

Table S6. Selected photophysical data of compound **4** at RT.

	Medium	λ_{max} (nm)	τ (μs) ^a	ϕ	k_r (10^5 s^{-1}) ^b
4	Solid(ground)	700	0.09 (94.6)/ 0.49 (5.4)	0.11	9.6
	Microcrystalline	610	0.39 (97.5)/ 0.72 (2.5)	0.75	19
	PMMA	630	0.27 (43.4)/ 0.59 (56.6)	0.30	6.6
	PS	650	0.28 (56.2)/ 0.53 (43.8)	0.34	8.7
	THF	785	n.d.	n.d.	-

(a) For lifetimes fitted with two exponentials, the pre-exponential factors B are given in parentheses. (b) k_r was calculated using amplitude-weighted averaged lifetimes.

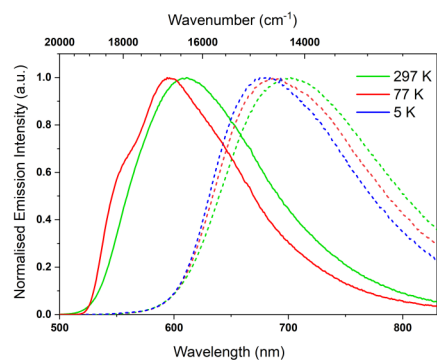


Figure S35. Normalized emission spectra of compound **4** in solid state (ground; short-dash lines), and microcrystalline state (solid lines) at various temperature. Green: 297 K, red: 77 K and blue: 5 K.

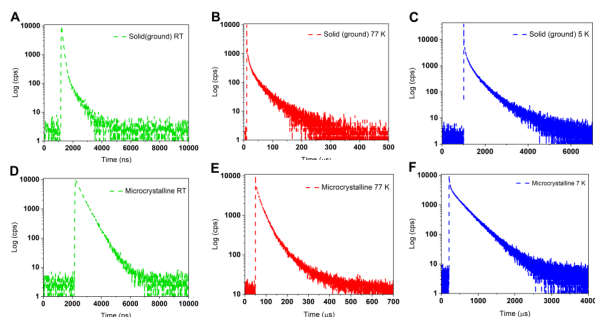


Figure S36. Emission decays of compound **4** at various temperature in solid state (ground; **A** (RT); **B** (77 K); **C** (5 K)), and microcrystalline state (**D** (RT); **E** (77 K); **F** (7 K)).

Table S7. Selected photophysical data of compound **4** at various temperature.

	Medium	λ_{\max} (nm)	τ (μs) ^a	ϕ	k_r (10^5 s^{-1}) ^b
4	Solid(ground; RT)	700	0.09 (94.6)/ 0.49 (5.4)	0.11	9.6
	Solid(ground; 77 K)	690	2.6 (52.6)/ 13 (35.9)/ 52 (11.5)	0.18	0.15
	Solid(ground; 5 K)	680	33 (35.0)/ 109 (33.9)/ 329 (25.7)/ 841(5.4)	-	-
	Microcrystal(RT)	610	0.39 (97.5)/ 0.72 (2.5)	0.75	19
	Microcrystal(77 K)	595	9.0 (30.1)/ 29 (62.3)/ 89 (7.6)	0.95	0.34
	Microcrystal(7 K)		38 (33.3)/ 297 (51.7)/ 594 (15.0)	-	-

(a) For lifetimes fitted with two exponentials, the pre-exponential factors B are given in parentheses. (b) k_r was calculated using amplitude-weighted averaged lifetimes.

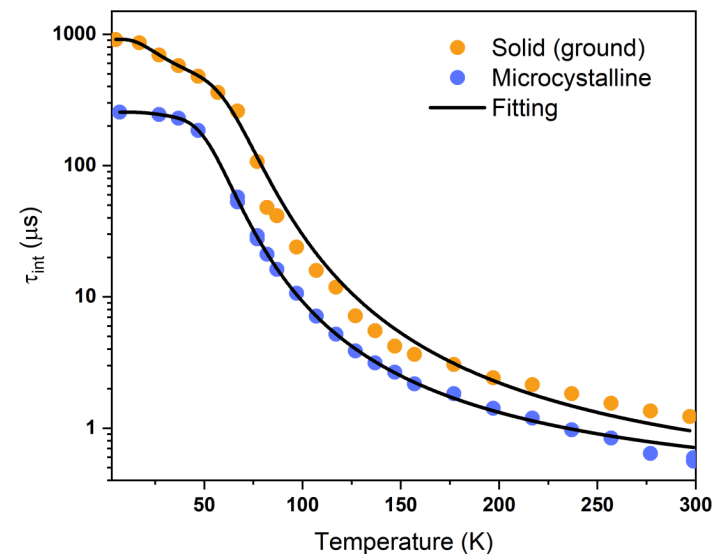


Figure S37. Variable temperature lifetimes of **4** in solid state (ground; orange) and in microcrystalline state (blue).

5-exponential TADF fitting equation:

$$\tau_{r,av}(T) = \frac{\left(2 + e^{\frac{-\Delta E(T_1^I - T_1^{II,III})}{k_B T}} + e^{\frac{-\Delta E(S_1 - T_1^{II,III})}{k_B T}} \right)}{\left(\frac{2}{\tau_r(T_1^{II,III})} + \frac{e^{\frac{-\Delta E(T_1^I - T_1^{II,III})}{k_B T}}}{\tau_r(T_1^I)} + \frac{e^{\frac{-\Delta E(S_1 - T_1^{II,III})}{k_B T}}}{\tau_r(S_1)} \right)}$$

Table S8. Temperature dependent life-times details for compound **4** in solid state (ground).

Temp (K)	τ_1 (μ s)	τ_2 (μ s)	τ_3 (μ s)	τ_2 (μ s)	τ <amp> (μ s)	τ <int> (μ s)	χ^2	$\Phi\%$	τ <intrinsic>
5	32.97(35)	109.44(34)	329.02(26)	841.36(5)	178.75	395.03	1.08	19.6	912.03
7	28.27(28)	111.85(34)	292.17(31)	611.79(7)	180.18	321.03	1.08	19.6	919.31
17	35.18(24)	156.23(56)	348.66(20)		165.89	231.76	1.07	19.3	859.55
27	26.11(33)	134.63(49)	318.60(18)		131.91	208.26	1.05	19	694.29
37	15.70(29)	59.33(27)	159.62(34)	331.67(10)	107.84	191.40	1.04	18.7	576.71
47	16.71(35)	57.01(29)	149.63(29)	309.55(7)	88.15	164.36	1.04	18.4	479.11
57	14.26(32)	41.11(35)	110.12(26)	244.36(7)	65.04	124.89	1.01	18.1	359.36
67	15.84(40)	35.08(31)	82.26(23)	181.26(6)	46.34	83.13	1.03	17.8	260.37
77	2.61(53)	13.34(36)	51.69(11)		12.11	30.95	0.97	17.6	68.84
87	1.86(54)	8.55(36)	28.45(10)		7.03	15.99	0.93	16.9	41.62
97	1.14(52)	4.87(38)	15.07(10)		4.01	8.30	1.01	16.8	23.88
107	0.87(52)	3.36(39)	9.73(9)		2.61	4.96	1.09	16.5	15.86
117	0.65(45)	2.25(45)	5.93(10)		1.92	3.20	1.08	16.2	11.86
127	0.30(40)	1.24(47)	3.47(13)		1.14	1.98	1.12	15.8	7.21
137	0.23(37)	0.91(50)	2.44(13)		0.85	1.40	1.10	15.5	5.52
147	0.17(37)	0.69(50)	1.72(13)		0.63	1.01	1.08	15.1	4.21
157	0.17(40)	0.64(50)	1.52(10)		0.53	0.81	1.13	14.6	3.65
177	0.18(43)	0.54(49)	1.08(8)		0.42	0.58	1.20	13.9	3.06
197	0.14(41)	0.39(50)	0.78(9)		0.31	0.42	1.02	13.2	2.41
217	0.18(72)	0.49(28)			0.27	0.34	1.25	12.6	2.15
237	0.17(82)	0.48(18)			0.22	0.28	1.13	12.3	1.82
257	0.15(88)	0.46(12)			0.18	0.24	1.07	11.9	1.55
277	0.12(91)	0.45(9)			0.15	0.21	1.36	11.4	1.35
297	0.11(93)	0.47(7)			0.13	0.19	1.16	11	1.22

τ <amp>: amplitude-weighted averaged lifetimes; τ <int>: intensity-weighted averaged lifetimes. A linear increase of $\Phi\%$ was found upon decreasing the temperature from 297 K to 77 K. At temperature <77 K, $\Phi\%$ were estimated by assuming this linear relationship.

Table S9. Temperature dependent life-times details for compound **4** in microcrystalline state.

Temp (K)	τ_1 (μ s)	τ_2 (μ s)	τ_3 (μ s)	τ <amp> (μ s)	τ <int> (μ s)	χ^2	$\Phi\%$	τ <intrinsic>
7	38.39(33)	296.96(52)	593.68(15)	255.35	387.56	1.13	100	255.35
27	73.70(21)	258.70(70)	498.49(9)	242.62	292.71	1.03	100	242.62
37	56.61(19)	231.73(69)	445.99(12)	224.80	275.08	1.10	98.89	227.32
47	59.87(21)	191.87(72)	411.78(7)	179.70	218.40	1.10	96.29	186.62
67	23.46(22)	52.05(74)	190.28(4)	50.75	67.91	1.18	95.02	53.40
77	9.01(30)	29.46(62)	88.71(8)	27.82	41.82	1.05	94.31	29.49
87	8.88(63)	25.81(37)		15.12	19.53	1.16	93.60	16.15
97	6.68(69)	16.83(31)		9.80	12.03	1.03	92.18	10.63
107	4.20(62)	10.18(38)		6.45	7.75	1.00	90.75	7.10
117	3.11(58)	6.83(42)		4.69	5.41	1.02	90.42	5.18
127	2.16(46)	4.58(54)		3.48	3.90	1.04	90.09	3.86
137	1.50(33)	3.29(67)		2.69	2.95	1.02	85.88	3.13
147	1.18(28)	2.56(72)		2.17	2.35	1.00	81.68	2.65
157	0.67(19)	2.02(81)		1.77	1.93	1.02	81.44	2.17
177	1.44(100)			1.44	1.44	0.96	78.06	1.84
197	0.27(12)	1.11(88)		1.01	1.08	0.94	76.38	1.32
217	0.23(15)	0.90(85)		0.81	0.88	0.92	73.69	1.09
237	0.10(15)	0.72(85)		0.63	0.71	1.06	73.29	0.85
257	0.14(13)	0.62(87)		0.56	0.61	0.99	72.90	0.76
277	0.14(21)	0.56(79)		0.47	0.53	1.04	71.76	0.65
297	0.20(33)	0.52(67)		0.41	0.47	0.91	74.72	0.54

τ <amp>: amplitude-weighted averaged lifetimes; τ <int>: intensity-weighted averaged lifetimes. A linear increase of $\Phi\%$ was found upon decreasing the temperature from 297 K to 77 K. At temperature <77 K, $\Phi\%$ were estimated by assuming this linear relationship.

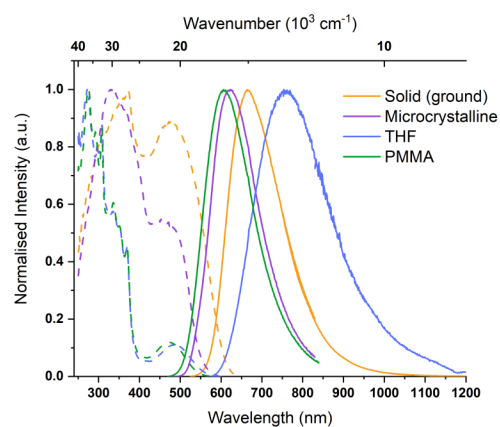


Figure S38. Normalized excitation and emission spectra of compound **5** in solid state (orange), microcrystalline state (purple), PMMA matrix (green; 1 wt% of the compound in DCM), and THF (blue) at room temperature. Solid lines for emission spectra and dash lines for excitation spectra.

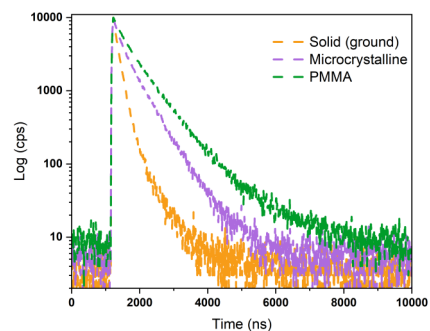


Figure S39. Emission decays of compound **5** at room temperature in solid state (ground; orange), microcrystalline state (purple), and PMMA matrix (green).

Table S10. Selected photophysical data of compound **5** at RT.

	Medium	λ_{\max} (nm)	τ (μs) ^a	ϕ	k_r (10^5 s^{-1}) ^b
5	Solid(ground)	665	0.15 (92.4)/ 0.48 (7.6)	0.15	8.4
	Microcrystalline	620	0.18 (39.5)/ 0.50 (60.5)	0.51	14
	PMMA	610	0.35 (52.2)/ 0.80 (47.8)	0.33	5.8
	THF	755	n.d.	n.d.	-

(a) For lifetimes fitted with two exponentials, the pre-exponential factors B are given in parentheses. (b) k_r was calculated using amplitude-weighted averaged lifetime.

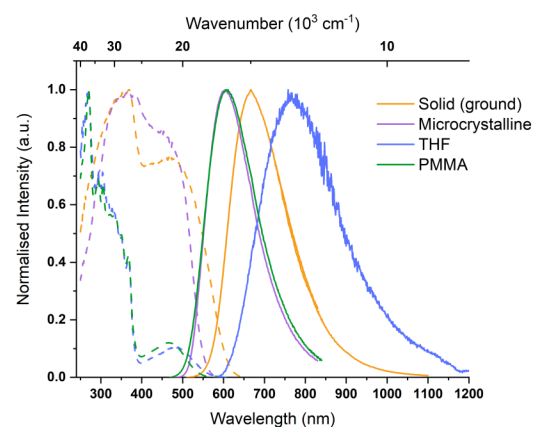


Figure S40. Normalized excitation and emission spectra of compound **6** in solid state (orange), microcrystalline state (purple), PMMA matrix (green; 1 wt% of the compound in DCM), and THF (blue) at room temperature. Solid lines for emission spectra and dash lines for excitation spectra.

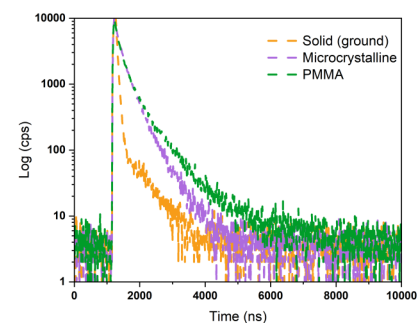


Figure S41. Emission decays of compound **6** at room temperature in solid state (ground; orange), microcrystalline state (purple), and PMMA matrix (green).

Table S11. Selected photophysical data of compound **6** at RT.

	Medium	λ_{\max} (nm)	τ (μs) ^a	ϕ	k_r (10^5 s^{-1}) ^b
6	Solid(ground)	665	0.034 (83.2)/ 0.078 (16.8)	0.03	8
	Microcrystalline	605	0.17 (70.5)/ 0.45 (29.5)	0.29	11
	PMMA	610	0.12 (64.4)/ 0.40 (30.9)/ 0.96 (4.6)	0.11	4.3
	THF	765	n.d.	n.d.	-

(a) For lifetimes fitted with two or multi exponentials, the pre-exponential factors B are given in parentheses. (b) k_r was calculated using amplitude-weighted averaged lifetime.

9. TD-DFT calculations

Calculations were performed with the ORCA 4.2.1 program suite^[7] and the PBE0^[8] hybrid functional, using density functional theory (DFT) by KOHN und SHAM^[9] on the Linux-HPC-Cluster of TU Dortmund University. For geometry optimisations and calculations of molecular orbitals the split-valence basis set def2-TZVP with zero-order regular approximation of relativistic effects (ZORA) and BECKE-JOHNSON damping (D3BJ) were used.^[10] Frequency analysis was used to confirm convergence into a global minimum structure. For time-dependent DFT calculations the single-valence base set ZORA-def2-SVP was used as implemented in ORCA 4.2.1. All calculations were performed with tight SCF convergence ($\Delta E = 1 \cdot 10^{-8}$ au).

Table S12. Singlet excitations calculated for **3** in the ground state geometry.

State	Energy [cm ⁻¹]	λ [nm]	f_{osc}
1	20389.8	490.4	0.109518062
2	23174.3	431.5	0.007314798
3	26254.5	380.9	0.000002476
4	28467.2	351.3	0.040752679
5	30519.2	327.7	0.063950082
6	31042	322.1	0.03578957
7	31259.1	319.9	0.013818053
8	31273.7	319.8	0.011977486
9	31505.9	317.4	0.0093057
10	31816.7	314.3	0.003602113
11	32173.5	310.8	0.00116711
12	32504.1	307.7	0.052118766
13	32703.1	305.8	0.016319577
14	33002.6	303	0.068659206
15	33538.3	298.2	0.003008278
16	34402	290.7	0.023140876
17	34611.5	288.9	0.001316569
18	34953.1	286.1	0.010739202
19	35402.2	282.5	0.014223935
20	35511.2	281.6	0.001419523

Table S13. XYZ coordinates of optimized molecule **3**.

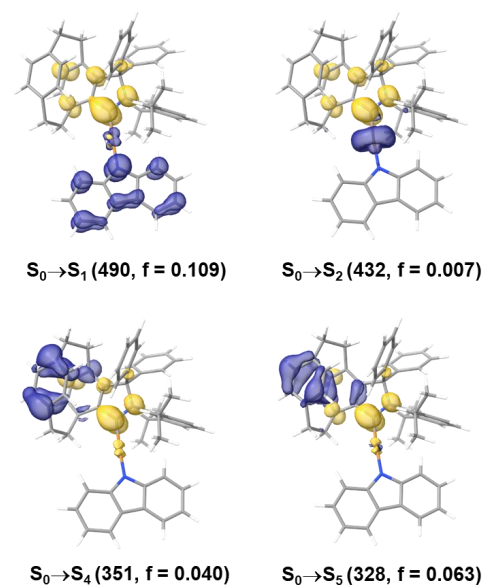
H	7.879319	7.214286	5.494719
H	8.044477	7.257443	7.251335
H	8.2808	9.754623	5.577153
C	8.602764	7.134456	6.31501
H	9.176721	4.197292	3.467002
H	8.688051	9.760638	7.307934
H	11.45465	12.98755	12.06017
H	9.026412	6.125512	6.298074
C	9.092602	9.605416	6.299954
H	9.553505	2.93508	5.58026
H	11.1036	10.77493	10.98928
C	11.62378	12.87482	10.9902
C	9.954863	4.509595	4.161481

C	9.686033	8.199918	6.160711
C	11.42434	11.62146	10.38243
H	9.501231	7.643732	8.78874
C	10.16338	3.805464	5.34369
H	9.848256	10.38288	6.127295
H	12.18633	14.93851	10.70669
H	10.0866	8.106713	5.145231
C	12.03298	13.96843	10.23398
H	10.5555	6.169196	2.935828
C	10.73697	5.625168	3.859058
H	10.90325	10.29377	0.401298
C	11.62783	11.43858	9.020428
C	10.53775	7.776655	8.485922
H	11.47103	10.46437	8.559176
H	11.33455	7.947549	-0.10199
C	10.82879	8.028135	7.143785
C	11.15488	4.231355	6.228281
C	12.24886	13.80764	8.860649
C	11.31637	9.655905	1.18115
H	11.32289	3.69813	7.16236
C	11.5599	8.316541	0.898488
C	12.04578	12.53532	8.253161
H	11.27637	12.24307	1.884364
C	11.74728	6.048556	4.726015
H	11.29891	7.504461	10.48227
C	11.7865	10.23187	2.362202
H	12.32847	5.54422	0.788543
H	13.00846	16.65628	8.616759
C	11.5456	7.707884	9.441379
C	11.93984	5.338426	5.921274
C	12.67422	14.68173	7.794882
C	12.25283	7.47146	1.778509
C	12.13549	9.311828	3.368722
C	12.32932	7.942422	3.096001
C	12.07987	11.70351	2.399062
N	12.32028	12.57911	6.902475
C	13.03033	16.03272	7.723037
C	12.18441	8.195057	6.777003
Cu	12.258232	11.11265	5.795749
C	12.28551	9.554488	4.791212
C	13.01101	6.301993	1.196613
N	12.46011	8.371801	5.374446
C	12.65759	7.230578	4.401559
H	12.09496	12.06643	3.434609
C	12.70248	13.87147	6.621153
H	12.71911	5.64466	6.615788

H	13.28825	12.89952	1.008791
H	13.23351	11.2237	-0.95905
H	13.58049	5.809679	1.989533
H	13.53697	6.568806	-0.92707
H	13.46529	8.884445	-1.68203
C	12.86071	7.950781	9.07136
C	13.46068	12.06782	1.701858
C	13.4136	16.57131	6.49928
C	13.74891	10.51583	-0.30893
C	13.20738	8.219051	7.742182
C	13.88532	9.186431	-0.72158
H	13.69218	17.62181	6.43066
C	14.00183	6.753002	0.049432
C	13.09516	14.42314	5.393358
H	13.80363	4.687592	4.3765
C	14.09079	10.89518	0.993905
H	13.63951	7.965006	9.831967
C	13.44578	15.76694	5.345701
C	14.37847	8.212548	0.153585
H	14.14408	12.43681	2.476515
H	13.12491	13.80633	4.495362
C	14.14347	6.818655	4.409781
C	14.5475	5.48042	4.375287
H	14.88637	6.104529	0.101852
H	13.75198	16.20639	4.396666
C	14.8561	9.984305	1.734463
C	15.00801	8.66939	1.315855
C	14.63452	8.611019	7.434208
H	14.68717	8.82125	6.364535
H	14.83516	8.854422	4.357417
H	14.31522	10.71947	7.901466
C	15.13048	7.807929	4.377148
H	15.23856	10.2861	2.709817
H	15.50064	7.953532	1.969555
H	15.37708	6.577082	7.163076
C	15.00522	9.907217	8.159183
H	14.98154	9.787341	9.24922
C	15.90181	5.14475	4.33709
C	15.61798	7.481704	7.734444
H	15.61463	7.222469	8.800875
H	16.19165	4.095525	4.313108
C	16.48191	7.478138	4.354979
H	16.01891	10.22028	7.879193
H	16.63907	7.781202	7.469419
C	16.87487	6.140328	4.337248
H	17.22893	8.270327	4.3419

H 17.93123 5.878035 4.319208

Figure S42. Electron density differences for compound 3.



10. References

- [1] W. L. F. Armarego, *Purification of laboratory Chemicals*, Butterworth Heinemann, Oxford; Boston, **1996**.
- [2] S. Maity, A. M. T. Muthig, I. Sen, O. Mrózek, A. Belyaev, B. Hupp, A. Steffen, *Angew. Chem. Int. Ed.* **2024**, e202409115.
- [3] R. B. Bedford, M. Betham, *J. Org. Chem.* **2006**, *71*, 9403.
- [4] G. M. Sheldrick, *Acta Crystallogr. C* **2015**, *71*, 3.
- [5] O. V. Dolomanov, L. J. Bourhis, R. J. Gildea, J. A. K. Howard, H. Puschmann, *J. Appl. Crystallogr.* **2009**, *42*, 339.
- [6] A. L. Spek, *Acta Cryst.* **2015**, *71*, 9.
- [7] a) F. Neese, *WIREs Comput Mol Sci* **2012**, *2*, 73; b) F. Neese, *WIREs Comput Mol Sci* **2018**, *8*, e1327.
- [8] J. P. Perdew, M. Ernzerhof, K. Burke, *J. Chem. Phys.* **1996**, *105*, 9982.
- [9] W. Kohn, L. J. Sham, *Phys. Rev.* **1965**, *140*, A1133.
- [10] a) F. Weigend, R. Ahlrichs, *Phys. Chem. Chem. Phys.* **2005**, *7*, 3297; b) S. Grimme, J. Antony, S. Ehrlich, H. Krieg, *J. Chem. Phys.* **2010**, *132*, 154104; c) S. Grimme, S. Ehrlich, L. Goerigk, *J. Comput. Chem.* **2011**, *32*, 1456; d) E. van Lenthe, E. J. Baerends, J. G. Snijders, *J. Chem. Phys.* **1998**, *101*, 9783.

Eidesstattliche Versicherung (Affidavit)

Name, Vorname
(Surname, first name)

Matrikel-Nr.
(Enrolment number)

Belehrung:

Wer vorsätzlich gegen eine die Täuschung über Prüfungsleistungen betreffende Regelung einer Hochschulprüfungsordnung verstößt, handelt ordnungswidrig. Die Ordnungswidrigkeit kann mit einer Geldbuße von bis zu 50.000,00 € geahndet werden. Zuständige Verwaltungsbehörde für die Verfolgung und Ahndung von Ordnungswidrigkeiten ist der Kanzler/die Kanzlerin der Technischen Universität Dortmund. Im Falle eines mehrfachen oder sonstigen schwerwiegenden Täuschungsversuches kann der Prüfling zudem exmatrikuliert werden, § 63 Abs. 5 Hochschulgesetz NRW.

Die Abgabe einer falschen Versicherung an Eides statt ist strafbar.

Wer vorsätzlich eine falsche Versicherung an Eides statt abgibt, kann mit einer Freiheitsstrafe bis zu drei Jahren oder mit Geldstrafe bestraft werden, § 156 StGB. Die fahrlässige Abgabe einer falschen Versicherung an Eides statt kann mit einer Freiheitsstrafe bis zu einem Jahr oder Geldstrafe bestraft werden, § 161 StGB.

Die oben stehende Belehrung habe ich zur Kenntnis genommen:

Official notification:

Any person who intentionally breaches any regulation of university examination regulations relating to deception in examination performance is acting improperly. This offence can be punished with a fine of up to EUR 50,000.00. The competent administrative authority for the pursuit and prosecution of offences of this type is the chancellor of the TU Dortmund University. In the case of multiple or other serious attempts at deception, the candidate can also be unenrolled, Section 63, paragraph 5 of the Universities Act of North Rhine-Westphalia.

The submission of a false affidavit is punishable.

Any person who intentionally submits a false affidavit can be punished with a prison sentence of up to three years or a fine, Section 156 of the Criminal Code. The negligent submission of a false affidavit can be punished with a prison sentence of up to one year or a fine, Section 161 of the Criminal Code.

I have taken note of the above official notification.

Ort, Datum
(Place, date)

Unterschrift
(Signature)

Titel der Dissertation:
(Title of the thesis):

Ich versichere hiermit an Eides statt, dass ich die vorliegende Dissertation mit dem Titel selbstständig und ohne unzulässige fremde Hilfe angefertigt habe. Ich habe keine anderen als die angegebenen Quellen und Hilfsmittel benutzt sowie wörtliche und sinngemäße Zitate kenntlich gemacht.
Die Arbeit hat in gegenwärtiger oder in einer anderen Fassung weder der TU Dortmund noch einer anderen Hochschule im Zusammenhang mit einer staatlichen oder akademischen Prüfung vorgelegen.

I hereby swear that I have completed the present dissertation independently and without inadmissible external support. I have not used any sources or tools other than those indicated and have identified literal and analogous quotations.

The thesis in its current version or another version has not been presented to the TU Dortmund University or another university in connection with a state or academic examination.*

***Please be aware that solely the German version of the affidavit ("Eidesstattliche Versicherung") for the PhD thesis is the official and legally binding version.**

Ort, Datum
(Place, date)

Unterschrift
(Signature)